Geometric and electronic structure of Dysprosium thin films on Tungsten surfaces

A thesis submitted in accordance with the requirements of the

University of Liverpool

for the degree of

Doctor in Philosophy

by

Nasser Moslemzadeh

of the

Surface Science Research Centre

December 2001

Acknowledgements

First of all I have to thank God for his help during whole my life including my Ph D studies.

In Persian culture, a good teacher has tremendous respect for his student which never ends. So as a Persian, I would like to express my ultimate thanks to my supervisor Dr. S. D. Barrett for introducing me to the world of surface science and rare earths. The constant support and attention of Steve was a great encouragement during my Ph D career.

The IRC has provided the ideal place to pursue my Ph D studies and there are a lot of people who need to be recognised and appreciated for their daily support, such as John (Ledward, Kitson), Tony, Geoff, Paul (Harisson, Unsworth) and how can I forget John Murray who as an angel helped me in my difficult technical problems. Special thanks is given to Sam and Colin for lots of technical assistance and scientific discussions that helped me to a better understanding of surface science, and to Julian and Erik for their help in my STM work. I also thank all my fellow students and friends for providing a nice and friendly atmosphere for study.

Part of this research has been done at Daresbury where I was supported by helpful people such as Vin Dhanak and George Miller.

I would also like to appreciate Ministry of Science, Research and Technology of Iran for supporting me with the grant during my Ph D.

I would like to express my gratitude to my family specially, my Mother, for their support and encouragement through my life including my Ph D studies.

Above all I would like to thank My wife for being with me from beginning to end.

Abstract

The rare earth thin films are frequently the focus of investigators due to their unusual structural and magnetic properties. Despite the potential interest of Dy/W systems to the surface/rare earth community, they have been little studied. This study is the first try of growing Dy on W(100) and W(112) and W(110) in which almost a complete set of information about film morphology and electronic structure of the surface and interface have been achieved. A set of different experiments have been done for this purpose including LEED, XPS, UPS (with synchrotron radiation) and STM.

The growth modes of Dy on different W substrates (W(100), W(112) and W(110)) at RT and at elevated temperatures have been determined by XPS of Dy $3d_{3/2}$ and W 4f intensities.

Crystallographic ordering and the epitaxial relationship between adsorbate Dy and different W substrates have been studied with LEED and the effect of annealing temperature on the resultant superstructures was investigated.

As a complementary study to the LEED and growth mode investigations of the film morphology, Dy/W(100) and Dy/W(112) systems have been studied by STM. Correlation between the STM results and associated LEED and growth mode studies have been discussed.

The electronic structures of different Dy structures on W(100) have been investigated by Core Level Shift (CLS) and valence–band analysis using a synchrotron radiation. CLS of the W $4f_{7/2}$ was used to investigate surface reactions which will take place between Dy and W during growth and subsequent annealing to understand what will happen to this system under annealing processes, necessary for improving film structure. The electronic band structure of Dy films have also been monitored during growth and annealing processes and correlation between changes in the film morphology, valance band changes and CLS of the W $4f_{7/2}$ features were discussed.

Contents

Chapter one:. Introduction 1

Chapter two:. Rare Earth Properties 5

2.1. What are RE's 5

2.2. Importance of RE's 6

2.3. Structure of RE's 8

2.4. Electronic Structure of RE's 12

2.4.1. Mixed–valence phenomena 15

2.4.2. Surface states 19

2.4.3. The surface order dependent state 20

2.4.4. SCLS of rare-earths 22

2.5. Magnetic properties of RE's 26

2.5.1. Surface Magnetism 28

2.5.1.1. Surface–Enhanced Magnetic Order 29

2.5.1.2. Surface–To–Bulk Coupling 29

Chapter three: Experimental details 31

3.1. Synchrotron based experimental details 31

3.1.1. Introduction 31

3.1.1.1. Synchrotron radiation 31

3.1.1.2. Advantages of Synchrotron radiation for photoemission spectroscopy 33

3.1.2. Synchrotron Radiation Source(SRS) at Daresbury Laboratory 35

3.1.3. Beamline 4.1 37

3.1.3.1. Beam characteristics of beamline 4.1 37

3.1.3.2. Experimental chamber of beamline 4.1 49

3.1.3.3. Sample holder used at beamline 4.1 41

3.1.3.4. Scienta SES analyser at beamline 4.1 41

3.2. LEED and XPS experimental details 45

3.2.1. Experimental chamber for LEED and XPS at Liverpool 45

3.2.2. LEED and LEED I–V 48

3.3. Experimental details of Scanning Tunnelling Microscopy 49

3.3.1. STM chamber 49
3.3.2. E-beam heater and sample holder for STM experiments 51
3.4. Evaporator 53

Chapter four: Growth characterisation of Dy films on different W surfaces **55**
4.1. Introduction 55
4.2. Growth mode study 56
4.2.1. Prediction of growth mode based on free–energy discussion 56
4.2.1.1. The Frank-van der Merwe (FM) growth mode 57
4.2.1.2. The Stranski–Krastanov growth mode 59
4.2.1.3. The Volmer–Weber (VW) growth mode 59
4.2.1.4. The Simultaneous Multilayer (SM) mode 60
4.2.1.5. The Monolayer Plus Simultaneous Multilayer (MSM) growth mode 60
4.3. Growth monitoring 64
4.4. Background subtraction 71
4.4.1. The Shirley background 72
4.4.2. Tougaard background 73
4.5. Experimental details 74
4.6. Growth monitoring results 75
4.6.1. Dy/W(100) 76
4.6.1.1. Growth at RT 76
4.6.1.2. Growth at elevated temperatures 76
4.6.2. Dy/W(112) 78
4.6.3. Dy/W(110) 80

Chapter five: Structural analysis using Low–Energy Electron Diffraction (LEED) **83**
5.1. Introduction 83
5.2. Previous work 84
5.3. Experimental details 86
5.4. Dy/W(100) 87
5.4.1. Discussion 90

5.4.1.1. Pseudo hexagonal LEED pattern of Dy/W(100) 90
5.4.1.2. c(2x2) structure 99
5.4.2. LEED I–V 99
5.5. Dy/W(112) 104
5.6. Dy/W(110) 109

Chapter six: Scanning Tunnelling Microscopy of Dy films on W(100) and W(112) substrates **113**
6.1. Introduction 112
6.2. Theory of Scanning tunnelling microscopy 114
6.3. Experimental detail 120
6.4. Clean W(100) 121
6.5. Dy/W(100) 123
6.5.1. Growth at RT 123
6.5.2. c(8x2) Structure 126
6.5.2.1. Annealing to 750K 126
6.5.2.2. Annealing to 820K 132
6.5.3. c(2x2) structure 133
6.6. Clean W(112) 137
6.7. Dy/W(112) 137
6.7.1. Growth at RT 137
6.7.2. Annealing to 500K 138
6.7.3. Annealing to 1100K 143
6.7.4. Annealing to 1500K 144
6.7.5. Annealing to 1600K 147

Chapter seven: Theory of the surface core–level shift **151**
7.1. Introduction 151
7.2. The theoretical origin of Surface Core–Level Shift 153
7.2.1. SCLS from Electronic Structure point of view (Band Approach) 153
7.2.2. Initial state–Final state approach 158
7.2.2.1. Initial state contribution 158
7.2.2.2. Final state contribution 160

7.2.3. The Thermodynamic Approach 161
7.2.4. The effect of adsorption on substrate core level shift 166
7.3. lineshape 168
7.3.1. Core–hole lifetime 169
7.3.2. Phonon broadening 171
7.3.3. Plasmon 173
7.3.4. Electron hole pairs 174
7.3.5. Decomposing lineshape 174

Chapter eight: Electronic Structure of Dy/W(100) system 177
8.1. Introduction 177
8.2. Experimental details 178
8.3. Clean W(100) 179
8.4. Growth at RT 183
8.5. Annealing investigation 187
8.5.1. Annealing of 1.2 Dy on W(100) 187
8.5.2. Annealing of 7.5 ML Dy on W(100) 192
8.5.3. c(2x2) structure 196

Chapter nine: Summary and conclusions 201
9.1. Growth mode studies 201
9.2. Structural analysis using LEED 201
9.2.1. LEED studies of Dy/W(100) 201
9.2.2. LEED I–V 202
9.2.3. LEED studies of Dy/W(112) 202
9.3. STM analysis 203
9.3.1. STM studies of Dy/W(100) 203
9.3.2. STM studies of Dy/W(112) 203
9.4. Electronic properties of Dy/W(100) 204
9.4.1. SCLS analysis 204
9.4.2. Valence band studies 205
9.5. Summary 206
9.6. Future work 207
List of acronyms and abbreviations 209
References 211

Chapter 1

Introduction

The study of surface properties is of fundamental importance in understanding the surfaces and interfaces of technologically important structures. The structures of surfaces are intimately linked to their electronic, magnetic and chemical properties. This means that surface structure can not be studied in total isolation from the other aspects. Therefore, surface science is an interdisciplinary science in which often no boundaries exist between physics, chemistry and material science.

The growth of ultra-thin metallic films, deposited on to single crystals of other metals, represent a specific class of adsorbates of considerable fundamental and technological interest. The interface between dissimilar metals can effect the state of both the adsorbate and substrate, and the reduced co-ordination of sub-monolayer structures can shift electronic energy levels, modify their density of states and influence the atomic geometry, where adsorbate-adsorbate or adsorbate-substrate interactions may dominate. Careful choice of the substrate material and crystal face can produce adsorbed layers which may be able to accommodate a large stress, leading to phases not normally observed in bulk structures at room temperature and pressure. Such novel structures may produce unique or unusual electronic effects. For example, transition metals or rare-earth metals can show unique magnetic effects caused by coupling across the layers.

The study of thin films of rare–earth elements is an area of increasing interest due to their potential applications for magnetic multilayers [1, 2]. They have been deposited on different substrates, such as semiconductors (see for example [3-5]) or transition metals (seer for example [2, 6-12]) and the formation of surfaces and interfaces has been studied as a key to further understanding of magnetic multilayer formation.

The Liverpool Rare Earth Group (REG) have spent many years studying the geometric and electronic structures of rare–earth single crystal surfaces with low-energy electron diffraction (LEED), low–energy electron diffraction intensity-voltage (LEED I-V), scanning tunnelling microscopy (STM) and synchrotron radiation photoemission. The study is motivated by a desire to understand fully the solid state properties of these rare-earth elements.

Dysprosium (Dy) is of particular interest among the rare–earth metals because the electronic configuration in its solid state is different from that of the atomic state [12]. However, to date few investigations of Dy thin films have been carried out compared with other rare–earth elements (see Ref. [6] for such studies).

The refractory metals (RM) as substrates provide no adsorbate–induced reconstruction and no interdiffusion of rare–earth films. Also, these substrates are stable against reaction with overlayers at elevated temperatures [13]. For this reasons most rare–earth film studies have used the surfaces of W or Mo as the substrate. The choice of Mo and W bulk single crystals as substrates for these studies is due both to their high surface energies and lattice matching considerations.

Despite the potential interest of Dy/W systems to the surface/rare earth community, they have been little studied. A few studies of Dy on refractory metals have been carried out over the last two decade [9, 10, 14-19]. Of these the only growth investigation for Dy on W(100), W(112) and W(110) surfaces (used in the current study) was by Ciszewski and Melmed [20] who used field electron emission from a sharp W tip. The W surface was not flat and had a very small effective area, and so their conclusions regarding growth can not necessarily be extrapolated to atomically flat surfaces. The only other investigations on Dy/W systems are that of the Li *et al* [8] who studied Dy/W(110) with LEED and Gonchar *et al* [14] who studied Dy/W(112) by work function analysis.

Therefore, this is the first study of the growth of Dy on W(100), W(112) and W(110) in which a very extensive set of information about film morphology and electronic structure of the surface and interface has been acquired. A set of different techniques has been used for this purpose, including LEED, XPS, UPS (with synchrotron radiation) and STM. While in image processing for LEED and STM the latest version of Image SXM software [21] has been used, a number of computer programs have also been written for the calculations in this study, from simple background subtraction macros to more complicated macros for SCLS analysis.

In this study the following topics have been considered:

*) In Chapter 2, properties of rare earths and especially Dy will be studied.

*) Chapter 3 is devoted to experimental details in which experimental apparatus used in this research are described.

Producing flat and well ordered films of Dy on tungsten surfaces is one of the major aims of this research. This is very important for the future applications of these films in complementary experiments such as magnetic properties investigations which can bring them closer to the practical applications. Therefore, chapters 4, 5 and 6 are devoted to this issue.

*) In chapter 4, growth of Dy on different W substrates including:W(100), W(112) and W(110) will be studied using XPS technique and Dy growth at different temperature will be investigated.

*) In chapter 5, film ordering and the epitaxial relationship between Dy as adsorbate and different W surfaces as substrate will be studied with LEED and the effect of annealing

temperature and the superstructures resulted by it will be investigated.

*) In chapter 6, STM results about the films morphology of the Dy/W(100) and Dy/W(112) systems are presented.

*) Because of importance of the theory behind SCLS analysis used in chapter 8, This theory has been fully studied in chapter 7.

*) In chapter 8, electronic structure of different Dy structures on W(100) are investigated by SCLS and valence band analysis using synchrotron radiation.

*) In chapter 9 a summary of the work done in the previous chapters will be presented.

Chapter 2

Rare Earth Properties

2.1. What are Rare Earths

The *lanthanides* are elements 57 – 71 as shown in the periodic table in Fig.1.1. These elements result from the filling of the 4f shell with electrons across the series. Often the term *'rare earths'* is used to refer to the lanthanides which is incorrect as the term RE specifically refers to the lanthanides *and* elements 21 and 39 (Sc and Y). The 4f electrons form a shallow core-level which does not play an active part in bonding with other atoms and so all interactions occur through the valence s and d electrons. Each of the REs possess the same basic valence configuration of $[ds]^3$ – $[3d4s]^3$ in the case of Sc, $[4d5s]^3$ in the case of Y and $[5d6s]^3$ for most of the lanthanides. This shared valence configuration leads to remarkably similar properties across the series. It is slightly modified in the cases of Eu and Yb where a valence electron is promoted to the 4f shell to provide a more stable half-filled or filled shell configuration. Due to the fact that neither Sc nor Y possess 4f electrons in their ground state they are often considered as 'prototype' REs and are particularly useful in testing whether any property of the REs is derived from the 4f electrons.

The REs are further split into two sub-groups. The 'lights' consist of the elements from La to Sm with the exception of Eu, the 'heavies' include the lanthanides Gd – Lu along with Sc and Y. Differences exist between these two groups (e. g. crystal structure) and in fact many elements from each subgroup are found together in ores of the Earth.

Due to their reactivity, the REs are not found in elemental form in the Earth's crust, but only as compounds requiring purification. Highly reactive, it took over 150 years to separate all of the rare earths from their ores. The final discovery was of Pm in fission

fragments. The difficulties associated with producing clean single–crystal surfaces of the hexagonal close–packed (hcp) rare earth metals has ensured that there is a shortage of even the most basic information regarding their surface atomic and electronic structure.

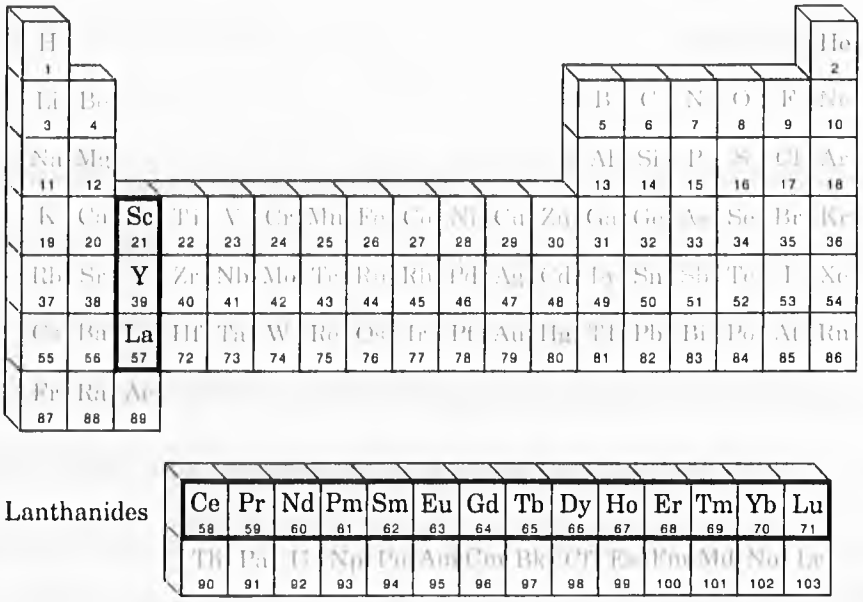

Fig.2.1. Periodic table of the elements.

The high reactivity of the REs was until recently a significant problem in their study. A comprehensive review of the methods used to obtain pure samples is given by Barrett and Dhesi [6], which also details the production of bulk single crystals. It is important to limit exposure to contaminating elements following purification, and REs are best stored in vacuum or an argon atmosphere. Even with these precautions, in situ studies of samples with clean surfaces in ultra-high vacuum (UHV) are limited, due to the high reactivity of the REs to the gases in the residual atmosphere (particularly hydrogen). Therefore, one of the most efficient methods of producing high quality samples is by epitaxial growth in situ, from well outgassed vapour sources.

2.2. Importance of REs

REs have been the subject of various research due to their unusual electronic, magnetic

and structural properties. In the 1960's and 1970's several important discoveries such as RE phosphors, cracking catalysts and RE-3d permanent magnets, etc. have made significant practical impact and stimulated much research. For example the lanthanides represent a group of metals which illustrate a wide range of magnetic phenomena which makes them of singular interest to the solid state physicist. The origin of these effects is the presence of a partially–filled 4f shell, a situation which has proven difficult to treat rigorously within any of the current theories of electronic structure.

Element	Z	A	Electronic configuration	Radius (nm)		Crystal structure	Lattice parameters (nm)		
				ionic	metallic		a	c	c/a
Scandium	21	45	(3d4s)3	0.0785	0.1641	hcp	0.3309	0.5268	1.592
Yttrium	39	89	(4d5s)3	0.0880	0.1801	hcp	0.3648	0.5732	1.571
Lanthanum	57	139	4f0(5d6s)3	0.1061	0.1879	dhcp	0.3774	1.2171	3.225
Cerium	58	140	4f1(5d6s)3	0.1034	0.1825	fcc	0.5161	-	-
Praseodymium	59	141	4f2(5d6s)3	0.1013	0.1828	dhcp	0.3672	1.1833	3.222
Neodymium	60	144	4f3(5d6s)3	0.0995	0.1821	dhcp	0.3658	1.1797	3.225
Promethium	61	(145)	4f4(5d6s)3	0.0979	0.1811	dhcp	0.365	1.165	3.19
Samarium	62	150	4f5(5d6s)3	0.0964	0.1804	rhom	0.3629	2.6207	7.222
Europium	63	152	4f7(5d6s)2	0.0950	0.2042	bcc	0.4583	-	-
Gadolinium	64	157	4f7(5d6s)3	0.0938	0.1801	hcp	0.3634	0.5781	1.591
Terbium	65	159	4f8(5d6s)3	0.0923	0.1783	hcp	0.3606	0.5697	1.580
Dysprosium	66	163	4f9(5d6s)3	0.0908	0.1774	hcp	0.3592	0.5650	1.573
Holmium	67	165	4f10(5d6s)3	0.0894	0.1766	hcp	0.3578	0.5618	1.570
Erbium	68	167	4f11(5d6s)3	0.0881	0.1757	hcp	0.3559	0.5585	1.569
Thulium	69	169	4f12(5d6s)3	0.0869	0.1746	hcp	0.3538	0.5554	1.570
Ytterbium	70	173	4f14(5d6s)2	0.0858	0.1939	fcc	0.5485	-	-
Lutetium	71	175	4f14(5d6s)3	0.0848	0.1735	hcp	0.3505	0.5549	1.583

Table.2.1 Electronic and structural properties of the REs. Crystal structures shown are the stable room temperature structures. Adapted from [22].

The applications of REs are many and varied, in compound or metallic form, some of which are outlined below:

They are an important constituent of some strong permanent magnets, such as $SmCo_5$ [23], Sm_2Co_{17} [24] and $SmCo_2$ [25].

The RE ions have fluorescent and luminescent properties which may be useful in optical applications and detection of radiation [26].

As the REs are all electropositive, they tend to lower the work function when deposited onto other metals and there is interest in their use in electron emitters [26].

A recent discovery was that of RE-containing, high temperature superconductors [26].

Due to the high reactivity of REs there is much interest in their use as catalysts [27].

RE-semiconductor interfaces have unusually low Schottky barrier heights due to high reactivity at the interfaces [4, 28, 29].

2.3. Structure of REs

Rare earths in their elemental metallic states occur in a wide variety of crystal structures (Fig.2.2). The complete range of crystal structures form complex phase diagrams, represented by Fig.2.3. Across the lanthanide series at room temperature, the hcp structure gradually takes over from fcc.

With the exception of only Eu, every member of the RE series adopts a close-packed crystal structure at room temperature and atmospheric pressure. As a general rule, the heavy REs all adopt the hcp structure at room temperature (with the exception of Yb which favours fcc), whilst the light REs, with the exception of Sm, adopt the dhcp structure. La, Pr, Ne and Pm adopt the dhcp structure while Sm has an orthorhombic structure shown in Fig.2.2. It is useful to think of this structure as comprising a mixture of one part fcc and two parts hcp in the same way that the dhcp structure can be thought of as an equal mixture of fcc and hcp.

Nearly all the REs undergo phase transitions at elevated temperatures. It has also been found that the REs undergo a phase transition upon the application of pressure. Skriver et al [30] attributed this change to the fall in d-band occupancy across the series as determined from band structure calculations. These temperature dependent phase transformations are summarised in Fig.2.3. Note the multiple structural transformations of La, Ce, Sm and Yb, which can cause severe problems during crystal growth; for example, Ce which is as follows

$$\text{fcc}\,(\alpha) \xrightarrow{96\ \text{K}} \text{dhcp}\,(\beta) \xrightarrow{326\ \text{K}} \text{fcc}\,(\gamma) \xrightarrow{999\ \text{K}} \text{bcc}\,(\delta)$$

The principal planes of the hcp crystal structure investigated in this work, and the corresponding surface unit cells, are shown in Fig.2.4. Fig.2.5 presents the relationship to the bulk and surface hcp Brillouin zones.

Fig.2.6 shows the variation of the metallic radius across the RE series. The noticeably smaller radius for Sc sets it apart from the other REs and in fact its label as a prototype RE must be treated with some reservation. Ignoring Eu and Yb for the moment a general trend of

decreasing radius can be seen across the series, this being known as the 'lanthanide contraction'. This is caused by the increased occupation of the 4f shell and increasing nuclear size leading to an greater electrostatic interaction and hence a decrease in the width of the radial distribution of the 4f and [6s5d] valence orbitals. A reduced 4f/nuclear charge ratio for Yb and Eu result in a larger radii. A fuller account of the lanthanide contraction is given by Goldschmidt [31].

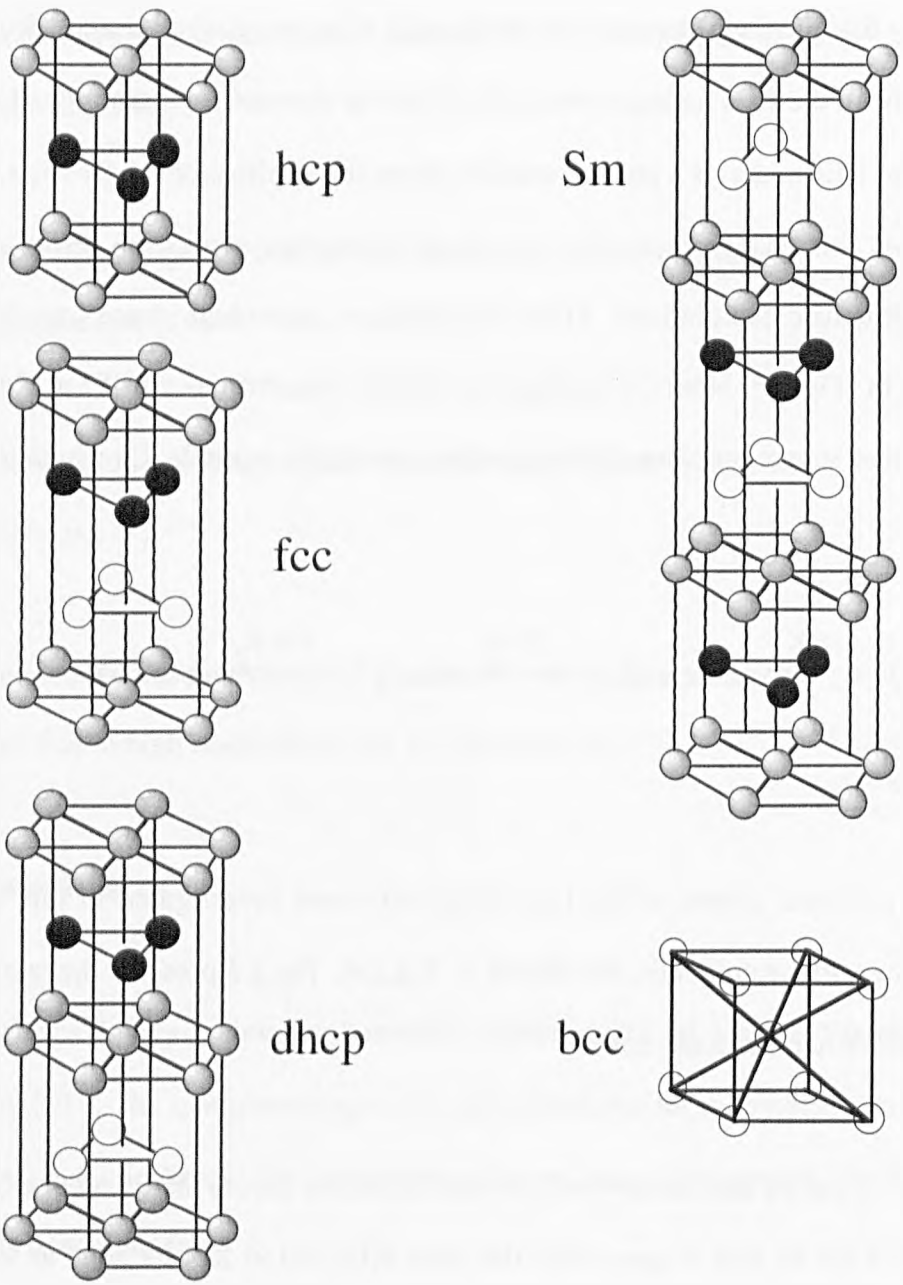

Fig.2.2. Crystal structures of the rare earth metals.

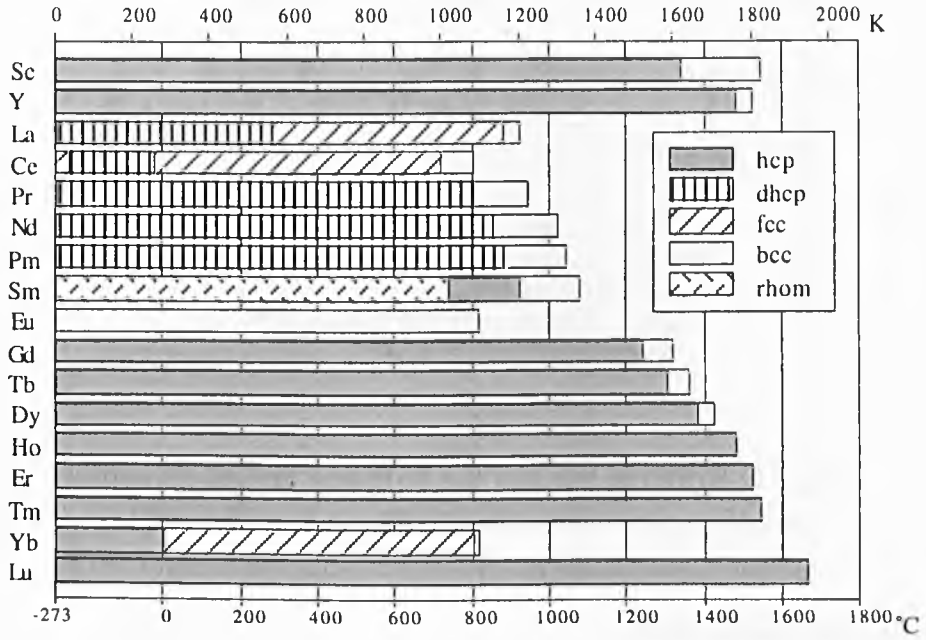

Fig.2.3. Crystal structures of the REs with temperature at atmospheric pressure. Adopted from Ref. [32].

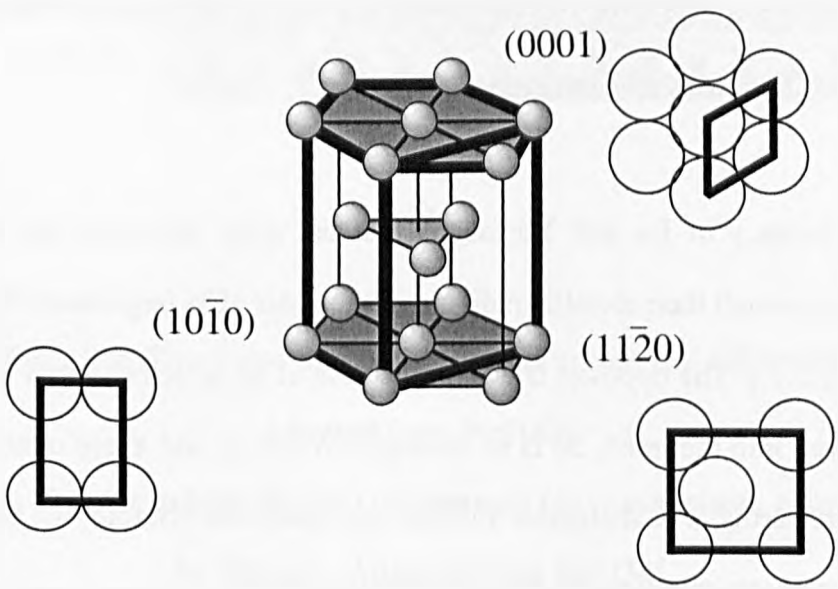

Fig.2.4. Principal planes and corresponding surface unit cells of the hcp bulk unit cell

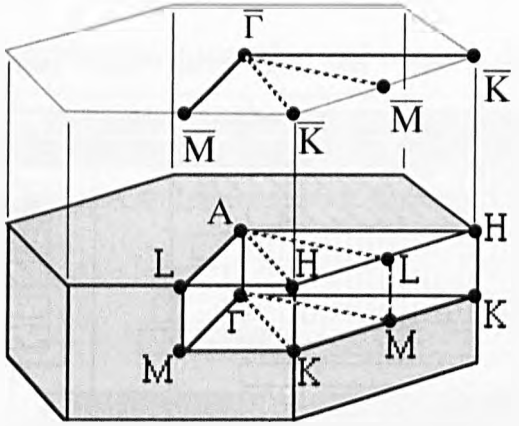

Fig.2.5. Brillouin zone of the bulk hcp crystal structure and its projected surface Brillouin zone for (0001)

2.4. Electronic Structure of REs

The electronic configuration of lanthanides is typically [Xe] $4f^n$ $5d^{(1\ or\ 0)}$ $6s^2$, although in the solid state, the valence band is best considered as $[5d\ 6s]^3$, with the exception of Eu and Yb which are divalent in the solid state. Sc and Y have analogous outer shell configurations, [3d 4s]3 and $[4d\ 5s]^3$ respectively. This gives them a large number of chemical and physical properties in common with the lanthanides.

The divalency of Eu and Yb means that the outer electrons are more efficiently screened and as a result their metallic radii are of the order 10% larger than the rest of the rare earths (see Fig.2.6). The opposite is true in the case of Sc which shows a ~5% contraction. While Y fits well into the trend, Sc is an anomaly. While Sc and Y are often considered as a "prototype" rare earths, i. e. analogous valence configurations without 4fs, the small metallic radius of Sc draws into question the wisdom of such a move.

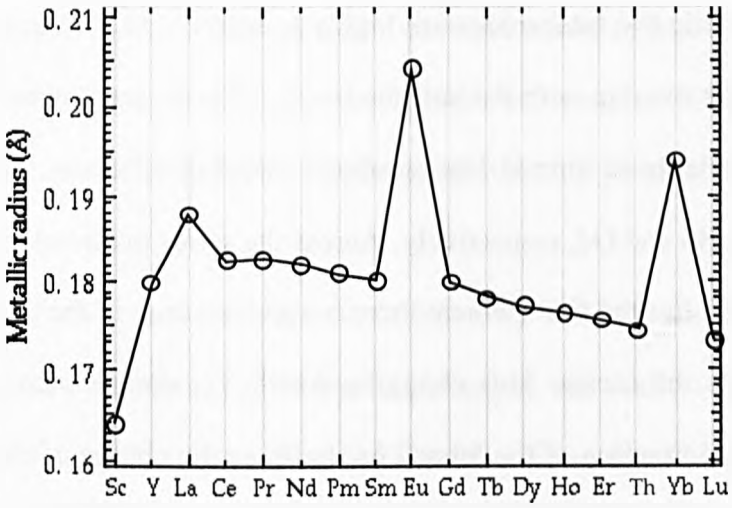

a)

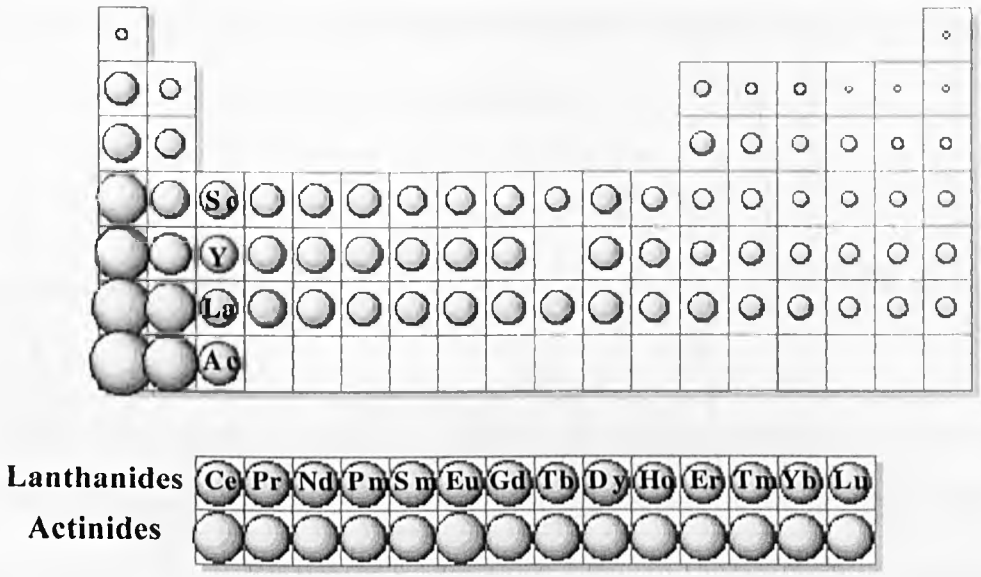

b)

Fig.2.6. a)The trend in metallic radius across the RE series.

Adapted from Ref [33].

b) Valence orbital R(max) of elements for comparison, coded

by ball size. Adapted from Ref [34]

The 4f levels in the lanthanides are highly localised and although they are relatively shallow there is little overlap with the valence levels. This is nicely demonstrated in Fig.2.7 which shows the calculated atomic Hartree–Fock radial distribution function for the outer electrons of atomic Ho and Gd, respectively. Across the series the overlap between the 4f and valence levels varies. For the first element there is a sudden drop in the overlap, followed by a slow fall off across the series. This changing overlap is due to incomplete 4f screening accompanied by a contraction of the 5d and 6s shells, as the charge of the nucleus increases. This effect manifests itself in the reduction of the lanthanide lattice parameter across the series, i. e. the lanthanide contraction.

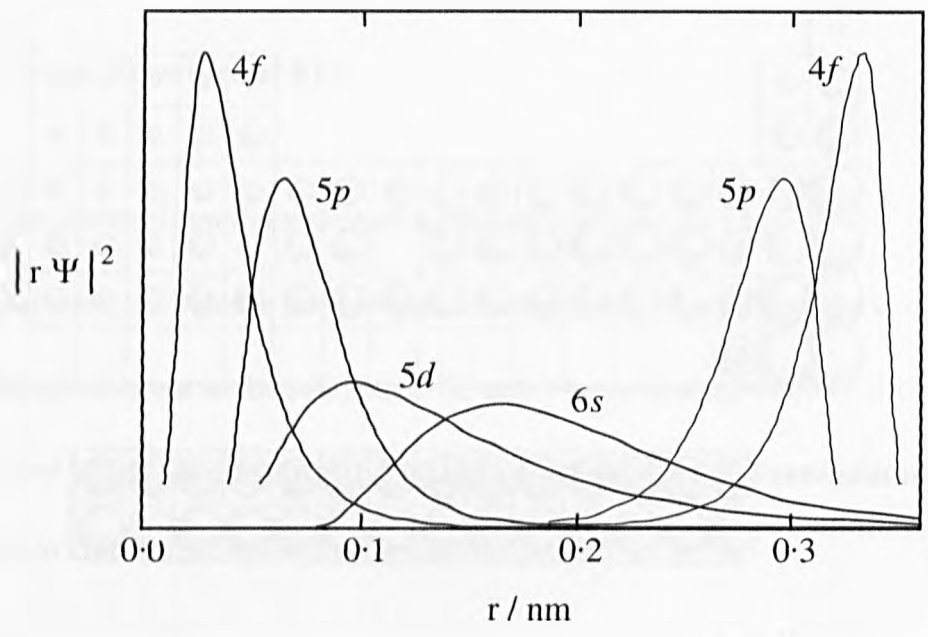

Fig.2.7. Radial distribution function, $|r\Psi|^2$, for the outer electrons of atomic Ho. This figure includes the 4f and 5p wavefunctions for a neighbouring atom positioned at the Ho metal lattice constant. For clarity the corresponding 5d and 6s electron wavefunctions have been omitted due to the large overlap between the valence electrons. Adapted from [32].

The electronic structure of the REs can be modelled only by using a combination of two different models. The first of these is the crystal field model, which completely ignores s, p and d valence electrons. This model is adequate for explaining the magnetic properties of the

magnetic REs due to the 4f levels. The second is the band model in which the 4f electrons are treated as atomic core levels, therefore ignored in the calculations. This model accurately predicts characteristics such as electron transport properties and geometric structure.

Neither of the two above models is satisfactory on its own as the 4f states are localised and core-like even though their binding energies are shallow and sometimes even degenerate with the valence bands, so that they do make some contribution to valence band electronic structure of the REs. In consequence, a unified approach has also been undertaken in which the localised f–states and their correlation effects have been included in a band model [35]. Early calculations of this type were mainly concerned with the mapping out of the Fermi surfaces of the REs [26] in order to explain their magnetic properties and to understand the role played by 4f electrons in the valence band structure.

2.4.1. Mixed–valence phenomena

The lanthanides have a varying number of 4f levels, some of which may be energetically degenerate with the valence band. This degeneracy leads to many interesting mixed-valence phenomena in lanthanide compounds [36]. In metallic states the cohesive energy gain is large enough to overcome the 4f–5d promotional energy and an electron of the 4f shell is transferred to the [5d6s] valence band. Consequently, the rare earth metals are trivalent (except for Eu and Yb). The reduced coordination of the atoms at the surface induces a core–level shift for these atoms [37] and in some cases, depending on the coordination number and the gain in cohesive energy, a surface valence transition back to the lower valence state, present in the gas phase, occurs [38, 39]. Thermochemical considerations of the energies involved [38, 39] predict such surface valence transitions for Sm and for low–coordinated surface sites on Tm, Dy and Ho. These predictions have been confirmed experimentally for Sm [40, 41], Tm [42] and for Dy [43]. The size–dependent valence changes in small Pr, Nd

and Sm clusters have been also investigated by Lubcke et al [44]. The critical coordination number for a valence change was estimated to be 7 for Tm [42, 43]. For Dy, however, this number was found to be around 4 [43] which makes observation of a possible valence change by photoemission techniques a very difficult task even on rough cold-condensed films.

To estimate the valence state of rare earth elements in the bulk and at the surface it is very instructive to consider the corresponding stability diagram [45]. Fig.2.8 represent this diagram where the energy difference $-\Delta E_{II,III}$ between the divalent and trivalent states of the rare earth metals is plotted. On the right hand side the critical lines labelled bulk, surface, edge and corner are indicated. For those elements where $-\Delta E_{II,III}$ falls below the corresponding critical line the divalent state will be adopted. For example, Dy surface atoms positioned at corner sites are predicted to be in the divalent state, whereas all other surface and bulk atoms will be trivalent.

In the case of compounds, for example in DyTe, a model has been used by Patthey et al [43] to predict stability diagrams. In this model the 4f binding energies in divalent compounds such as EuTe and YbTe are used to find stability diagrams for RETe compounds including DyTe. For EuTe the $4f_{II}$(4f level in divalent case) binding energy is 1.4 eV [46] and for YbTe it is 1.5 eV [46]. Assuming that $\Delta E_{II,III}$(the energy difference between divalent and trivalent states) for Eu and Yb in their compounds with Te are same as theirs in pure metal i. e. $\Delta E^{Eu}_{II,III} = 0.9$ eV and $\Delta E^{Yb}_{II,III} = 0.5$ eV (see Fig 2.8). Then the 4f binding energies of Eu and Yb in Te compounds, in trivalent case can be calculated:

$$E_b(4f^{Eu}_{III}) = E_b(4f^{Eu}_{II}) - \Delta E^{Eu}_{II,III} = 1.4 - 0.9 = 0.5 \text{ eV} \quad (2.1)$$

$$E_b(4f^{Yb}_{III}) = E_b(4f^{Yb}_{II}) - \Delta E^{Yb}_{II,III} = 1.5 - 0.5 = 1.0 \text{ eV} \quad (2.2)$$

By interpolation the 4f position on the trivalent side of the Fermi level ($4f_{III}$) for the REs in their compound with Te is obtained. This has been shown by E_F Bulk in Fig.2.8. By assuming the same surface shift as TmTe, which is 0.4 eV [47], for the other RETe compounds, $4f_{III}$ for the surface atoms has been found. This has been shown as E_F Surface in Fig.2.8. Now from these stability diagrams, for ReTe (Fig.2.8), it is inferred within the experimental uncertainty of the interpolated stability line E_F^S, that divalent Dy surface atoms might conceivably occur for DyTe compounds.

It is useful to ask what kind of 4f–photoemission spectra are to be expected for Dy under the combined influence of a 4f surface core level shift and a possible valence transition of a part or of the whole surface. The 4f configurations to be considered in the photoemission final state are therefore $4f^8$ for the bulk and $4f^9$ for the surface atoms undergoing a valence transition to the divalent $4f^{10}$ initial state [48]. The relative energy positions of the individual components of the $4f^8$ configuration were taken from UV–absorption measurements [49], while for the $4f^9$ multiplet the energies were obtained from trivalent Ho by correcting for the difference in nuclear charge by a factor of 1.1 [50]. The lowest $4f^9$ multiplet term is set deliberately at E_F. The relative intensities of the multiplet lines were taken from the results of intermediate–coupling calculations [50]. The bar diagram at the bottom of Fig.2.9 illustrates the situation. Assuming a surface core level shift for the trivalent 4f-components of 0.6 eV and allowing for a gradually increased proportion of surface atoms involved in a surface valence transition and taking account of an instrumental spectrometer resolution (Gaussian) of 0.1 eV of full width half maximum (FWHM)) calculated spectra has been obtained by Patthey et al [43] as shown in Fig.2.9. The bottom spectrum contains only the bulk and surface shifted components of the $4f^8$ final state multiplet whereas the top spectrum represents a superposition of $4f^8$ bulk and $4f^9$ surface multiplet without surface shifts, because all surface atoms have undergone the valence transition. The other spectra simulate cases between these

two extremes. The figure will facilitate the determination of what kind of surface effect manifests itself in the 4f photoemission spectra of the systems contained Dy.

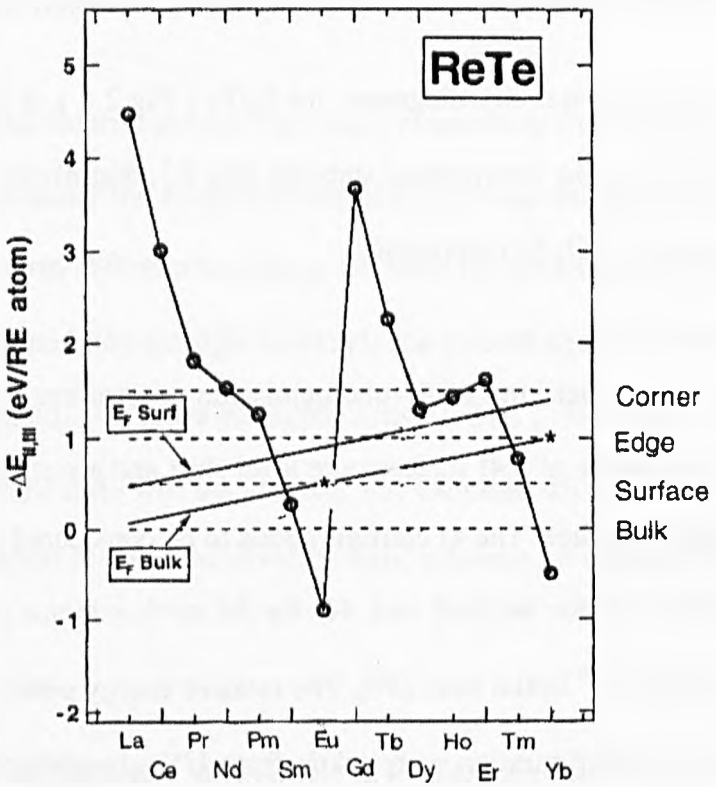

Fig.2.8. Stability diagram for the REs and the rare earth tellurides. The horizontal dashed lines denote the stability for surface atoms of the pure metals in the indicated positions, adopted from [45]. For those elements where $-\Delta E_{II,III}$ falls bellow the critical lines the divalent state will be adopted. The solid lines indicates stability for the RETe. Adopted from Ref. [43].

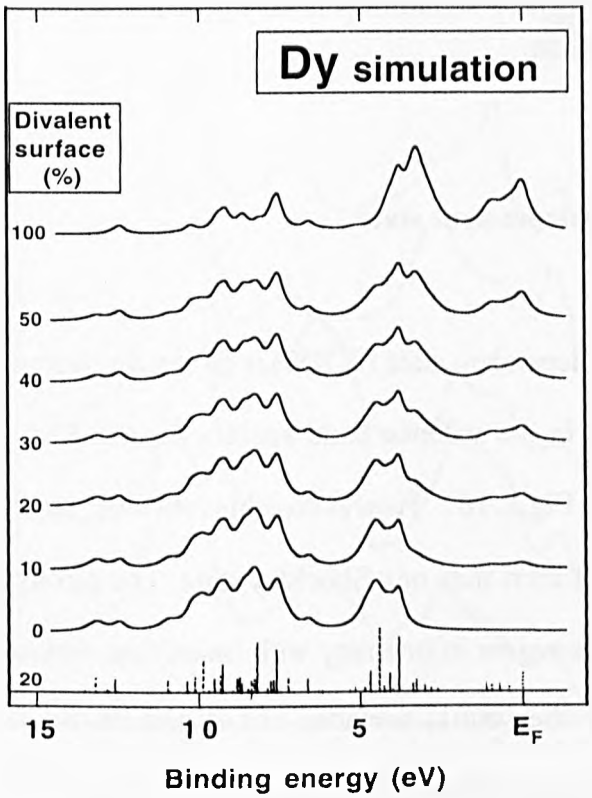

Fig.2.9. Calculated 4f photoemission spectra for Dy for an increasing proportion of a divalent surface layer. The bar diagram at the bottom of the figure represents the positions and relative intensities of the final–state 4f–multiplet components originating from the bulk (solid bar) and from a surface layer partly in the surface trivalent valence state (dashed bars) and partly (20%) in the divalent valence state (dotted bars). adapted from Ref. [43].

2.4.2. Surface states

Metal surfaces can produce two types of surface states — Tamm states and Shockley states. Tamm states are not often observed as distinct features in UPS valence–band spectra due to their proximity in energy to other (bulk) states. Shockley states are solutions of the Schrödinger equation that take account of the potential at the surface, and often manifest themselves in valence–band spectra as sharp features just below the Fermi energy. The existence of such a state is taken to indicate a clean and well–ordered surface, as there is

substantial evidence that disruption of the surface through roughening or the addition of even small concentrations of surface contaminants can produce significant attenuation of these states.

2.4.3. The surface order dependent state

The surface order dependent state (SODS) is an intense feature that occurs at a binding energy of about 9-10 eV in the valence band spectra for the RE(0001) bulk single crystal surfaces, as shown in Fig.2.10 . However, this surface state does not exhibit the characteristics of either a Tamm state or a Shockley state. The acronym SODS has its origin in the fact that this feature increases in intensity with improving surface crystallographic order. It was first observed for the (0001) surfaces of Gd and Pr. So far this feature has been observed for all the bulk single crystal REs studied to date: Sc, Y, Gd, Tb, Ho, as shown in Fig.2.10 , and Pr and Er. This feature, however, has not been observed in any RE epitaxial film VB UPS spectra. The binding energy of the SODS for all these REs is 9.6 $\pm$ 0.2 eV, except for Pr and Sc where it occurs at 9.0 and 10.0 eV respectively. Observation of SODS in a photoemission study of Y(0001) [51], indicates that it should not be interpreted as being related to 4f emission as Y has no 4f electrons. It was this study of Y(0001) that led to the discovery of the relationship between surface order and the intensity of the SODS peak.

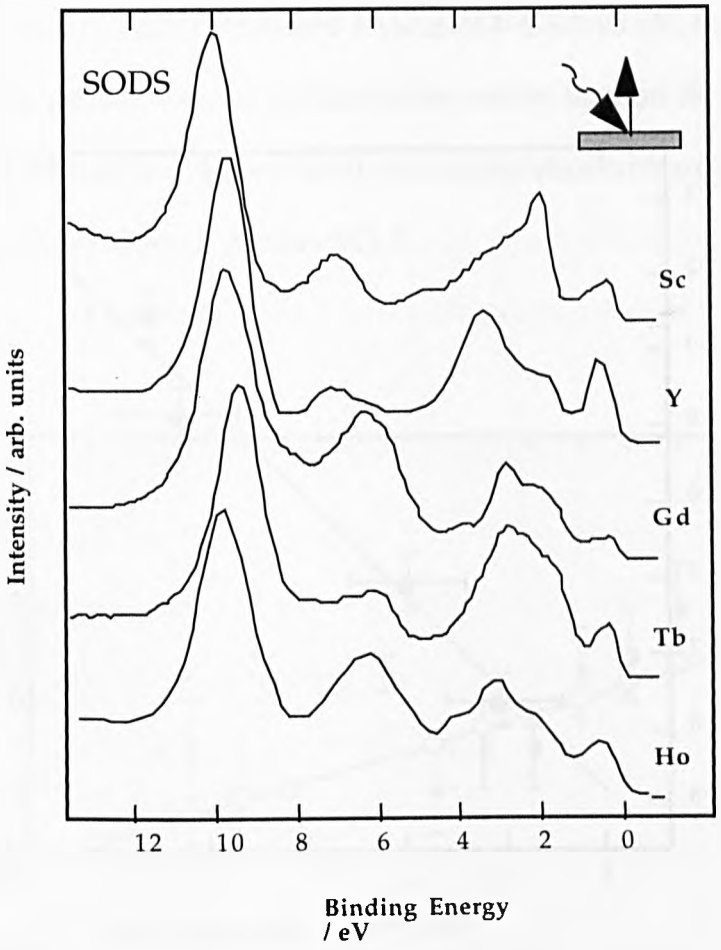

Fig.2.10. Comparison of normal emission spectra from the (0001) surfaces of five hcp RE metals at hν=40 eV. From [32].

The behaviour of the SODS as described here suggests that it is not only an excellent indicator of both the level of the RE crystal surface order but also its cleanliness. This relationship was confirmed by a study of Sc(0001) [32]] where improvements in the quality of the LEED pattern (sharper spots on a lower background) as the sample was cleaned with argon bombard-anneal cycles were correlated to the reduction in the FWHM of the SODS feature, as shown in Fig.2.11. Alternatively this result can be explained in terms of an unresolved contamination peak to a slightly higher binding energy than the SODS peak, as this would be expected to decrease as the sample is cleaned thus apparently reducing the FWHM of the SODS peak.

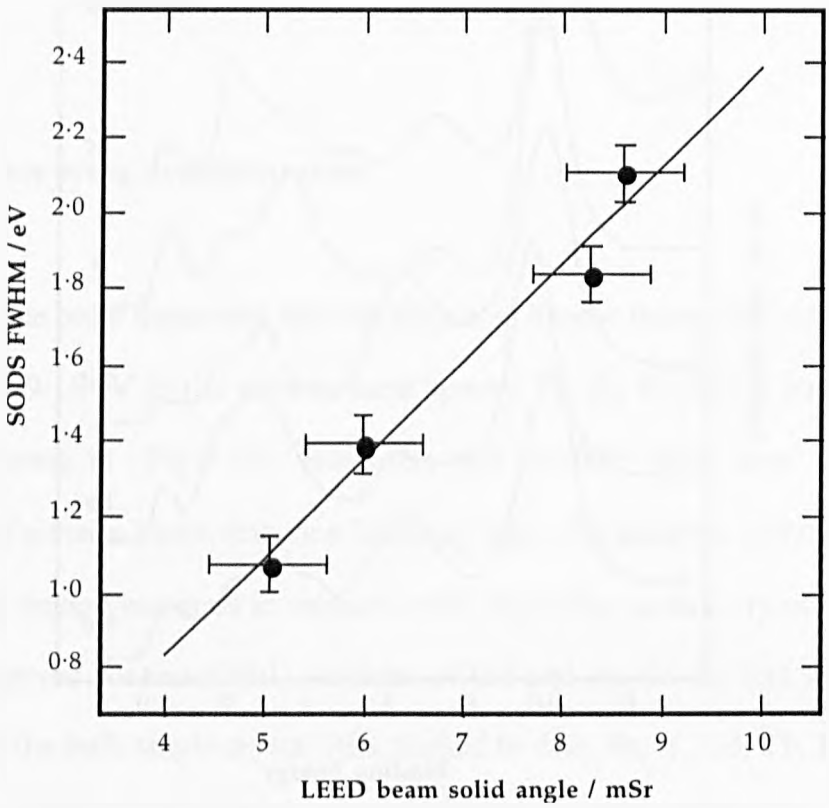

Fig.2.11 Relationship between the FHWM of the SODS peak to the sharpness of the LEED spots for Sc(0001). From [32].

2.4.4. SCLS of rare-earths

Surface atoms have their structural environment modified which gives rise to a redistribution of valence-band electrons and therefore their core-levels are shifted from their bulk positions, giving a surface core-level shift (SCLS). The first experimental evidence for a SCLS was produced by Citrin et al. [52]. The Au 4f lineshape in their XPS spectra showed increasing weight at lower binding energy as they increased the emission angle from normal emission to grazing angles, thus increasing the surface sensitivity.

The first determination of an SCLS on a RE metal was by Alvarado et al [53] who

studied the 4f levels of Yb. They determined a value of 0.6 ± 0.03 eV, but assigned this to a chemical shift due to surface oxygen contamination rather than an SCLS. Johansson and Mårtensson [37] argued that the observed shift was inconsistent with oxygen contamination, indicating that the observation was a genuine SCLS.

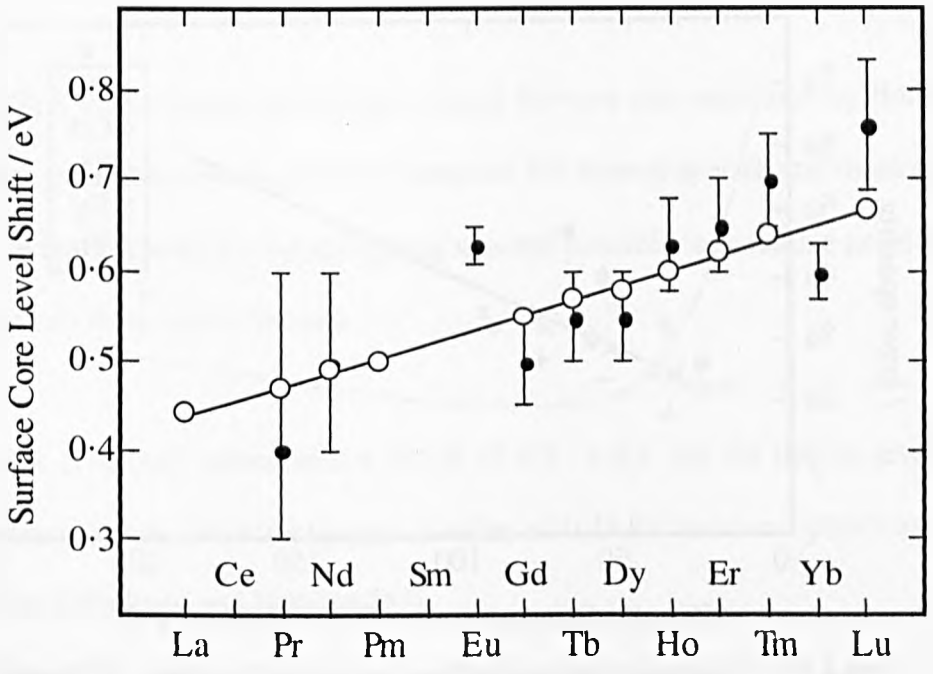

Fig.2.12 Comparison of the experimental (•) [41] and calculated (o) [54] values for the SCLS of the 4f levels of the lanthanides. adapted From Ref. [32].

The localised nature of the 4f levels in the REs allows them to be considered as core levels. The SCLS measurements of the 4f levels were used by Gerken [55] to demonstrate that for Sm, whilst the bulk atoms exist in a trivalent state, the surface atoms are divalent.

Gerken and Kammerer [55, 56] measured SCLS for all the REs. This work demonstrated that the SCLS varies from 0.3 to 0.8 eV, increasing monotonically across the series. These observed values and the calculated SCLS values from Begley et al [54] are shown in Fig.2.12 . For Gd no surface components were resolved although the peak was asymmetric

suggesting the existence of an extra component to a higher binding energy. Also, in the case of Ho a value for the SCLS could not be determined due to the complex nature of the 4f lineshape. As there is good agreement between Gerken and Kammerer's experimental values and ab–initio calculations performed by Begley et al [54] it might be suggested that if the 4f level is considered to be localised then the changes are due to d-band occupancy.

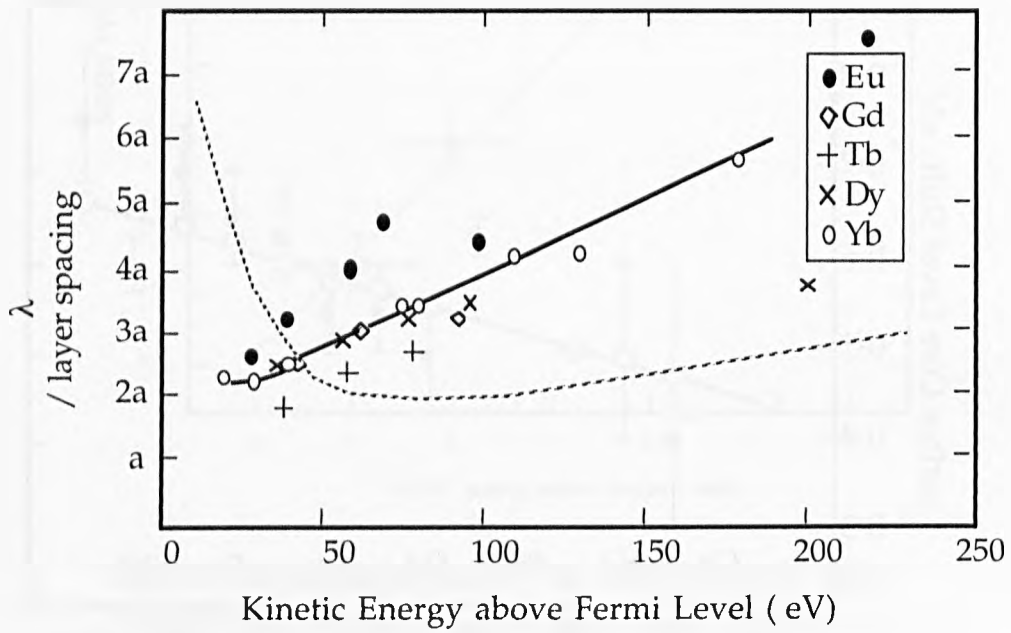

Fig.2.13 . Photoelectron mean free path as a function of kinetic energy for various RE metals. The solid line drawn connects the data points for Yb and the dashed line is the universal curve [57]. Adapted from [32].

From the measured SCLS, values for the photoelectron mean free paths (mfp) were calculated for the REs by comparison of the bulk to surface peak intensities. From these measurements, it was determined that the minimum in the mfp is at a kinetic energy of 30 eV or even below, which is ~ 20 eV lower than the broad minimum of a kinetic energy of the universal curve [57], as shown in Fig.2.13 .

Barrett et al. [58, 59] reported the first evidence of the SCLS of the 4p levels of Y, which was measured in the range of 0.7 -0.9 eV, and then calculated the 4p SCLS of Y using

the Self–Consistent Field Linear Muffin–Tin Orbital method coupled with the Atomic–Sphere–Approximation (SCF-LMTO-ASA method) in a supercell geometry and found a SCLS of 0.6 eV, which is good agreement with the experimental value. They showed that in the case of 4p levels of Y, the level has a finite bandwidth of ~ 0.5 eV and a hole lifetime of 0.5 -1.0 eV, so the usual procedure of fitting theoretical line-shapes to this level was not appropriate.

The SCLS of the 3p levels of single-crystal Sc were also measured by Barrett [32] for which a change of lineshape was observed between the normal spectra and those taken at 60° off normal. Owing to the spin orbit splitting it was not possible to calculate an accurate value for the SCLS from these measurements.

Erbudak et al [60] determined a SCLS of 0.5 ± 0.1 eV for the 3p levels of Sc by fitting to Doniach-Sunjic (DS) lineshapes. A value of 0.48 eV had been previously predicted for Sc(0001) by Feibelman and Hamann [61].

Kammerer et al [56] measured 0.63 eV of SCLS for Eu, and found evidence of a SCLS (0.48 eV) for Gd 4f level by comparison with XPS data. They [55] also found that the SCLSs of Tb, Dy, Eu and Yb are 0.51, 0.53, 0.63 and 0.63 eV, respectively.

McIlroy et al [62] measured a SCLS of 400 ± 20 meV for the 4f levels of Gd with their spin-resolved photoemission spectra. They found this shift was reduced from 400 meV to an 250 meV at oxygen exposure of 0.25 L, which was due to a smaller shift to higher binding energies of the surface component, as compared to the bulk component. From this they concluded that oxygen goes to subsurface sites at initial stages of adsorption. They suggested that the loss of the magnetic order of surface Gd layer when exposed to oxygen was due to a reduction in the exchange coupling between the 4f core levels through the conduction electrons

as a consequence of hybridisation of the Gd s-p-d bands with the oxygen p bands.

2.5. Magnetic properties of REs

One of the most interesting properties for rare earth metals is their unique magnetic properties. Considering the components in electronic equipment, magnets make a greater proportion of the materials cost than the semiconductors. Given the huge market for semiconductors, this is a truly awesome prospect. Semiconductor research has enabled the doping of tailor-made devices for specific purposes, and the creation of the whole new field of compound semiconductors. The domain of magnetic materials is fast approaching the same point – magnetic properties can already be tuned to a certain extent. The combination of the Molecular Beam Epitaxy (MBE) technique with multilayer materials will make it possible to design magnets with specific properties, thereby channelling interesting physics into the commercial world.

Due to screening of the 4f orbitals from the environment by valence electrons, this magnetic moment is not modified significantly in the bulk, unlike the case for transition metals where orbital angular momentum quenching occurs. In order to produce magnetic ordering of the sample there must be some interaction between atoms on different crystal sites. The 4f levels are well confined within the atoms, so the interaction is not due to direct overlap of neighbouring 4f wavefunctions. The communication between sites is by an indirect exchange interaction through the conduction electrons–the Ruderman-Kittel-Kasuya-Yoshida (RKKY) interaction, for which detailed mechanisms are given by Kondo [63] and Freeman [64]. The central hypothesis of this model is the existence of a spin density cloud set up around each site by the direct exchange interaction between the 4f electrons and the valence electrons. The spin of the 4f electrons at a site is determined by the net polarisation of the valence electrons at that site, which is in turn induced by all the other spins within the radius of the spin cloud.

This cloud is effective over a very long range. The coupling is affected by magnetoelastic interactions and anisotropic crystal field effects, leading to the variety of complex magnetic structures displayed by the rare earths (Fig.2.14). The complicated magnetic phases are a result of the temperature–dependent competition between these interactions.

From Pr to Gd the magnetic moment of the localised 4f shell increases as the spins line up in parallel according to Hund's rule. Across the remainder of the lanthanide series, the moments decrease as the spins pair up. Of primary interest in magnetic studies is Gd, where all of the seven electrons of the half-filled 4f shell have their spins aligned in parallel according to Hund's rule, resulting in an large 4f moment of $7\mu_B$, in addition to the 5d6s contribution of 0.6 μ_B. Gd is one of the four simple ferromagnets, and the only one to exhibit a localised magnetic moment, in contrast to the itinerant (band-like) ferromagnetism of Fe, Co and Ni.

Amongst these magnetic phases, only Gd, Tb and Dy display ferromagnetism. The ferromagnetism of these metals have been studied extensively and recent investigations of its influence on electronic structure have provided information on localisation of electronic states [65, 66]. The phase transitions in Tb and Dy accompany a structural phase transition from orthorhombic to hexagonal close-packed. With the exception of Lu, the heavy lanthanides exhibit a number of periodic magnetic structures, both commensurate and incommensurate with the crystal lattice. These have been described in terms of the spin-slip model around the six easy directions of magnetisation. In addition, Nd and Sm exhibit separate ordering on the hexagonal and cubic sites.

Temperature dependent magnetic phase transitions are reviewed by Sinha [67]. As mentioned earlier, it is known that the RKKY interaction is highly sensitive to parameters such as ion separation. In consequence, the temperature range over which the different magnetic structures order is relatively short. It is for these reasons that surface configurations

have a drastic effect on the magnetic state in the REs. Therefore, surface magnetism of the REs is of interest as the magnetic surface structures can be correlated to general magnetic behaviour and help in its understanding.

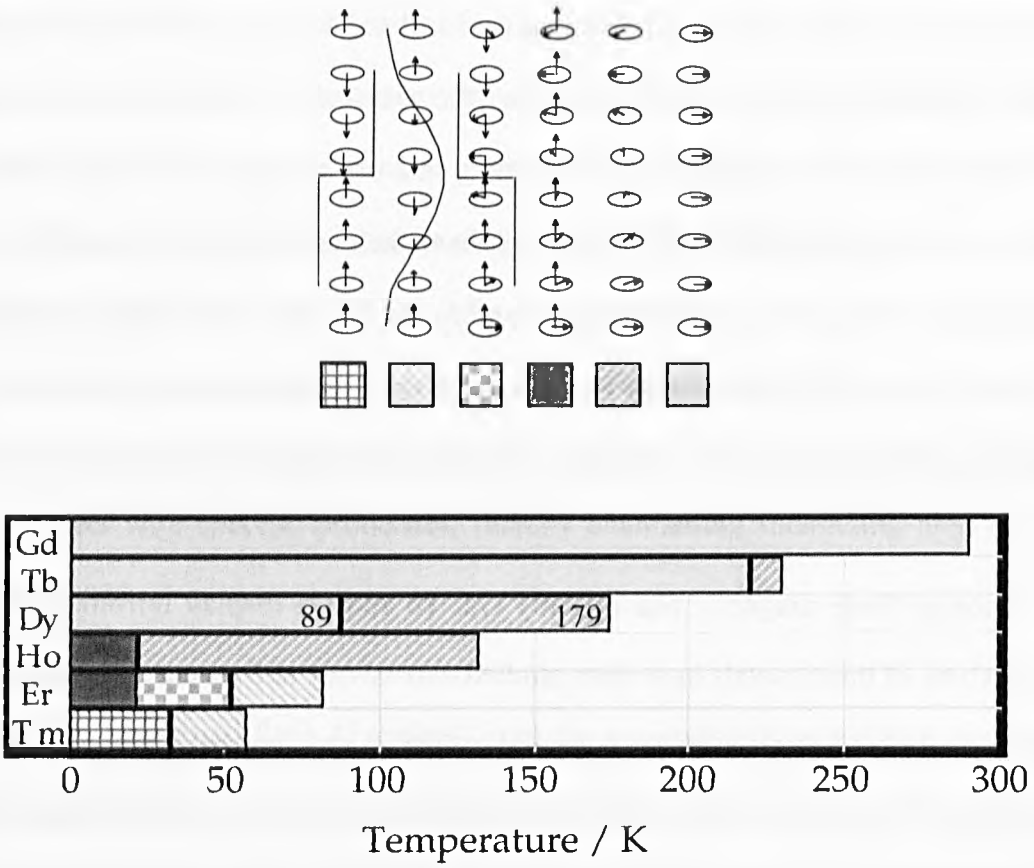

Fig.2.14. Magnetic phase transformations exhibited by the lanthanides and their associated spin structures. Adopted from Ref. [26]

2.5.1. Surface Magnetism

The loss of symmetry brought about by the abrupt boundary at a surface offers a situation in which magnetic properties can be altered from those inside the bulk material. Predicted theoretically, surface-enhanced magnetic order (SEMO) and magnetic surface

reconstructions (MSR) have been discovered during the study of surfaces and ultra-thin films. Although never seen in 3d transition metals, they have been observed in the rare earths, with their highly localised 4f moments.

2.5.1.1. Surface–Enhanced Magnetic Order

The first observation of SEMO at the surface of Gd was carried out by Rau [68] using electron capture spectroscopy (the technique is reviewed by Rau [69]). This gave a surface Curie temperature of ~ 310 K (*cf* the bulk Curie temperature of 293 K, indicating an enhancement of ~ 15 K). Later experiments involving spin–polarised LEED and the magneto-optic Kerr effect (MOKE) determined an enhancement of 22 K (Weller *et al* [70-72]). More recent spin–polarised photoelectron and secondary electron spectroscopy experiments have confirmed the SEMO effect for Gd (and Tb), with values of the enhancement as large as 60 K (Tang H *et al* [73, 74]) or possibly even 80 K (Vescovo *et al* [75]). The largest effect reported to date is that derived from a spin–polarised photoelectron diffraction (SPPD) study by Tober *et al* [76], which indicated an enhancement of 85 K. The steady increase in the magnitude of the apparent enhancement has been attributed to improvements in the quality of the epitaxial thin films grown, but the correlation between SEMO and the structural quality of the films has not yet been established quantitatively.

2.5.1.2. Surface–To–Bulk Coupling

Some of the early experiments observing SEMO on the (0001) surface of Gd also involved techniques that gave information about the surface–to–bulk magnetic coupling. For thin films of Gd(0001), the magnetisation is in the basal plane of the hcp crystal structure and is thus in–plane.

Using spin–polarised UPS (SPUPS) technique, the Weller *et al* [72] indicated an antiferromagnetic surface–to–bulk coupling, which was later supported by electronic structure calculations [6]. However, subsequent results from SPUPS (by various groups, including those of Dowben, Erskine and Hopster) [6] and magnetic dichroism (by Kaindl's group) [6] indicated ferromagnetic coupling (in the latter case, for Tb as well as for Gd). Again, the experimental results were supported by electronic structure calculations [77, 78] based on the local–spin–density approximation (LSDA). By measuring both the in–plane and out–of–plane components of the electron polarisation in SPUPS and spin–polarised secondary electron emission spectroscopy (SPSEES), Tang H *et al* [73, 74] showed that the surface magnetic moments are canted, producing a measurable out–of–plane component to the surface moment (Fig.2.15).

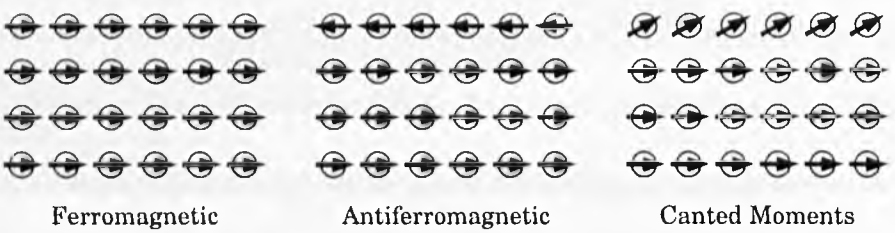

Fig.2.15. Proposed models for the surface–to–bulk magnetic coupling in rare–earth metals (the top layer of magnetic moments represents the surface layer). The first experimental evidence indicated antiferromagnetic coupling, later experiments preferred ferromagnetic coupling, and the most recent experiments indicate that the surface moments are canted out of the surface plane. Adapted from Ref. [6].

Chapter 3

Experimental details

3.1. Synchrotron based experimental details

3.1.1. Introduction

3.1.1.1. Synchrotron radiation

It is known from electrodynamics theory, when charged particles are accelerated they will emit radiation in all directions. When the speed of the charged particles is non-relativestic, the radiation is emitted in all directions which are roughly perpendicular to the acceleration direction. In the case where electron is moved with a relativistic velocity in a circular (curved) path the light is emitted in a narrow cone tangential to the orbital path and is highly polarised in the orbital plane. Synchrotron light sources work on this principle. Electrons are injected into a storage ring where their path is maintained by dipole magnets. They are then accelerated to, and maintained at, relativistic velocities. Beamlines are placed tangentially to the dipole magnets and guide the light to experimental stations as shown in Fig.3.1.

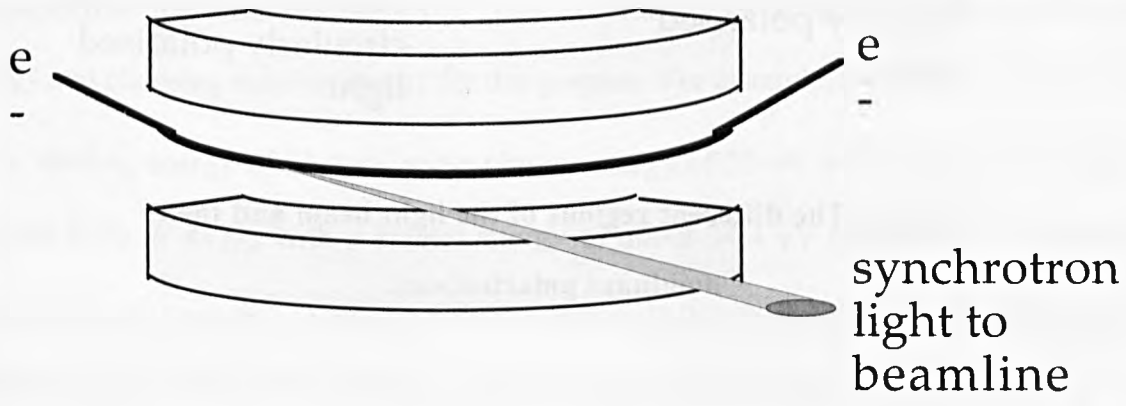

Fig.3.1. A simple figure showing how part of the light produced by the accelerating electrons is directed along a beam line placed tangentially to a point on the electrons' path.

The intensity of synchrotron radiation is orders of magnitude higher than for either a UV lamp or an x–ray source.

The synchrotron radiation is also highly polarised in such a way that the central part of the light contains more than 99% linearly polarised light (Fig.3.2). The top and bottom portion of the beam are circularly polarised with opposite sense. While by moving away from the centre of the beam the percentage of the circular polarised light is increased, the intensity drops rapidly. Therefore, by choosing appropriate parts of the beam, the polarisation of interest can be selected with suitable intensity.

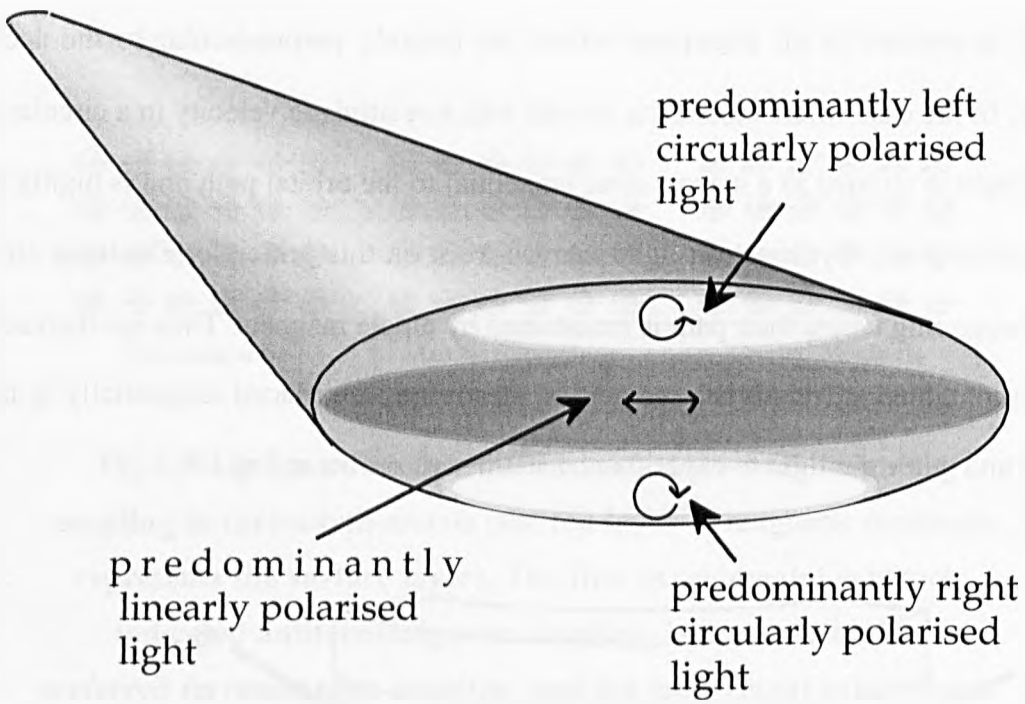

Fig.3.2. The different regions of the light beam and their dominant polarisations.

3.1.1.2. Advantages of Synchrotron radiation for photoemission spectroscopy

Tunability, high flux and low bandwidth are major advantages of synchrotron radiation over conventional excitation sources:

1) Photoemission cross–sections of energy levels are dependent on photon energy [79]. Therefore, it is possible to chose photons with specific energy suitable for investigation of a desired energy level. For example, by choosing a photon energy corresponding to the 4d –> 4f resonance of the RE metal, the intensity of photoemission features increases dramatically, reducing acquisition time and increasing signal to background ratio (see for example Ref [80-84]). Another example is tuning the photon energy to suppress a specific peak which has super position with the peak under investigation. For example Tucker et al [85] used a photon energy of 152 eV to suppress W-VB (W–5d) photoemission (a phenomena known as Cooper minima) while investigating Gd 4f resonance.

2) The kinetic energy dependence of the inelastic mean free path (IMFP) of electrons through solids are as shown in Fig.2.13 and Fig.3.3. To have optimum surface sensitivity for a specific energy level, the kinetic energy of photoelectrons emitted from that level should correspond to the minimum of IMFP. This criteria can be achieved by tuning the photon energy and choosing suitable energy for this purpose. For example, the $4f_{7/2}$ level of tungsten has a binding energy of 31.4 eV and a photon energy of 70 eV will produce photoelectrons emitted from W $4f_{7/2}$ with a kinetic energy of about 34.4 eV (assuming ~4.2 eV for the tungsten work function) which is at the minimum IMFP for photoelectrons through the W (and Dy films over the W substrate). Therefore, this will give optimum surface sensitivity for investigating the SCLS of W $4f_{7/2}$ on adsorption of Dy.

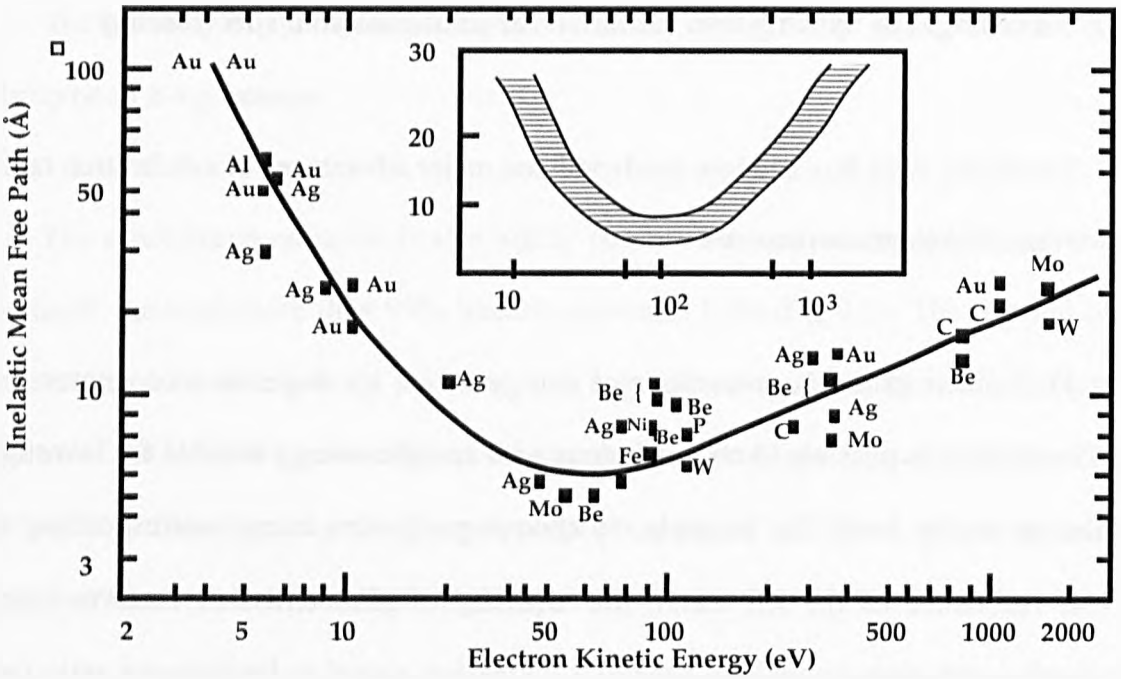

Fig.3.3 Kinetic energy dependence of the IMFP of electrons in solids [86]. The inset shows, the region occupied by the experimental points for most materials studied to date [87].

3) Synchrotron radiation provide higher flux which is orders of magnitude brighter than that of the conventional source of photon (UV lamp and X–ray gun). This results in better signal to noise level and reduces time of data acquisition.

4) Synchrotron radiation has substantially better resolution than conventional photon sources (X–ray gun). For example while typical natural line width of Al – K_α (hν=1483 eV) is 1 eV and even with the help of a monochromator (which results in loss of flux) it is of about 0.25 eV, the synchrotron radiation line width at the same energy, can be less than 0.1 eV or 10–50 meV using an undulator source.

3.1.2. Synchrotron Radiation Source (SRS) at Daresbury Laboratory

Fig.3.3 shows a layout of the Daresbury Laboratory SRS, a three–stage machine for accelerating electrons. This includes an electron gun and its linear accelerator (LINAC), a booster synchrotron and a storage ring of about 30 m in diameter which acts as the heart of the SRS.

Electrons with energy of 12 MeV are injected into a 600 MeV booster synchrotron from the linear accelerator. This is then used to feed the electrons into the storage ring in pulses. When enough electrons have been stored in the storage ring (typically 250 mA), they are accelerated to an energy of 2 GeV. There are some beam lines tangential to the storage ring that take the emitted light from the electrons to the experimental stations, called Beamlines. The beamlines are numbered with reference to the magnet from which they originated. The SRS can be operated in two modes:

i) Multi–bunch mode: in this mode 160 bunches of electrons are stored, each separated by 2 ns. This mode results in maximum current and therefore maximum energy (his is the mode which was used for the experiments in this research). In this mode every 2 ns a set of photons is emitted which can be used to bombard the sample in photoemission experiments. In normal multi–bunch operation the circulating current is typically 200 mA with a lifetime up to 24 hours.

ii) Single–bunch mode: In this mode a small number of bunches of electrons are stored in the storage ring. Here the delay between two successive sets of photon bunches is 320 ns. This mode is suitable for time–resolved experiments where a time delay is required between two sets of photon bombardment. The current here is around 30 mA, much lower than the case of multi–bunch.

Because of the collision of electrons with gas molecules in their path, the number of circulating electrons is usually reduced by time. Therefore, the intensity of the electrons beam and hence the emitted light, gradually decreases. When the intensity is too low, the electron beam must be removed and a new one injected. This process, called refill, is done every 12 hours at the Daresbury SRS. One of disadvantages of this process is that experiments cannot run during refilling process. Another disadvantage is that the loss of intensity will affect the experiments which usually required constant intensity during the experiment.

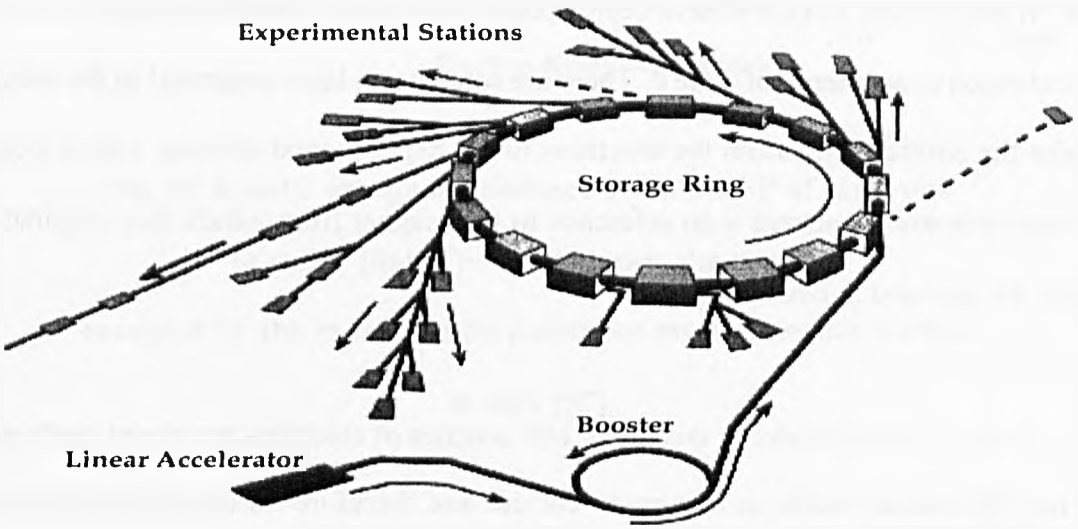

Fig.3.4. Layout of the Daresbury SRS.

In addition to the sixteen bending magnets (1.2 T), the SRS has an undulator and two wiggler magnets (5 T and 6 T). These are called insertion devices, which are positioned in straight sections between the bending magnets of the storage ring. The spectra produced by a 1.2 T bending magnet and a 5 T wiggler magnet are shown in Fig.3.5. Beamlines 9 and 16 have superconducting wiggler magnets for the intense hard X-rays, whereas beamline 5 has an undulator for an intense X–rays at discrete energies. The light radiated by an undulator is highly collimated with a small source area, resulting in high flux output with a brilliance of four

to five orders of magnitude higher than an SRS bending magnet source.

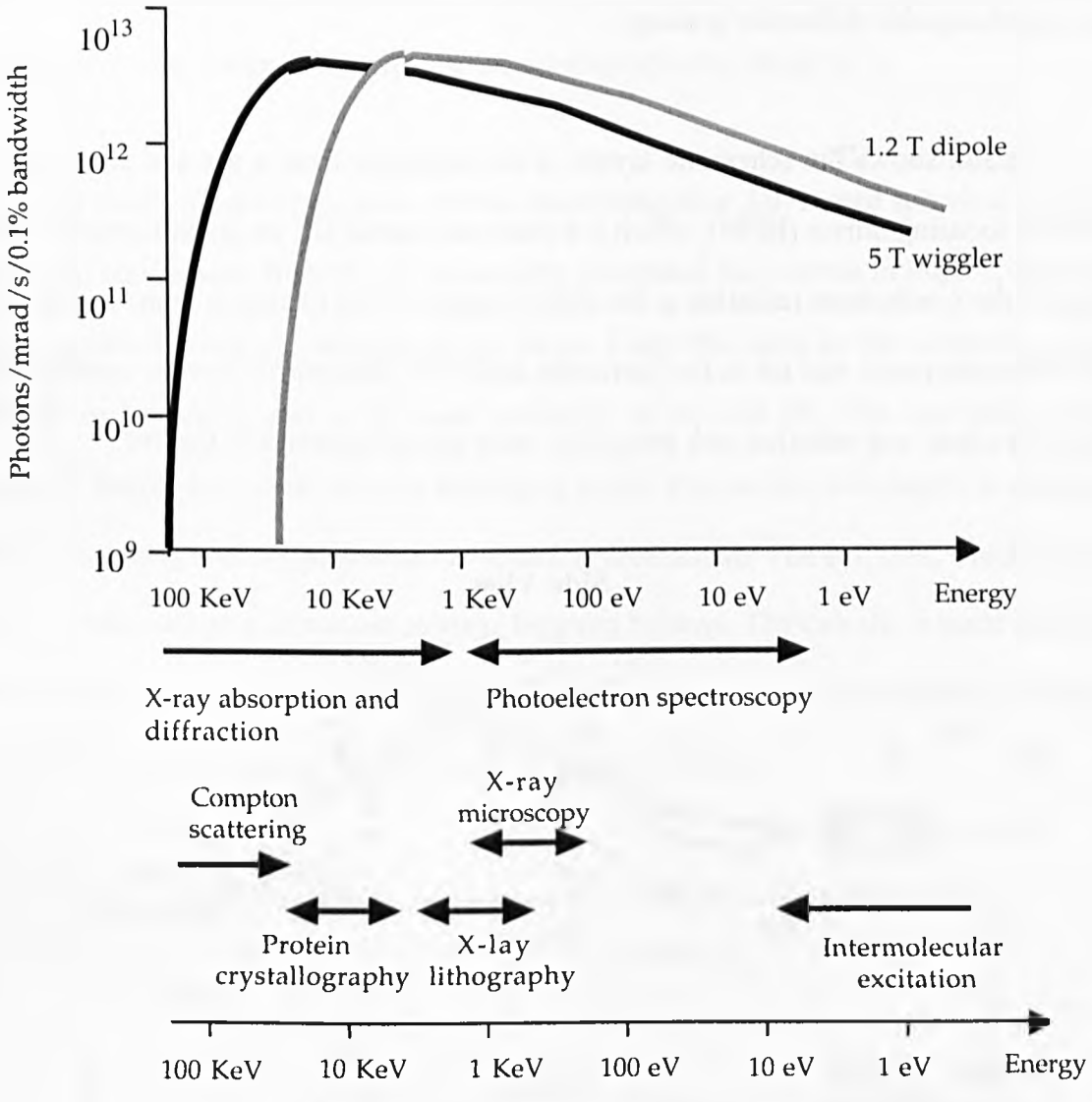

Fig.3.5. Synchrotron radiation spectrum and a range of experimental techniques in the Daresbury SRS.

3.1.3. Beamline 4.1

3.1.3.1. Beam characteristics of beamline 4.1

The UPS studies described in this thesis were carried out on beamline 4.1 of the SRS.

This beamline is a high–resolution, low photon energy beamline based on the spherical grating monochromator design. It has been designed to work over a photon energy range of 14–170 eV using interchangeable diffraction gratings.

Fig.3.6. shows the schematic layout of the beamline from a top and side view. The horizontal focusing mirror (HFM), which is a platinum coated SiC on graphite mirror, collects 6 mrad of the synchrotron radiation at the dipole magnet 4 and focuses it at the mean position of the monochromator exit slit in the horizontal direction. This mirror is water cooled because it serves as a heat and radiation sink protecting other optical elements in the line.

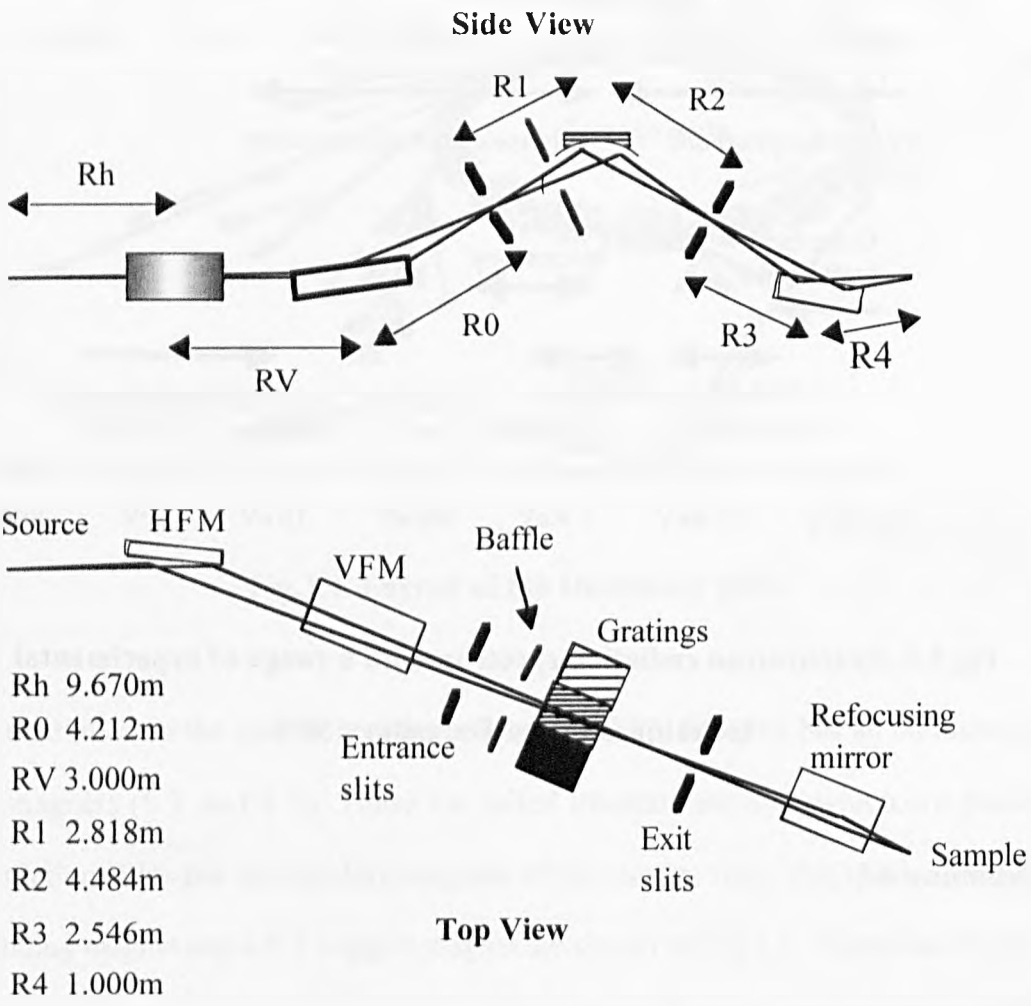

Fig.3.6. Layout of beamline 4.1, showing the optical path and instruments.

The Vertical Focusing Mirror (VFM), which is a platinum coated Spectrosil mirror, has a cylindrical radius of 90.63 m, and focuses the light vertically (in the dispersive direction) at the monochromator entrance slit with a source demagnification factor of 3.

The monochromator consists of three interchangeable Au–coated spherical diffraction gratings. As can be seen from the corresponding calculated flux curves in Fig.3.7, these three gratings together cover the desired energy range. Light that falls on the selected grating is diffracted in first order and is focussed vertically at the exit slit. The required grating is selected by lateral movement into the impinging beam. The correct wavelength is selected by rotating the grating with a simple sine bar scanning mechanism. The exit slits, which vary with energy are mounted on a motorised carriage between bellows. The exit slit is made movable in order to follow the focus at different energies. These slits move automatically along the beamline as the photon energy is set with the beamline software.

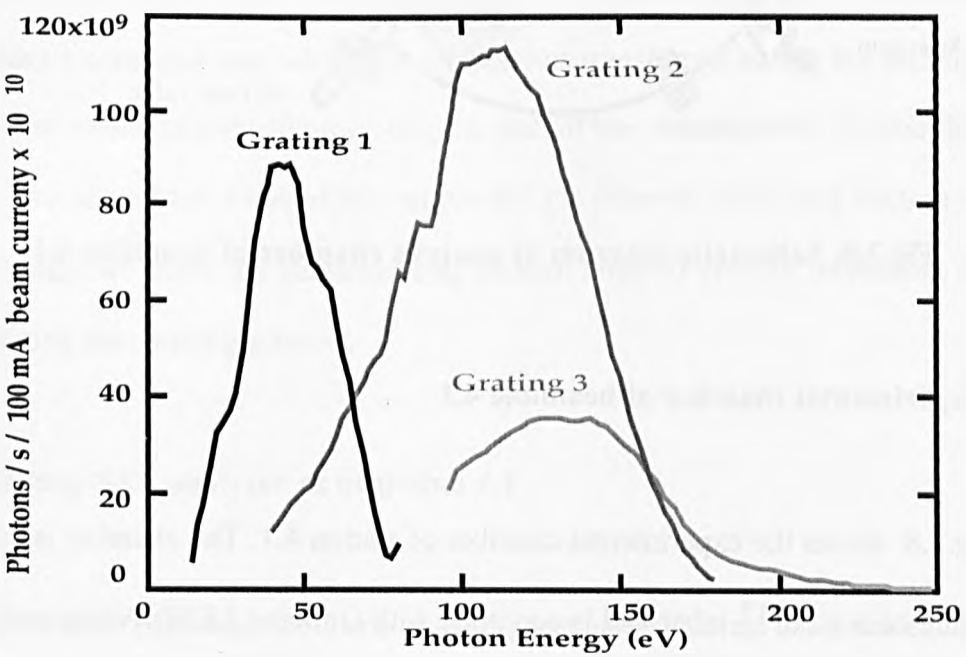

Fig.3.7. Measured photon flux from different slit settings[88, 89]

Immediately prior to the monochromator gratings there are four orthogonal baffles which can be used to control the spot size incident on the gratings in both the horizontal and vertical directions. The interchangeable gratings diffract and focus the photon beam vertically at the exit slit. After the exit slit, there is a re-focussing ellipsoidal mirror which focusses the photon beam to a small spot at the centre of the experimental chamber. Photon energy resolution is defined by the entrance slit, which represents the source size, as well as the exit slit, grating aberrations and slope errors.

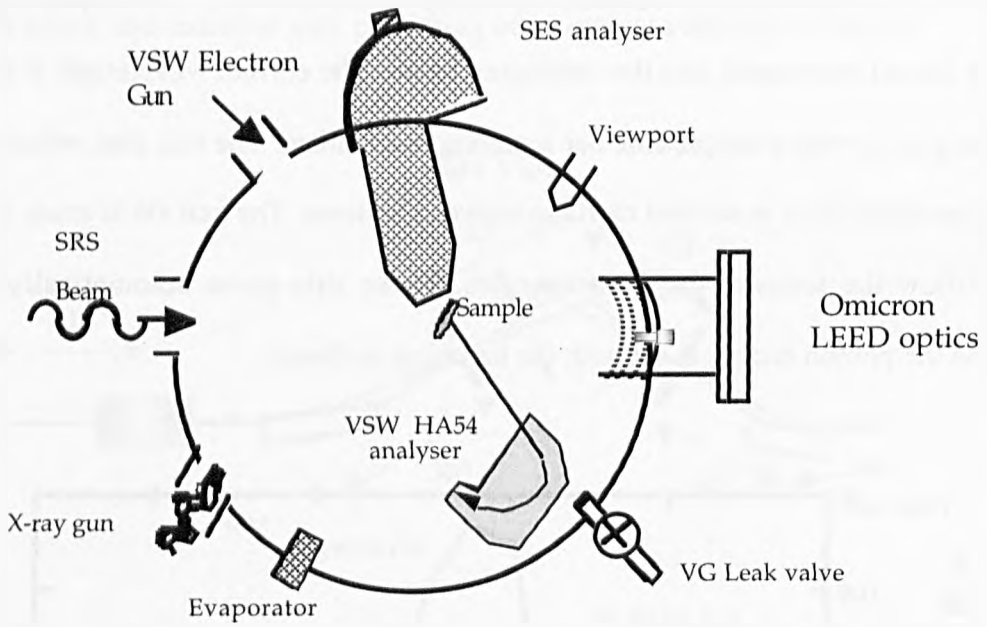

Fig.3.8. Schematic diagram of analysis chamber of beamline 4.1.

3.1.3.2. Experimental chamber of beamline 4.1

Fig.3.8. shows the experimental chamber of station 4.1. The chamber is capable of a base pressure of 8 x 10^{-11} mbar and is equipped with Omicron LEED/Auger optics, sample sputtering facilities, X-ray source and motorised Omniax 5-axis manipulator with sample heating and liquid nitrogen cooling system. The main measurement instrument is a Scienta SES hemispherical analyser.

3.1.3.3. Sample holder used at beamline 4.1

The chamber of beamline 4.1 had been exposed to contamination (oil of the vacuum pumps, mainly Fombline) due to vacuum failure prior to our experiment. Although the chamber had been cleaned by a series of long bakes at high temperature and the vacuum of the chamber could recover to 4×10^{-11} mbar, by putting current through the filament of the e-beam heater, the contamination partial pressures increased up to 9×10^{-10} mbar (which depends on the radiation power of the filament). It was inferred that a small amount of oil was still inside the analyser which, by baking the chamber, was transferred inside the chamber. After baking, though the pressure recovered itself, some part of the chambers wall was covered by the oil. When the wall of the chamber was bombarded the by electrons coming out of the filament, it resulted in desorption of the contaminant. To prevent this a new sample holder was designed and tested on station 4.1, allowing annealing the W sample to over 2500 K without compromising UHV conditions. Fig.3.9. shows a layout of this sample holder. This includes a container into which the sample was transferred during the cleaning process. This container works as a shield protecting the wall of the chamber from bombardment by the electrons. The suspension wires of the sample and the filament were long enough to put them down the container while the container was enough large to prevent increasing of the local pressure during the cleaning process.

3.1.3.4. Scienta SES analyser at beamline 4.1

The Scienta SES analyser is one of the biggest hemispherical analysers equipped with a 5-element lens and two micro-channel plates (Fig.3.10). The mean radius of the hemisphere is 200 mm and the separation of the outer and inner hemispheres is 80 mm. The electron trajectories are bent in the radial electrostatic field between two concentric hemispheres with a

voltage difference between them. The bending radius will depend on the electron kinetic energies and an energy dispersion is displayed on the detector. Since this energy dispersion is determined by the pass energy and the analyser radius, the energy range that can be simultaneously detected in the SES analyser with the 40 mm diameter multichannel detector is about Ep/10, where Ep is the pass energy.

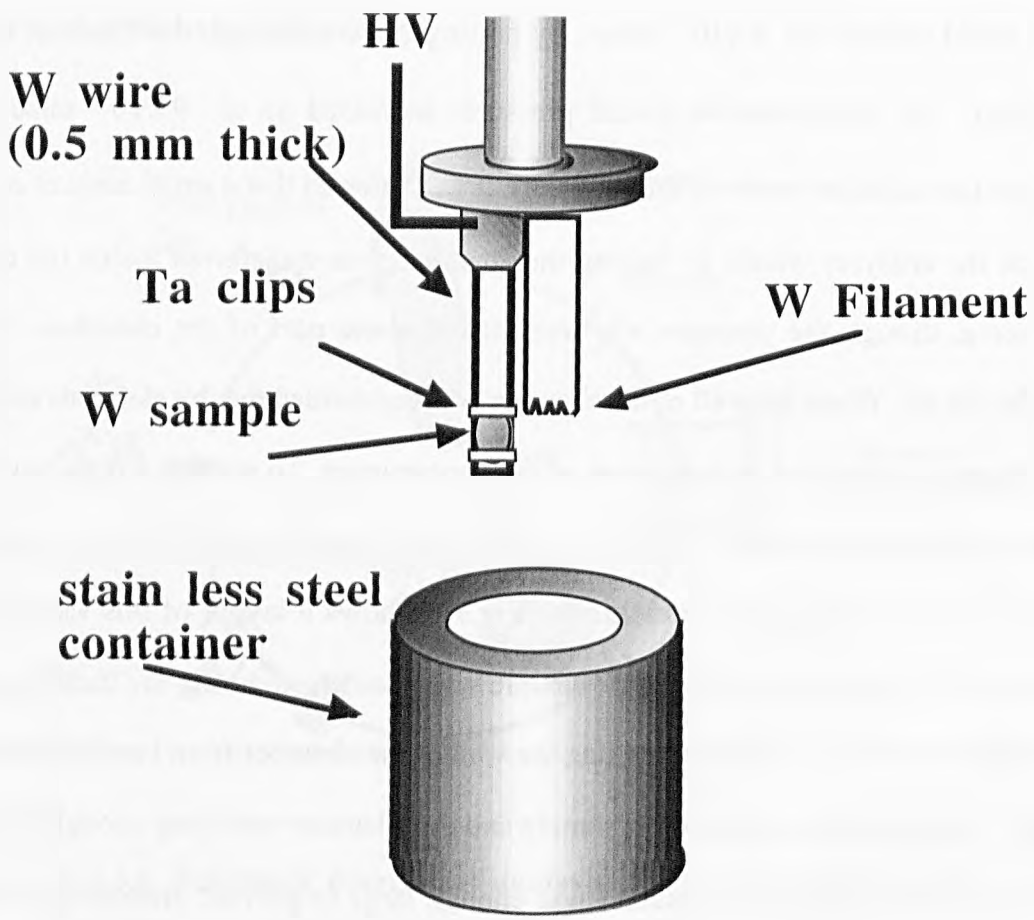

Fig.3.9. Layout of the sample holder used at beamline 4.1 for cleaning W sample

The detector assembly consists of the two micro-channel plates (MCP), a phosphor screen and a CCD camera. Under normal operating conditions, the voltage over the MCP pair is 1700-1850 V and the acceleration voltage between the last MCP and the phosphor screen is normally 3800 V.

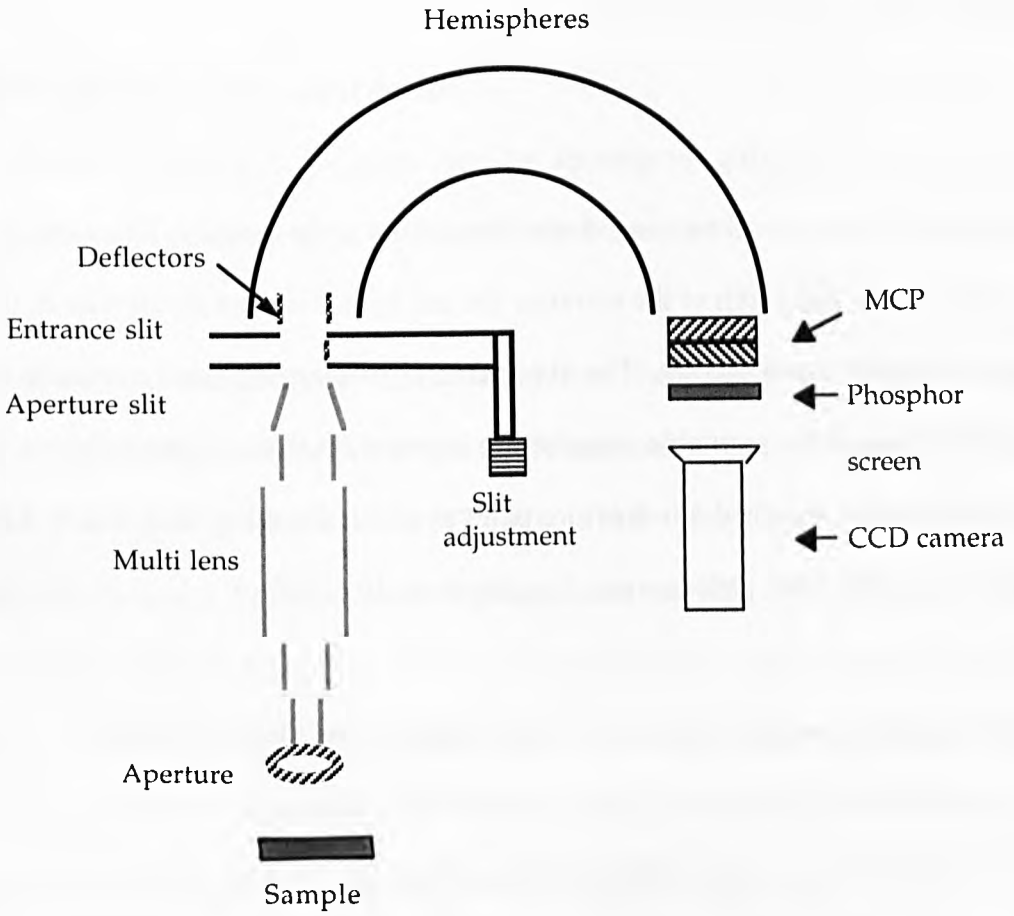

Fig.3.10. Schematic drawing of the SES analyser.

The MCP pair multiplies each incoming electron about 10^8 times and these electron pulses are accelerated to the phosphor screen, where they produce a light flash. This is subsequently detected by the CCD camera, where the camera is mounted in such a way that the camera axis are perpendicular to the energy dispersion direction, therefore, to a good approximation, the energy dispersion is linear with the lines. The video signal from the CCD camera is connected to the camera electronics. This contains a micro-processor, which is set up for a specific experiment from the PC. The micro processor evaluates flash positions in every line which corresponds to the kinetic energy of the electrons, and counts the number of flashes on these lines. This value is stored in the counter and completed data are transferred upon request from the PC. The monitor which is connected to the detector electronics displays a histogram of counts versus energy. This monitor can be used to position samples by centering the counts

on the MCP and maximising the count rate.

Due to the imaging properties of the analyser a narrow (straight) line of monochromatic electrons will be imaged as a narrow line at the detector. The width of this line is defined mainly by the width of the entrance slit and by the angular divergence in the energy dispersion direction along the slit. The slit-aperture pairs are adjusted manually through a rotational feedthrough for a suitable compromise between resolution and sensitivity. There are nine different sets of matched slit-aperture pairs available (ranging from 0.2 to 2.5 mm slit width) and seven selectable pass energies (ranging from 10 to 500 eV).

In the hemispherical electron analyser the FWHM resolution (ΔE) is given by

$$\Delta E = \frac{PE}{4}\left(\frac{W}{R} + 2\alpha^2 + \frac{W^2}{R^2} + \frac{Z^2}{R^2}\right)$$

where PE=pass energy, W=slit width, R = mean radius of hemispheres, α = radial entrance angle, and Z = slit length. The slit-aperture pair at the entrance to the analyser determines α and W, and is normally chosen so that the first two terms on the right of the equation make equal contributions to the resolution. With this assumption and ignoring higher terms:

$$\Delta E = \frac{PE\ W}{2R}$$

The convolution of ΔE and photon beam line–width gives the overall energy resolution of 90 meV at $h\nu = 70$ eV.

3.2. LEED and XPS experimental details

3.2.1. Experimental chamber for LEED and XPS at Liverpool

This chamber was designed initially for Inverse Photoemission (IPE) experiments. The chamber is a cylindrical shape with a height of 776 mm and an internal diameter of 260 mm. It is made of μ-metal, a nickel-iron alloy (77% Ni, 15% Fe plus Cu and Mo). The chamber is equipped with common surface science facilities such as XPS, UPS, LEED, and IPE. The chamber can be separated into two levels, an experimental level and a sample preparation level as shown in Fig.3.11(a). The sample preparation level contains an evaporator, LEED optics used for surface characterisation and a load lock which is used for sample transfer without having to bring the main chamber up to atmospheric pressure. The experimental level includes a commercial 150° hemispherical analyser, UV discharge lamp and X-ray source.

The lowest base pressure in the main chamber, 1.5×10^{-11} mbar, is possible with a pumping system comprising a water-cooled turbo pump, which is backed by a molecular flow rotary pump, and Titanium Sublimation Pump (TSP). The most important factor in achieving low pressure during experiments was the careful preparation of the sample and thin films and degassing of the experimental apparatus – a pressure of 8×10^{-11} mbar was routinely achieved during data acquisition.

The electron energy analyser used in this chamber for both the XPS and UPS is a Vacuum Generators MDS50, 150° hemispherical electron energy analyser. It is mounted on an aluminium ring which is free to rotate in the horizontal plane. Rotation is controlled by means of rotary drive in the mounting flange.

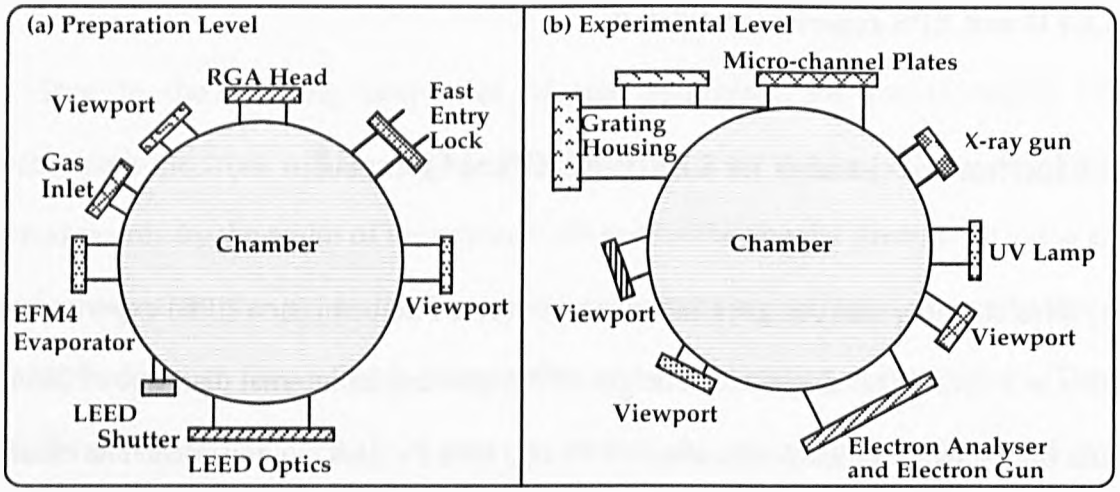

a)

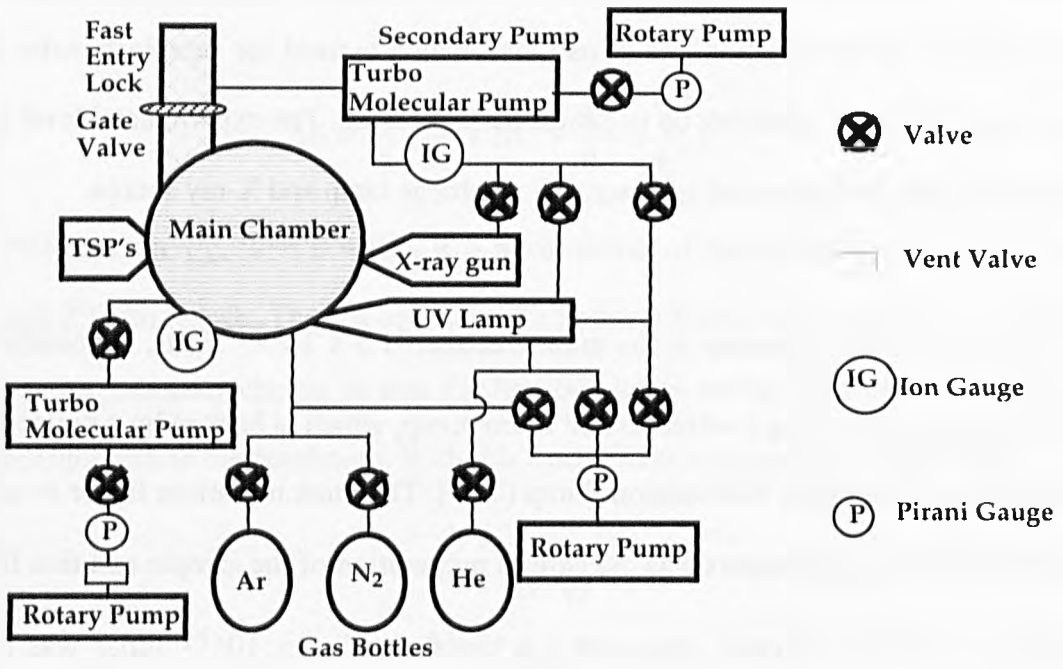

b)

Fig.3.11. Layout of the Inverse Photoemission chamber.

a) Separate levels and their equipment

b) Pumping system

The analyser consists of two concentric sectors with a mean radius of 50 mm. The entrance aperture is 2 mm width channeltron at the exit position such that the output response to one electron input is around 10^8 electrons. There is a slot in the back of the analyser which allows any higher energy unwanted electrons to pass out. The analyser was operated in constant analyser pass energy mode. In this mode of operation, the pass energy of the analyser is kept constant so that electrons which enter the analyser are retarded by an amount dependent on their kinetic energies.

The X–ray source, attached to the IPE chamber for the use in the XPS experiments was a water cooled Henke type with twin anode source (Al–Mg).

The IPE chamber had a VG Omniax manipulator. The sample holder, shown in Fig.3.12, was made specifically for these experiments, as no commercially available sample holder was capable of reaching temperatures of >2000K. This has an electron beam heater which rapidly heats the sample to > 2300 K. The heater filaments are made from 5% thoriated-tungsten wire as this alloy has a very low work-function. One side of the filament is held at ground potential while a 900 – 1500 V potential is applied to the sample. The final sample temperature reached depends on the emission current as measured (HT supply), the potential difference between the filament and sample and the surface area of the sample and its holder. If the sample holder is bulky it acts as a heat reservoir drawing heat from the crystal, and hence this increased surface area increases power required to heat the sample to a specified temperature. The temperature of the sample was measured using a C–type thermocouple connected to the sample and by an optical pyrometer.

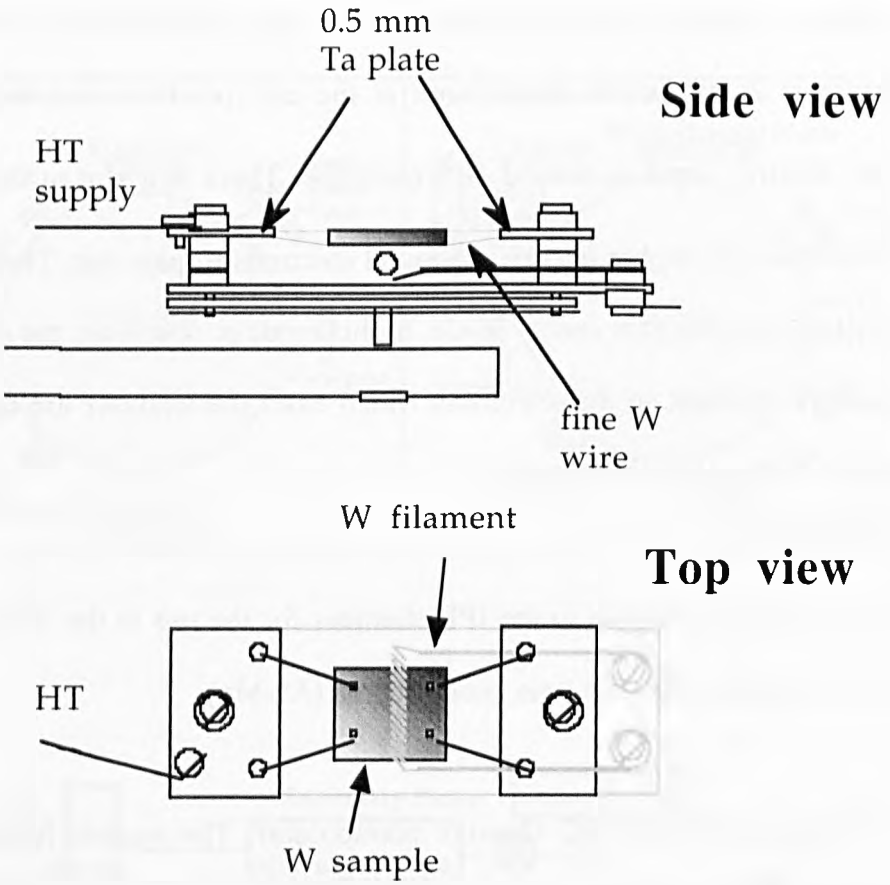

Fig.3.12. Sample holder for LEED and XPS experiments.

3.2.2. LEED and LEED I–V

LEED and LEED I–V data acquisition was carried out using the system described in Ref. [21]. It includes a Vacuum Generator LEED system, which was mounted onto the analytical chamber. The camera was set parallel to the LEED screen to reduce any misalignment errors before taking images of the LEED patterns. The images were then calibrated using the Image SXM software [90] to minimise any x-y distortion of the raw images which could be caused by any misalignments of both the sample and the camera from the central axis of the LEED screen. The images used in this analysis have a high pixel resolution of 704 x 506 [21] and all the measurements were carried out using the image analysis software. The experimental set up for LEED and LEED I–V data acquisition is shown in Fig.3.13.

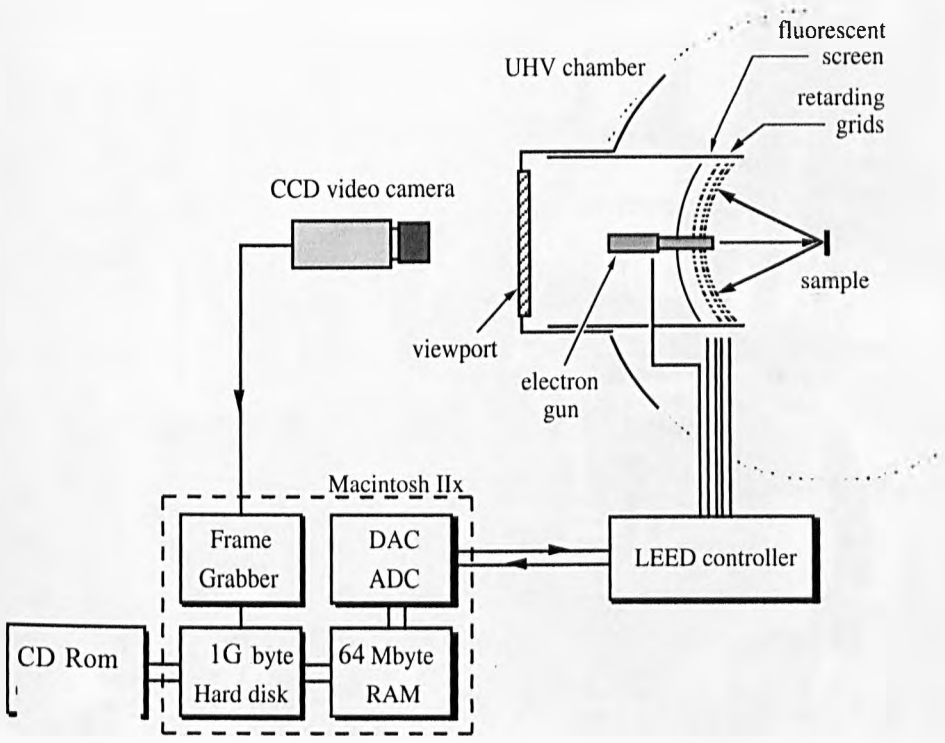

Fig.3.13. Experimental set up for LEED and LEED I–V experiments.

3.3. Experimental details of Scanning Tunnelling Microscopy

3.3.1. STM chamber

STM experiments were performed using a commercial Omicron STM operated at room temperature in a UHV chamber (Fig.3.14). This chamber consists of two separate sub–chambers – an STM chamber and a sample preparation sub–chamber as Fig.3.15. The preparation sub–chamber is equipped with an Omicron LEED facility. The samples were transferred between the STM and manipulator in the preparation sub–chamber using a wobble stick. The chamber was pumped with a TSP, turbo molecular pumps and ion pumps. When the sample had been transferred from the manipulator sample holder to the STM, the turbo pumps were switched off to reduce vibrations as much as possible. The pressure during imaging remained around 2×10^{-11} mbar.

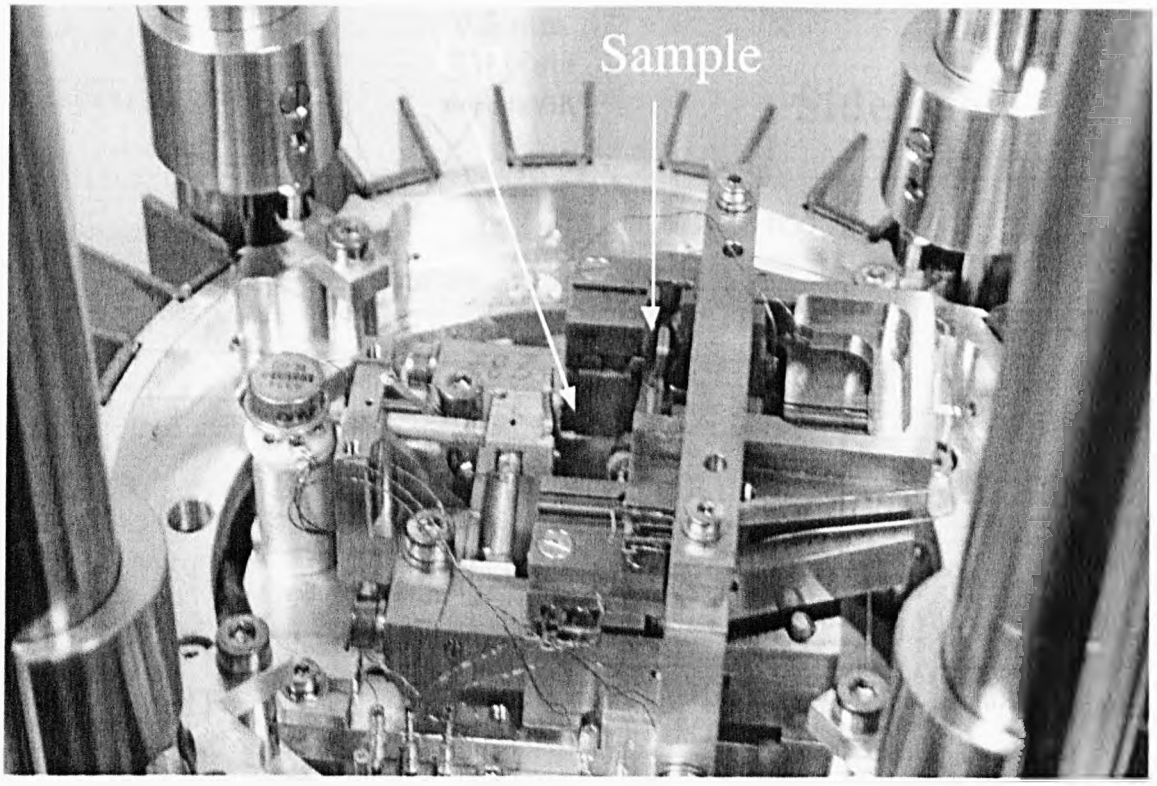

Fig.3.14. The Omicron STM used in these STM studies.

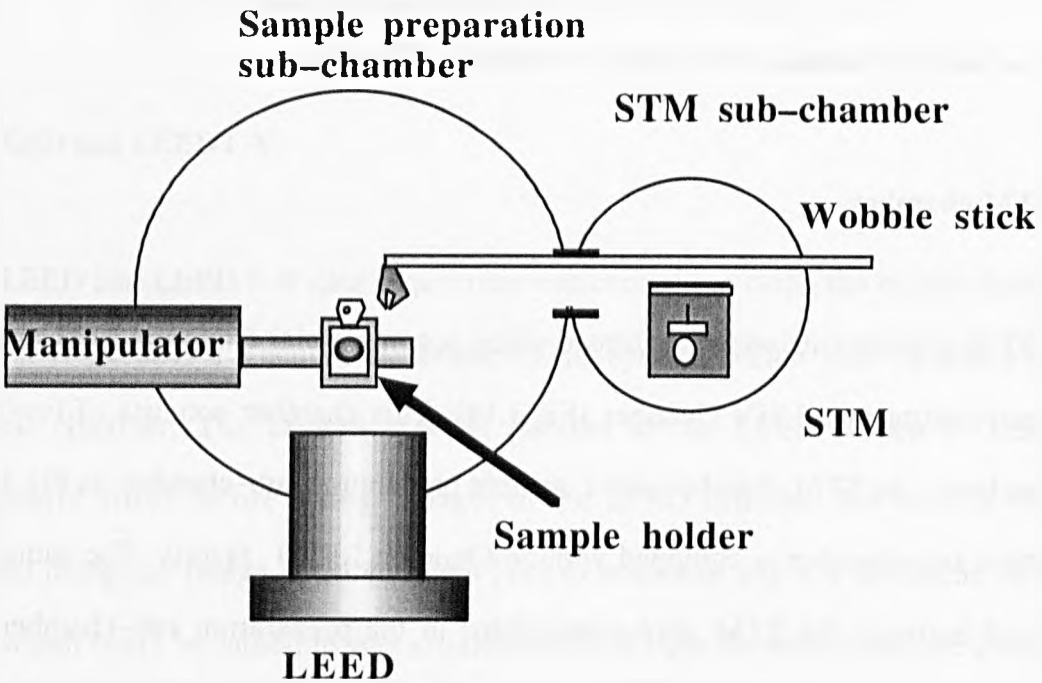

Fig.3.15. Layout of STM chamber.

3.3.2. E-beam heater and sample holder for STM experiments

Since tungsten needs high temperatures for cleaning (up to 2500K-2800K), the cleaning process had to be carried out in a place far from the STM. When the sample had cooled back to RT, it was transferred to the STM. To reach such a high temperature an e–beam heater had to be used. The sample had to be mounted on a temperature resistant RM such as Mo, Ta or W in such a way that it could be transferred to the STM. Such a sample holder was designed and built (Fig.3.16) based on the above requirements and the following technical factors:

i) The amount of power that could be put into the system was limited to 600 W by the maximum voltage (1500V) and the maximum emission current (400 mA) of the Glassman power supply. The principal power loss during the flashing process (increasing temperature of the sample to ~2500 K for a few seconds) of the sample is radiation loss. To produce the required temperature with this power limit, the surface area of the sample and the sample mounting system in the e–beam heater had to be reduced as much as possible. Therefore a number of holes were made in the STM sample holder. These holes had to be small enough to maintain the strength of the sample holder against thermal deformations and the force exerted by the wobble stick during transfer between the STM and the e–beam heater. Also, they had to be large enough to prevent a significant increase of the area due to the production of new area on the inside of the holes.

ii) One of the problems with the W wires is that after heating to the high temperatures (1800-2800K) required for the cleaning process of W, they become fragile. Therefore the W wires used in the STM e–beam heater have to be strong (thick) and as far as possible from the centre of the e–beam heater. However, they have to be kept thin to reduce their radiative area and thermal conductivity as small as possible.

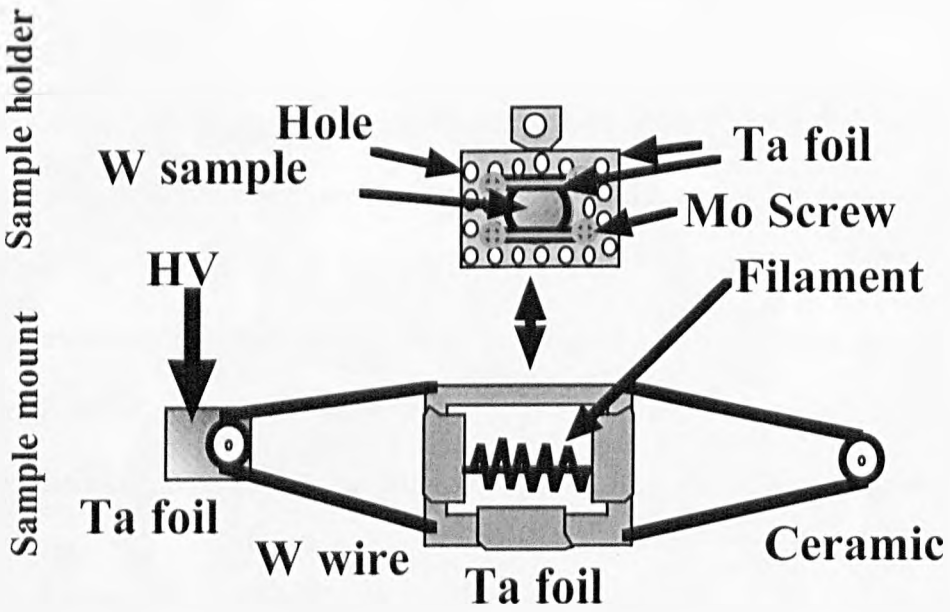

Fig.3.16. Schematic diagram of STM e-beam heater and its sample mounting system for cleaning W sample

iii) Ta is a soft metal which deforms easily, especially when it is hot. Therefore the STM sample holder has to be made from thick Ta foil while the area has to be kept as small as possible. Ta has a melting point of 3290 K [34] which is close to the 2800 K of the W flashing temperature. Therefore great care had to be taken not to increase the temperature by mistake.

iv) At high temperatures, the STM sample holder and the e–beam heater sample mount could deform and stick together. To separate them, it was necessary to shake the sample holder strongly with the wobble stick to take it out of the e–beam heater. This was a dangerous part of the experiment because there was high risk of breaking the fragile W wires of the e–beam heater or loosing the sample during the process. To make this separation easier sometimes it was necessary to warm up the system before the dismounting process.

v) To prevent any vibration during movement of the STM tip on the samples which will cause noise in the STM images, the sample has to be firmly attached to the STM sample holder.

Fortunately, the designed e–beam heater sample holder worked very well without breaking for the two set of experiments designed in this chapter, in which the sample was transferred between STM and the e–beam heater tens of times.

3.4. Evaporator

For the evaporation of Dy a commercially available WA Technology Knudsen evaporator (K-cell) cell was used. A schematic of this device is shown in Fig.3.17. The suitability of this type of evaporation cell for Dy evaporation is due to the high vapour pressure of this metal (70 Pa) [32].

A filament is wrapped around an oven, and by varying the current passed through the filament the oven could be run over a range of temperatures. The evaporator is rated to work up to temperatures of 1700 K although in practice heating to above ~ 1300 K resulted in extensive N_2 outgassing from the Pyrolytical Boron Nitride (PBN) liner. This evaporator was used to deposit Dy which was grown at temperatures between 1050–1200K. This evaporator has internal water cooling to keep the walls close to the evaporator at a low temperature and adsorbed gases were purged from the Dy during initial warming.

As the evaporant warms up the rate of metal evaporation gradually increases until equilibrium is reached at the temperature selected. This temperature can be maintained constant within ±1 °C. During this time the deposition rate cannot be accurately ascertained, and to prevent deposition onto the substrate during this period the evaporator is fitted with a shutter. Though here is no flux monitor on this evaporator, the evaporation rate was calibrated against time of completion of the 1st ML by XPS and controlled using the temperature reading of the oven as monitored with a thermocouple.

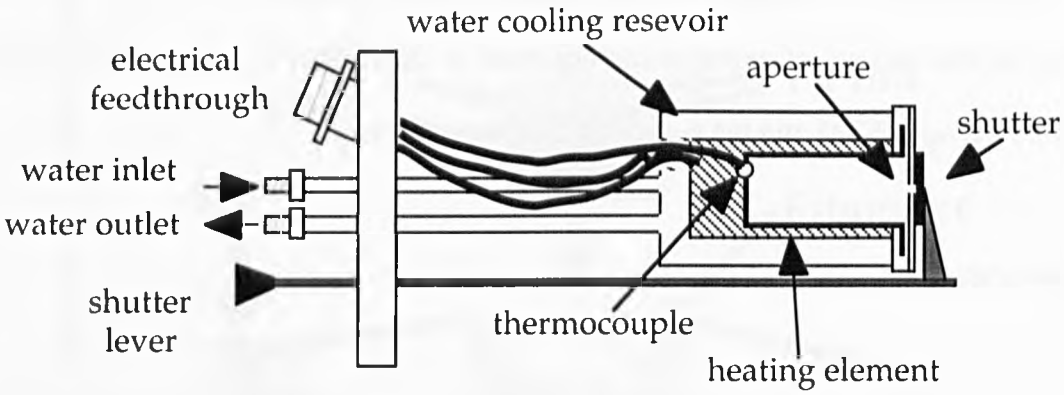

Fig.3.17. Schematic diagram of the WA Technology Knudsen evaporator (K-cell) used for the evaporation of Dy.

Chapter 4

Growth characterisation of Dy films on different W surfaces

4.1. Introduction

The growth of thin films is a physical problem of far–reaching consequences, both from a fundamental and an applied aspect. While the theoretical foundations of thin film growth have been laid very early [91, 92] it is only in recent years with the development of molecular beam epitaxy (MBE) and related techniques that thin film growth has become a very important tool for the creation of new materials. Non–equilibrium structures, exhibiting novel physical properties, have become possible to produce quite routinely [93].

So far the only growth investigation for Dy on W was by Ciszewski and Melmed [20] who used field electron emission from a sharp W tip. In this experiment the substrate, which was a poly–faceted crystal, was heated during deposition to give the adsorbate atoms sufficient energy to migrate over the substrate. They found epitaxial relationship of $(0001)\mathrm{Dy}\,\|\,(001)\mathrm{W}$ with $[01\bar{1}0]\mathrm{Dy}\,\|\,[001]\mathrm{W}$ for slow growth rates and $(0001)\mathrm{Dy}\,\|\,(011)\mathrm{W}$ with two epitaxial relationships of $[11\bar{2}0]\mathrm{Dy}\,\|\,[001]\mathrm{W}$ and $[11\bar{2}0]\mathrm{Dy}\,\|\,[111]\mathrm{W}$ for rapid growth rates. These epitaxial growth conditions were found only for the cases in which the substrates were held at 800K-930 K during the growth. However, these epitaxial information do not say anything about the growth mode and it was not clear whether the Dy grew as islands having those epitaxial relationships or in a layer–by–layer mode. Furthermore, the W surface was not flat and had a very small effective area, and so their conclusion regarding growth can not necessarily be extrapolated to atomically flat surfaces.

In this chapter the growth of Dy on different W substrates (W(100), W(112) and W(110)) and at different temperatures is investigated with XPS technique.

4.2. Growth mode study

4.2.1. Prediction of growth mode based on free–energy discussion

Adatoms arrive randomly on the surface from the gas phase and generally will adopt preferred local registry sites on the substrate, although they may possess considerable mobility to hop between other sites. At sufficient coverage these adsorbed atoms may display long-range as well as short-range order. During these stages the submonolayer adsorption structures are continuously changed as the coverage increases and thus give rise to various phase transformations, which can be observed in LEED patterns.

At higher coverage there may occur a transition from the nucleation to the growth stage, where the density of existing islands is so high that arriving adatoms will mostly stick on existing islands rather than hitting another mobile atom and form a new nucleus. Island formation is dependent upon the interactions between adsorbate atoms and substrate atoms. In the case of a heteroepitaxial film, where the lattice constants of the overlayer and substrate are often different from each other, the overlayer material distorts somewhat to achieve lattice-fitting where the atoms of the overlayer are permitted to strain away from their equilibrium positions but the energy gain for this strain is compensated by the energy lost sitting in minima of the substrate corrugation potential.

Traditionally, growth modes have been determined from thermodynamic equilibrium arguments, determined by Young's equation [92], and will depend on the surface free energy, defined as the energy required to increase the surface area by 1 unit of area, of the adsorbate γ_a, the interface γ_i, and the substrate γ_s.

$$\Delta\gamma = \gamma_a + \gamma_i - \gamma_s \quad (4.1)$$

It is also possible to write a similar equation in which the effect of pressure and temperature of the adsorption has been introduced [94]

$$\Delta\gamma = \gamma_a + \gamma_i \cos\theta - CkT \ln\left(\frac{P}{P_0}\right) - \gamma_s \quad (4.2)$$

where γ_s, γ_a and γ_i are surface tension, i. e. the surface free energy (per unit area) , of the substrate, adsorbate and interface of substrate and adsorbate film, respectively, k = Boltzmann constant, T= temperature of the substrate (Kelvin) , p (T) = solid phase pressure, P_0 (T) = equilibrium vapour pressure, C = a constant, and $CkT \ln\left(\frac{P}{P_0}\right)$ is the change in Gibbs free energy, known as chemical potential, when a particle is transferred from the gas phase into the solid phase of the deposited film at solid pressure P. The ratio $\frac{P}{P_0}$ is called the degree of super-saturation, which is one of the driving forces for the formation of a film deposited from an ambient vapour phase. θ (Fig.4.1) is the angle between γ_a and γ_i, which is zero for flat islands (layer–by–layer mode) and non–zero for island growth.

4.2.1.1. The Frank-van der Merwe (FM) growth mode

This growth mode is pictured schematically in Fig.4.2 (a). The FM growth mode, also known as laminar growth, is the idealised case. In both equations (4.1) and (4.2) this growth mode requires $\Delta\gamma < 0$. In this description, it is assumed that the flux of impinging atoms and the sticking probability remain constant during growth. As can be seen in Fig.4.2 (a) , straight

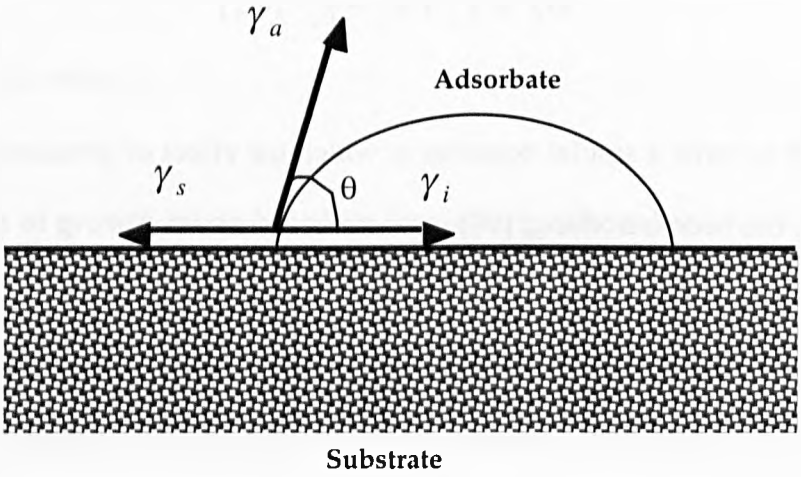

Fig.4.1. Simplified picture of an island of a deposited film. γ_s (γ_i) is the surface tension between substrate and vacuum (adsorbate). γ_a is surface tension between adsorbate and vacuum and θ is the angle relative to the substrate plane.

lines connected by "knees" or "breaks" are expected for the adsorbate (or substrate) Auger (or photoemission) signal versus time (or coverage) plot. These knees occur upon the completion of each layer and are due to the attenuation of the signal from the underlying adsorbate layers as the succeeding layers intercept smaller fractions of the substrate signal. The intensity of the substrate signal after forming a film with the thickness of d should be:

$$I_s = I_o \exp(\frac{-d}{\lambda}) \quad (4.3)$$

where s denotes the substrate, I_o is the initial intensity, before growing the film, d is the film thickness and λ is the inelastic mean free path of the electrons producing the substrate signal.

The case for the adsorbate signal is determined by:

$$I_a = I_o\left(1 - \exp(\frac{-d}{\lambda})\right) \quad (4.4)$$

In which a denotes the adsorbate, I_o is the saturation intensity, after growing a very thick film, d is the film thickness and λ is the inelastic mean free path of the electrons producing

the adsorbate signal. Assuming a constant dose rate dosage and constant sticking coefficient for different layers in the laminar growth, each layer formation will occur in a similar time interval. Using this assumption and the equation 4.4, the following relationship can be found between the slopes of the growth mode graph between the formation of successive layers:

$$\frac{m_1}{m_2} \approx \frac{m_2}{m_3} \approx .. \approx \frac{1}{\exp(\frac{-d_o}{\lambda})} = \textbf{constant} \quad (4.5)$$

in which m_i is the slope of the growth mode graph in ith layer formation time interval, d_o is thickness of one ML and λ is inelastic mean free path of the electron with the kinetic energy associated with the adsorbate signal. The "almost equal" notation has been used in equation 4.5 to emphasise that due to difference in sticking coefficients in different layer formation the terms in equation 4.5 might not be exactly equal.

4.2.1.2. The Stranski–Krastanov growth mode

The case of $\Delta\gamma = 0$, known as Stransky-Krastanov (SK) growth, is desired growth mode in which one or more layers are grown completely and then three-dimensional islands grow on top of the full layers. The nature of this growth mode is illustrated in Fig.4.2 (b) , and can be distinguished by the appearance of a well defined plateau in the growth plot. The straight line up to the point where the first break occurs corresponds to the formation of the first monolayer, as for FM growth mode. If the islands are large and have a high surface density, then the growth plot will tend to that of the FM growth mode.

4.2.1.3. The Volmer–Weber (VW) growth mode

The VW growth mode can be considered as a very extreme case of the SK mode where

the islands will start to grow directly on top of the substrate. This 3–D growth requires $\Delta\gamma > 0$. The VW growth mode is unsuitable for analysis using the Auger signal–time (As-t) or Photoemission signal–time (PEs-t) techniques as no break points appear in the plot to provide a reference for the coverage (Fig.4.2 (c))

In addition to these three standard types of growth mode, another growth mode has been suggested which can be considered as extreme case of the above modes. Two common types of this growth mode will be discussed below.

4.2.1.4. The Simultaneous Multilayer (SM) mode

This is also known as the Poisson growth mode and was first suggested by Rhead et al [95, 96]. Like the FM mode, the SM mode is an idealised case but this time for negligible surface mobility (Fig.4.2. d). Unlike the FM case, in the SM mode the diffusion rate for the adsorbate on the substrate is either very slow or non–existent. Here as the impinging atoms come into contact with the surface they stick where they land, without any lateral movement of the atoms. For this growth mode the n^{th} layer can start to form as soon as a fraction of the (n-1) th layer is present. The effect of slow diffusion processes on layer–by–layer growth curves is the rounding of the monolayer break points, such that the plots have an exponential form with time. In many studies where the SM growth mode has been suspected, a gradual increase in the background of the LEED pattern without appearance of extra spots has been noted.

4.2.1.5. The Monolayer Plus Simultaneous Multilayer (MSM) growth mode

In the MSM growth mode a complete monolayer is formed initially followed by growth as in the SM mode, see Fig.4.2 (e). Differentiation between the growth plots for this

mode and the SK mode may be difficult. The main difference between the SK and MSM modes is that for the MSM mode the variation after the first break point is exponential whilst for the SK mode it is close to linear.

As it is clear from the equation (4.2) , the crystal growth mode of a certain system is dependent not only on a constant material parameters, but also on the chemical potentials (the third term in equation 4.2) which can be controlled by the vapour pressures and temperatures. For example, a rough surface annealed in UHV may become planar by the process of surface diffusion. This process can be understood by considering the increased chemical potential term in the equations. In the case of in situ UHV deposition, which has high super–saturation ($z = P/P_O$) at low substrate temperature, i. e., low equilibrium vapour pressure P_O, layer growth mode is favoured.

The usually desired, laminar, layer–by–layer growth mode is rare in equilibrium [97] and can occur only if the film and the substrate have the same lattice constant [98]. In the presence of strain, the film either forms islands immediately (VW mode) or on top of a small number of laminar layers (SK mode). The thickness of the film that in the SK–mode grows laminar before the onset of island formation is called the critical SK–layer thickness Θ_{SK}. It has been shown that the SK–layer thickness is temperature dependent and increases with increasing temperature [97, 99]. This is in agreement with the theoretical prediction as mentioned above.

Although γ_a and γ_s are well known for most systems, γ_i is difficult to obtain, thus causing some uncertainty. Furthermore the above formulas are the general conditions for determining crystal growth modes on the basis of simple thermodynamic equilibrium arguments. In practice, deviations from these three distinct growth modes exist in many cases due to effects such as (i) presence of strain energies, which appear when very thin films strain to cope with lattice mismatch with the substrate, (ii) many films are grown under conditions far from equilibrium, (iii) kinetic and defect effects which very often happen in normal growth conditions. Nevertheless, the principal thermodynamics formula is helpful as a guide for predicting general trends in film growth.

Of the published work on REs grown on metals substrates, the refractory metals have been used most extensively, with the transition metals also receiving some attention. Few studies of REs grown on other metal substrates exist.

Rare earths have been grown on different transition metals such as Sm [100, 101] and Yb [102, 103] on Al, Sm [104] and Tb [105] on Co, Dy [2, 11, 12, 106] and Sm [107, 108] on Cu, Dy and Ce [109] and Sm [110] on Pd, Gd, Dy and Tb [111] and Gd [112, 113] on Fe, Yb [114] and Gd, Tb and Dy [106] on Ni. More references can be found in [6]. Growth on each of the substrates described so far has lead to an element of interdiffusion and hence alloying at the interface. This is not always desirable, especially in the pursuit of growing a well-ordered RE film with properties as similar as possible to a single crystal. An optimal substrate must ensure thermodynamic stability of the adsorbate layer at submonolayer coverage and must be as stable as possible against reaction with the layer at elevated temperature, while at the same time encouraging multilayer formation [13]. Such substrates should be the most densely packed surfaces of refractory metals (RM) such as the (110) surfaces of W and Mo or the (0001) plane of REs.

The RM substrates provide no adsorbate–induced reconstruction and no interdiffusion of RE films. These substrates are stable against reactions with adlayer at elevated temperatures [13]. For these reasons most RE film studies have used the surfaces of W or Mo as the substrate. For example Sm [115-117], Gd [72, 118], Yb [115, 119, 120], Tb [121], Dy [8, 15]. The choice of Mo and W bulk single crystals as substrates is due both to their high surface energies, and lattice matching considerations. The bcc (110) plane of both RM is close packed, and roughly matches the hcp (0001) planes of REs. The atomic roughness of the (100) plane complicates ordered growth on this surface, although geometrical considerations are more favourable. With the exception of Pb, all metal adsorbates on this face appear to force a c (2x2) reconstruction of the substrate, and the resulting interface is highly strained [122]. On both faces, metals have been observed to grow according to the SK mode, with 1-3 monolayers of adsorbate forming before nucleation of 3-D islanding.

Since the rare earths are chemically similar to each other, the parameters for growth of different rare earths on W (or Mo) are broadly similar, although there is a small variation in the optimum substrate temperature and evaporation rate.

There have also been reports of RE films on other substrates. These include deposition on to semiconductors [4] incorporating RE/Si interfaces [3, 123] and RE/Ge interfaces [124, 125]. In addition to these there are also several studies growing RE films using molecular beam epitaxy (MBE) with non- (0001) orientations [1, 126]. This has been achieved by growing RE films on RE single crystal substrates. It is known that the growth of the more open surfaces such as the $[10\bar{1}0]$ and $[11\bar{2}0]$ faces can only be achieved by growth on to a RE single crystal of that orientation. However, as has been shown by Barrett *et al* [127], the more open RE single crystal surfaces reconstruct to form a pseudo- (0001) face.

4.3. Growth monitoring

It is common to monitor the growth mode of a thin film in UHV using electron probe techniques. e. g. Auger spectroscopy [128], RHEED [129], secondary electron current [130] and photoemission spectroscopy [85]. To choose a suitable technique for growth monitoring, and specially to extract quantitative information from it, a number of factors must be taken into consideration: (i) It is important for the signal intensity of the adsorbate and the substrate monitored by the technique to be dependent to the amount of material present. (ii) In the growth of thin films, and specially at submonolayer coverages, the amount of the adsorbate material is low and so the adsorbate cross–section has to be large. (iii) To see changes in signals during changes in the adsorbate layer, the adsorbate and substrate signals have to have small inelastic mean free paths. (iv) Finally it is important that substrate and adsorbate features chosen for monitoring do not overlap in energy. Therefore, one of the problems dealing with growth monitoring of ultra thin films with spectroscopy methods, is to find suitable peaks for monitoring. This problem is more crucial for low coverages because of the low intensity of the adsorbate signals and weak effect of the adsorbate on substrate signals, especially on those with high inelastic mean free path.

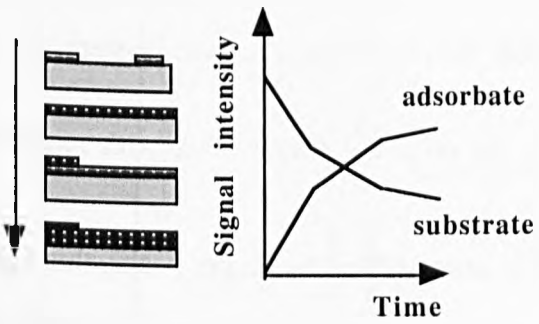

a) FM growth mode

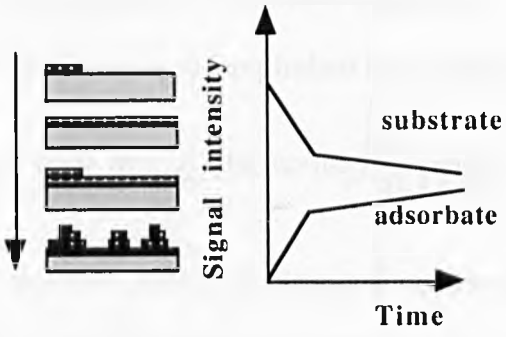

b) SK growth mode

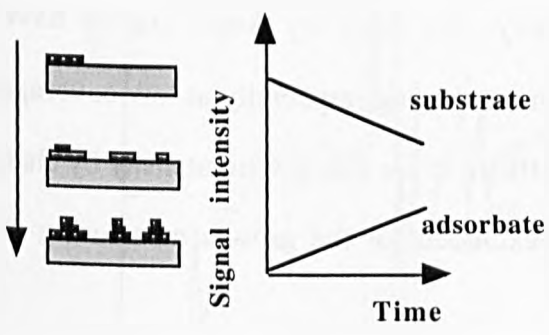

c) VM growth mode

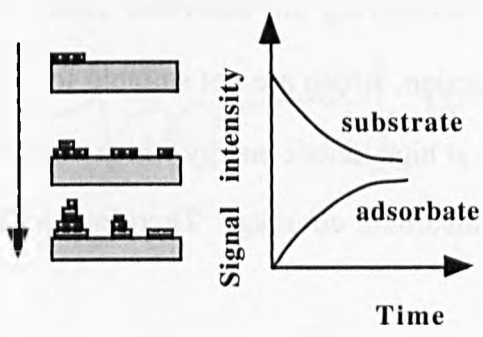

d) SM growth mode

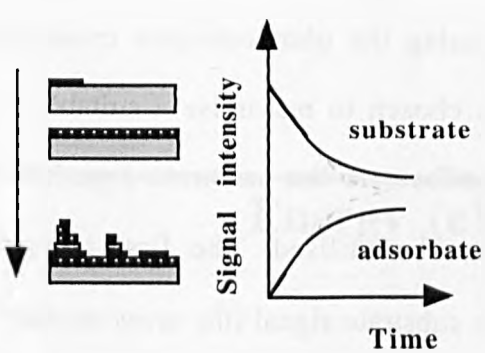

d) MSM growth mode

Fig.4.2 Growth mode and AS-t Plot for different growth conditions

Although most UHV chambers are equipped for AES and this technique is the most commonly used technique but it is not very suitable for the Dy on Tungsten system. As it is clear from $\frac{dN}{dE}$ curves of Dy and W (Fig.4.3) , the only Dy Auger peak with reasonable cross–section is a peak, at 151 eV. However, as it is expected for the Auger peaks, this peak is broad and has overlapped with the broad and the most intense Auger peaks of the W at 163 eV. Since the substrate signal is predominant at low coverages, this will cause a significant error in measuring the adsorbate signal intensity. The other Dy Auger signals have low cross–section, which are not suitable for growth monitoring, especially at low coverages, or they are at high kinetic energy which makes it difficult to see changes in intensity by changing in the adsorbate coverage. Therefore AES is excluded for the growth monitoring of this system.

Another technique suitable for monitoring growth mode of such a system is photoemission spectroscopy using the photoemission cross–section effect [85]. In this technique a photon energy is chosen to maximise a suitable photoemission peak of the adsorbate and minimise the effects of the substrate signals on it. There are two main cross–section effects that can be utilised. The first is using atomic photionisation cross–sections to minimise the substrate signal (the cross–section of all elements have been calculated and tabulated by Yeh & Lindau [79]). From the point of view of minimising the substrate signal, the most important feature of photoionisation cross–sections is the existence of Cooper minima [131]. This is where the atomic subshell wavefunction has a node resulting in a minimum in the photoionisation cross–section for the subshell. In particular, this allows the valence bands of the 4d and 5d transition metals to be suppressed effectively if the correct energy is chosen.

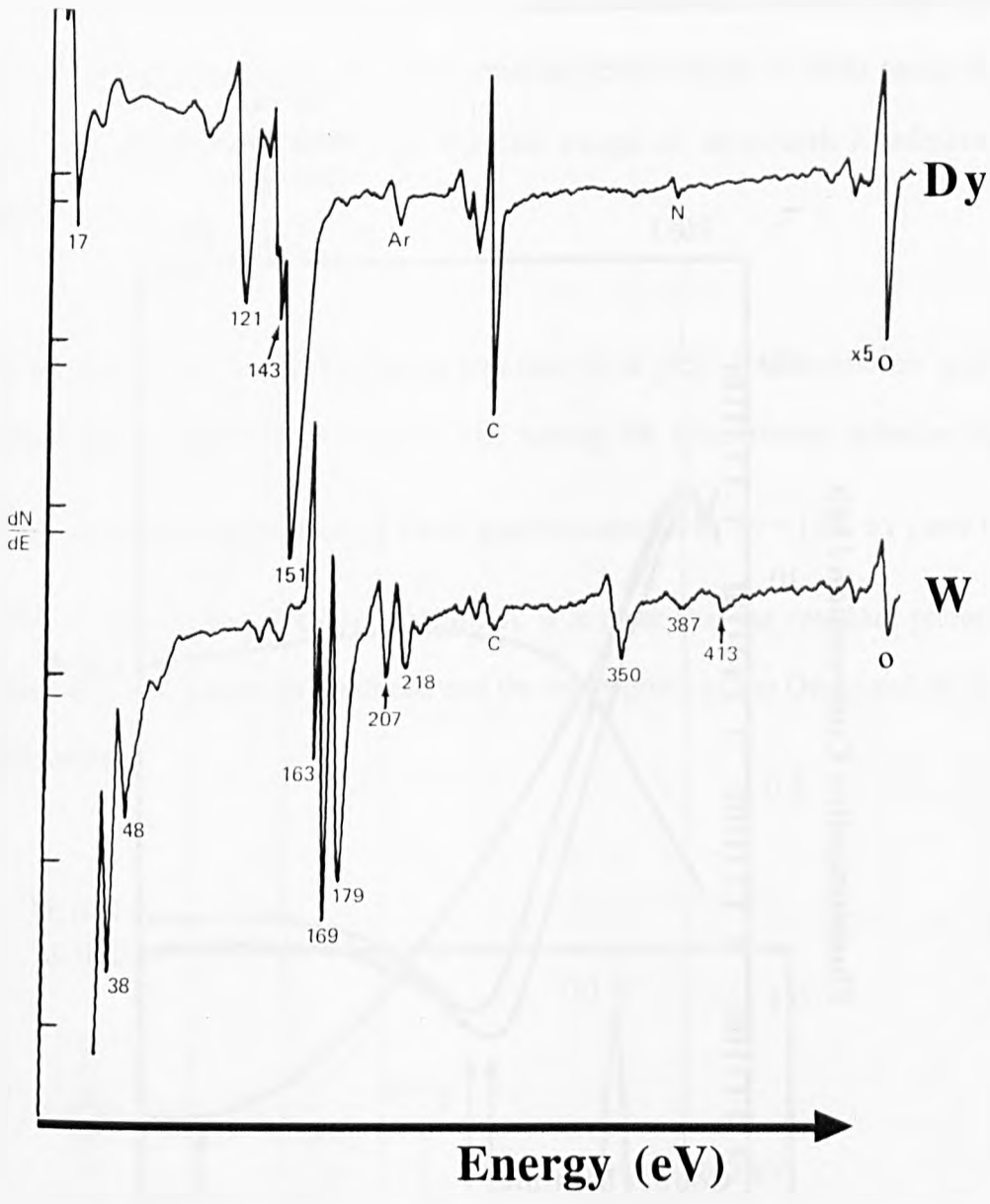

Fig.4.3. AES signals ($\frac{dN}{dE}$) from Dy and W.
Adapted from Reference [132]

The second cross–section effect that can be used involves maximising the adsorbate signal via resonant photoemission. This occurs at core–level ionisation thresholds for elements which also have a partially filled level, and causes an enhancement of photoemission signal. The best example of this is giant resonance in rare–earth metals [133], where the

core level (4d) and partially filled level (4f) are both from the same shell. This is will provide very large signal from the rare–earth atoms.

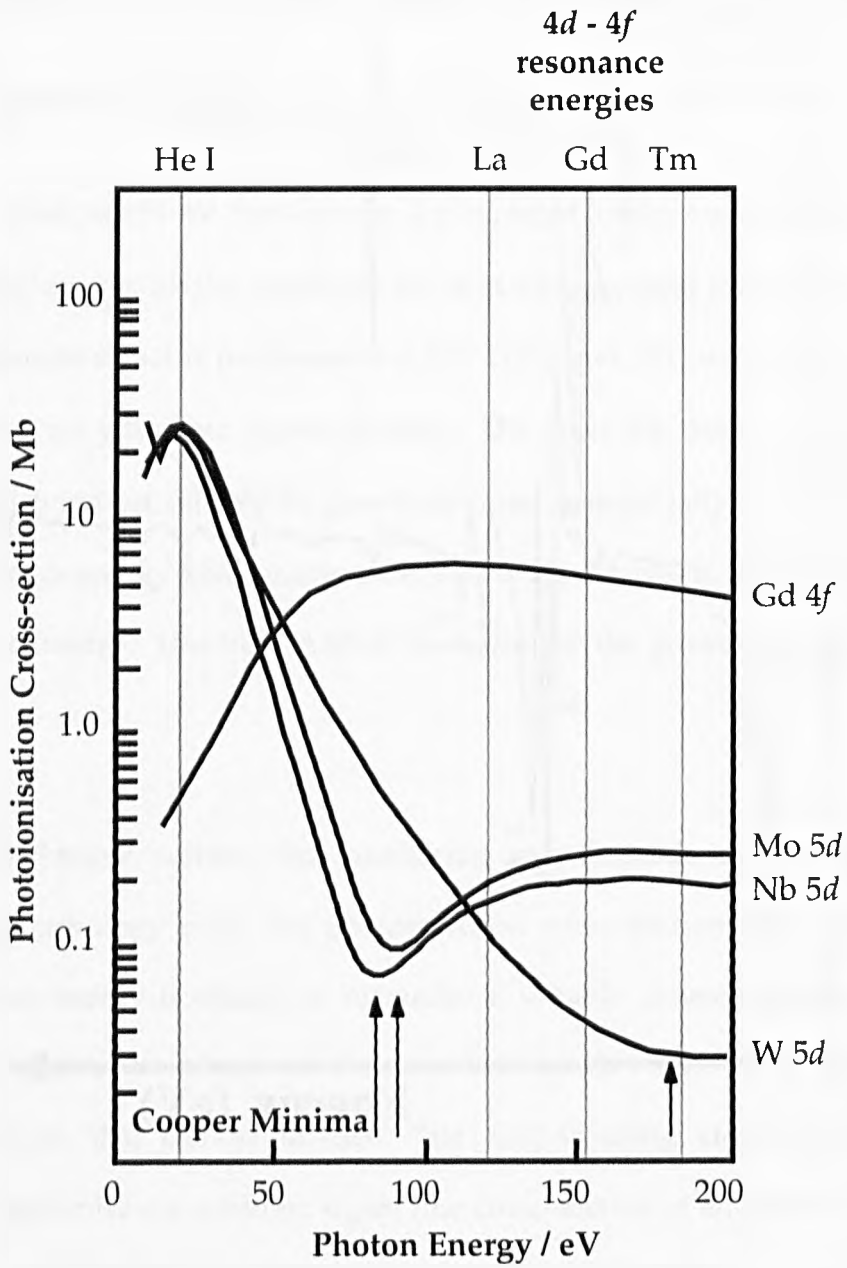

Fig.4.4. Photoionisation cross-sections for three lanthanides and the three commonly used substrates showing the resonance energies and Cooper minima. The arrows indicate the Cooper minima. Adapted from calculations of Yeh & Lindau [79].

As shown in Fig.4.4. the resonance energies of all the lanthanides occur close to the Cooper minima of W, Nb and Mo, so photoemission spectroscopy at these energies may be very useful for growth monitoring of the full range of rare-earth / refractory-metal combinations.

Fig.4.5. shows an example of using this technique [85]. Photoemission spectra were taken on the same film of Gd on W(110) , by tuning the synchrotron radiation energy to maximise the adsorbate signal, the Gd 4d-4f giant resonance at $h\nu = 152$ eV, and minimise that from the substrate (due to Cooper Minima). It is clear that the resonant photoemission signal of the Gd is much more pronounced and the two signals of the Gd 4f and W 4f are well separated in energy.

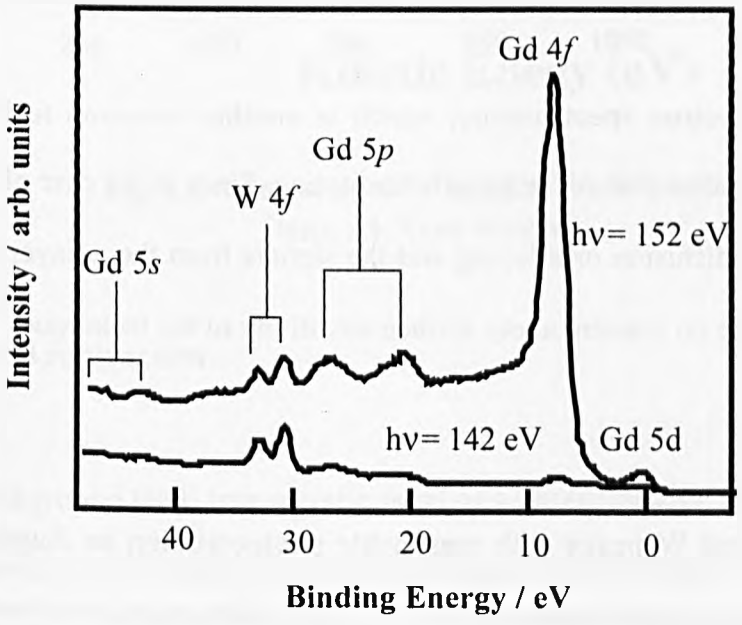

Fig.4.5. PES spectra of 3 ML of Gd on W(110) showing the effects of the giant 4d resonance at hν=152 eV. Adopted from reference [85]

It is also possible to suppress the adsorbate signal and enhance the substrate signal by exploiting the same cross–section effects, which then allows the growth to be monitored using the photoemission signal of the substrate. However, this can lead to difficulties as it is known that photoelectron diffraction can cause an enhancement of the substrate signal with increasing coverage [134]. This is particularly clear during the deposition of the first monolayer when the number of substrate atoms with neighbouring adsorbate atoms is increasing. However this is only seen for photoelectrons with a kinetic energy of a few hundred eV or more [135]. Therefore, if photoelectrons in this range are to be monitored the adsorbate signal should be used to avoid any diffraction effects.

Another advantage of this technique, which is common for all photon– excited techniques, is that unlike electron–excited techniques such as AES (in electron–excited type) and HREED, which may lead to structural damage and local heating effects over the area being sampled, the photoemission methods use photon–excitation which do not have this problem. However this technique needs synchrotron radiation which is not widely available.

X–ray photoelectron spectroscopy, which is another common technique in UHV analysis, could be a good candidate for growth monitoring. Since in the case of rare-earth films on W there is no interdiffusion or alloying and the signals from the adlayer are going to be monitored, there will be no concern about surface sensitivity of the technique.

To have Dy and W peaks with reasonable photoemission or Auger cross–section (producing high signal to noise ratios) and far from other photoemission or broad Auger peaks (to prevent overlap between signals) , XPS with Mg and Al X-ray sources has been checked. However XPS with a Mg Kα source has been excluded because Dy signals produced by this

photon energy have low cross–section and have high kinetic energy with high inelastic mean free path (Fig.4.6). However, XPS with a Al Kα source was the best choice among the above techniques. As can be seen from Fig.4.7 and Fig.4.8 the best peaks for this technique are Dy $3d_{\frac{3}{2}}$ and W 4f.

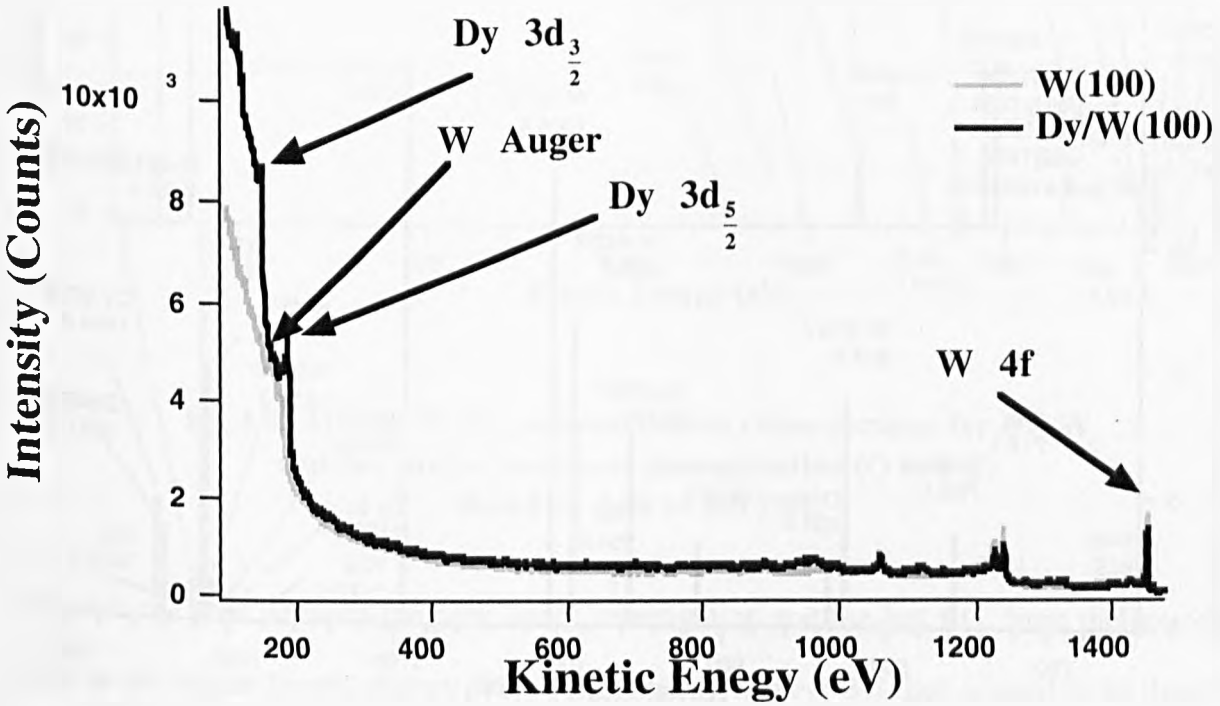

Fig.4.6. Wide scan of W and Dy/W(100) taken with Al–Xray source.

4.4. Background subtraction

The background (BG) in a specific point of a photoemission spectrum is produced by inelastic scattering of the photoelectrons with higher kinetic energy. This phenomenon will place the photoelectrons in a lower kinetic energy position of the spectrum. The amount of the energy reduction depends on the type of inelastic interaction. To extract quantitative information from a XPS, or other photoemission spectrum this BG has to be subtracted from the spectrum. Two types of BG, named Shirley BG and Tougaard BG, have been used in the

XPS analysis of this chapter. Prior to use of these BG's algorithms, a constant BG sitting at the higher kinetic energy side of spectra was subtracted from the spectra and then the spectra were normalised to their maximum intensity. The XPS results show the same growth monitoring results for both Tougaard and Shirley BG subtraction (see next section).

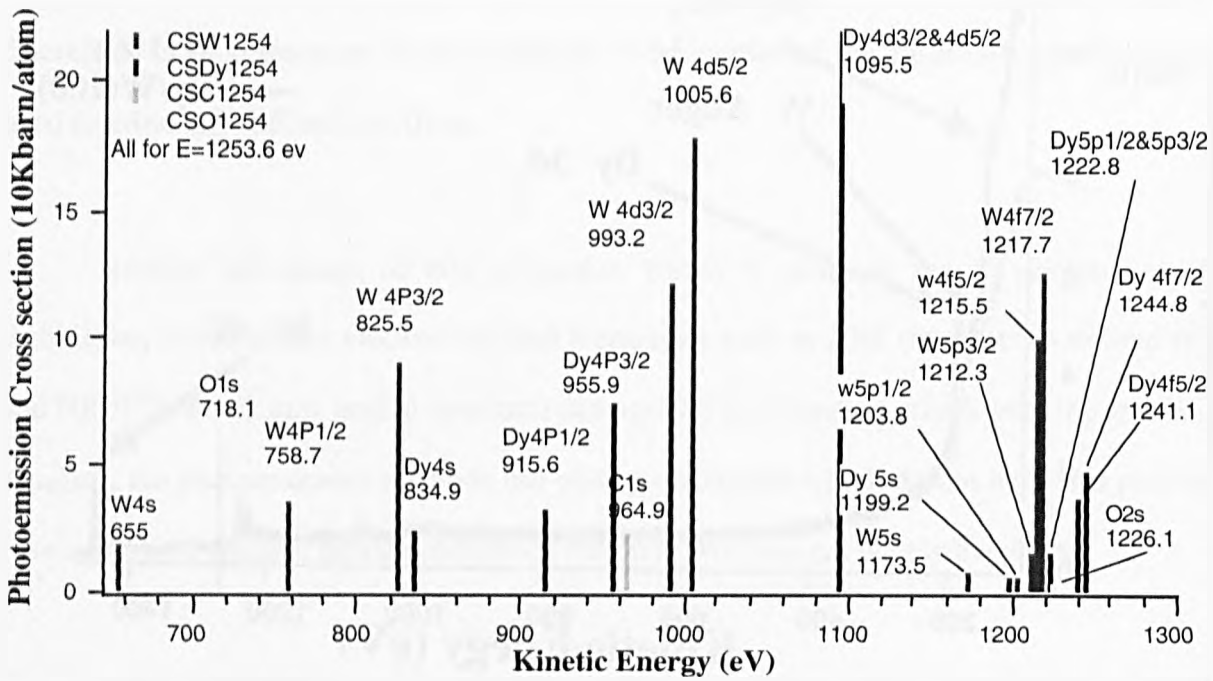

Fig.4.7. Mg – Kα X–ray photoionisation cross–sections for Dy, W and two major sources of contamination (O and C). Based on data in Ref [79]

4.4.1. The Shirley background

To find the BG under a specific peak by this method, two boundary points are first chosen on each side of the peak. These points have to be far from the peak such that they can be assumed to be merely on the BG of the spectrum. Then a constant line, drawn from the boundary point at the higher kinetic energy side is used as the first guess for the BG point. Now a new BG is calculated in such a way that the intensity of every point on the new BG is

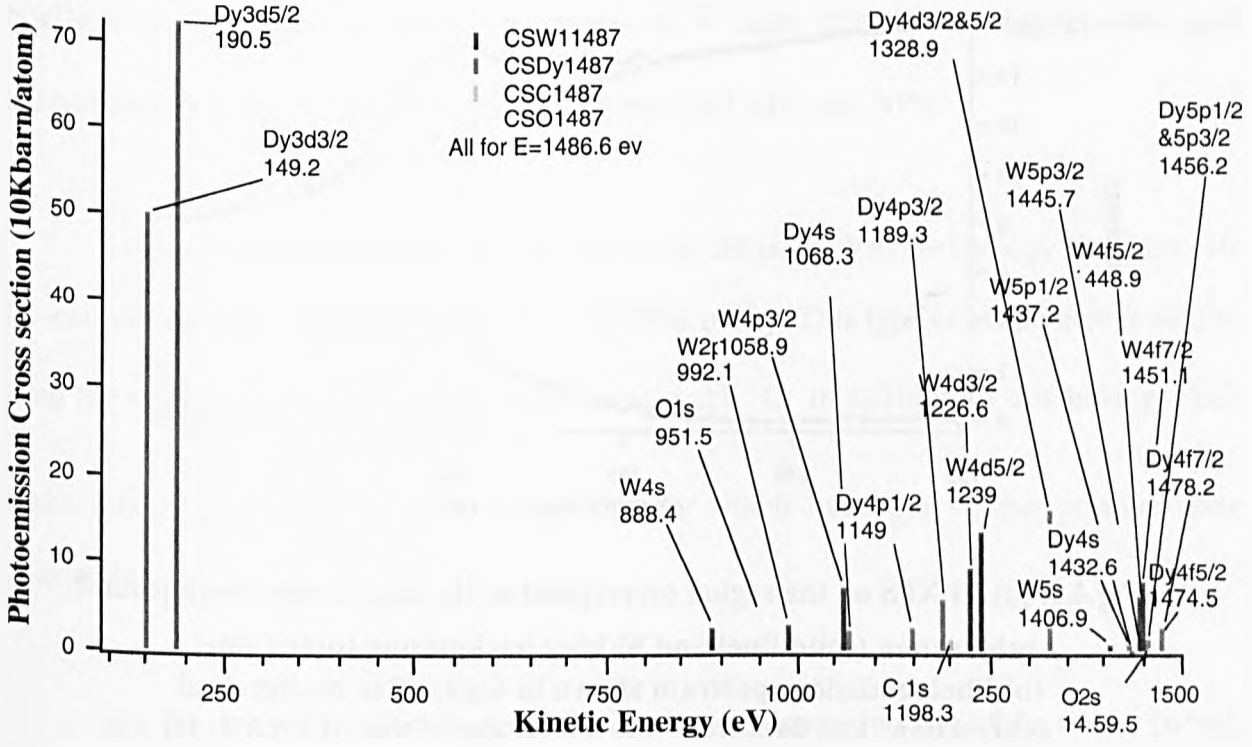

Fig.4.8. Al – kα X–ray photoionisation cross–sections for Dy, W and two major sources of contamination (O and C). Based on data in Ref [79]

equal to the area between the peak under investigation and the last BG, from the boundary point at the higher kinetic energy side to that point. The new BG then is used in an iteration as the old BG to find a new BG. This procedure is repeated until the change between successive calculated BG's is small. This background algorithm is commonly used in XPS data analysis because of its easy implementation, in an iterative computer program, to determine the background value. Fig.4.9 shows an example of such a background subtraction used in this chapter. More information about this kind of BG can be found in Ref [136-138].

4.4.2. Tougaard background

In the Tougaard method the fact that the inelastic scattering of the photoelectrons will reduce the kinetic energy of the electrons, and they will appear in the lower kinetic energy part of the spectrum, is used to calculate the BG. The BG in each point is calculated by

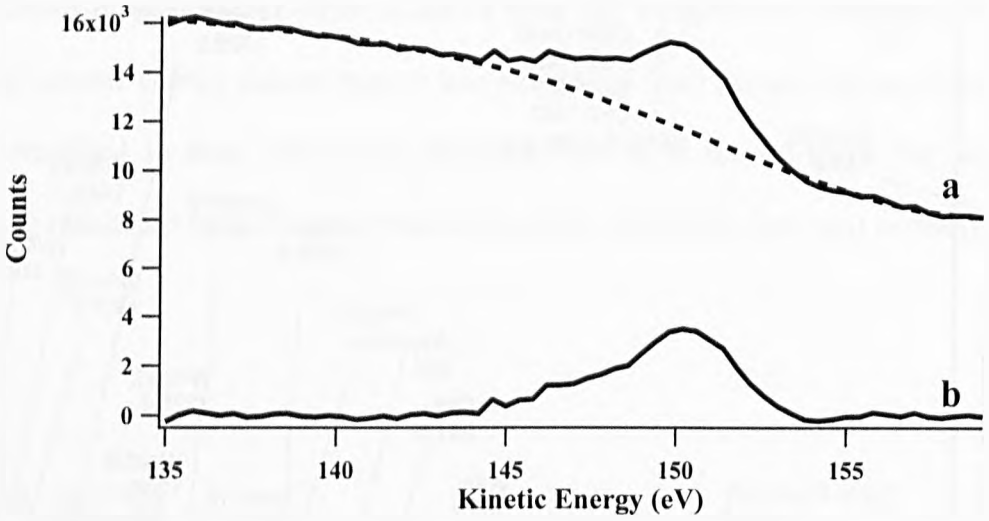

Fig.4.9. (a) Al-XPS of the region correspond to Dy 3d3/2 before background subtraction (solid line) and Shirley backgroung (doted line). (b) Photoemission spectrum shown in fig(a) after background subtraction. The data were taken after deposition of 1.5 ML Dy on W(100) at 460K.

considering the portion of electrons with higher kinetic energy to that point. This method needs a wide energy range (~ 40 eV) on the higher kinetic energy side of the peak under investigation to account properly for the effect of higher kinetic electrons in the background. More information about this kind of BG can be found in Refs [139-143].

4.5. Experimental details

The XPS experiments were carried out at the Surface Science Research Centre of the University of Liverpool. The X–ray source was a water cooled Henke type with twin anode source (Mg – Al) and the electron energy analyser was a hemispherical Vacuum Generator MDS50 type. The base pressure of the chamber was 8×10^{-11} mbar and during evaporation the pressure remained below $1x10^{-10}$ mbar.

The W crystals were prepared by backfilling the chamber with $\sim10^{-6}$mbar O_2 and heating the sample to 1800 K for 30 minutes to remove C, followed by cycles of flashing

briefly to 2500 K, when the pressure reached ~ 10^{-10} mbar. This process was repeated until the surface was judged to be clean and well–ordered by LEED and XPS.

Evaporation of Dy was carried out by a well–degassed WA Technology Knudsen cell (K–cell) evaporator which contained Dy of 99.99% purity. This type of evaporator is able to keep the evaporation temperature constant within ±1 °C. In addition to this having a cell make this evaporator suitable for degassing Dy which has high vapour pressure (see chapter 3).

The Dy coverage was calibrated using the known deposition rate of the source (which was regularly checked and remained stable over the experiments) and by the intensity of the W 4f levels in XPS. Due to the high reactivity of rare–earth metals [22], the sample was flashed every 30 minutes and new films were grown to ensure that the films were clean during the experiment.

The substrate temperature was measured using an optical pyrometer and a C-type thermocouple.

4.6. Growth monitoring results

Because of the large inelastic mean free path of the Al–Xray–excited photoelectrons from the W4f levels (~16 A) compared to Dy monolayer thickness (~2.5 Å) the changes in growth mode are not clear in the intensities of the W 4f levels. Therefore only the Dy signal intensities will be discussed in the next sections.

4.6.1. Dy/W(100)

4.6.1.1. Growth at RT

Fig.4.10. (a) shows the growth mode of Dy/W(100) determined by Al-XPS, of Dy $3d_{3/2}$ and W 4f intensities, after Shirley BG subtraction. The substrate was at RT during this experiment. This figure shows a clear break in the Dy curve, confirming completion of the first layer. After the break, the curve is close to a straight line, which suggests SK growth mode. However, significant features (shown by arrows) appear in this line which indicate that some kind of reconstruction might have happened on the film after the first monolayer completion, i. e., some Dy has moved from a lower layer to a higher layer (or vice verse) resulting in increasing (decreasing) Dy signal. To make sure that these features are not artificial features arising from X–ray gun instability, or other systematic errors such as temperature fluctuation, this experiment was repeated. It is clear from Fig.4.10 (b) that the same features were found at almost at the same positions of Fig.4.10 (a) , indicating that these are genuine features of the growth mode at RT.

4.6.1.2. Growth at elevated temperatures

The results of Dy/W(100) growth–mode monitoring at different substrate temperatures are shown in Fig.4.11. As is clear from these figures, there is a linear growth up to the first monolayer for all of the growth temperatures. The gradient of this line is significantly different from the rest of the graph. This suggests the SK growth mode for Dy/W(100) even at these temperatures. However, by increasing the temperature from 470 K to 770K, the break point becomes less distinguishable such that at 770K, due to modulations, linear behaviour can not be distinguished from the exponential after the break point. Therefore, this graph can be judged as a linear increase of intensity followed by an exponential (MSM) growth. The gradient of the graph after the break points is decreased by increasing the

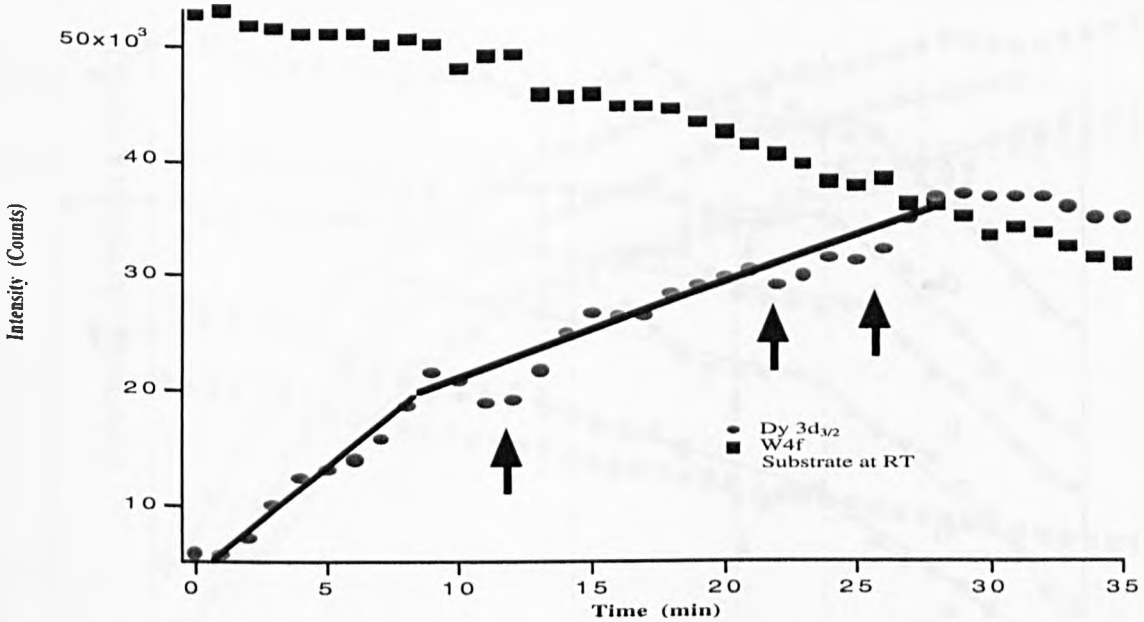

a)

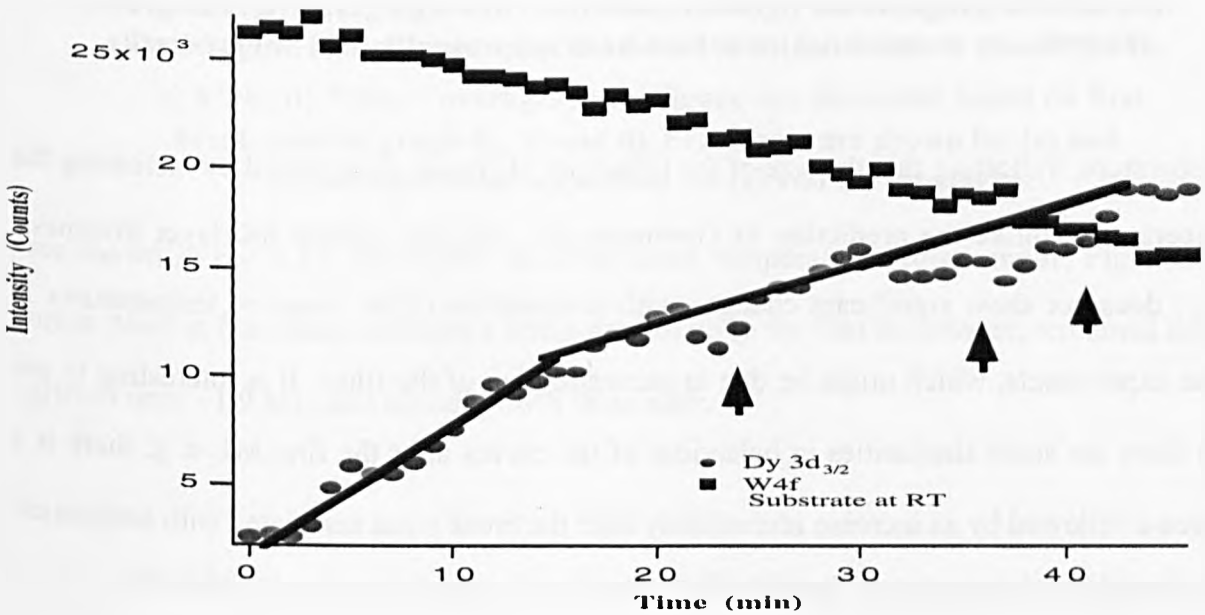

b)

Fig.4.10. Growth mode of Dy/W(100) determined by Al-XPS, of Dy 3d3/2 and W 4f, after Shirley BG subtraction. The substrate was at RT during these experiments. Fig b) is a repeat of Fig a) showing same feature after the first monolayer completion (break point). Due to the different deposition rate of Dy, figures (a) and (b) have different time–scale .

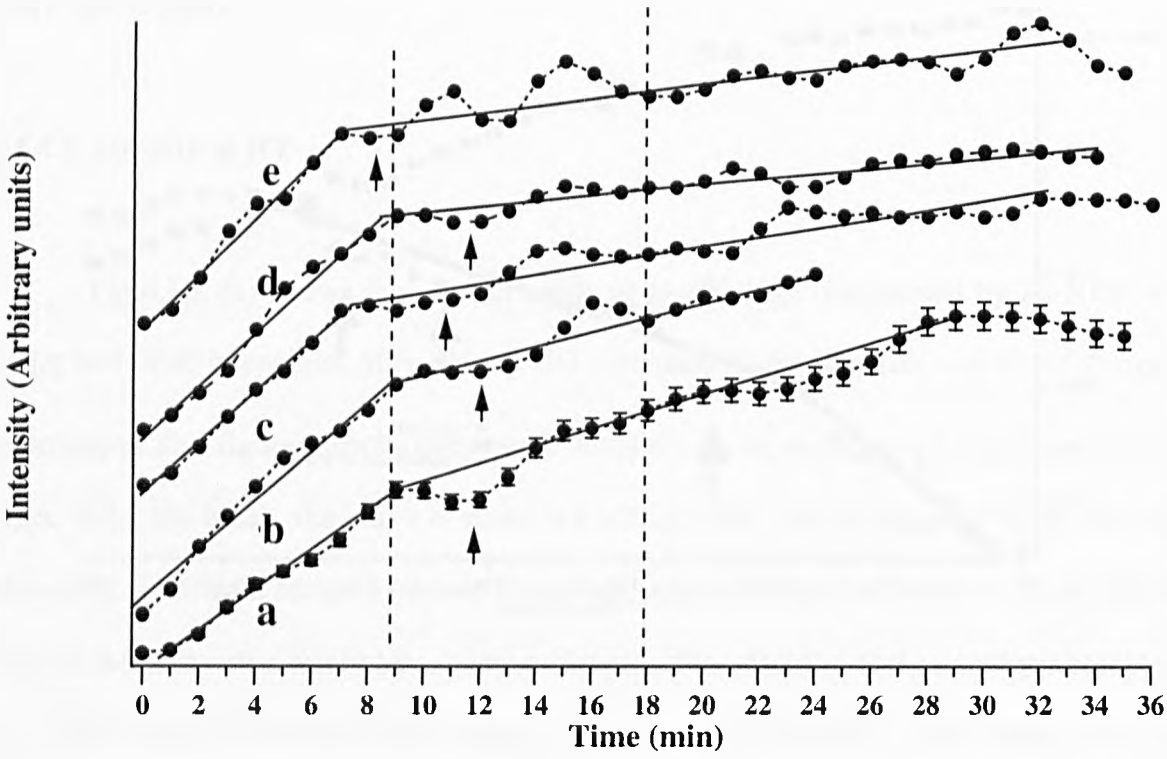

Fig.4.11. Dy/W(100) growth mode determined by Al–Xray of Dy $3d_{3/2}$ after Shirley BG subtraction. Substrate at a) RT, b) 470K, c) 570K, d) 670 K and d) 770K. Coverages in the figure are estimated based on graph (a). Error bars of ±3.5% are shown for (a), but have been suppressed for (b)–(e) for clarity.

temperature, indicating that the size of the islands in SK mode is decreased by increasing the temperature. Unlike the prediction of Gossmann [97, 99], the critical SK–layer thickness, Θ_{SK}, does not show significant changes with temperature in the range of temperatures in these experiments, which might be due to reconstruction of the films. It is interesting to see that there are some similarities in behaviour of the curves after the first ML e. g. there is a decrease followed by an increase immediately after the break point associated with completion of the first layer, as shown by the arrows.

4.6.2. Dy/W(112)

The result of Dy/W(112) growth–mode monitoring at different substrate temperatures

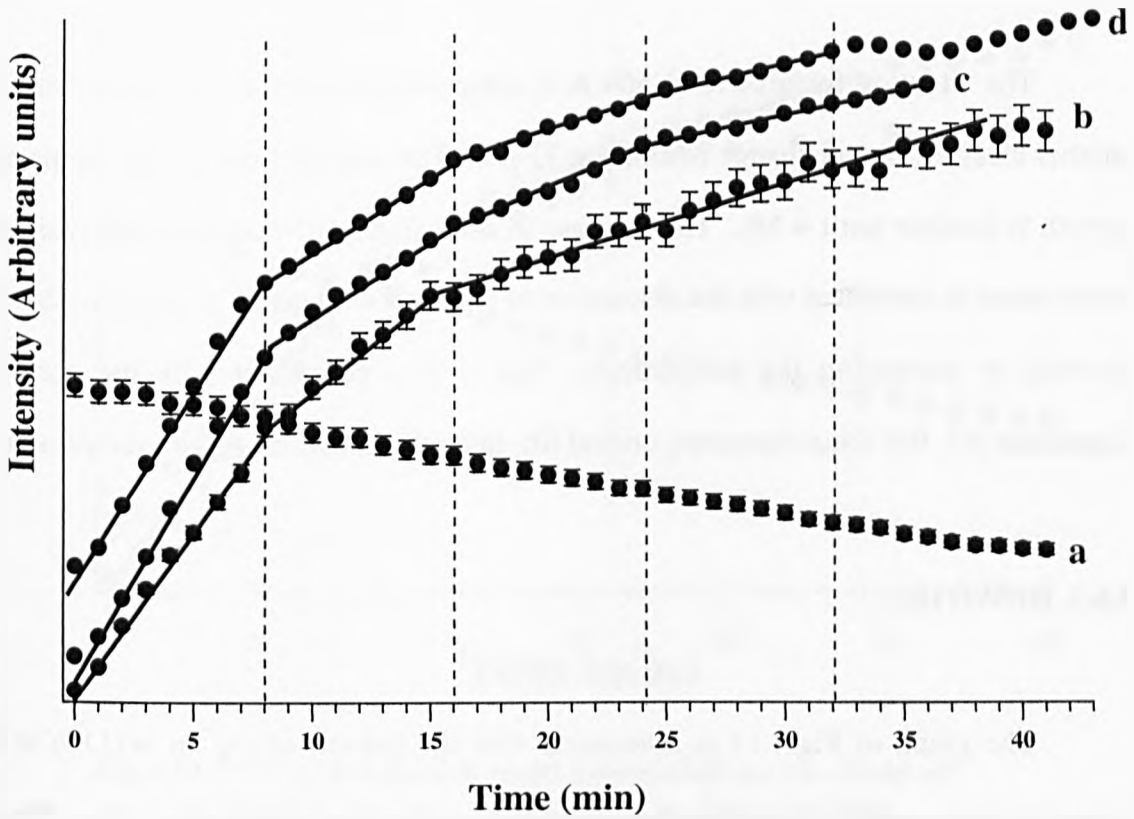

Fig.4.12. Dy/W(112) growth mode determined by AL–Xray of: W4f (a) and Dy $3d_{3/2}$ (b, c, d) after Shirley BG subtraction. Substrate at a) and b) RT, c) 470K, d) 570K. Coverages in the figure are estimated based on first break point in graph b) , c) and d). Error bars are shown for (a) and (b) but have been suppressed for (c) and (d) for clarity.

are shown in Fig 4.11. As is clear from the room temperature growth mode, Fig.4.12. b, a break point at 8 minutes indicates a linear growth up to the first monolayer, remained laminar growth until ~1.9 ML, and island growth there after.

At 460K, the graph shows clear breaks at 8, 16 and 24 minutes. In addition to this constant time interval between successive breaks, the slope of the graph in the time regions associated with the ML completions is such that $\frac{m_1}{m_2} \approx \frac{m_2}{m_3} \approx \frac{m_3}{m_4} \approx 2$. However, after completion of 3rd ML, no break or change of slope has been found in the graph. Therefore, the growth mode is laminar until 3ML and then it started island formation.

The situation for growth at 560 K is same as growth at 460 K except that there is another clear break and change of slope at 32 min. This suggests that at this temperature the growth is laminar until 4 ML. The increase in the number of laminar layers with substrate temperature is consistent with the discussion of equation 4.2 leading to negative $\Delta\gamma$ (laminar growth) by increasing the temperature. This is also consistent with the prediction of Gossmann [97, 99] about increasing critical SK–layer thickness, Θ_{SK}, with temperature.

4.6.3. Dy/W(110)

The graph of Fig.4.13 is associated with the growth of Dy on W(110) at RT and 570K. Two clear break points at 8 and 16 minutes and constant slope ratio $\frac{m_1}{m_2} \approx \frac{m_2}{m_3}$ indicate a linear growth up to 2ML for the growth at 570K. Although the graph of RT growth shows slight deviation from laminar growth almost immediately after the first break point, it returns and follows the laminar growth until second break point at 16 minutes. Therefore, the total graph of RT growth is very similar to that of the 570 K growth, until the second break point. The graph of the 570 K growth continues to grow as laminar until ~2.7ML, while that of the RT deviates from laminar growth almost immediately after the second break point. This is consistent with the discussion of equation 4.2 leading to negative $\Delta\gamma$ (laminar growth) by increasing the temperature and with the prediction of Gossmann [97, 99] concerning increasing critical SK–layer thickness, Θ_{SK}, with temperature. Both graphs have very low slope after the laminar growth, indicating that very small islands have been formed on the surface.

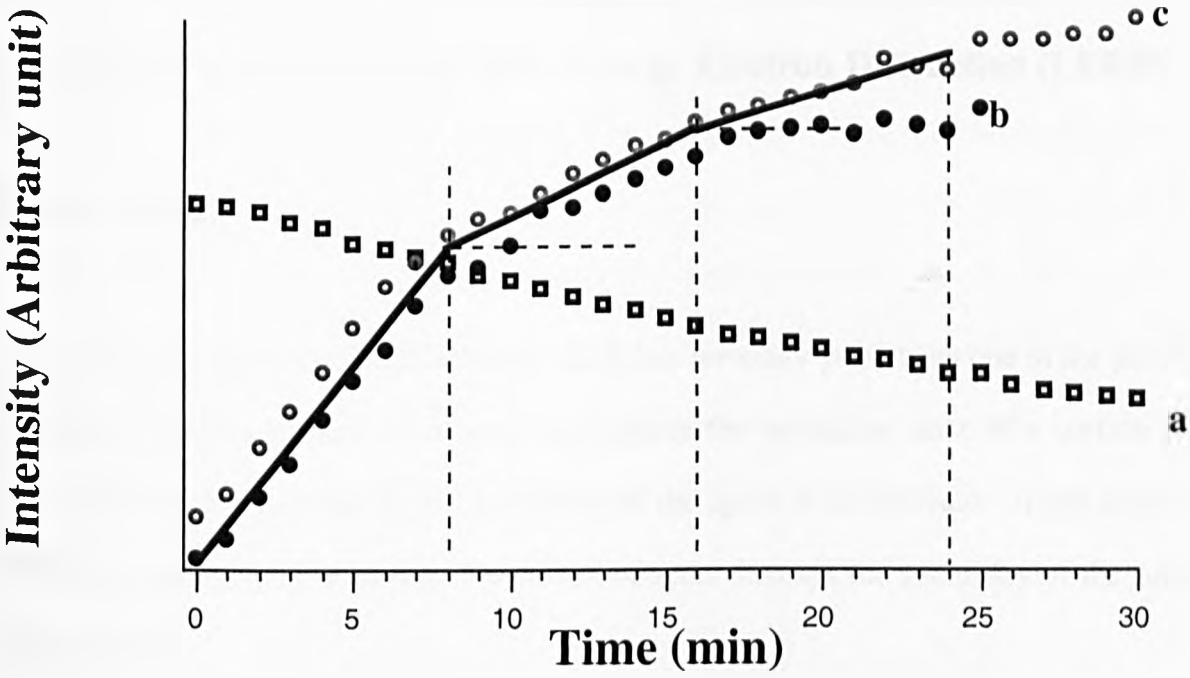

Fig.4.13. Dy/W(110) growth mode determined by AL–Xray of: a) W4f and b) Dy $3d_{3/2}$ at RT and c) Dy $3d_{3/2}$ at 570K, after Shirley BG subtraction.

Chapter 5

Structural analysis using Low–Energy Electron Diffraction (LEED)

5.1. Introduction

Low-energy electron diffraction (LEED) has for many years been one of the principal techniques used by surface scientists to investigate the crystalline state of a surface [144, 145]. Used on clean surfaces, the sharpness of the spots is an indicator of the degree of surface crystallographic order and the pattern of spots displays the symmetry of the surface crystal lattice.

The electronic structure of a material is intimately related to the geometric structure. Any structural change at a surface will give rise to a redistribution of valence-band electrons. This valence state changes can cause not only the modification of surface core levels [107, 108, 146] but also the modification of the atom sizes which can cause surface reconstructions or can affect the growth mechanism in film growth [115]. Therefore it is important to study electronic structure and geometrical structure together. However, little is known about the geometric structure of Dy on different W surfaces. This is the first work carried out on Dy/W(100) and Dy/W(112) systems with LEED.

In this work W substrates were used for growing Dy thin films and annealing at elevated temperatures to study the structure and growth mechanism of Dy thin films by STM and LEED. Interesting structures were observed in the case of Dy/W(100) system. These were a c(8x2) structure for coverages more than 1ML and a c(2x2) structure at submonolayer coverage produced by annealing the Dy film to high temperature which showed high–temperature stability up to 1500K. In the case of Dy/W(112), a complicated structure

could be seen in the LEED pattern after annealing to 1400K.

5.2. Previous work

Ciszewski and Melmed [20] used field electron emission from a sharp W tip. The substrate, which was a poly–faceted crystal, was heated during deposition to give the adsorbate atoms sufficient energy to migrate over the substrate. They found epitaxial relationship of $(0001)\mathrm{Dy} \| (001)\mathrm{W}$ with $[01\bar{1}0]\mathrm{Dy} \| [001]\mathrm{W}$ for slow growth conditions Dy and $(0001)\mathrm{Dy} \| (011)\mathrm{W}$ with two epitaxial relationships of $[11\bar{2}0]\mathrm{Dy} \| [001]\mathrm{W}$ and $[11\bar{2}0]\mathrm{Dy} \| [111]\mathrm{W}$ for rapid growth. These epitaxial growth were found only for the case in which the substrate was held at 800K-930 K during the growth. However, the W surface was not macroscopically flat and had a very small effective area, and so their conclusion regarding growth can not necessarily be extrapolated to atomically flat surfaces.

The most relevant structural study to the work in this thesis on Dy/W(100) is the Gd/W(100) system studied by White *et al.* [147] with STM and LEED, in which a c(8x2) overlayer was observed. This was very similar to a close–packed layer with hexagonal symmetry, but with a small surface–induced strain, giving rise to the description of "pseudo–hexagonal".

For Dy/W(112) the most relevant study is Sm/W(112) [10, 148] in which chain–like structures of p(1x7) have been reported for small coverages, which are a result of indirect interaction of the adsorbate via SES of the substrate. By increasing the coverage this structure passed into c(2x2) islands. The other relevant study is Dy on Ta(112) by Smereka et al [86] in which no chain like structure has been found at small coverages and they attributed this to absence of partly filled SES on Ta(112). They reported formation of a c(2x2) structure at 0.25 ML coverage which covers the surface at 0.5 ML. They also reported high–temperature

stability for this superstructure even at temperatures close to the melting point of the Dy. The other relevant study is that of Dy on pre–oxidised Mo(112) by Losovyj *et al* [10], in which they reported no chain–like structure in the early stages of the film formation and they attributed this to partly filled SES due to this oxidation (even at ~0.1 ML). However, they reported c(2x2) islands, for this system. The other relevant study is Gd/Mo(112) by Waldfried *et al* [149], in which they have grown 15 to 50 ML thick Gd films on a corrugated Mo(112) surface. Growth on these films resulted in domains of the hexagonal lattice of Gd with preferred direction of growth along the $\langle 1\bar{1}1 \rangle$ directions of the substrate, with a dispersion in domain width along the $\langle 1\bar{1}0 \rangle$ directions. This dispersion resulted in streaks in the LEED patterns along this direction. Finally, Gd/Mo(112) has been studied at low coverages by Losovyj *et al* [150]. They found no ordered structure up to 0.6 ML, then a series of different structures such as $c(2\times\frac{1}{\theta})$, $p(1\times\frac{1}{\theta})$, (1x4) and (1x5) for coverages of $\boldsymbol{\theta}$ < 1.25 ML.

For Dy/W(110) the most relevant study is that of Li et al [8]. In the initial stages of growth they reported complex LEED patterns, which they found similar to the results of Kolaczkiewicz et al [151] for submonolayer coverages of Eu, Gd and Tb on W(110). For thicker films (~10 ML) they found a sixfold hexagonal pattern associated with the basal plane of the rare–earth metals. Based on the LEED analysis they inferred the Nishiyama–Wasserman (NW) orientation [152] for which $[01\bar{1}0]\mathrm{Dy} \| [011]\mathrm{W}$. They have also presented LEED I–V spectra of Dy films with a thickness of 15-20 ML.

5.3. Experimental details

LEED experiments were carried out using a Vacuum Generators system mounted onto the analytical chamber (IPE chamber at at Surface Science Research Centre of the University of Liverpool). A camera was set carefully co–axial to the LEED screen to reduce any misalignment of the camera before taking images of the LEED patterns and then the images were calibrated using the Image SXM software [90] to minimise any x-y distortion of the raw images which could be caused by any misalignments of both the sample and camera from the centre axis of the LEED screen. The image used in this analysis has a high pixel resolution of 1536 x 1024 and all the measurements were carried out using the image analysis software. The experimental set up for LEED and LEED I–V data acquisition was the one mentioned in Ref. [21] and explained in chapter 3.

The LEED pattern of the clean W(100) substrate was found to have split spots along W [001] direction. Therefore it has been concluded that the W substrate was faceted with steps edge parallel to the W [010] direction. The average distance between the split W spots has been measured on the LEED pattern. By comparing this to the distance between W spots in the LEED pattern and using 3.16 $\mathring{A}$ for the W lattice constant [34] the average width of terraces was found to be ~45 $\mathring{A}$. This was later confirmed by STM analysis (see next chapter).

The Dy coverage was calibrated using the known deposition rate of the source (which was regularly checked and remained stable over the experiments) and by the intensity of the W 4f levels in XPS. Due to the high reactivity of rare–earth metals [22], the sample was flashed every 30 minutes and new films were grown to ensure that the films were clean during the experiment.

The annealing temperature was measured using an optical pyrometer and C-type thermocouple attached to the sample.

The base pressure of the chamber was $8x10^{-11}$ mbar and during evaporation the pressure remained below $1x10^{-10}$ mbar.

5.4. Dy/W(100)

As mentioned in the previous chapter on growth mode studies, Dy grows layer by layer on W(100) up to first ML and then it will grow as islands with relatively complicated surface reconstructions at different substrate temperatures. By growing the Dy film at RT, the background (background) intensity in the LEED pattern increased substantially and the pattern showed W spots on a high background. However, no Dy spots could be seen in the submonolayer regime.

The LEED pattern of 1-3 ML of Dy grown on W(100) at RT showed high background with W spots and a very faint and broad pattern of two hexagonal–shape domains of Dy spots rotated by 90° relative to each other. Spots of one of the Dy hexagonal domains were matched to the W spots in the [001] direction and it was the case for the other domain in [010] direction. This was very similar to the pattern of Gd/W(100) [147] but with a very high background. The pattern did not show significant change by growing at different temperatures. However, the growth at 470 K was the best temperature among the other temperatures (RT, 470K, 570K, 670K, 770K). However, even at 470K, the background was high and the Dy spots were very faint.

These observations indicate that the surface of the Dy films grown on W(100) is highly disordered. As one of the aims of this study is to find the conditions under which clean and well–ordered films can be produced, the annealing process was carried out at different temperatures. By annealing the films (grown at RT) to different temperatures up to 770 K it was found that the background decreased and hexagonal spots of Dy became sharper. However, only one domain of Dy remained in the pattern after annealing whose spots matched the W spots along W [001] direction. Remaining only one domain under annealing process is related to the size and direction of the steps of the substrate, which were in W [010] direction with average width of 25 $\mathring{A}$.

The best annealing temperature was found to be 770K. The LEED result of annealing 3ML of Dy was very sharp and intense spots of hexagonal Dy with low background were observed as shown in Fig.5.1. The W spots were still clear in this picture. This annealing caused an increase (decrease) in Dy (W) intensity in XPS, indicating flattening of the Dy film. By increasing the annealing temperature from 770 K to 820K, the intensities of the Dy (W) LEED spots and the XPS signal of Dy (W) decreased (increased) slightly. However, the LEED pattern still consisted of sharp W and Dy spots and no change in background could be recognised. These observations are attributed to accumulation of the Dy film and the formation of ordered islands of Dy. By increasing the annealing temperature to above 820K, the background increased in the LEED pattern and Dy spots started to become broad and faint. Simultaneously, the XPS signal of Dy (W) started to decrease (increase). This is an indication of evaporation of the Dy film.

By increasing the temperature of annealing above 870K, a c(2x2) structure started to appear. At first the LEED spots were broad and faint and the background was high. However,

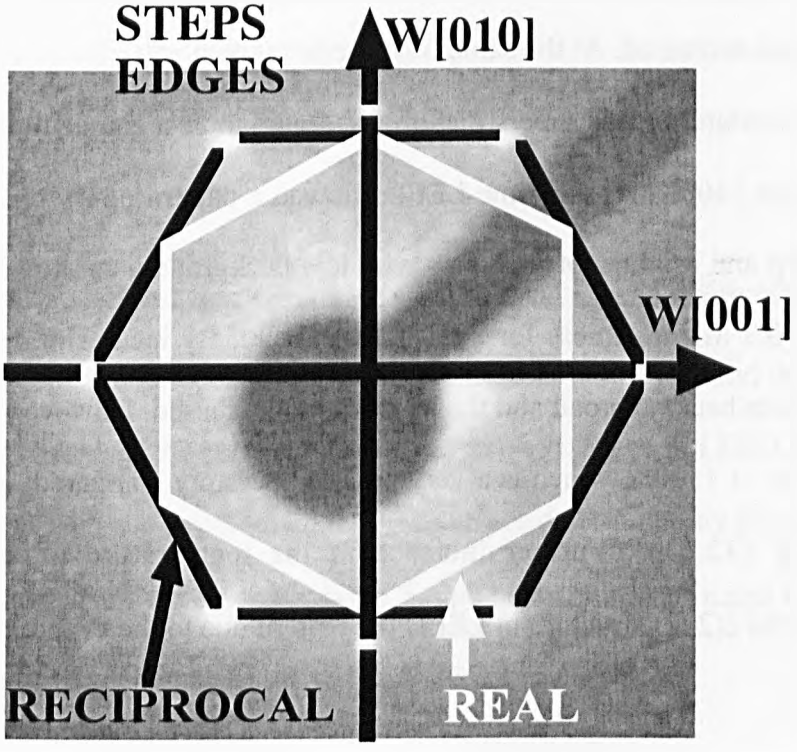

Fig.5.1. LEED pattern taken at 110 eV electron beam energy of 3ML Dy grown at RT on W(100) and annealed at 770K. The real space lattice direction is based on the assumption of a purely hexagonal LEED pattern. Step direction were found based on the direction of splitting of clean W spots (which are normal to the step edges).

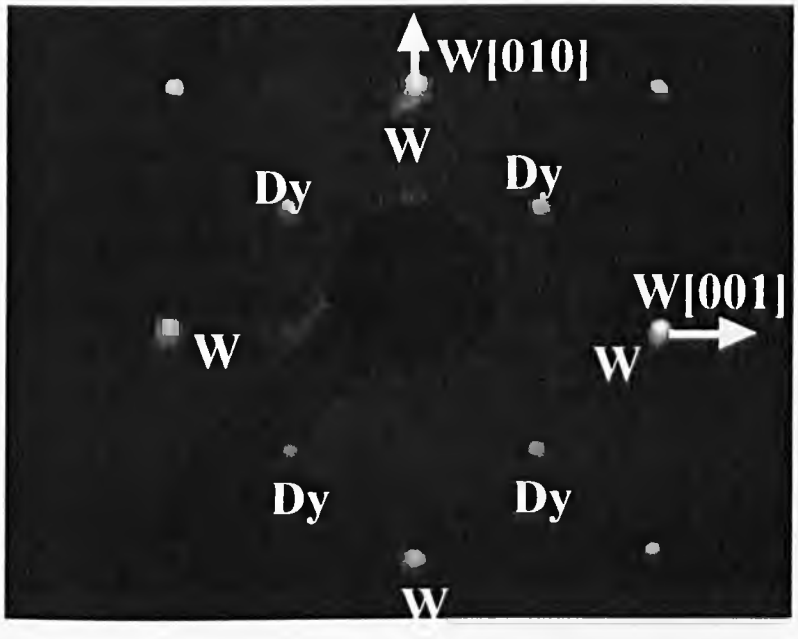

Fig.5.2. c(2x2) structure of 0.3 ML of Dy on W(100), taken at 84 eV electron beam energy.

by increasing the temperature of annealing, the c(2x2) spots became more intense and sharper and the background decreased. At the same time the hexagonal pattern was disappearing. The best annealing procedure for this superstructure was found to be a couple of short flashes of 3 seconds duration to 1400K. At this time LEED showed a pattern of Dy c(2x2) structure on W(100) with sharp and bright spots and also with low background, as shown in Fig.5.2. The XPS indicated ~ 0.3 ML thickness for this superstructure. By increasing temperature from 1400 K the Dy spots became broad and the background increased. However, a c(2x2) pattern could be seen even at 1500K, which is a very high temperature compared to the Dy melting point of 1680 K [32, 34]. Further increase in the temperature of annealing led to disappearance of the c(2x2) structure in LEED the pattern due to the evaporation of the Dy.

5.4.1. Discussion

5.4.1.1. Pseudo hexagonal LEED pattern of Dy/W(100)

The nearest neighbour separation of bulk Dy is 3.592 Å [32, 34] and the lattice constant of W(100) is 3.165 Å, which is assumed to be the same lattice constant as that of bulk W. Since Dy and W have dissimilar lattice constants, when Dy grows epitaxially on a W substrate, it is expected that the Dy overlayer lattice will be extended, contracted or rotated in some way along the W lattice axis to have lattice match. By doing this the system can relieve the strain energy due to the lattice misfit and achieve minimum total epitaxial energy of the system.

The relation between real space and reciprocal space vectors are

$$\hat{a}_i^* = 2\pi\left(\frac{\hat{a}_j \times \hat{a}_k}{\hat{a}_i \cdot (\hat{a}_j \times \hat{a}_k)}\right) \quad (5.1)$$

in which $\hat{a}_i$,$\hat{a}_j$ and $\hat{a}_k$ are real space primitive vectors along i, j and k directions and $\hat{a}_i^*$ is reciprocal vector corresponding to $\hat{a}_i$. It is possible to rewrite (5.1) to find the other reciprocal vectors by cyclic change of the subscript from i to j to k to i. Since in LEED, one of the primitive vectors, say $\hat{a}_k$, is perpendicular to the surface determined by the other vectors, $\hat{a}_i$ and $\hat{a}_j$, the direction of $\hat{a}_i^*$ is perpendicular to $\hat{a}_j$ and its magnitude is equal to 2π multiplied by the inverse of the projection of $\hat{a}_i$ to the direction normal to the $\hat{a}_j$.

$$|\hat{a}_i^*| = \frac{2\pi}{\text{projection of } \hat{a}_i \text{ to the direction normal to } \hat{a}_j} \quad (5.2)$$

Since in the case of Dy/W(100), $\hat{a}_i$ and $\hat{a}_j$ are vectors determining atomic rows on the surface above equation is equivalent to say

$$|\hat{a}_i^*| = \frac{2\pi}{\text{distance between atomic rows along } \hat{a}_j} \quad (5.3)$$

In the case where the LEED spots of overlayer matches that of the substrate ($\hat{a}_{i_{ad}}^* = \hat{a}_{i_{sub}}^*$), the above expression predicts that atomic rows of the overlayer and the substrate, perpendicular to $\hat{a}_i^*$, match each other.

The LEED pattern of Dy/W(100) in Fig.5.1 indicates one domain with a hexagonal

pattern of spots, two of which are overlapped with the (1, 0) and $(\bar{1},0)$ of the W (1 x 1) spots. This suggests that the Dy overlayer and the W substrate have same reciprocal vector of a_1^* along the [001] direction. According to the above argument, leading to equation (5.3), the atomic rows of Dy along $a_{2_{Dy}}$ match the atomic rows of W along a_{2_W}, see Fig.5.3. However, though the lattice constant of Dy is larger than that of W, because of the angle between $a_{1_{Dy}}$ and $a_{2_{Dy}}$, α in Fig.5.3(a), the distance between atomic rows of Dy along $a_{2_{Dy}}$ is less than that of the W along a_{2_W} (i. e., $d_{Dy} < d_W$ in Fig.5.3(a)). To have row matching, the overlayer lattice has to expand itself along W [001]. There may be two possible Dy overlayer structures, which satisfy the lattice matching condition. The two model structures are indicated in Fig.5.3. In one way the Dy lattice along $a_{1_{Dy}}$ can be expanded which will also cause expansion of $a_{2_{Dy}}$. In the other way, the $a_{1_{Dy}}$ may change its angle relative to $a_{2_{Dy}}$, α. This will cause contraction of Dy lattice along $a_{2_{Dy}}$. Because of the mirror reflection symmetry operation, (to the plane perpendicular to the surface), the atoms have to rearrange themselves symmetrically. Therefore these are the only possible ways to produce row matching between the Dy and W(100) surface.

To have a close–packed Dy structure on W(100) in a way which the above row matching along W [010] could take place and also minimise the misfit, there must be the following relationship between Dy and W lattice constants along that direction

$$(n-1)a_{2_{Dy}} = na_w \qquad (5.4)$$

Where n is an integer. Using 3.16 $\mathring{A}$ for a_W, a value for $a_{2_{Dy}}$ has been found for different values of n, see Fig.5.4. It is clear from this figure that three values of $a_{2_{Dy}}$ correspond to n=7, n=8 and n=9 are possible and the other values are physically meaningless.

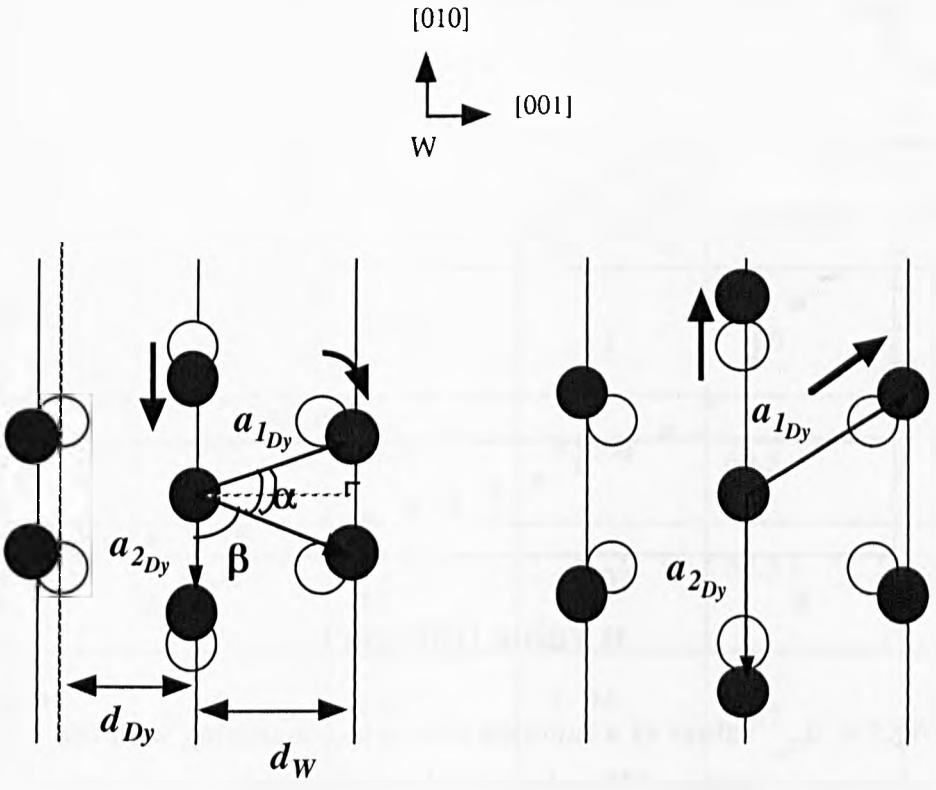

(a) In the case of contraction (b) In the case of expansion

Fig.5.3. Schematic diagrams of two possible distorted hcp structures of a Dy overlayer on the W(100) substrate, matching to the W rows. Full circles represent the atoms of the distorted hcp structure of contraction(a) and of expansion (b), respectively. Open circles represent the bulk hcp structure, and its unit vectors a_1 and a_2

For example in the case of n<7 the value of of $a_{2_{Dy}}$ will produce too large Dy surface area which is far from close–packed, and in the case of n>9, the $a_{2_{Dy}}$ becomes smaller than atomic diameter of Dy in its close–packed form ($a_{2_{Dy}} < 3.56$ Å).

In the case of n=7, n=8 and n=9, the estimated values for $a_{2_{Dy}}$ are

$$n=7: \; a_{2_{Dy}} = 3.69 \text{ Å} \qquad (5.5)$$

$$n=8: \; a_{2_{Dy}} = 3.62 \text{ Å} \qquad (5.6)$$

$$n=9: \; a_{2_{Dy}} = 3.56 \text{ Å} \qquad (5.7)$$

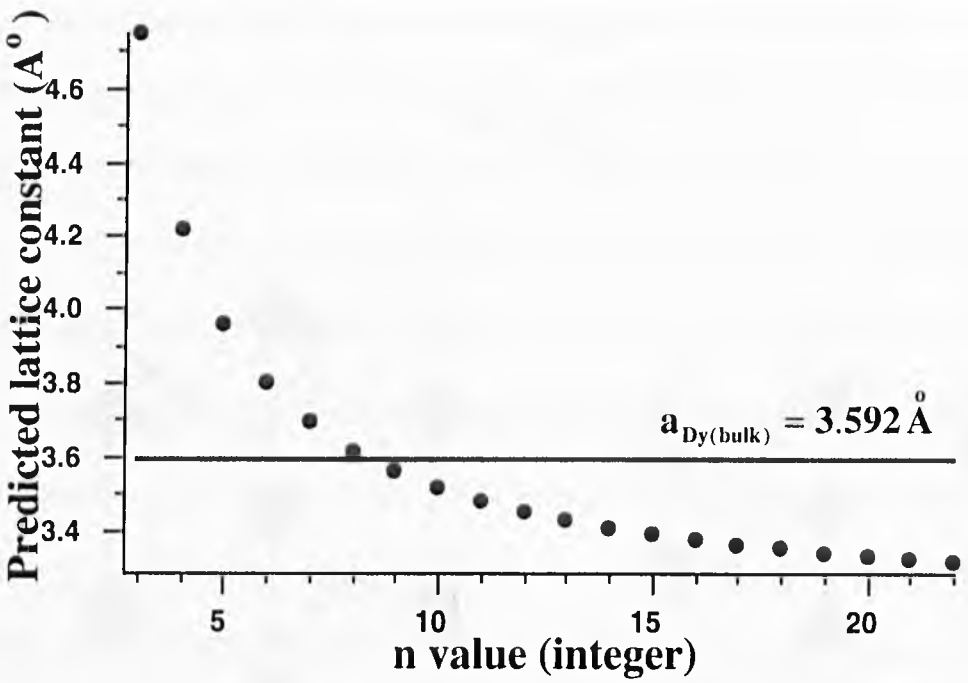

Fig.5.4. $a_{2_{Dy}}$ values as a function of n value, matching with the lattice of W substrate along [010] axis.

According to Fig.5.3 (a)

$$a_{1_{Dy}} = \frac{a_{2_{Dy}}}{2\sin\frac{\alpha}{2}} \quad (5.8)$$

and

$$\alpha = 2\tan^{-1}\left(\frac{a_{2_{Dy}}}{2a_W}\right) \quad (5.9)$$

and

$$\beta(\text{deg}) = (90 - \frac{\alpha(\text{deg})}{2}) \quad (5.10)$$

Now, knowing $a_{2_{Dy}}$ from minimum misfit considerations it is easy to find α and then

$a_{1_{Dy}}$ and β from equations 5.9, 5.8 and 5.10. These results are shown in table.5.1.

	$a_{1_{Dy}}(\overset{o}{A})$	$a_{2_{Dy}}(\overset{o}{A})$	$\frac{a_{1_{Dy}}}{a_{2_{Dy}}} = \frac{a^*_{2_{Dy}}}{a^*_{1_{Dy}}}$	α(Deg)	β(Deg)
Bulk	3.592	3.592	1	60	60
n=7	3.664	3.692	0.992	60.5	59.7
n=8	3.645	3.617	1. 007	59.5	60.3
n=9	3.63	3.56	1. 02	58.7	60.6
LEED			1. 007 ± 0. 001	59.3 ± 0.1	60.3 ± 0.1

Table.5.1. Predicted and measured parameters of Dy unit cell on W(100)

Regarding the relationship between real space and reciprocal space, Eq.5.1, it is clear that reciprocal vectors and real space primitive vectors are not in the same direction. However, if the angle between primitive vectors in the real space is less (more) than 90°, this angle will be the same as the (complement of the) angle between their reciprocal vectors. Therefore, in this case which angle between the real space primitive vectors of Dy is less ~ 60°, α is the angle between two $a^*_{2_{Dy}}$ in the LEED pattern, and β is the angel between a^*_{1Dy} (which matches $a^*_{2_W}$ in the LEED pattern) and $a^*_{2_{Dy}}$. To find out which case has happened on the surface of Dy/W(100) careful measurements of angles α, β and the ratio $\frac{a^*_{2_{Dy}}}{a^*_{1_{Dy}}}$ has been made on the LEED pattern (Fig.5.1) and the results are shown in the table 5.1. These results

confirm that the case of n=8 is the actual case and Dy formed a (8x2) commensurate cell. A primitive (8x2) cell is expected to produce a LEED pattern as shown in Fig.5.5. However, only spots specified by circles, can be seen in the LEED pattern. This means that the intensities of the other spots are very low. The same situation has happened for Gd on W(100) [147] and Mn on Cu(100) [153, 154] in which the ratio between the size of Gd(Mn) and W(Cu) is very similar to that of the Dy and W. Though in the case of Mn/Cu(100) the LEED pattern was different from that of the Gd/W(100) and Dy/W(100) (Fig.5.1), based on LEED–IV calculations Flores *et al* [153] and Gauthier *et al* [154] have shown that in the case of c(8x2) the same pattern as Fig.5.1 is produced. In this case the spots shown by squares in fig.5.5. are cancelled because of the nature of the centred lattice and the other missing spots are cancelled because of the destructive interference resulted from the specific atomic arrangement of the c(8x2) structure.To explain the difference of the Mn/Cu(100) LEED pattern from the ideal c(8x2) LEED pattern , Flores et al [153] and Gauthier et al [154] proposed a model in which Mn atoms formed a bridge shape structure in the c(8x2) lattice, Fig.5.6., in which Mn atoms have vertical displacements. This will result in phase shifts in the electron beams scattered from different Mn atoms in the cell, due to differences in path lengths, which causes some destructive interference (which happened for the flat c(8x2)) not to occur for the Mn/Cu(100). Based on the above discussion the Dy/W(100) LEED pattern implies formation of a flat c(8x2) structure shown in Fig.5.7.

The c(8x2) structure with lattice constant shown in table.5.1 for n=8, has values of $a_{1_{Dy}}$ and $a_{2_{Dy}}$ extended by 1.47 % and 0.69 %, respectively, relative to the Dy bulk lattice constant. The unit mesh is expanded by 1.9% relative to the basal plane of the Dy. It is interesting to see that in the case of Dy with the bulk lattice constant $a = 3.592\,\mathring{A}$ on W(100), both $a_{1_{Dy}}$ and $a_{2_{Dy}}$ are extended while in the case of Gd with the bulk lattice constant

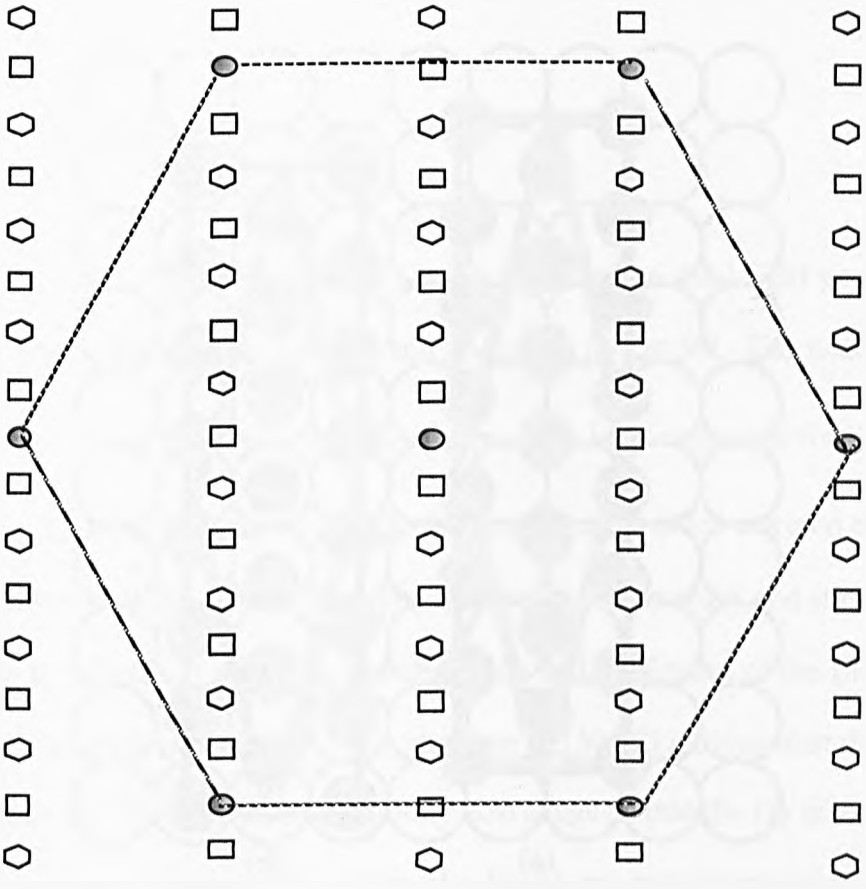

Fig.5.5. Schematic pattern of a (8x2) and c(8x2) structure.
□ indicates missing spots due to c type nature of c(8x2).
⬡ indicates missing spots due to destructive interference resulted from specific atomic arrangement of the close–packed c(8x2). (proposed by Ref [153, 154])
● remaining spots which forms LEED pattern.

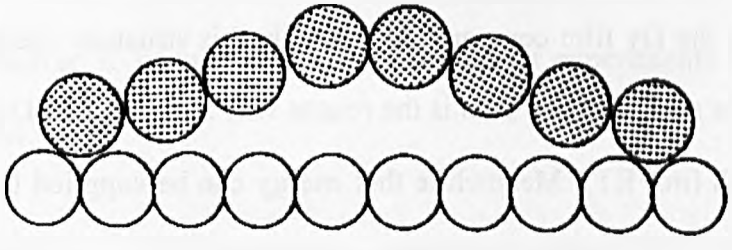

Fig.5.6. Side View of Mn atoms on Cu(100) along longer side of the c(8x2) unit cell which will cancel some destructive interferences expected in Fig.5.5. The vertical distances are not drawn to scale. Adopted from Ref [153]

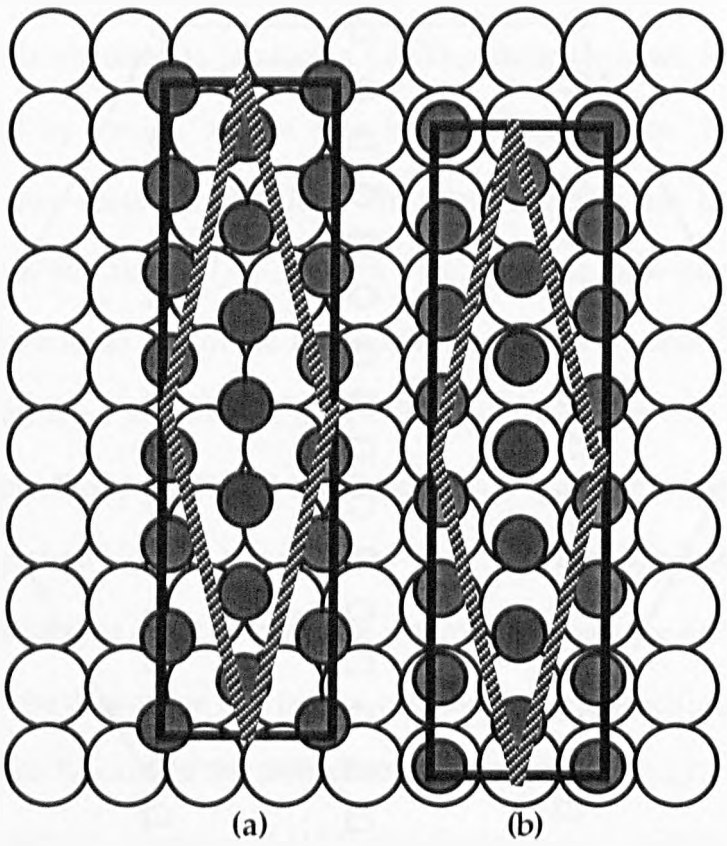

Fig.5.7 Schematic diagram of two possible Dy c(8x2) structures on W(100) in which open circles are W and dark circles are Dy. To indicate registry points of each Dy atom in the unit cell of c(8x2), the Dy circles have been drawn smaller than actual size, relative to the W circles.

$a = 3.634\,\mathring{A}$, only $a_{1_{Gd}}$ is extended and $a_{2_{Gd}}$ is contracted. Therefore, the Gd lattice expands by only 0.1 %, which is significantly smaller than that of the Dy. Because of the relatively large expansion of the Dy film compared to the bulk, this structure needs a large amount of energy to overcome such a strain. This is the reason why a c(8x2) LEED pattern is clear only after 200 K growth (not RT). Meanwhile this energy can be supplied by annealing process resulting in a c(8x2) LEED pattern with sharp and intense LEED spots and low background.

Although from a thermodynamic point of view, occupying larger area of surface is unstable, it seems that the surface free energy of the extended Dy area successfully competes with Dy–W interfacial energy.

5.4.1.2. c(2x2) structure

The real space structure of Dy c(2x2), corresponding to the LEED pattern in Fig.5.2 was achieved after annealing to 1400 K and is shown in Fig.5.8. The nearest neighbour distance between Dy atoms is 4.46 $\mathring{A}$. The coverage has been measured for Fig.5.2 by XPS and found to be 0.3 ML. This means that Dy formed domains which covered around 60% of the surface. However, the coverage does depend on the temperature and time of annealing process leading to the c(2x2) structure. The sharpness and brightness of the LEED pattern in Fig.5.2 and the high thermal stability of this structure (~1500K) indicate that the Dy domains are very well ordered. The high thermal stability also suggests that the Dy atoms should be in positions with minimum energy. Therefore, the Dy atoms most likely have occupied the hollow sites on the surface in which each Dy atom is bonded directly to four W atoms in the top layer. Furthermore, since the distance between Dy atom at hollow site and W atom under nit it, in the second W top layer, is 3.82 $\mathring{A}$, which is comparable to the lattice constant of Dy bulk, a gap of 0.65 $\mathring{A}$ is between the Dy and the W in the second top layer. Therefore, there may also be an electronic bond between Dy atoms in the hollow sites and W atoms in the second top layer, even via indirect interaction, which might increase the thermal stability of Dy on W(100). However, to be sure about this case further experiments such as LEED I–V have to be carried out.

5.4.2. LEED I–V

Quantitative analysis can involve either measuring the intensity profile of a spot (spot profile analysis, or SPA-LEED [155]) or the variation of the integrated intensities of the spots

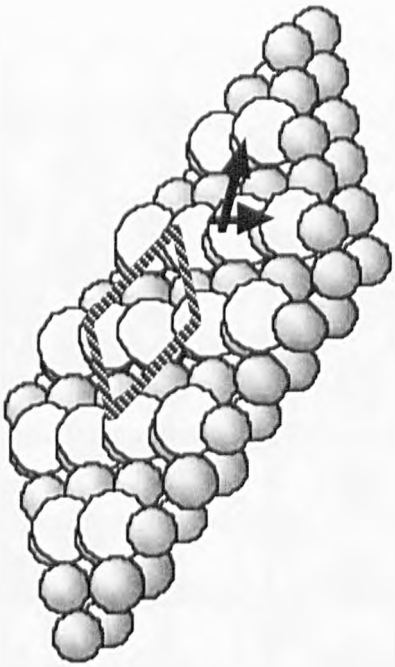

a)

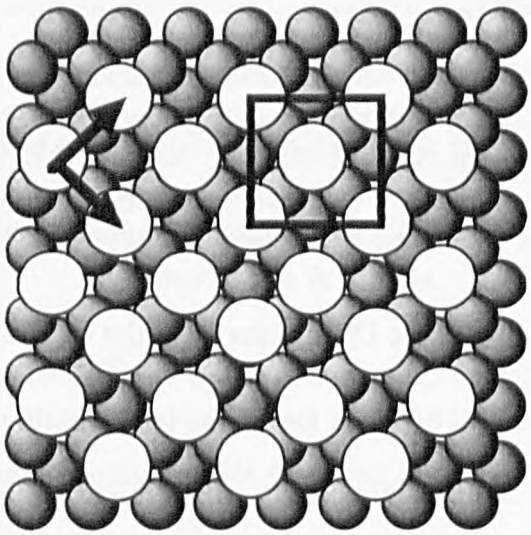

b)

Fig.5.8. Real space c(2x2) structure for Dy/W(100).
a) side view and b) top view.

with incident beam energy (LEED *I-V*). SPA-LEED can probe the deviations from perfect surface order that cause the spots to become diffuse – studies such as monitoring defects at a clean surface or phase changes in adsorbate overlayers can be carried out with this technique.

Conventional LEED optics designed principally for qualitative studies do not have the spatial resolution to perform SPA-LEED experiments – this requires an electron beam with a coherence length of > 100 nm (*c.f.* ~ 10 nm for conventional systems). However, such optics are suitable for LEED *I-V* studies. To determine the structure of a surface, *I-V* spectra from all visible spots are recorded over as wide an energy range as possible. These are then compared to spectra calculated for a number of plausible models of the surface. The comparison is carried out using reliability factors (*r*-factors [1, 2, 4]) in order to quantify the match between the experimental spectra and those of the various theoretical models – the model that produces the best (lowest) *r*-factors is taken to be the most likely surface structure, with the level of confidence determined by the value of the minimum *r*-factor. The intensities of the spots can be measured using a number of techniques, subdivided into those that measure directly the current of electrons (*e. g.* Faraday detector or electron multiplier) and those that measure the intensity of a spot on a fluorescent screen (*e. g.* spot photometer or video camera). The advantage of the video technique is that the intensities of all of the LEED spots are recorded simultaneously, and so the data required to produce a full set of *I-V* spectra can be acquired on relatively short time scales. This is of crucial importance when the surface being studied is susceptible to contamination from its environment or damage from electron bombardment.

In this work LEED *I–V* curves have been collected for Dy/W(100). The *I–V* curves corresponding to c(8x2) structure, Fig.5.1, are shown in Fig.5.9 and that of the c(2x2) structures, Fig.5.2, are shown in Fig.5.10. In both cases the sample was kept at RT during data acquisition. To find more information about the Dy c(8x2) and c(2x2) structures on W(100), computer calculations based on these LEED I–V curves are now in progress by the Rare Earth Group of the University of Liverpool.

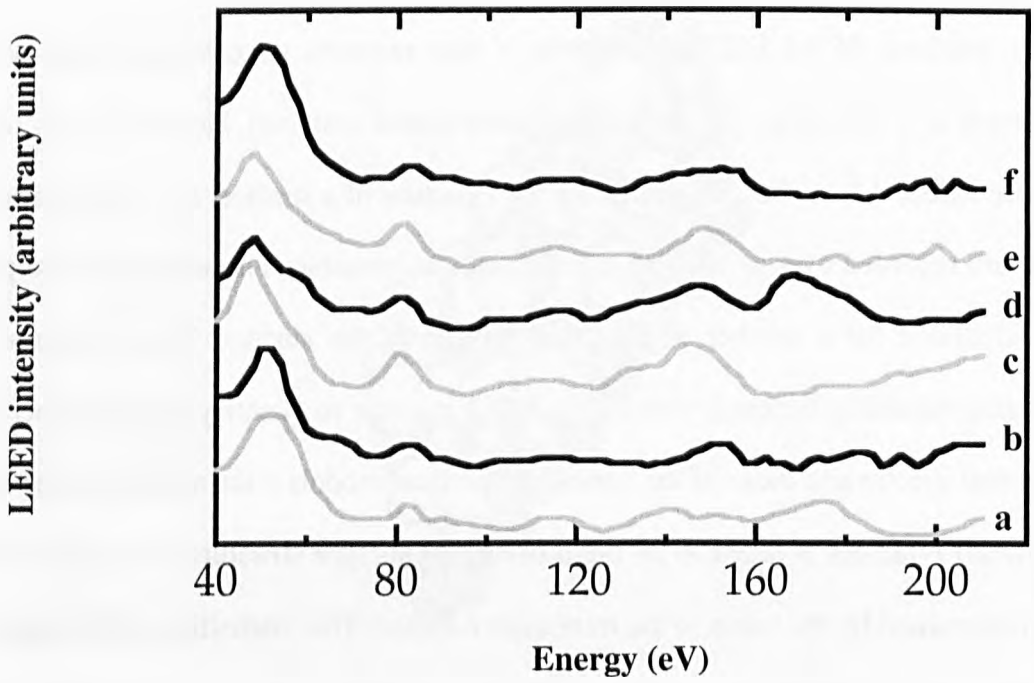

Fig.5.9. Dy/W(100) LEED I–V for spots of: a) (10), b) (01), c) (0 -1), d) (-1 0), e) (1 -1), f) (-1 1). Assignment for every point is as Fig.5.12.

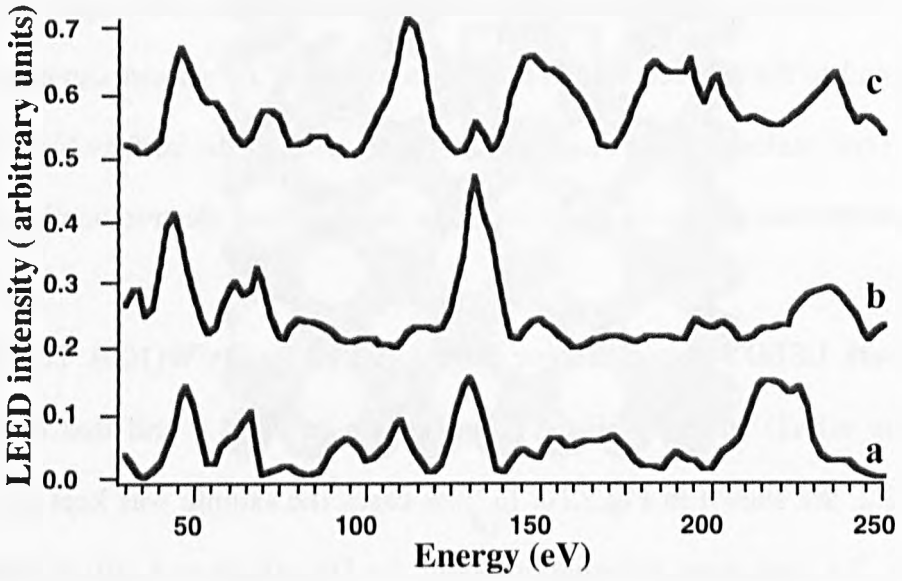

Fig.5.10. LEED I–V curves of a) (100), b) (110) and c) $(\frac{1}{2}\frac{1}{2}0)$ spots for Dy c(2x2) structure on W(100).

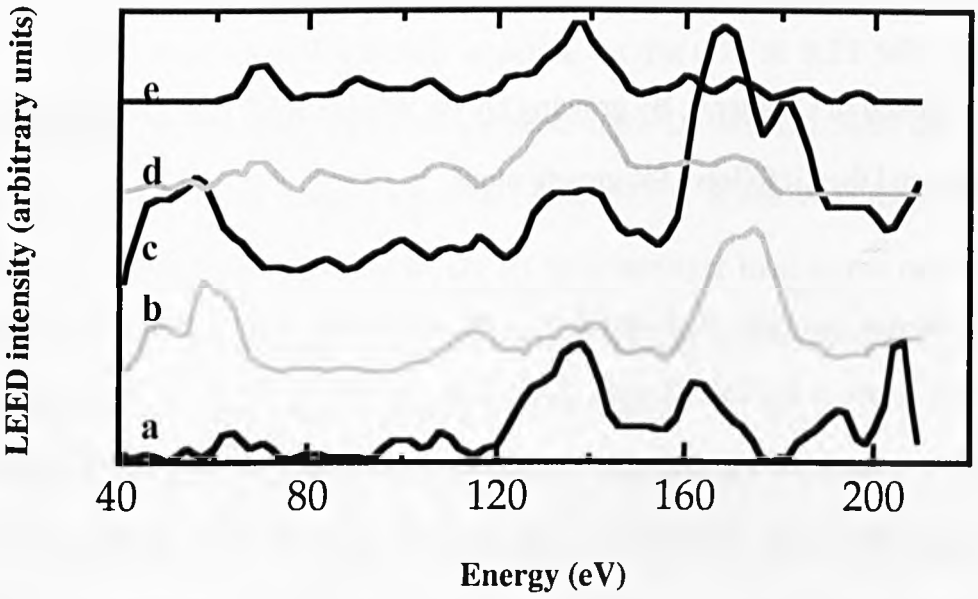

Fig.5.11. Clean W(100) LEED I–V of spots for comparison. a) (-1 -1), b) (-1 1), c) (1 -1), d) (0 -1), e(0 1). These curves are consistent with the results of Ref [156]

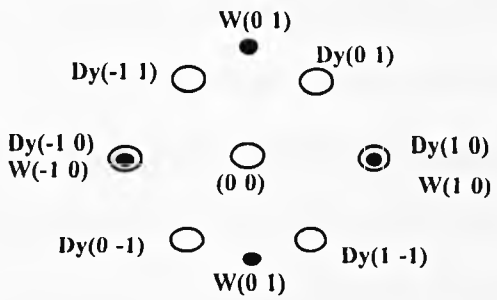

a)

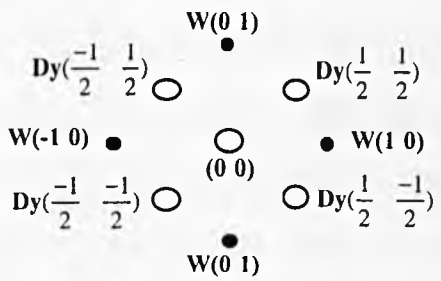

b)

Fig.5.12. Schematic LEED pattern of a) Dy c(8x2) and b) Dy c(2x2) on W(100). The spot indices correspond to the LEED I–V curves in Fig.5.9 to Fig.5.11. Open circles indicate Dy spots and the dark circles are that of W

5.5. Dy/W(112)

As mentioned in Chapter 4, By growing Dy on W(112) at RT, Dy grows laminar until the second layer and then it follows SK growth mode.

While most of the rare–earth metals formed chain–like structures on RM in the early stages of growth (such as La/Ta(112) [86], Eu and Tb on W(112) [157] and Eu, Gd and Tb on W(110) [151]) no such LEED patterns could be seen for Dy on W(112). Formation of chain–like structures is a result of strong attractive interaction between adatoms which will bring them together and form an specific shape. When the distance between adatoms is high (at very low coverage), this interaction can be mediated via the substrate. This indirect interaction is highly dependent on electronic structure of the adsorbate and substrate. More free electrons in the adatom, or the presence of SES of substrate, will intensify this indirect interaction. For example, La with a $5d^16s^2$ electronic configuration forms chain–like structures on Ta(112), while Dy atoms with a $6s^2$ configuration do not [86], or indirect interaction on Mo(112) and W(112) which have SES is stronger than Ta which has not partly filled SES [17].

The presence of SES has been verified for W(110) and W(112) [17, 158]. Therefore, most of the rare–earth metals form chain–like structures on these surfaces. However, Dy does not show such a structure on W(112) and W(110). The reason is most likely due to the strong atomic dipole moment of Dy on W surfaces. This strong dipole–dipole repulsive interaction between Dy atoms will prevent Dy atoms coming close enough to form an ordered domain.

While Dy has formed a c(2x2) structure on Ta(112) at 0.25 ML [86], with high thermal stability, such a structure could not be seen for Dy/W(112). Here the LEED pattern showed only W spots and a high background below 1ML. Since W is more electronegative than Ta, the atomic dipole moment of Dy on W is stronger than in the case of Dy on Ta. Therefore, stronger dipole–dipole interactions between Dy adatoms on W(112) could be the reason for the absence of a c(2x2) structure for Dy/W(112).

By increasing the coverages to more than 1 ML, Dy LEED spots started to appear, but were faint and could be seen only at low electron beam energies. For example, the LEED pattern of ~ 5 ML of Dy on W(112) showed very faint spots of Dy with high background which could only be seen below 50 eV and were at the edge of the LEED screen (Fig.5.13.), which could be due to low mean free path of the electron at these energies.

Comparing it with the Fig.5.14 of clean W(112) this shows epitaxial growth of Dy on W(112) for which $(0001)\mathrm{Dy} \parallel (112)\mathrm{W}$ with $[1\bar{1}00]\mathrm{Dy} \parallel [\bar{1}10]\mathrm{W}$ or $[11\bar{2}0]\mathrm{Dy} \parallel [11\bar{1}]\mathrm{W}$. High background and limited energy range in which Dy spots are visible suggests that the film is not well ordered.

Increasing the temperature up to 500K, improved the intensity of the spots and reduced the background slightly. By increasing the temperature of annealing the LEED pattern changed to streaks and at 800 K the pattern showed only streaks along the W [110] direction. By increasing the temperature of annealing the streaks became sharper and the background decreased (Fig.5.15).

By increasing the temperature above 1200K, streaks disappeared and extra spots appeared in the pattern. By annealing to 1370 K a complicated pattern appeared.

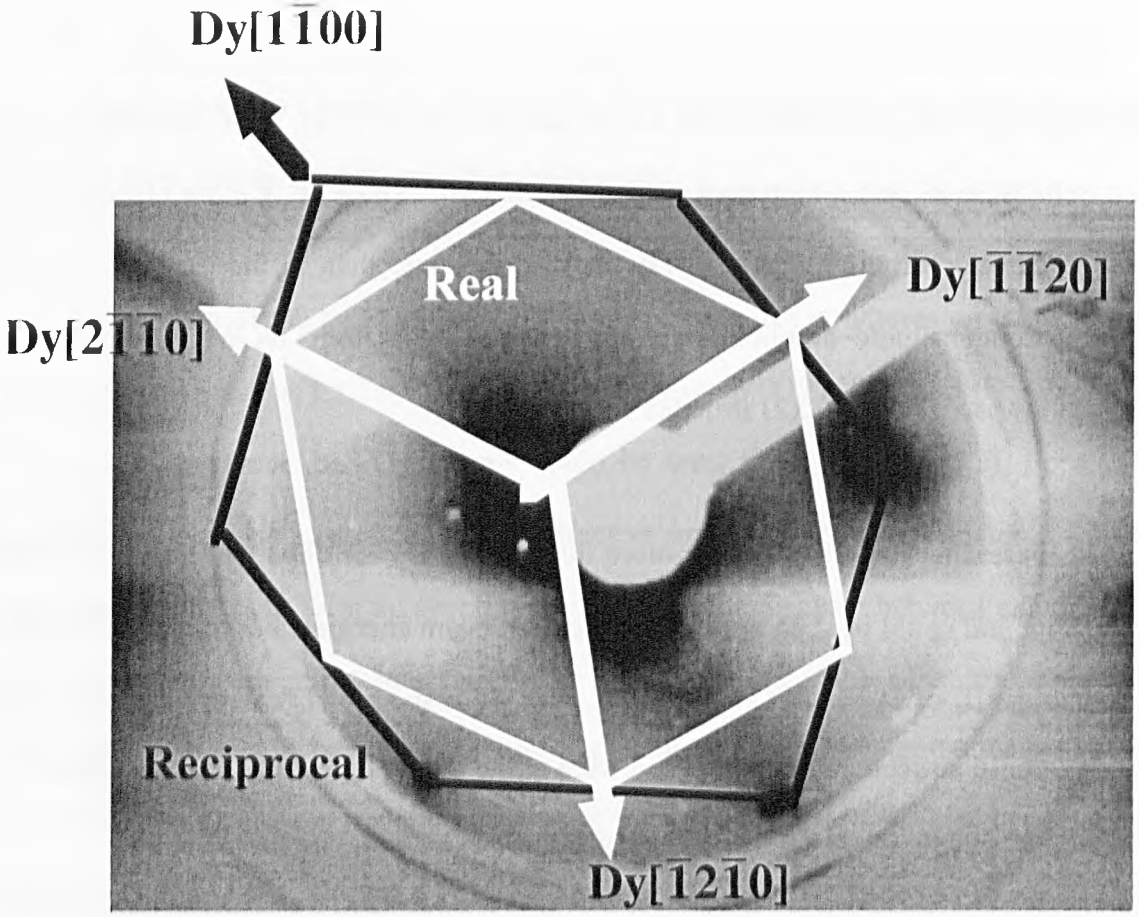

Fig.5.13. LEED pattern taken at 40 eV of Dy/W(112) with 4ML Dy grown at RT. Schematic hexagonal LEED has been drawn based on the position of LEED spots and the real space lattice shape and direction has been inferred from it.

By increasing the annealing temperature to 1670K, the background increased and the coverage decreased substantially, but still Dy spots could be seen in the LEED pattern.

Unlike growth at room temperature, growing Dy when the substrate was kept at 470 K and 570 K produced a LEED pattern with streaks. Despite this difference, the effect of annealing temperature on LEED pattern was the same as for the case of RT growth.

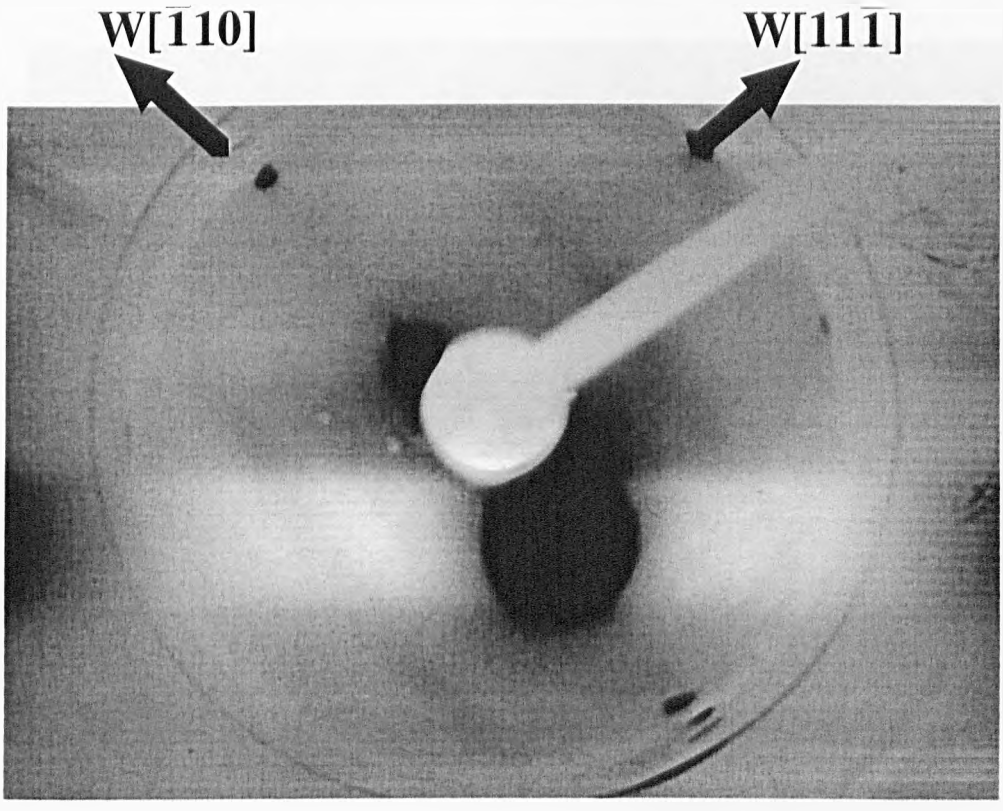

Fig.5.14. LEED pattern of clean W(112) taken at 40 eV for comparison with Fig.3.13.

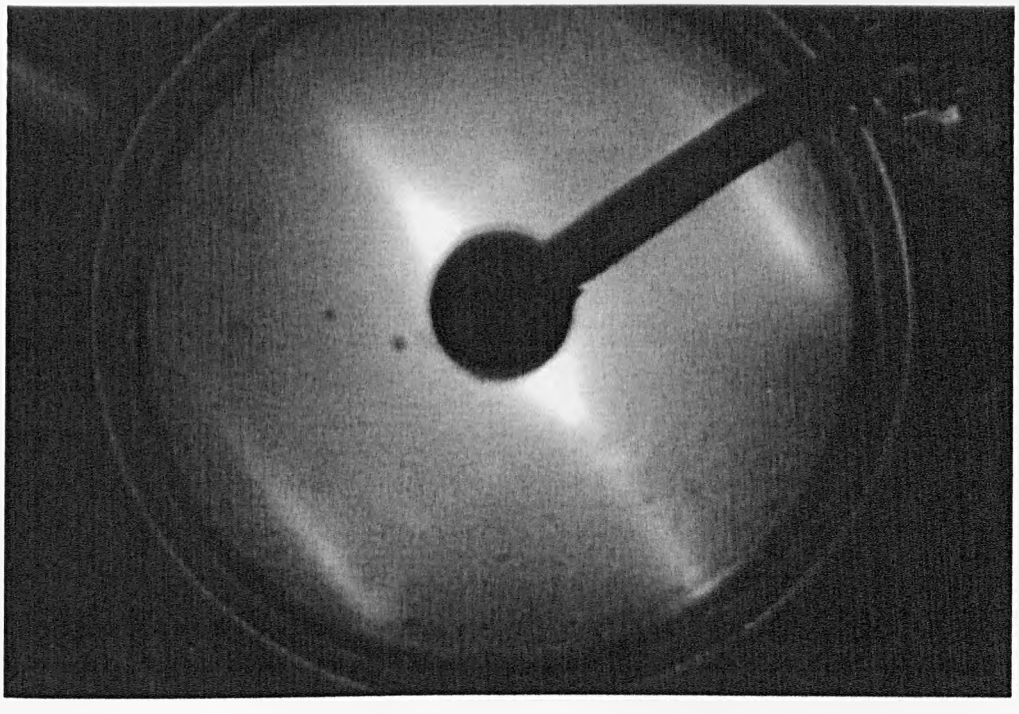

Fig.5.15. LEED pattern taken at 40 eV of Dy/W(112) with 4ML Dy grown at RT and annealed to 1200K.

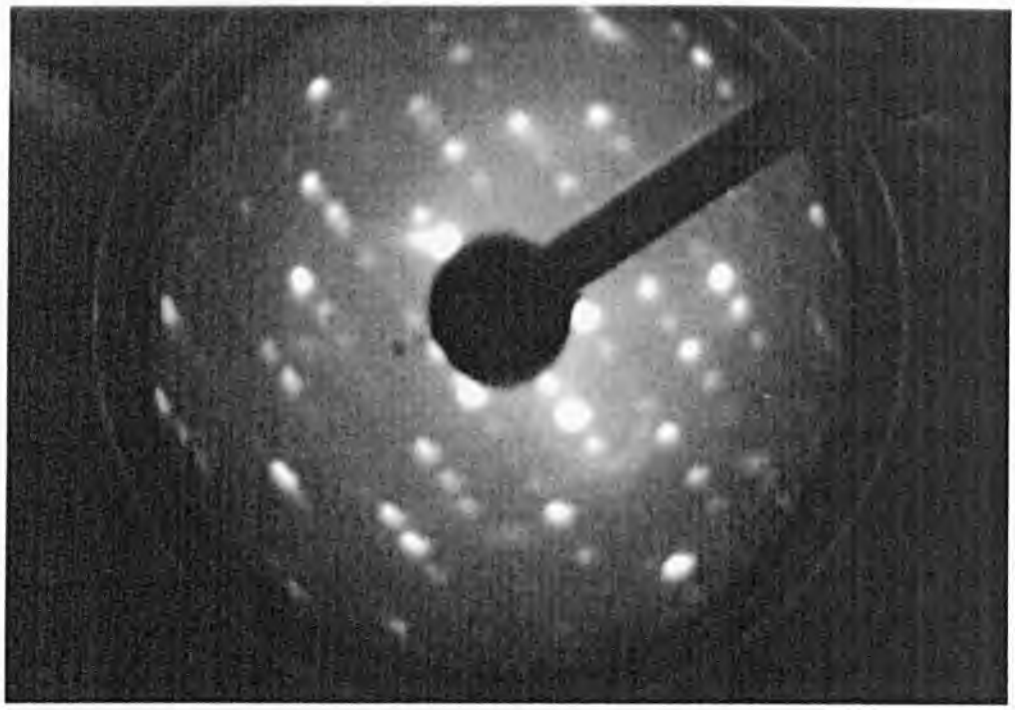

a)

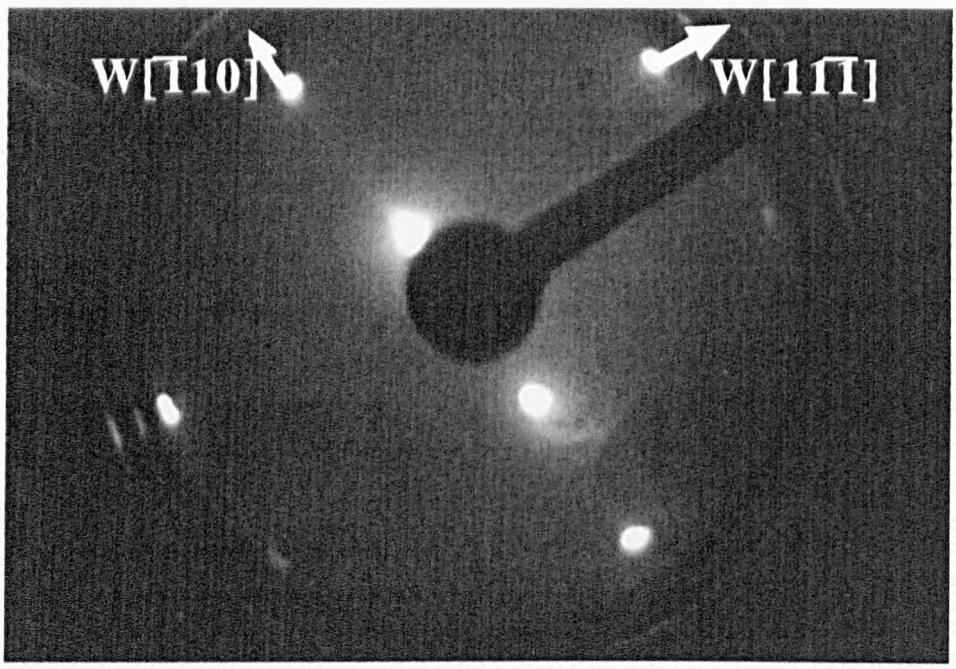

b)

Fig.5.16. LEED pattern taken at 50 eV of
a)Dy/W(112) with 4ML Dy grown at RT and annealed to 1400K.
b) clean W(112) for comparison

By increasing the temperature above 1200K, streaks disappeared and extra spots appeared in the pattern. By annealing to 1370 K a complicated pattern appeared.

By increasing the annealing temperature to 1670K, the background increased and the coverage decreased substantially, but still Dy spots could be seen in the LEED pattern.

Unlike growth at room temperature, growing Dy when the substrate was kept at 470 K and 570 K produced a LEED pattern with streaks. Despite this difference, the effect of annealing temperature on LEED pattern was the same as for the case of RT growth.

5.6. Dy/W(110)

Li et al [8] have found (0001)Dy‖(110)W with epitaxial relationship of $[\bar{1}100]$Dy‖[110]W or $[11\bar{2}0]$Dy‖[001]W, known as Nishiyama–Wasserman (NW) orientation [152]. As is clear from Fig.5.17, the same epitaxial relation has been found in this work for Dy on W(110) at low coverages (up to 4ML). Despite this, it is now believed that according to chapter 4, Dy grows laminar only up to 2 ML. At submonolayer coverages a couple of structures such as those shown in Fig.5.18 appeared on the LEED screen. However, because of existing studies of this regime, such as that of Li et al [8], no further attempt has been made to investigate these structures.

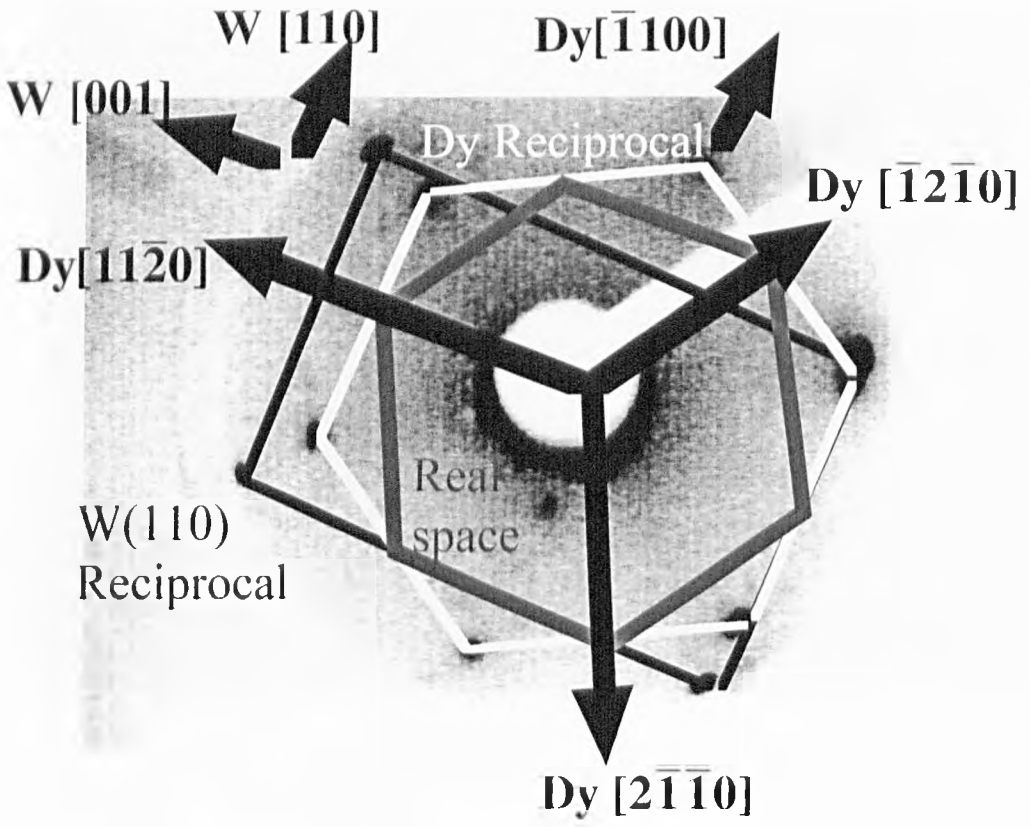

Fig.5.17. Dy hexagonal LEED pattern after 4ML Dy grown on W(100) at RT. The W LEED pattern shown in the picture is that of the clean W(110) and has been attached to the picture for comparison of directions. Both taken at 55 eV.

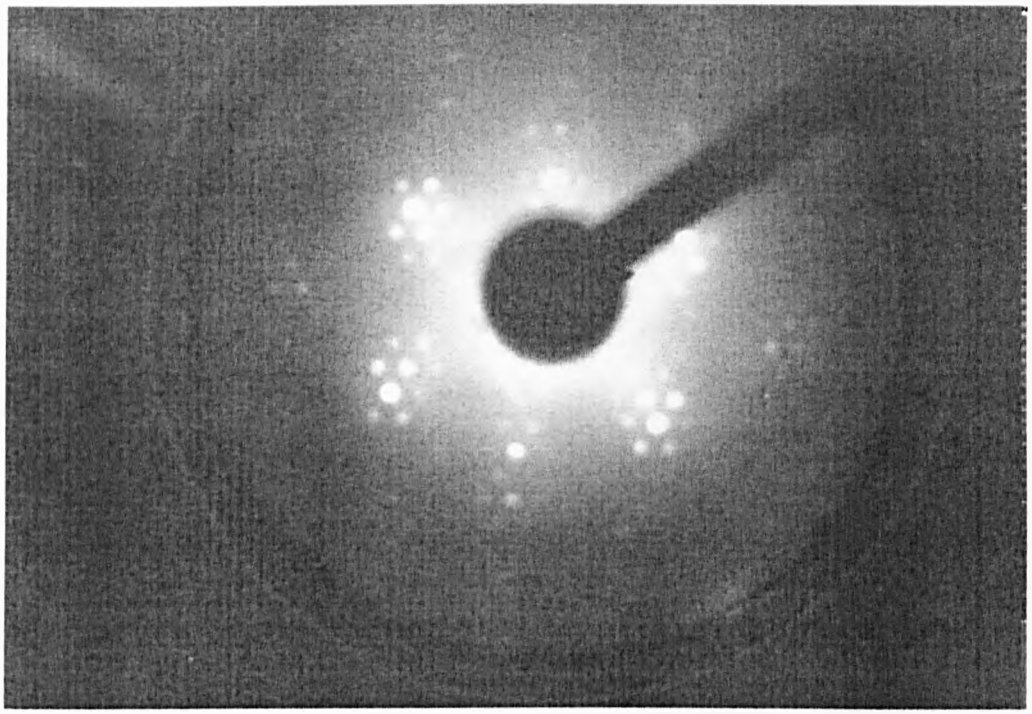

a)

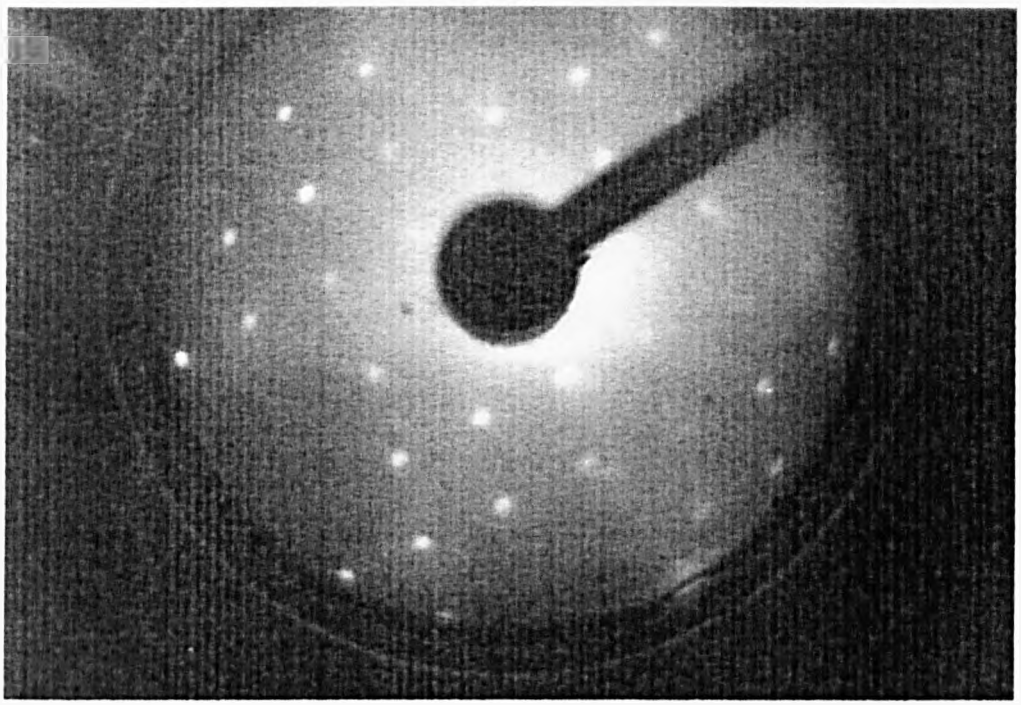

b)

Fig.5.18 a) hexagonal structure of ~0.5ML Dy on W(110) taken at 230 eV . b) chain like structure at low coverages (<0.3ML) taken at 45 eV .

Chapter 6

Scanning Tunnelling Microscopy of Dy films on W(100) and W(112) substrates

6.1. Introduction

Producing flat and well ordered films of Dy on tungsten surfaces is one of the major aims of this research. This is very important for the future applications of these films in the complementary experiments such as magnetic properties investigations which can bring them closer to the practical applications. Growth mode studies (Chapter 4) indicated S–K growth mode for Dy on both W(100) and W(112) surfaces at RT and at elevated temperature. LEED patterns also revealed that no well–ordered films have been produced after the growth. Annealing as–grown films led to very high–quality LEED patterns indicating the formation of flat and very well–ordered films (Chapter 5). However, it is not clear what macroscopic structure the films have, e. g. is it well–ordered large islands or well–ordered flat films. Therefore, STM experiments have been carried out on the Dy/W(100) and Dy/W(112) systems to obtain such information about the morphology of the films. Furthermore, when atomic resolution is achieved in the STM experiments, lattice matching criteria will be more easily interpreted with real (STM) and reciprocal (LEED) space representations..

Since this is the first attempt to grow Dy on W(100) and W(112), there is no existing information about the STM analysis of these films in the literatures. There are no papers published on STM studies on Dy films on any kind of substrate. The STM studies that are most relevant to this research are the STM work on a bulk crystal of Dy [122], which not only can not be used for comparison with the Dy films on different substrates, which usually have different kind of strains, but also it is not very good from an image–quality point of

view. Another relevant study is Gd/W(100) by White et al [147] in which they have confirmed a local S–K growth mechanism for this system at RT. They have also reported formation of flat islands whose sizes are related to the deposition temperature. Finally they have reported the formation of inverted islands of Gd on W(100) after annealing to 800K. These are islands for which the direction of increasing steps is opposite to that of the substrate.

The study most relevant to Dy/W(112) is Gd/Mo(112) by Waldfried et al [149] in which they have have studied Gd films 15-50 ML thick with STM and LEED. They reported preferential domain growth directions of Gd films along the ⟨111⟩ directions of Mo. They have also reported thickness dependent domain structures.

In this work, growth of Dy on W(100) and W(112) was studied by STM. The effect of the substrate and also the effect of annealing temperature on the morphology of the Dy films are investigated. In each stage of the work, correlation between the associated LEED patterns (Chapter 5) and the STM images will be discussed. Because of the important role of the substrate structure on the film morphology, clean substrates have been studied by STM prior to the study of the films.

6.2. Theory of scanning tunnelling microscopy

In principle, quantum mechanical tunnelling can occur between two conductors simply by bringing them sufficiently close together, since the electron wavefunctions at the Fermi level leak out of their confining potentials wells with a characteristic exponential inverse decay length K [129] given by

$$K = \hbar^{-1}(2m\phi)^{\frac{1}{2}} \qquad (6.1)$$

where m is the electron mass and ϕ is the effective local work function. If two such wells are brought sufficiently close together (about 4 $\mathring{A}$) [129] and a potential V applied between them, then overlap of the electron wavefunctions permits quantum mechanical tunnelling and a current I will flow across the gap. This current is a function of bias voltage and exponentially dependent on the gap distance. When $V>\bar{\phi}$, where $\bar{\phi}$ is the average of the potential height between the two electrodes, the tunnelling current dependence on bias voltage is described by the field emission formula, i. e. the Fowler–Nordheim relation [159]. Depending on the gap distance and bias voltage, the tunnelling electrons form a standing wave in this region. If the bias voltage is less than the workfunction $V<\bar{\phi}$, then the tunnelling current between tip (t) and the surface (s) can be expressed by first–order perturbation theory [160]:

$$I = \frac{2\pi e}{\hbar} \sum_{ts} f(E_t)\,\left[1 - f(E_s + eV)\right]\,|M_{ts}|^2\;\delta(E_t - E_s) \qquad (6.2)$$

in which M_{ts} is the tunnelling matrix element between the tip and the surface wavefunctions, and its square is an indication of transition probability from an occupied state of the tip (E_t) to an empty state of the surface (E_s), or vice versa depending on the sign of the bias voltage, V. It can be shown that

$$M_{ts} = \frac{\hbar^2}{2m}\int \bar{ds}.(\Psi_t^*\bar{\nabla}\Psi_s - \Psi_s\bar{\nabla}\Psi_t^*) \qquad (6.3)$$

where m is the free electron mass, and the integral is taken over a surface lying entirely within

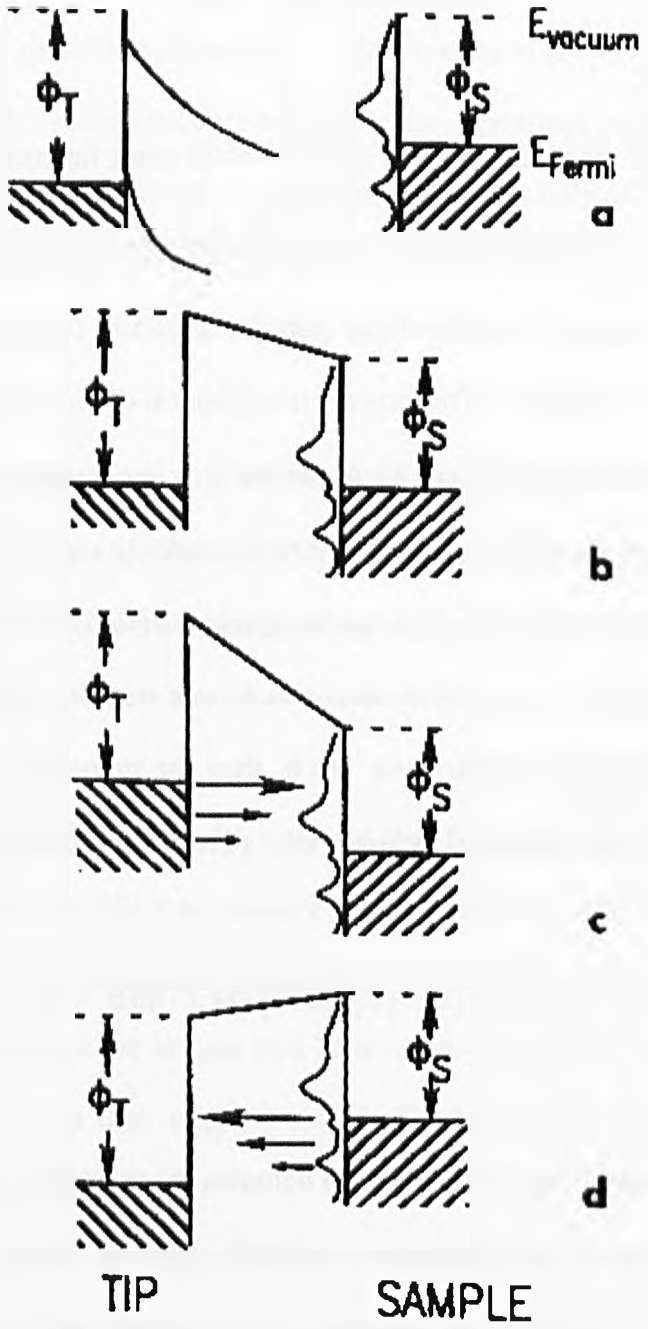

Fig.6.1. Energy level diagrams of the sample and the tip: (a) with the sample and tip independent, the vacuum levels are equal; (b) with the sample and tip connected with no potential difference, the Fermi levels are equal; (c) application of a negative tip bias, $V_t < 0$, allows electron to flow from occupied states of the tip to unoccupied states at the sample surface; (d) application of a negative sample bias, $V_t > 0$, allows electrons to flow from occupied states of the sample surface to unoccupied states in the tip. Adopted from Ref [160]

the vacuum barrier region between the tip and the sample.

$f(E_t)$, defined in equation 6.4, is the tip Fermi function, which is the probability that the energy level E_t of the tip is occupied, in which μ is the chemical potential of the tip, k_b is Boltzman

$$f(E_t) = \left\{ \frac{1}{\frac{E_t - \mu}{k_b T} + 1} \right\} \qquad (6.4)$$

constant and T is the tip absolute temperature. In the same way $[1 - f(E_s + eV)]$ is the probability that the energy level E_s is empty when the surface is connected to the positive potential (i. e. when magnitude of E_s is increased due to the positive voltage).

For small bias voltages and low temperatures ($k_b T < 50$ eV), f(E) can be expanded which will lead to [160]

$$I = \frac{2\pi e^2 V}{\hbar} \sum_{ts} |M_{ts}|^2 \; \delta(E_t - E_F) \; \delta(E_s - E_F) \qquad (6.5).$$

If the integral in equation (6.3) was in one dimension (e. g. tunnelling occurred in the z direction)

$$\Psi_s(z) = \Psi_s^o \exp(-Kz) \qquad (6.6)$$

$$\Psi_t(z) = \Psi_t^o \exp(-K(d - z)) \qquad (6.7)$$

where K is inverse decay length defined in equation (6.1), Ψ_t^o (Ψ_s^o) is wavefunction at the position of the tip (surface), d is the distance between tip and the surface and $\bar{\phi}$ is the average of the potential height between the two electrodes. Therefore from equation 6.3 it is possible to show that

$$M_{ts} \propto -2K\Psi_s^o\Psi_t^o e^{-Kd} \qquad (6.8)$$

Equation 6.5 can now be written as

$$I \propto V\sum \left|\Psi_s^o\right|^2 \left|\Psi_t^o\right|^2 e^{-2Kd} \qquad (6.9)$$

This means that the tunnelling current is related exponentially to the distance between the tip and the sample (d). This also shows that the characteristics of the wavefunctions play a role in determining the tunnelling current. The more delocalised s states contribute more to the tunnelling current than the contracted d states of the same energy. Similarly, p_Z orbitals will affect the tunnelling current much more than p_X and p_Y orbitals which are counteracted in a plane parallel to the surface. Finally, using a spherical configuration for the tip it can be shown that [160]

$$I \propto V \quad D_t(E_F) \quad \rho_s(r_o,E) \quad e^{2Kr} \qquad (6.10)$$

where $D_t(E_F)$ is the tip density of states and $\rho_s(r_o,E)$ is density of states at the surface for energies around E_F and for a particular tip position r_o (r_o is the position of the centre of curvature of the tip). Thus the current is proportional to the surface LDOS at E_F measured at the tip position. This dependence of tunnelling current on surface LDOS can be used to investigate surface electronic structure by Scanning Tunnelling Spectroscopy. In this method,

the tip is kept at a specific position above the surface then changes of the tunnelling current with variation of the bias voltage is measured and a series of curves of I or $\frac{d\ln I}{d\ln V}$ versus V is plotted. Then knowing the relationship between I, V and surface LDOS, information about the surface LDOS can be extracted [159].

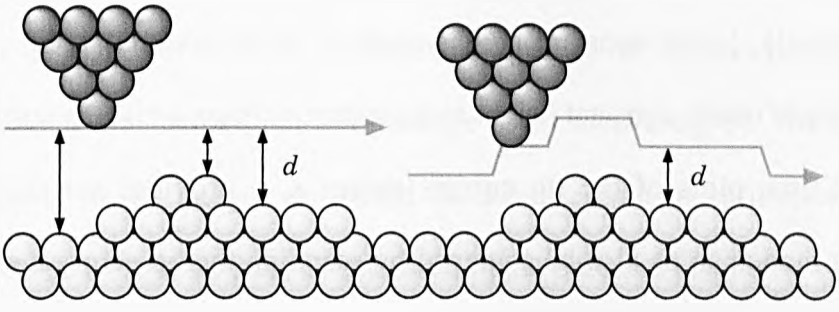

Fig.6.2. Operational modes of the STM: Constant height (left) and constant current (right). From Ref [6]

Assuming the same wave function and therefore the same density of states for the whole tip and the surface area under STM investigation, the tunnelling current (eq.6.10) can be simplified to [129]

$$I \propto \left(\frac{V}{d}\right)\exp(-2Kd) \qquad (6.11).$$

For example for a case in which $\bar{\phi}$ = 4 eV, K=1.0 $\mathring{A}^{-1}$ and the current decreases by an order of magnitude when the gap d is increased by only 1 $\mathring{A}$. Put another way, if the current is kept constant to within a few percent, then the gap d remains constant to within about 0. 01 $\mathring{A}$.

There are two basic modes for the scanning process, namely, constant current mode or constant height mode (Fig.6.2). In the constant current mode, the tip is brought close to the

surface such that at a convenient bias voltage (typically 2meV-2V), the tunnelling current is measurable (usually ~ nA). A feedback network changes the distance d between tip and the surface to maintain constant current whilst the tip is scanned laterally over the surface. A plot of d versus the x and the y coordinates of the tip is a set of contours of the surface below the tip.

Alternatively, in the constant height mode (a faster method), a tip can be scanned across the surface at nearly constant height and constant voltage, while the current is measured (Fig.6.2). This time plots of the tip current versus x, y provides surface contours. The constant height mode can be also be achieved by scanning the tip across a surface at nearly constant height and constant current while monitoring the voltage.

6.3. Experimental details

The W(100) crystal was prepared by initial annealing in a partial pressure of oxygen ($\sim 10^{-10}$ mbar) followed by cycles of flashing to 2500 K until judged clean and ordered by LEED and STM. Because of this high temperature it was necessary to carry out the cleaning process of W(100) far from the STM and then transfer it to STM position. Therefore a sample holder has been designed for the STM experiments. A description of this sample holder has been given in Chapter 3.

Evaporation was carried out by a well degassed Knudsen cell (k-cell) evaporator (manufactured by WA Technology) which contained Dy (99.99% pure).

To prevent any contamination the sample was flashed every 60 to 120 minutes and new films were grown.

STM experiments were performed using a commercial Omicron STM operated at room temperature in an ultrahigh vacuum chamber. The base pressure of the chamber was 2×10^{-11} mbar and during evaporation the pressure remained below 9×10^{-11} mbar. The STM images were obtained in constant current mode and represented as grey tone images. The data presented by U and I in the figure captions refer to sample bias voltage and tip current, respectively. The *xyz* piezoelectric system was calibrated by measurements of graphite with known periodicity. The error in measurements was found to be ~ 4% in x, y and z directions. All image processing was carried out using Image SXM software [90]. The crystallographic directions assigned to the images are based on the direction of split spots in the LEED patterns of the clean W(100) surface, as discussed in the previous chapter.

6.4. Clean W(100)

Fig.6.3. shows a large–scale STM image of clean W(100) at RT taken 30 minutes after a high temperature flash to 2500K. Terraces along [001] can be seen with rather irregular step edges. The terraces had monoatomic height (1.6 Å). The average size of terraces along [010] was found to be ~48 Å, in agreement with the result of a LEED calculation (Chapter 5).

Fig.6.4 shows a 500 Å x 300 Å image of the W(100) surface. The image shows a number of defects on the surface which are mostly due to presence of contamination, missing atoms and missing atomic rows. These missing rows make it possible to resolve some atomic rows along [010]. However, no atomic structure can be resolved on most of the surface of the terraces. Further attempts to achieve atomically resolved images of the clean W(100) at RT were not successful. The same situation was found by other researchers attempting to resolve atomic arrangements on clean W(100) at RT, such as Wengelink *et al* [161]. They attributed this difficulty to the particular thermal vibrational properties of the clean surface of W(100)

which is responsible for the noise of the tunnelling current. Therefore, due to the noise level in our measurements it was impossible to judge whether the room temperature arrangement of W atoms corresponds to an ordered or to a disordered state.

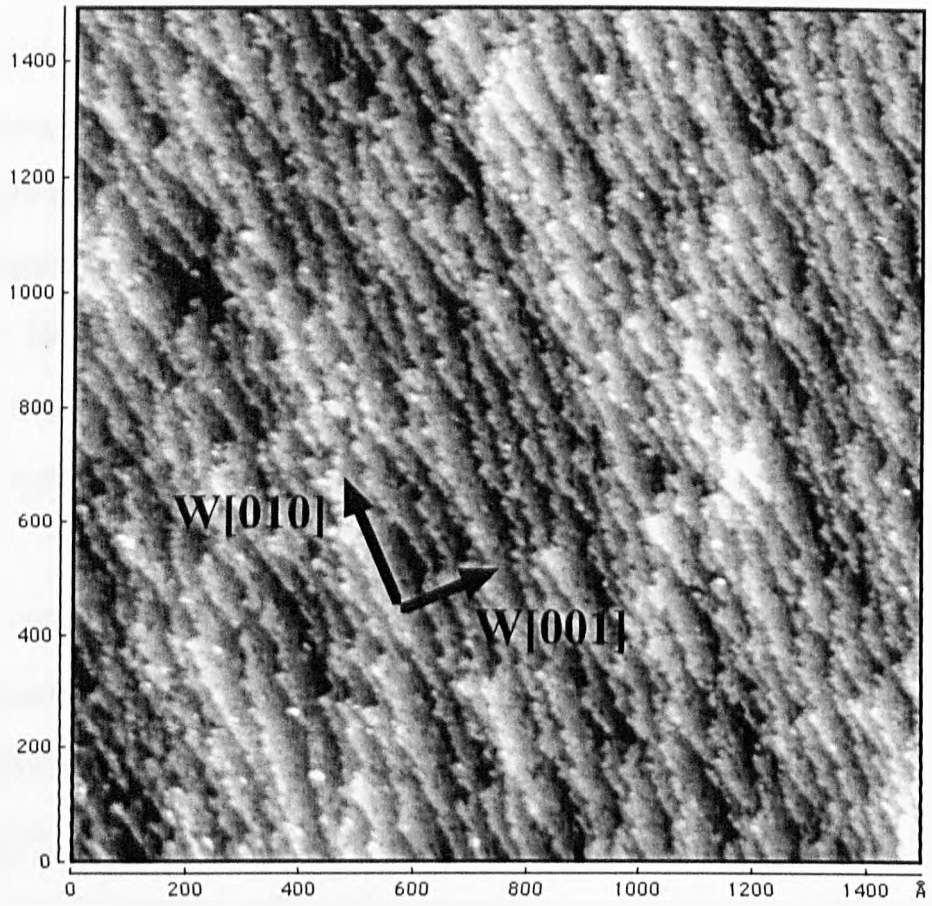

Fig.6.3. Large–scale STM image from W(100) (1x1) at room temperature acquired after a high–temperature flash. U=1 V, I=0.5 nA

Fig.6.5 shows another kind of defect on some part of the W(100) sample known as an edge dislocation This has been shown by arrow(a). In this defect there is a perfect crystal with the addition of an extra half–plane of atoms. Fig.6.5 (b) shows a profile of the vertical change across this dislocation, along line (b) in Fig 6.5 (a). It is clear that there is a height difference of 1ML between the two parts of the image. Fig.6.5 (c) is a profile of the vertical change along terraces shown by arrow(c), indicating a step edge of ~1.6 Å.

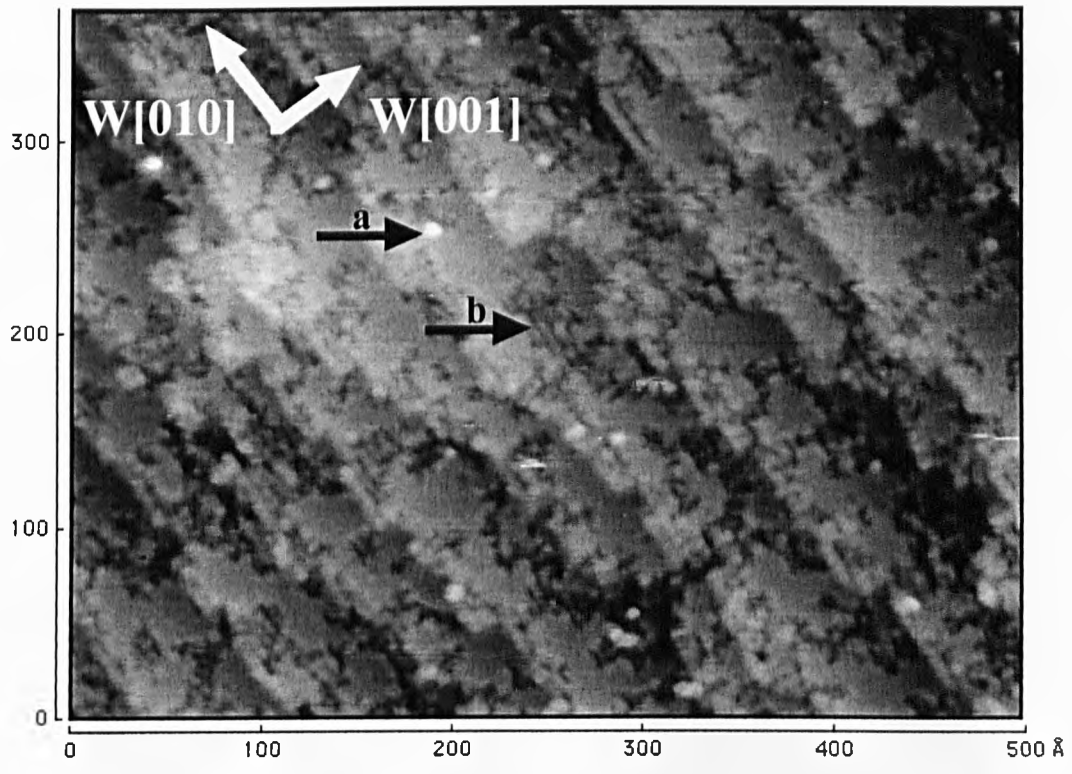

Fig.6.4. STM image from W(100) 1x1 at room temperature acquired after a high–temperature flash. The arrows show typical defects due to a) contamination and b) missing rows. U=1 V, I=0.5 nA.

6.5. Dy/W(100)

6.5.1. Growth at RT

It has been shown in Chapter 4 that Dy follows a rather complicated growth mode on W(100) that can be best described by a SK growth mode. To investigate this with STM, Dy

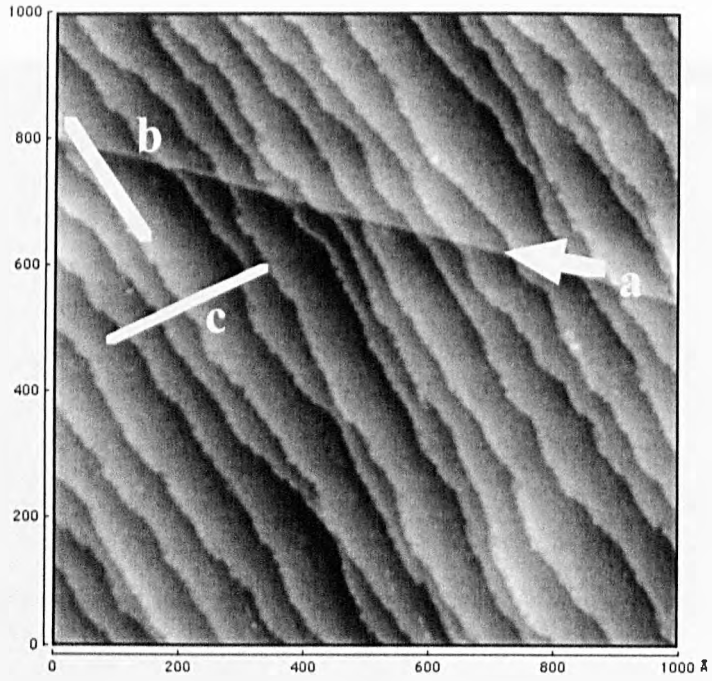

a)

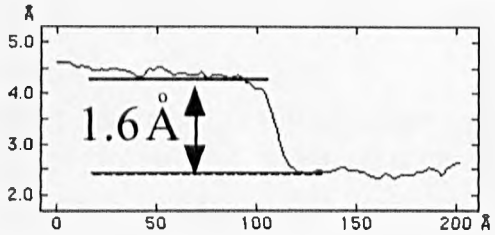

b)

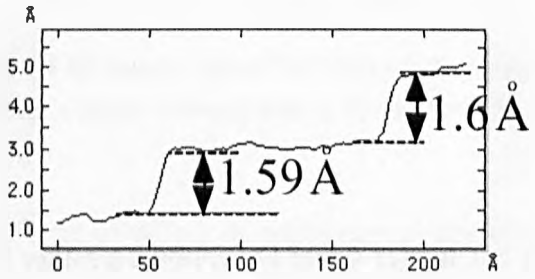

c)

Fig.6.5. STM image from clean W(100) 1x1 at RT indicating edge dislocation, shown by arrow(a). (b) profile of the vertical change across the dislocation. (c) profile of vertical change along terraces indicating a step edge of ~1.6 Å

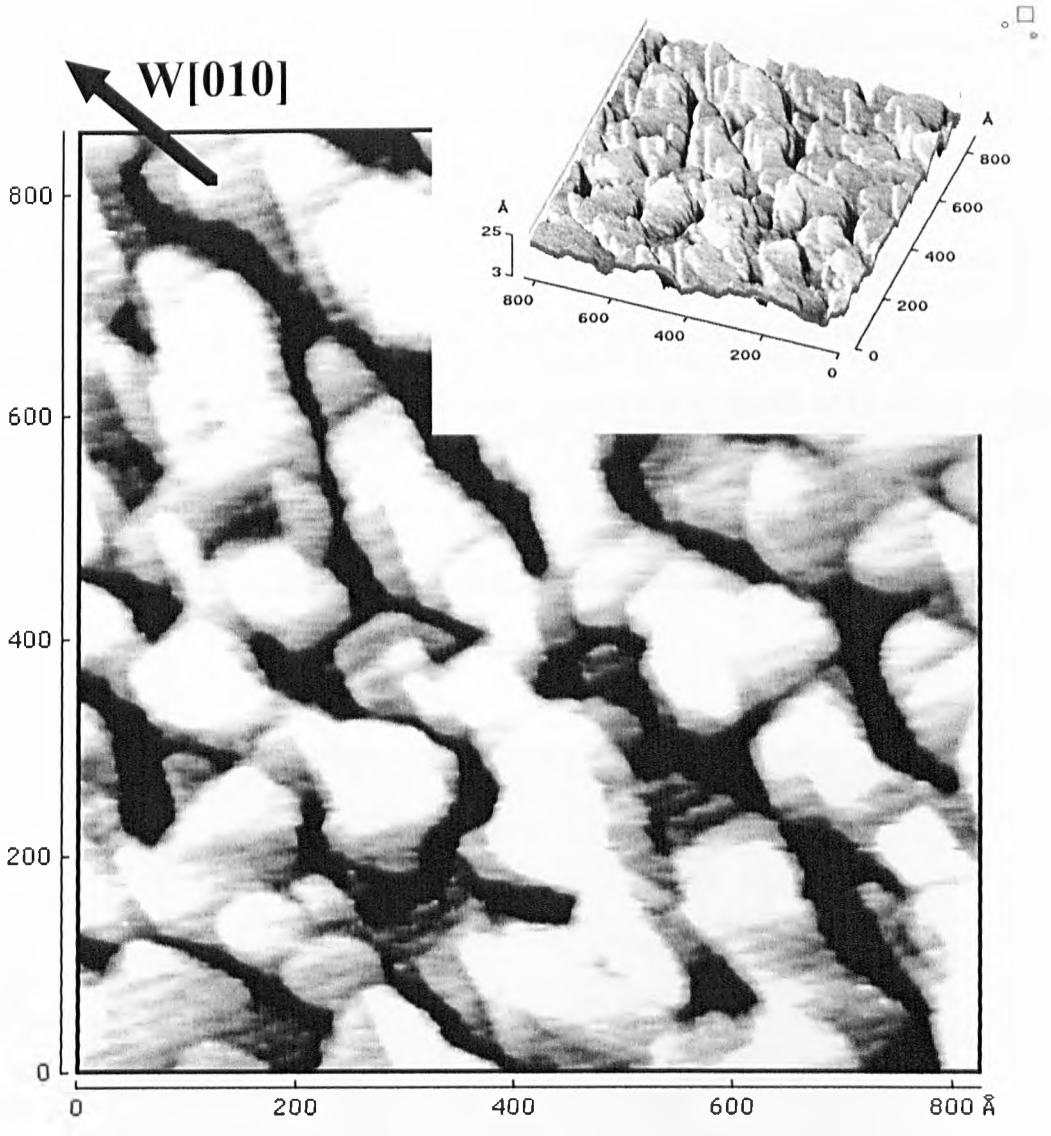

Fig.6.6. STM image from Dy/W(100) for 8ML coverage grown at RT. U=0.5V and I=1nA. The inset show a 3D view of this image.

has been grown at RT on W(100) and scanned at RT with STM. Fig.6.6 shows an STM image of Dy/W(100) system taken after growing 8ML Dy at RT. The inset shows a 3D view of this region. It is clear from this image that Dy grows as single–step islands (with height of 2.82 Å) with a rather preferred rhombic shape in a way that their sharp edges, with average angle of $52° \pm 1°$, point along the W[010] direction.

6.5.2. c(8x2) Structure

6.5.2.1. Annealing to 750K

By annealing Dy films grown at RT on W(100) to 750K, LEED started to show a pseudo–hexagonal pattern (Fig.5.1) corresponding to the close–packed structure of c(8x2) (see Chapter 5). An STM image of this system is shown in Fig.6.7. It is clear from this image

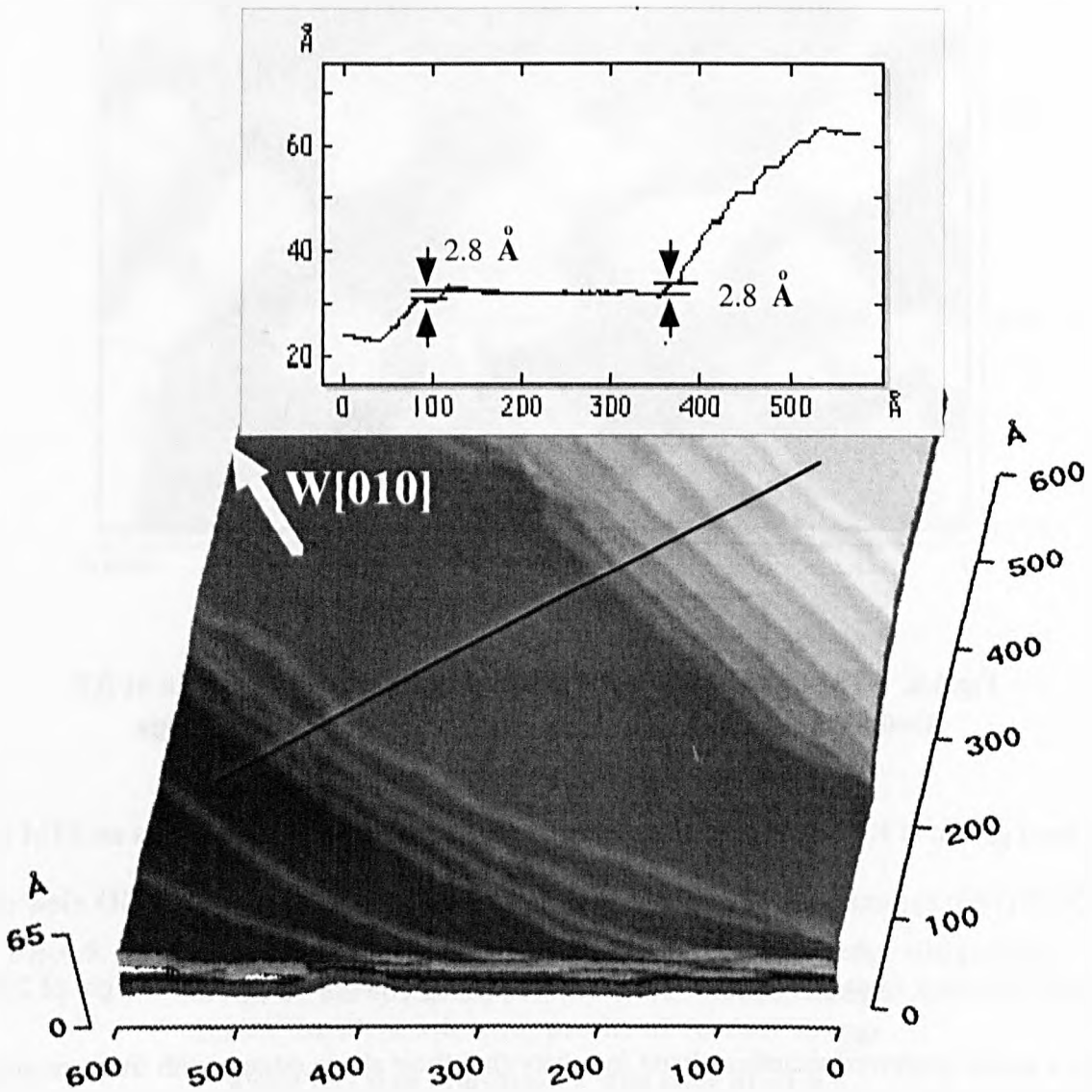

Fig.6.7. 3D STM image of Dy/W(100) in STM image mode of 8ML Dy annealed to 750 K correspond to c(8x2) structure. The inset shows a profile of vertical changes along the line shown in the picture. U=1 V, I=1 nA.

that the film consists of flat and large terraces (compared to those of W) terraces of Dy which are along the step edge direction of the substrate, i. e. W[010]. Step heights have been measured and found to be (multiples of) 2.82 Å as expected for (multiple) single step(s) of Dy (1000) layers. The average sizes of terraces was found to be at least five times larger than the average size of W terraces. Further attempts to achieve atomic resolution of the close–packed c(8x2) structure were not successful. Fig.6.8 shows an image of one of such terrace. It is clear from this image that defects on the surface, such as missing rows and atoms resulted in increasing of corrugation of nearby areas which led to atomic resolution in the image.

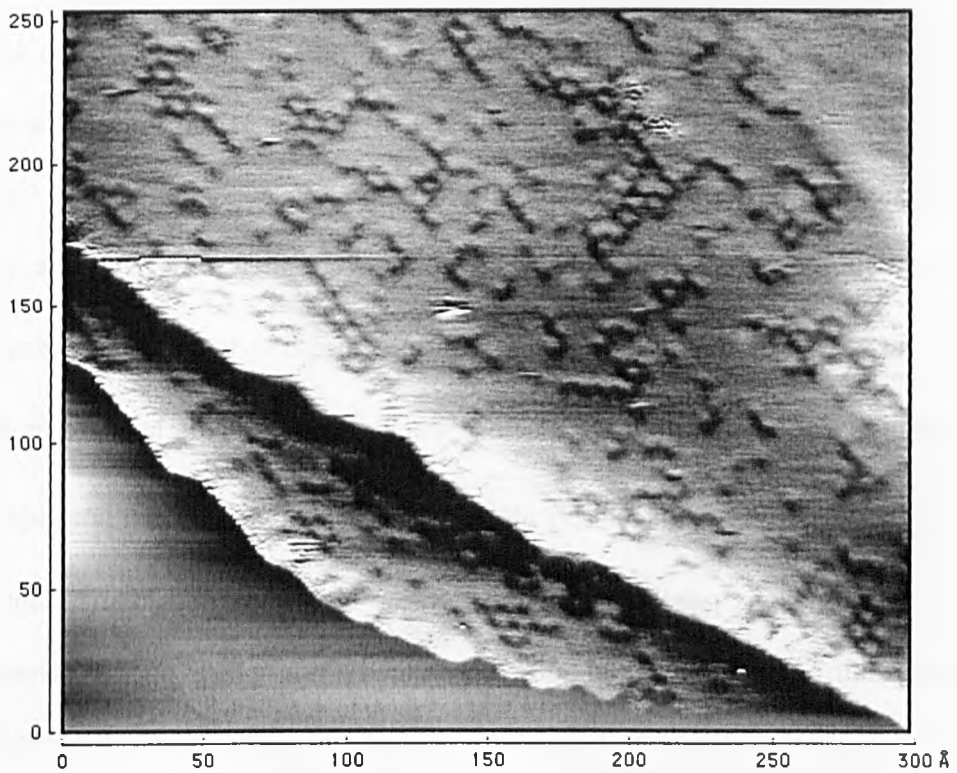

Fig.6.8. STM image of one of the terraces shown in Fig.6. 7. The defects on the surface, such as missing rows and atoms resulted in atomic resolution in the image. U=-0.8 V, I=2 nA.

The reason that no atomic resolution can be achieved for the close–packed c(8x2)

structure is most likely due to electronic changes of Dy at the surface. The fact is that Dy in a c(8x2) structure will have 12 nearest neighbours with bond lengths of 3.62 Å. It has been discussed in section 2.4.1 of chapter 2 that any increase in nearest neighbours of Dy to more than 4 will lead to a valence Change in Dy atoms from $4f^{10}\ 6s^2$ to $4f^9\ (5d6s)^3$. This will cause an increase in electronic overlap between valence electrons of the adjacent Dy atoms and reduces the electronic corrugation around Dy atoms. When the sample is connected to negative bias this will affect the resolution of scan, because the STM is scanning the electronic cloud around the Dy atoms. In the case which the sample is connected to positive bias the tunnelling of electron from the tip to empty states of the Dy will also be perturbed by increase in valence electrons.

By further investigation of different areas on the film a small region with atomic resolution was found (Fig.6.9). This area consists of regular Dy atomic rows along steps which is consistent with the LEED considerations of the close–packed c(8x2) (see Fig.5.1). However the distance between adjacent Dy atoms were different from the case in the close–packed c(8x2). For example, the inter–atomic distance was 6.4 Å along the step direction, which is larger than the case of close–packed c(8x2). This leads to an increase of corrugation to 0.2 Å between adjacent Dy atoms (Fig.6.9), which makes it possible to achieve the atomic resolution. It is possible that in this area Dy atoms had insufficient energy to change their structure to close–packed and so produced a non–close–packed structure on top of the close–packed area, shown as even and dark patches in the image. Fig.6.9(b) shows a profile of vertical changes between the close–packed area and the non–close–packed area on top of it. It is possible to recognise a distorted hexagonal pattern for this non close–packed structure. Fig.6.10 shows a closer view of the area shown by the circle in Fig.6.9. Profiles along arrows (a), (b) and (c) indicate that atomic distances along these directions are 6.6 Å, 6.3 Å and 7.5 Å respectively. These measurements show that Dy does not form hexagonal

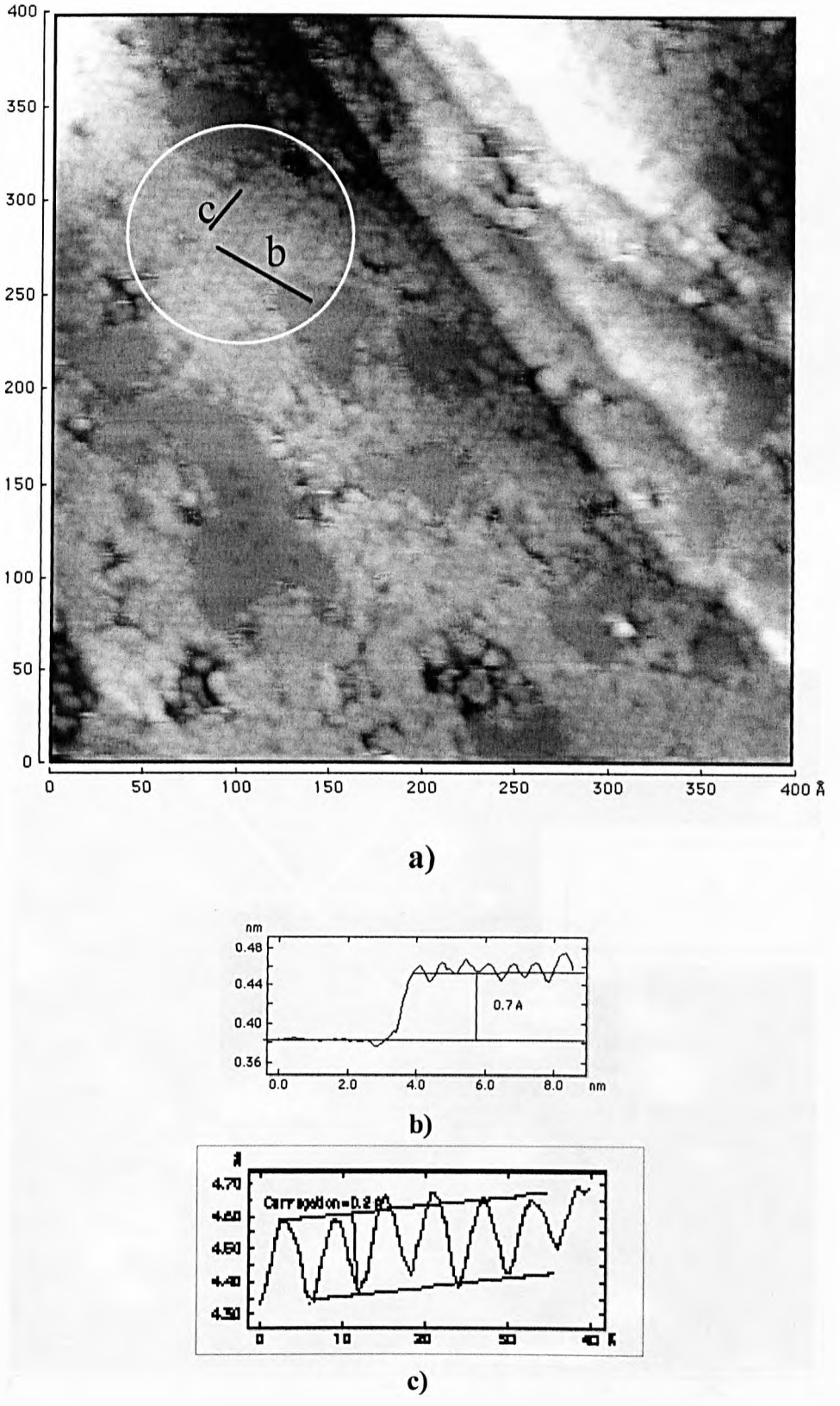

Fig.6.9. STM image of a region with atomic resolution of Dy film produced by annealing 8ML Dy to 750K. (b) profile of vertical displacement along direction show by line b. (c) profile of vertical corrugation between atoms along direction shown by line c. The circle indicates the region shown in Fig.6.10. U=-0.5 V, I=0.5 nA.

structures in this area.

A (6x2) structure is proposed for this non–close–packed structure (Fig.6.11). A Fast Fourier Transform (FFT) of this proposed structure is shown in Fig.6.11 (b). Absence of these spots in the LEED pattern of Fig.5.1 indicates that the area covered by this non-close–packed structure is very small, such that the intensity of its LEED spots are less than the background intensity.

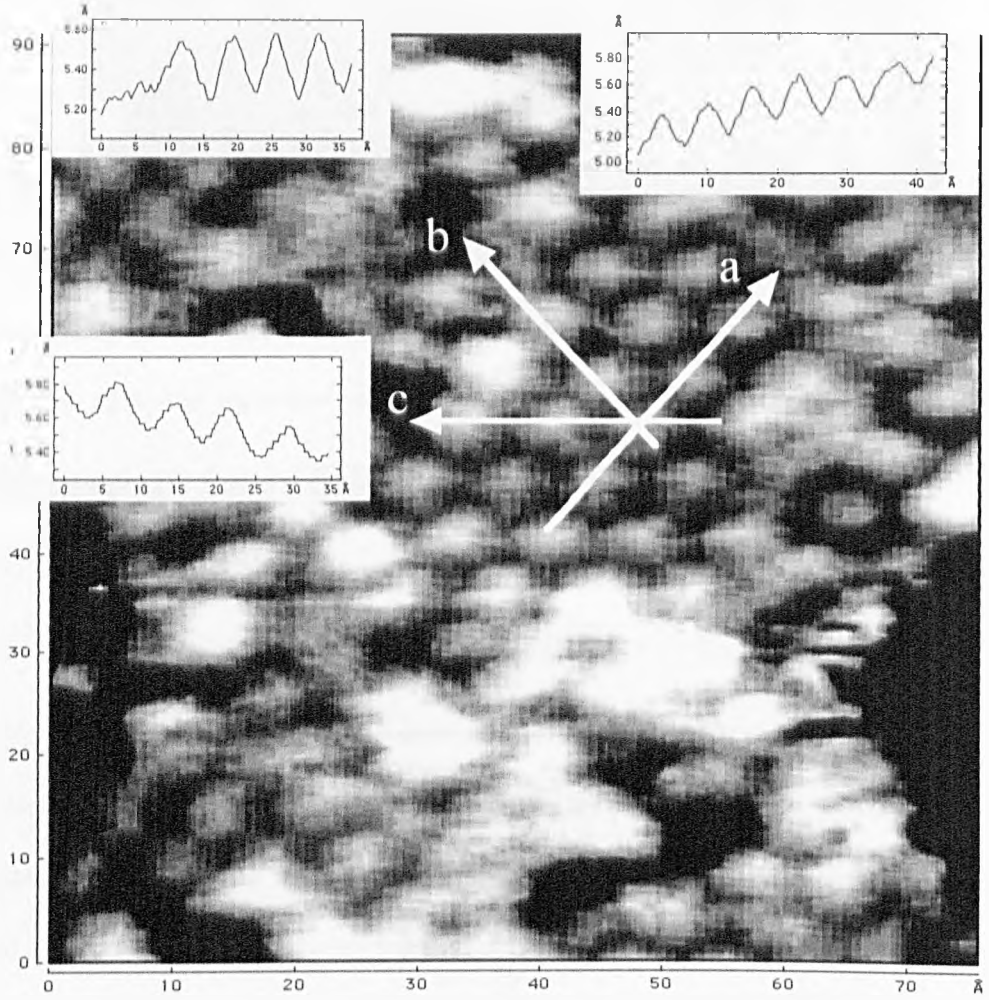

Fig.6.10. Enlarged view of the area shown by the circle in Fig.6.9 (a). The insets show profiles of atomic rows along arrows shown by a, b and c. These profiles show the atomic distances are 6.6 Å, 6.3 Å and 7.5 Å, respectively.

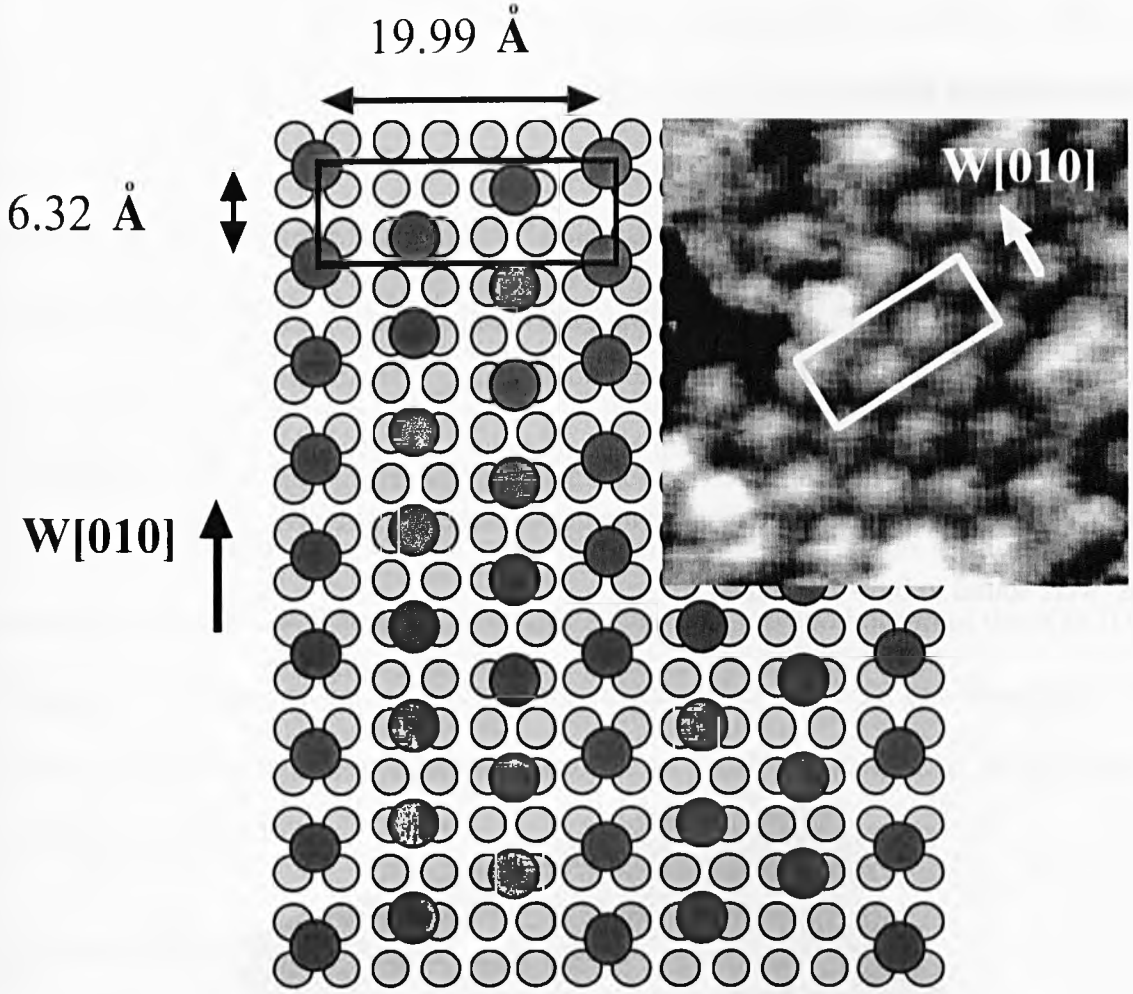

a)

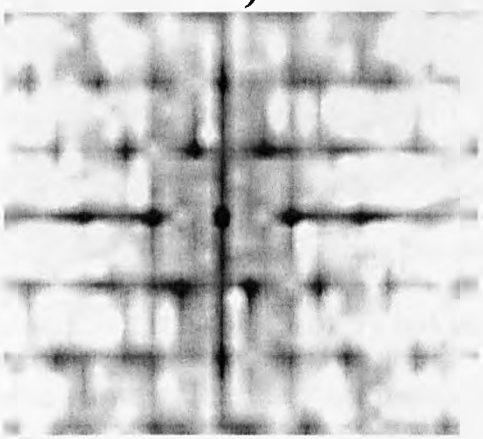

b)

Fig.6.11. a) Proposed (6x2) structure corresponding to the non–close–packed structure in Fig.6.10. b) FFT of Fig (a)

6.5.2.2. Annealing to 820K

Fig.6.12. shows the effect of annealing to 820 K on the Dy film on W(100). The LEED pattern remained the same as Fig.5.1. The only change was that the W spots became brighter. This annealing will tend make Dy accumulate and form large islands on the W surface. The islands are strained perpendicular to the step edge direction, W[010]. The shape of islands are such that the angle between edges are close to the hexagonal case. The averages of the angles of the edges were found to be ~ 52° and ~130°.

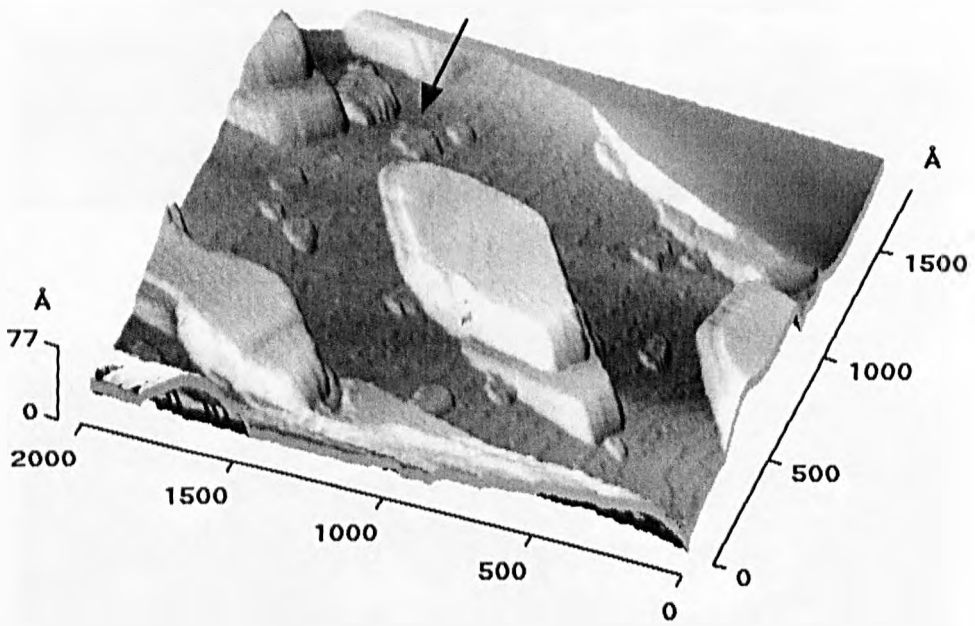

Fig.6.12. Three dimensional STM image taken in STM image mode from 8ML of Dy on W(100), annealed to 820K. The island shown by arrow is considered in Fig.6.13. U=0.5 V, I=1 nA.

Fig.6.13. shows a small island indicated by the arrow in Fig.6.12. It is clear that unlike Gd, Dy does not produce inverted–step islands on W(100) (see Ref [147]).

Fig.6.14 (a) shows another large island of Dy produced by annealing to 820K. Fig.6.14 (b) is top of the island, shown by arrow in Fig (a), after compensation for tilt and expanding the contrast.

Despite defects on the surface, atomic rows can be seen, and the distance between them is ~12.7 Å. This is equal to half of the c(8x2) lattice constant. Fig.6.15 shows the position of the Dy atoms in the case of c(8x2) on top of W(100). To make it more clear only atoms at the top, bottom and middle of the unit cell are shown and the registry has been chosen to be at top sites. It is clear that Dy will adopt the same registry position at the top, bottom and middle of the unit cell. Therefore, if atomic rows at the top and bottom of the c(8x2) cell have enough corrugation to be recognised, the middle rows can also be recognised. Thus, the distance observed between repeating features in STM would be half of the unit cell, as observed in Fig.6.14.

6.5.3. c(2x2) structure

By annealing Dy to 1400 K the coverage of the Dy film reduced to the submonolayer regime and a c(2x2) structure appeared on the LEED pattern (Fig.5.2). Fig 6.16 shows an STM image from such a structure. It is clear that the domains of the Dy c(2x2) have accumulated near the step edges of W(100). By measuring the area covered by Dy from STM images at different part of the sample the coverage of Dy has been estimated to be ~0.3 ML, which covered ~ 60% of the area. However, the coverage depends on the temperature and time of the annealing process leading to the c(2x2) structure.

Because of the large inter atomic distance in c(2x2), ~4.5 Å, it was expected to see atomic resolution for this coverage. However, because of the noise level in our experiment it was not possible to achieve atomic resolution.

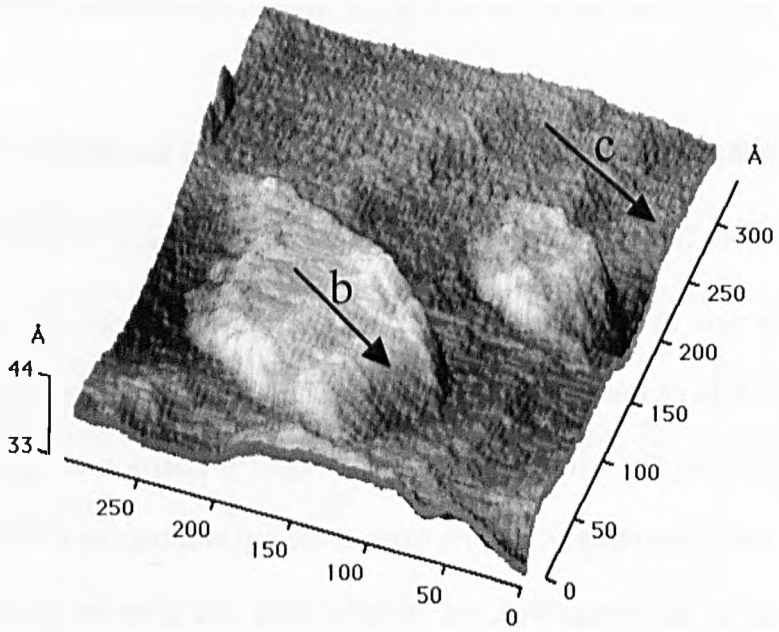

a)

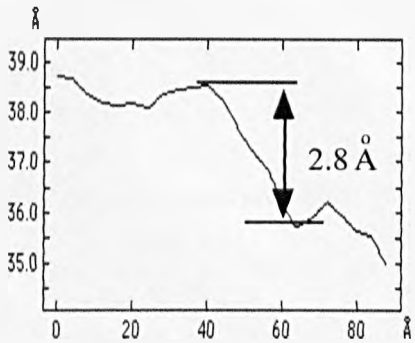

b)

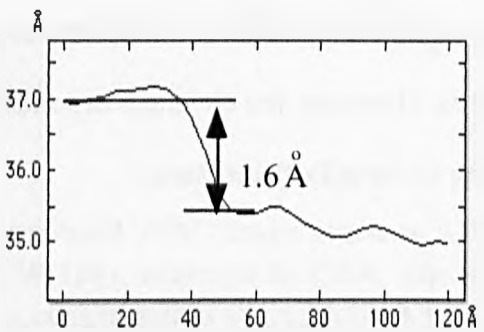

c)

Fig.6.13. a) Close up view of the area shown by the arrow in Fig.6.12. Figures (c) and (b) are profiles of vertical changes along lines (b) and (c) shown in Fig (a).

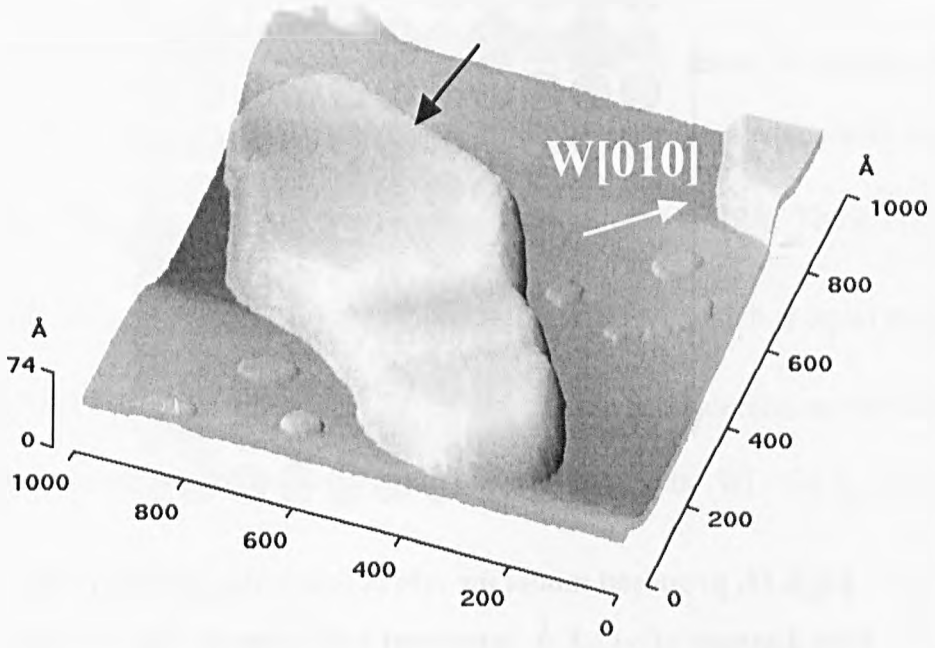

a)

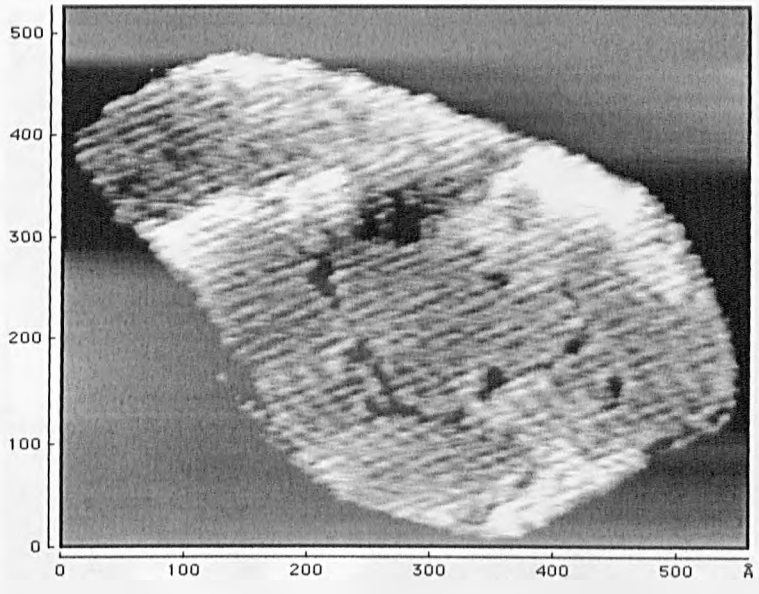

b)

Fig.6.14. a) A 3D image of 8ML of Dy on W(100) annealed to 820K. b) top of island after compensation for tilt and expanding the contrast. U=0.5 V, I=1 nA.

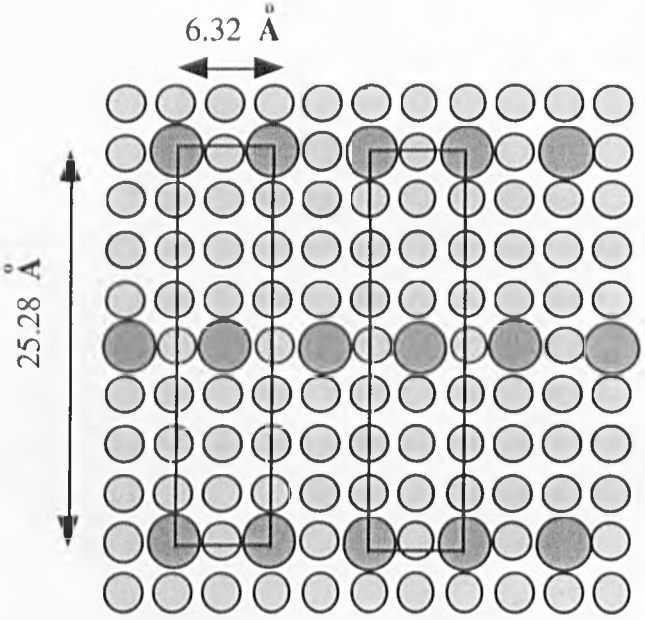

Fig.6.15. proposed model for c(8x2) describing atomic rows with distance of ~12.3 Å consistent with rows of Fig.6.14 (b). To make it more clear only atoms at top, bottom and middle of the lattice were shown and the registry of them have been chosen to be at top sites.

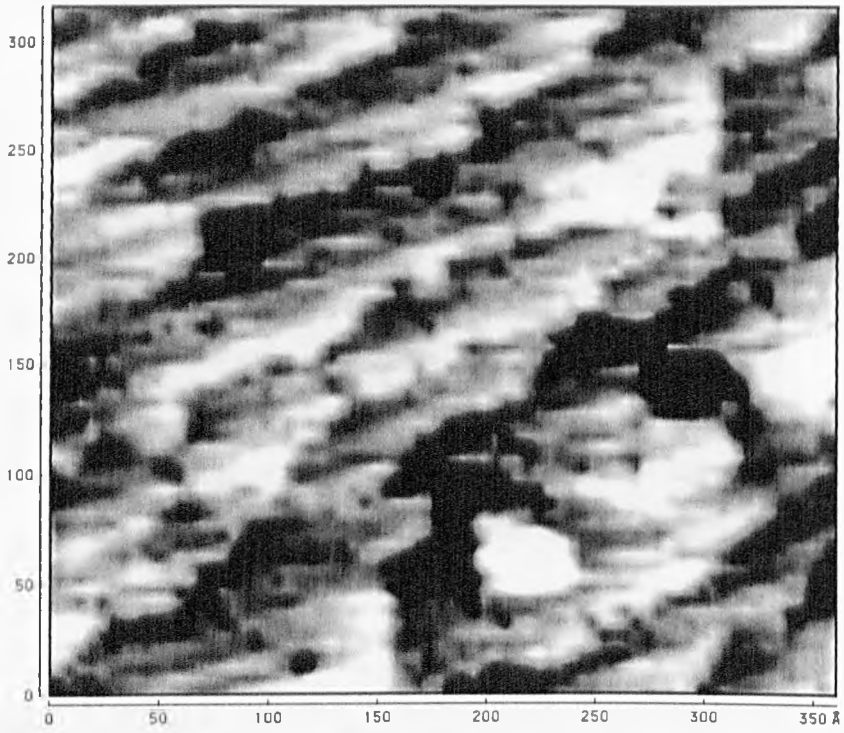

Fig.6.16. STM image from c(2x2) structure. Islands of c(8x2) structure are formed near the steps edges. U=-1 V, I=1 nA.

6.6. Clean W(112)

Fig.6.17 shows STM images of the clean W(112) at RT taken 30 minutes after a high temperature flash to 2500 K. The terraces had rather irregular step edges with average step heights of 1.3 Å. The average size of terraces was found to be ~72 Å. The average distance between atomic rows in Fig.6.17 (b) was found to be ~4.23 Å which is equal to interatomic distance along W[1 $\bar{1}$ 0]. Fig.6.17 (b) also shows that despite some defects on the surface, such as missing atoms and accumulation of atoms at step edge, the W(112) is clean and well ordered.

6.7. Dy/W(112)

6.7.1. Growth at RT

It has been shown in Chapter 4 that Dy follows a laminar growth, at least up to 2 ML, on W(112). To investigate this with STM, Dy has been grown at RT and scanned with STM. Fig.6.18 shows an STM image of Dy/W(112) system taken after growing 0.8 ML Dy at RT. The image shows that Dy grows with domains of atomic rows which are perpendicular to the atomic rows of W(112) in Fig.6.17, i. e. they are along W[1 $\bar{1}$ 0]. An average distance of ~7.0 Å was found between the rows.

Fig.6.19 shows an STM image of Dy/W(112) with ~1.4 ML Dy grown at RT. Step heights are 1.3 Å, the same as clean W(112), and the sizes of the terraces do not change on completion of the first ML. The surface is covered with chain–like atomic rows with irregular lengths and distances on top of the first ML of Dy. The rows are almost along W[1 1 $\bar{1}$].

Fig.6.20 shows STM images from two different areas on W(112) after deposition of ~5ML Dy at RT. In Fig.6.20(a) the steps edges are parallel with W(112) step edges while steps in the area of the Fig (b) are almost along W[11$\bar{1}$]. Fig (a) shows an area with step heights of ~1.3 Å which is same as for steps on W(112). However, the other area had steps with heights of ~2.7 Å. This is almost the same as the interlayer spacing of Dy(1000), 2.82 Å , and it is also twice the step heights of W(112). This can be interpreted either by assuming that the area in Fig.6.20(b) is covered with thick layers of Dy, forming hcp structure with inter layer spacing of ~2.8 Å, or by assuming that in this area W(112) had double–step terraces with a different edge direction than that of the area in Fig (a). The growth mode prediction for Dy on W(112), which has small deviations from layer–by–layer growth for coverages more than 2ML, indicates that the first assumption is more likely to happen.

6.7.2. Annealing to 500K

Fig.6.21 shows a STM image from Dy/W(112) with 5ML Dy grown at RT and annealed to 500K. It is clear from this image that by annealing to this temperature Dy films produced islands which are long and have a strip shape which are strained along W[11$\bar{1}$], in agreement with the appearance of streaks in W[1$\bar{1}$0] direction in the LEED pattern (see Chapter 5). The domains were monoatomic Dy layers with thickness of 2.8 Å and an average width of ~30 Å and separated by ~5 Å. Because of the overlap of islands it was not possible to measure their average length.

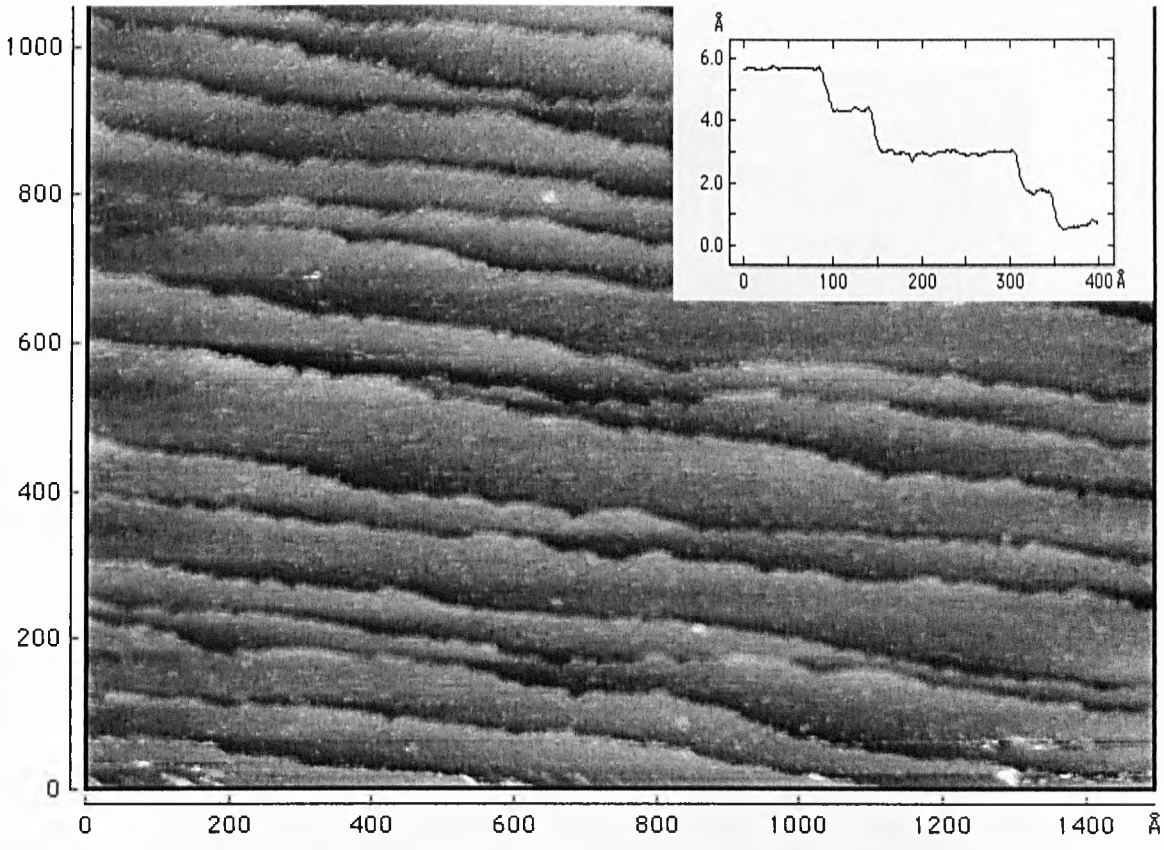

a)

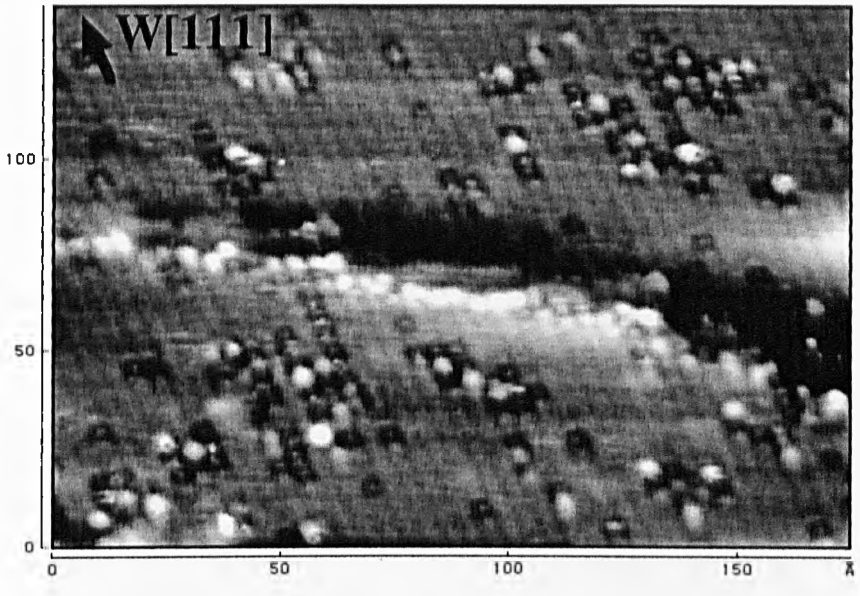

b)

Fig.6.17. a) STM image from clean W(112). The inset shows a series of profiles. b) An atomically resolved image of W(112) shows atomic rows along W[1 1 $\bar{1}$]. U=-1 V, I=2 nA.

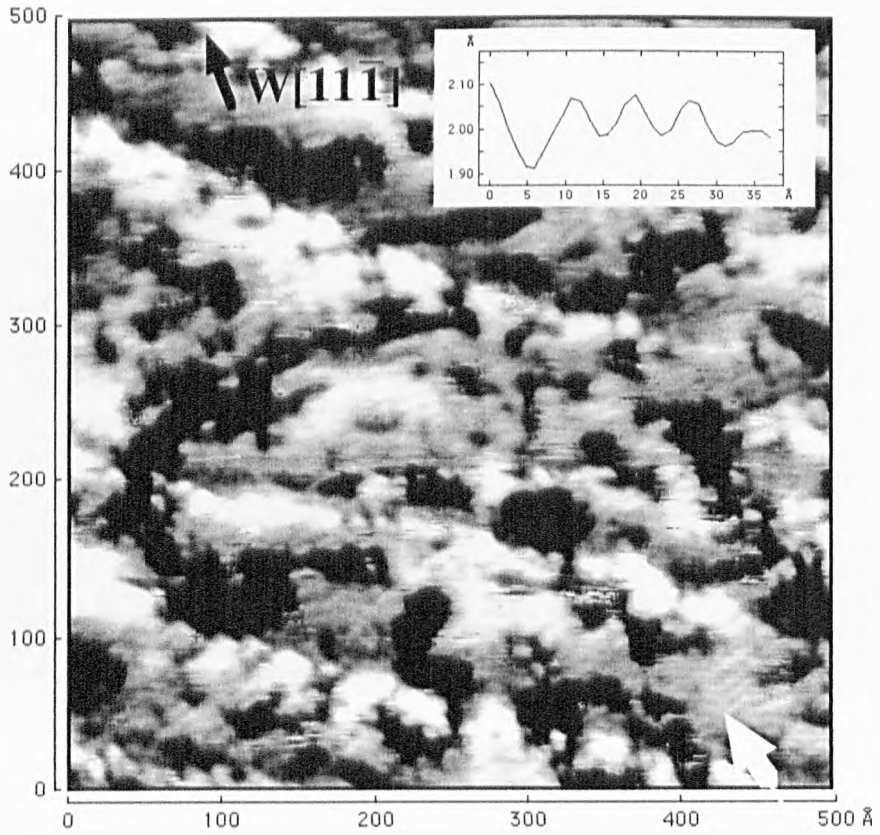

Fig.6.18. STM image from Dy/W(112) with 0.8 ML Dy grown at RT. U=-0.4V, I=1.5nA. The inset shows the vertical profile along the arrow.

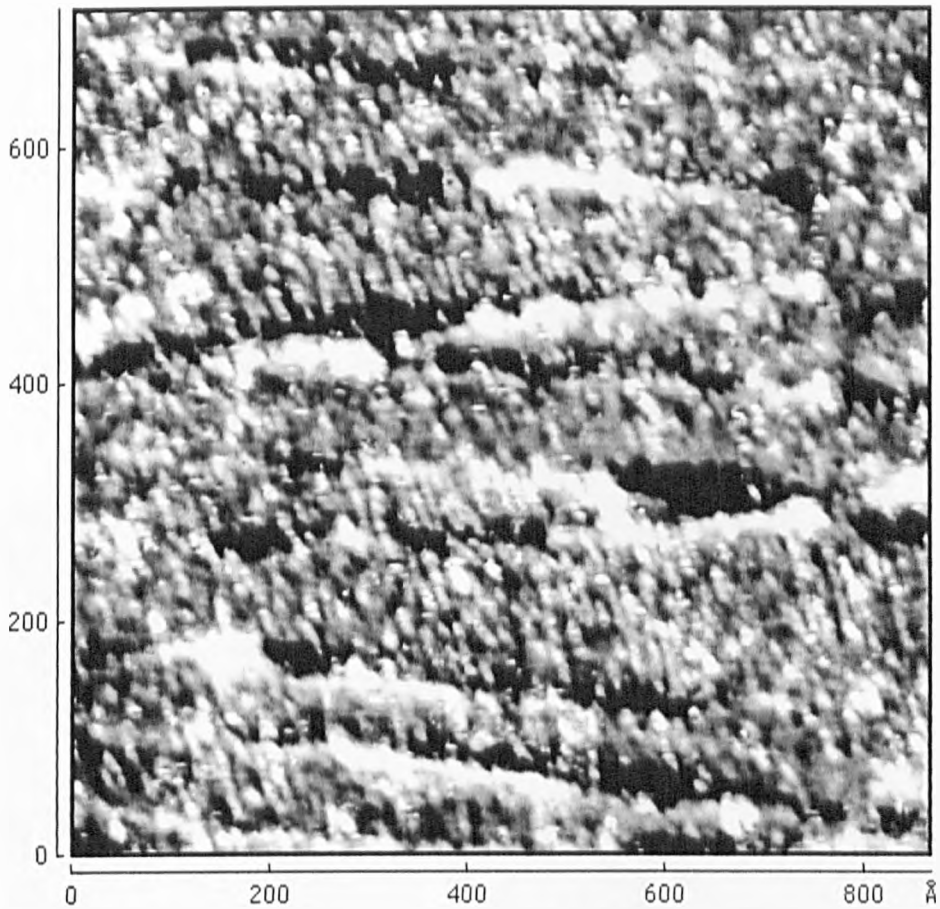

a)

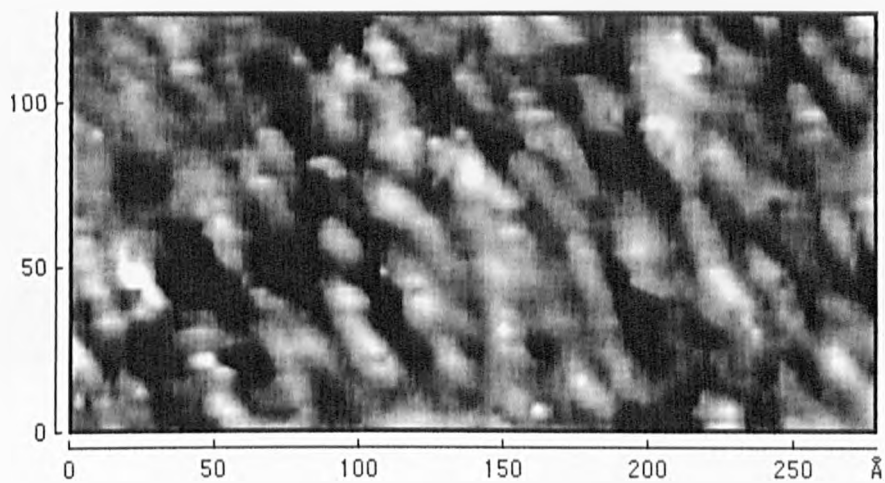

b)

Fig.6.19. a) STM image of Dy/W(112) with 1.5ML Dy grown at RT. b) a close up image of one of the terraces in Fig (a) shows atomic rows of Dy. U=-0.4 V, I=1.5 nA.

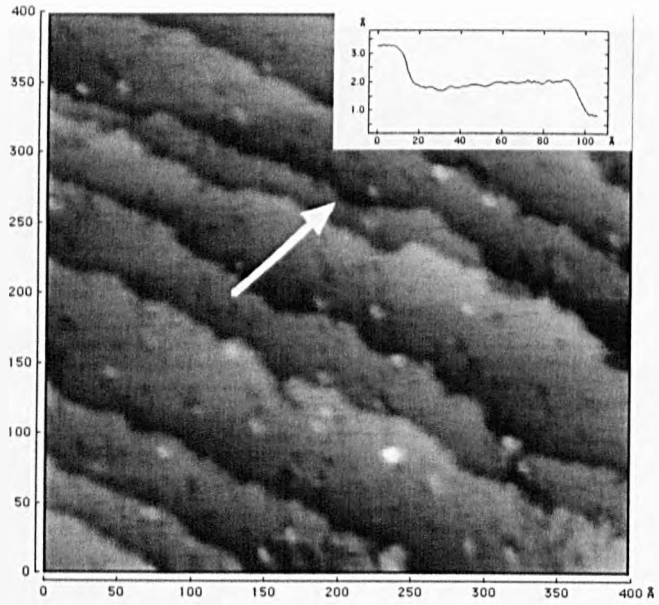

a)

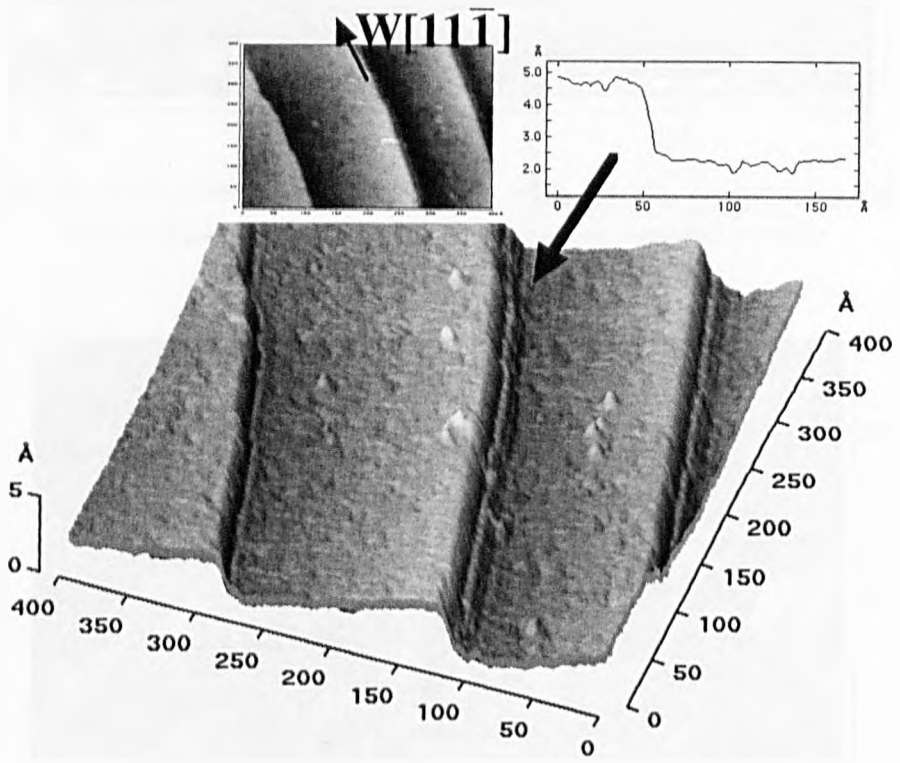

b)

Fig.6.20. STM image from Dy/W(112) with ~5ML Dy grown at RT. a) An area with single–atom step heights, b) a 3D image of an area with double step heights. The insets are profiles of the vertical changes across the indicated steps and a 2D image showing direction of steps edges in the Fig. (b). U=-1 V, I=1 nA.

6.7.3. Annealing to 1100K

By annealing to 1100K, the rough and stripe shape islands in Fig.6.21 formed flat domains which contained small stripes along W[11$\bar{1}$]. Fig.6.22 shows such an flat area

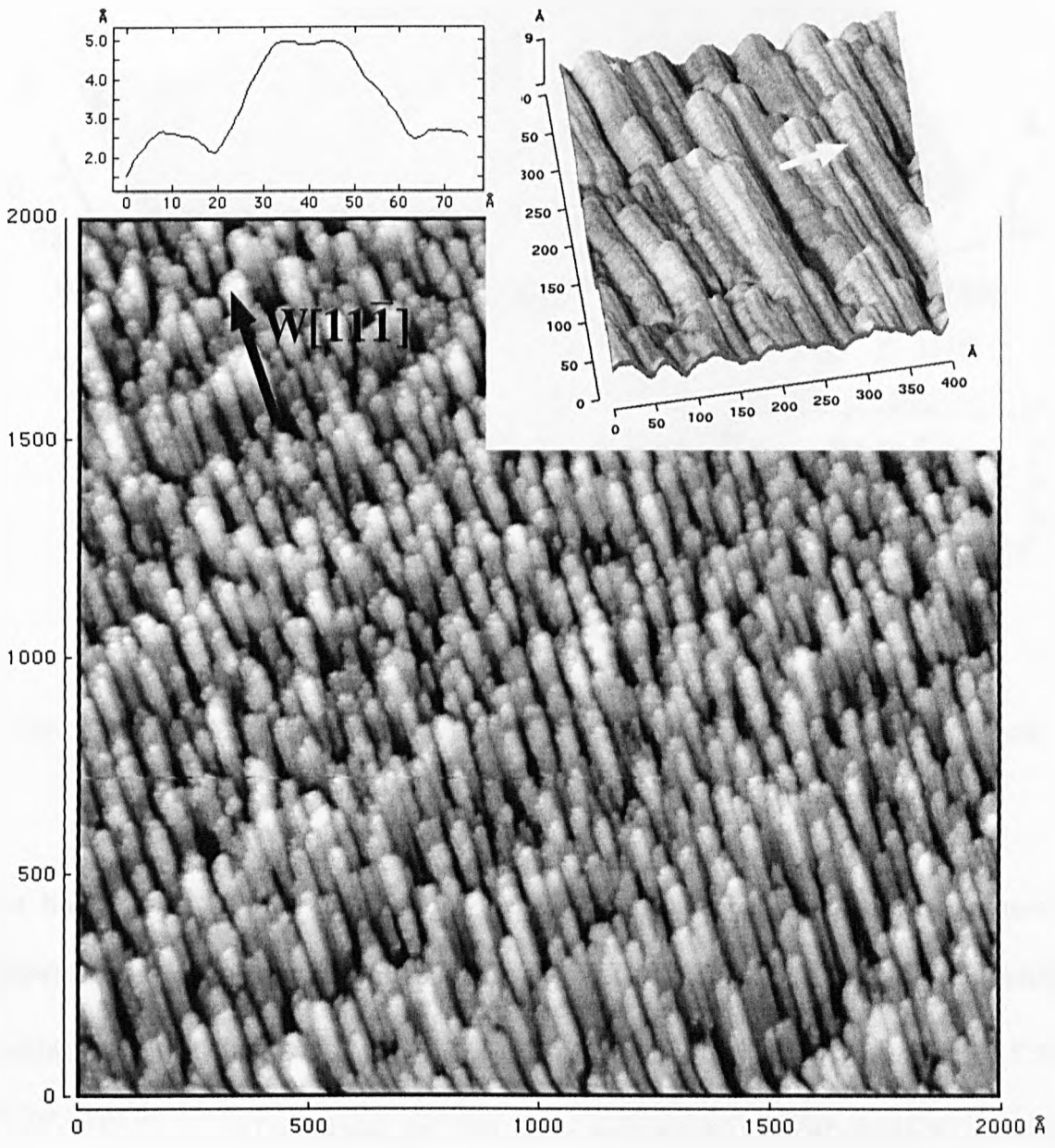

Fig.6.21. STM image from Dy/W(112) with 5ML Dy grown at RT and annealed to 500K. U=0.5V, I=1nA. The insets are (right) a 3D view of the image and (left) a profile of the vertical changes across a domain shown by the arrow in the 3D image.

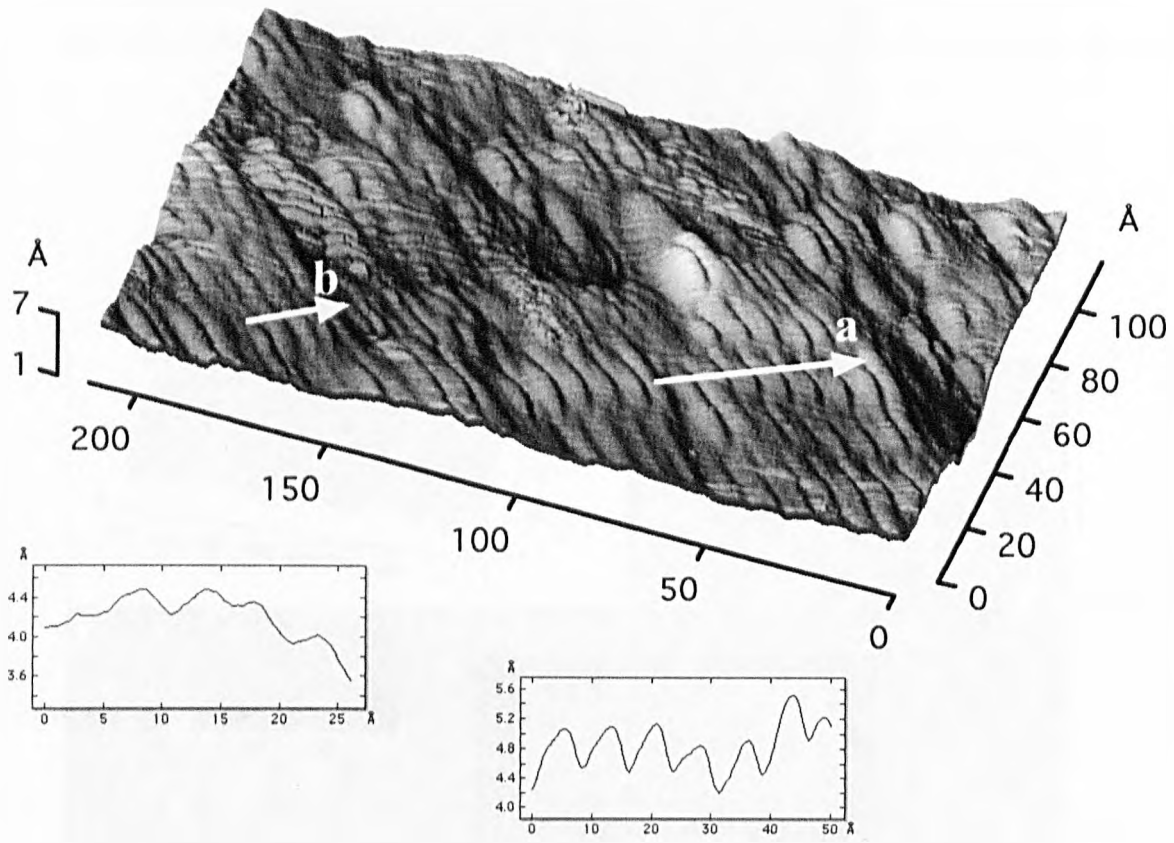

Fig.6.22. An STM image from Dy/W(112) with 5ML Dy annealed to 1200K. The insets show profiles of atomic rows along the arrows shown by (a) and (b). U=-0.1V, A=1. 0 nA.

contains narrow stripes. The distance between stripes along $W[1\bar{1}0]$ was found to be irregular. For example, while the distance between the stripes along arrow (a) was found to be ~8.7 Å, it was ~5 Å along arrow (b). This irregularity along $W[1\bar{1}0]$ is the reason for the appearance of streaks in the LEED pattern along $W[1\bar{1}0]$ (see Fig.5.15).

6.7.4. Annealing to 1500K

Fig.6.23 show an STM image of Dy/W(112) with 5ML Dy after annealing to 1500K. This picture shows that flat and large terraces have been produced by this annealing. Step

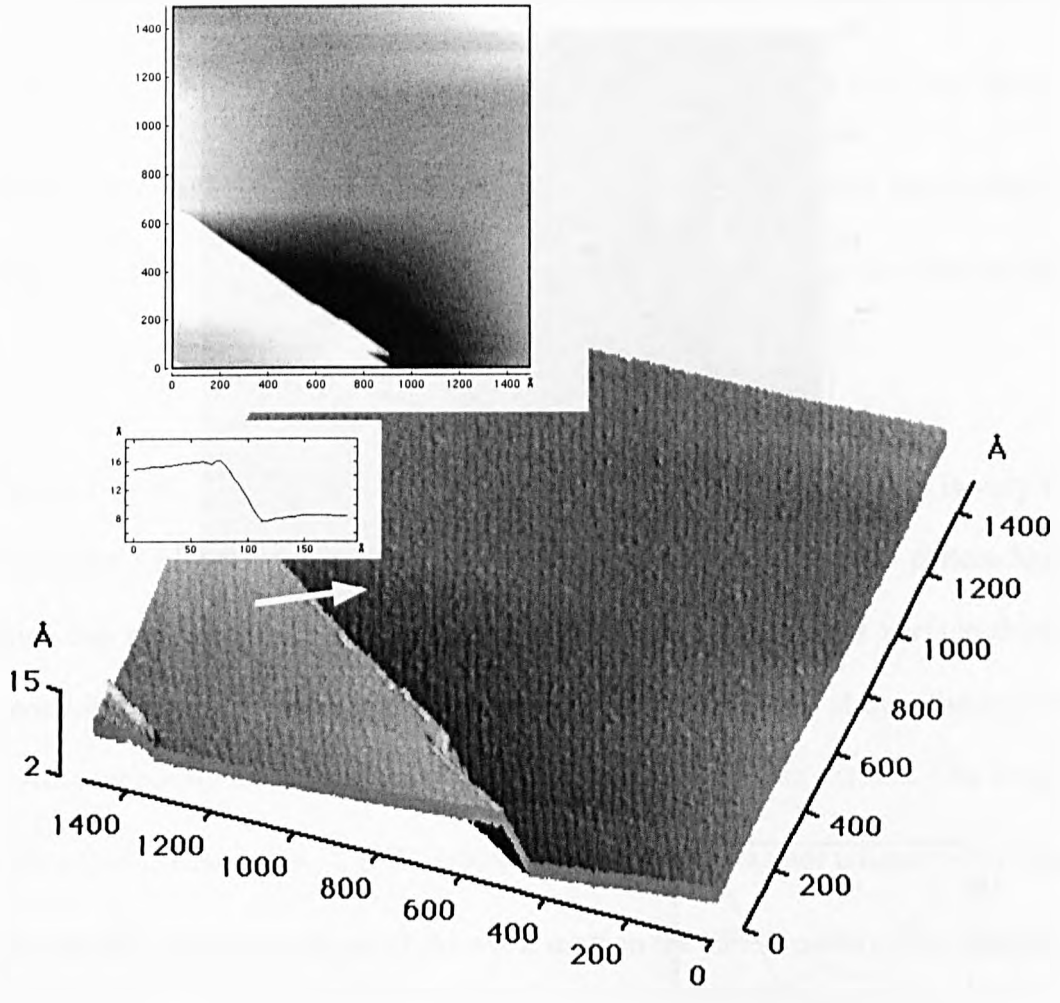

Fig.6.23. STM image from Dy/W(112) system with 5ML Dy annealed to 1500K. The insets are a 2D image for comparison of step edge direction with the directions of clean W(112) in Fig.6.17, and a profile of the step along the arrow shown in the picture. U=-0.2V, I=1 nA.

heights in this images are ~8.5 Å, which is three times the atomic layer distance of Dy(1000) in the hcp crystal. The steps edges had kinks, as shown in Fig.6.23, and made a ~45° angle with the steps direction of W(112). A close up view of this this terrace is shown in Fig.6.24. It is clear from this Figure that the surface is made from domains along W[11$\bar{1}$], giving a furrowed appearance. These domains contain atomic rows parallel to the steps in Fig.6.23. The domains have an average width of 31.7 Å and average distance of 6.6 Å. Therefore, atomic rows of the subsurface can be seen in the images. The height of these domains relative to the atomic row of

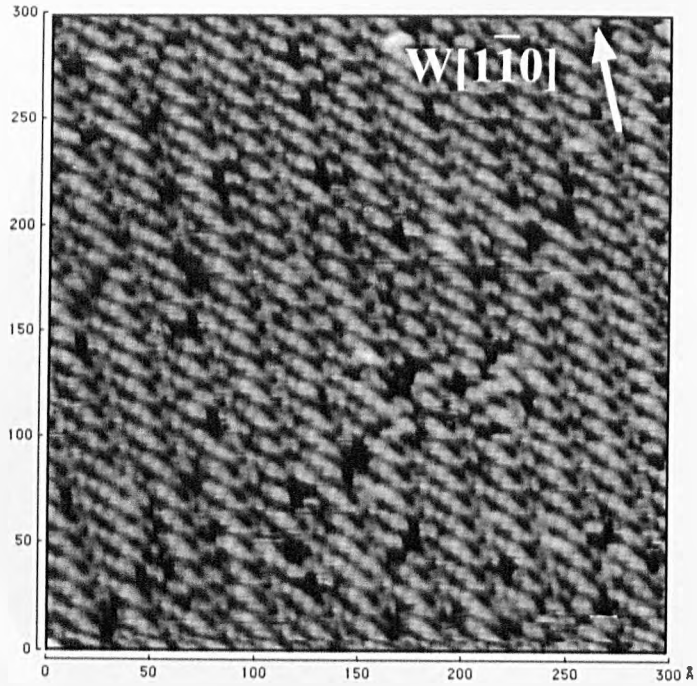

a)

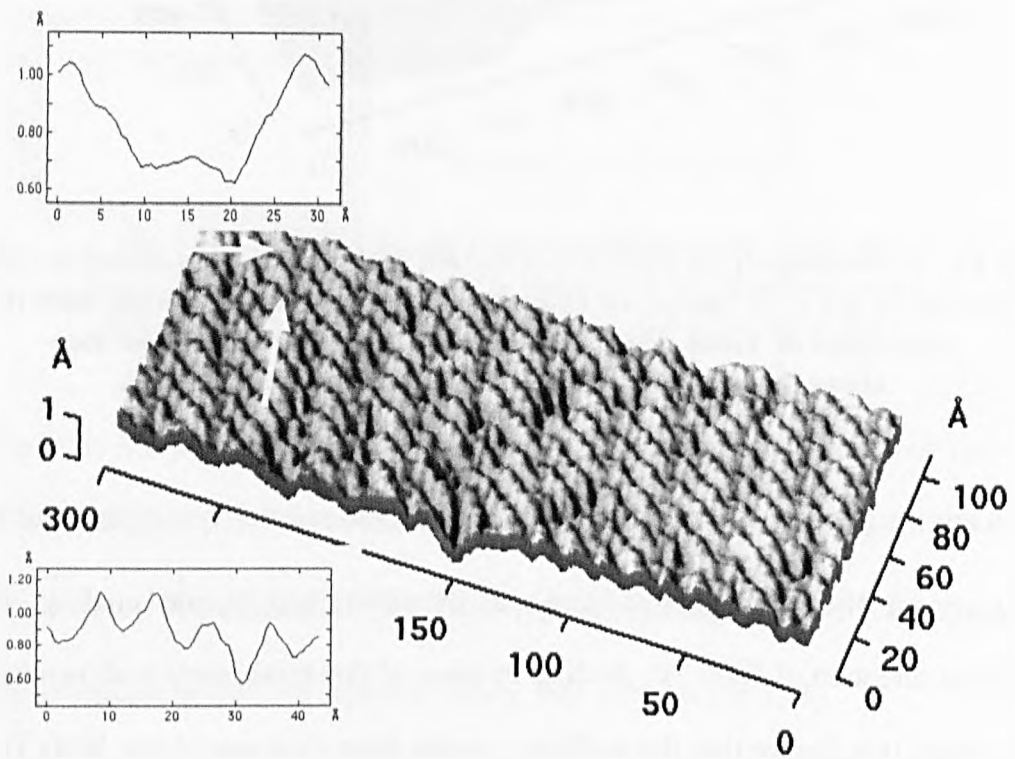

b)

Fig.6.24. a) A close up view of Fig.6.23, with atomic resolution. (b) 3D image of atomic structure on the surface of Fig (a). The insets are profiles of vertical changes between the furrows and across the atomic rows in the furrows, shown by the arrows.

the subsurface was found to be 0.35 Å. The distance between atomic rows across the domains is 9. 0 Å, while interatomic distance between atoms in each row was found to be 6.6 Å. Atomic rows are shifted along domain directions by ~5.5 Å from one domain to the other. This makes it look like the rows of one domain are in between the rows of the next domain.

An FFT of the atomic structure in Fig.6.24 is shown in Fig.6.25. This is very similar to the chain–like LEED pattern seen in Fig.5.16 (a). However, that LEED pattern had extra spots which can not be seen in this FFT. A search on other parts of the surface shows that though most of the surface was covered with the structure described above, there is another structure simultaneously on the surface. Fig.6.26 shows one of these regions. The step height between these two phases was ~2.8 Å. However, this height was not unique every where. It is possible that this area is the origin of the extra spots in the LEED pattern (Fig.5.16(a)).

6.7.5. Annealing to 1600K

By increasing temperature of annealing to 1600 K all of the surface has been covered with the structure shown in Fig.6.27. Though the atomic structure of this phase seems very similar to that of the second phase found after annealing to 1500K, the step edges are completely different. Here steps are almost along W[1 $\bar{1}$ 0] with teeth–like edges. The edges of these teeth are sharp with average angle of 66° and pointed toward W[11 $\bar{1}$]. The average size of terraces was ~200 Å and the average step height was 5.6 Å (double steps). At the edges of the teeth there were domains of atomic rows parallel to the edges with average width of ~20 Å and average height of ~1.3 Å, the same as the step height of W(112). Fig.6.28 shows

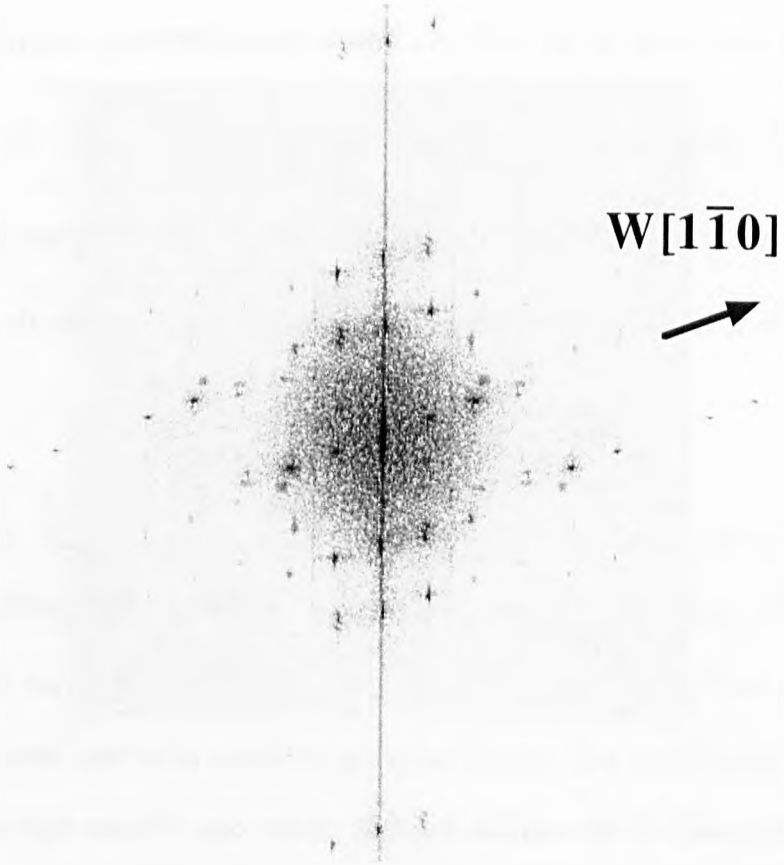

Fig.6.25. FFT of atomic structure shown in Fig.6.24.

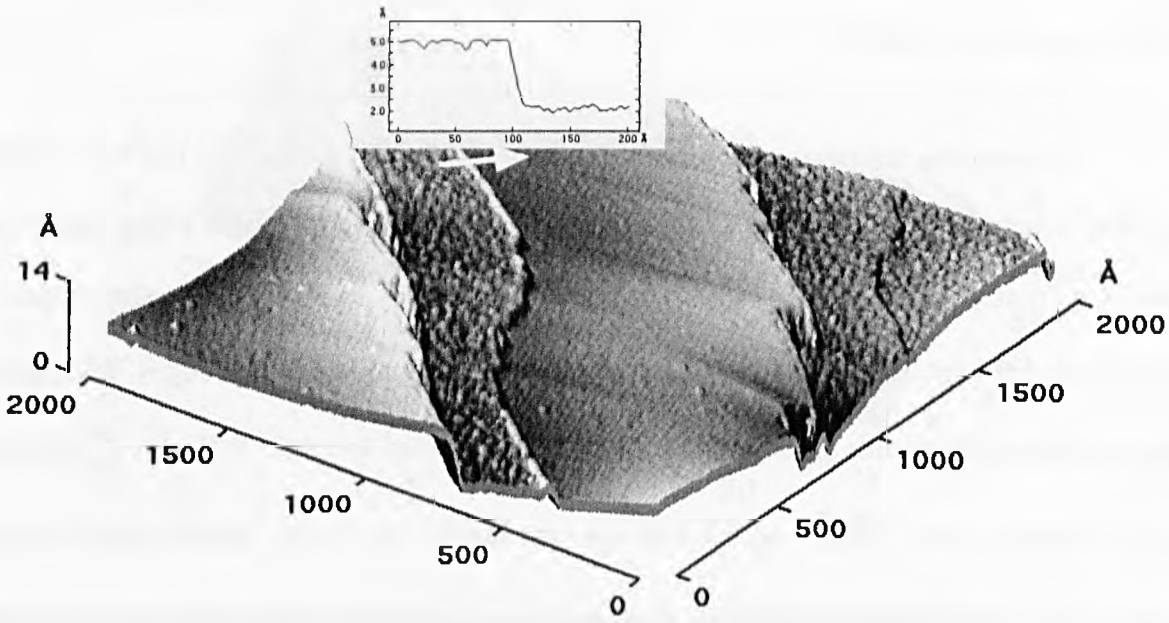

Fig.6.26. STM image from Dy/W(112) system with 5ML Dy annealed to 1500K. Two different phases of Dy can be seen on the surface. The inset shows a profile of vertical change across the step shown by arrow, between the two structures. U=-0.2 V, I=1 nA.

a close up view of one of the terraces of the Fig.6.28. It is clear that despite some defects (likely to be contamination) shown by bright blobs, the surface contains atomic rows which are approximately 6 Å wide and separated by 3 Å. It is possible to see that some atomic rows are almost parallel and some are perpendicular to W[11$\bar{1}$].

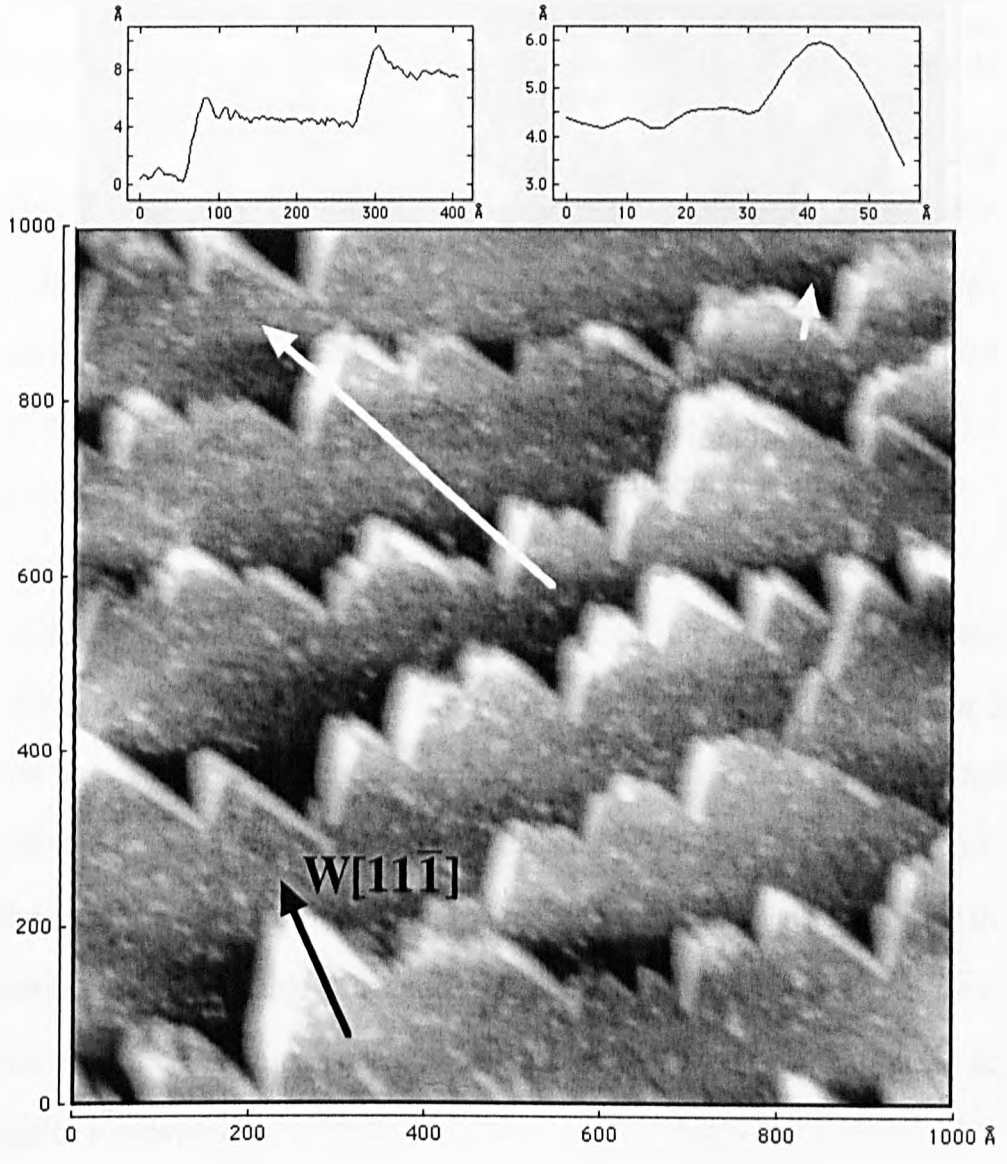

Fig.6.27. STM image from Dy/W(112) system with 5ML Dy annealed to 1600K. The insets are profiles of the steps along the lines indicated. U=-1 V, I=1.4 nA.

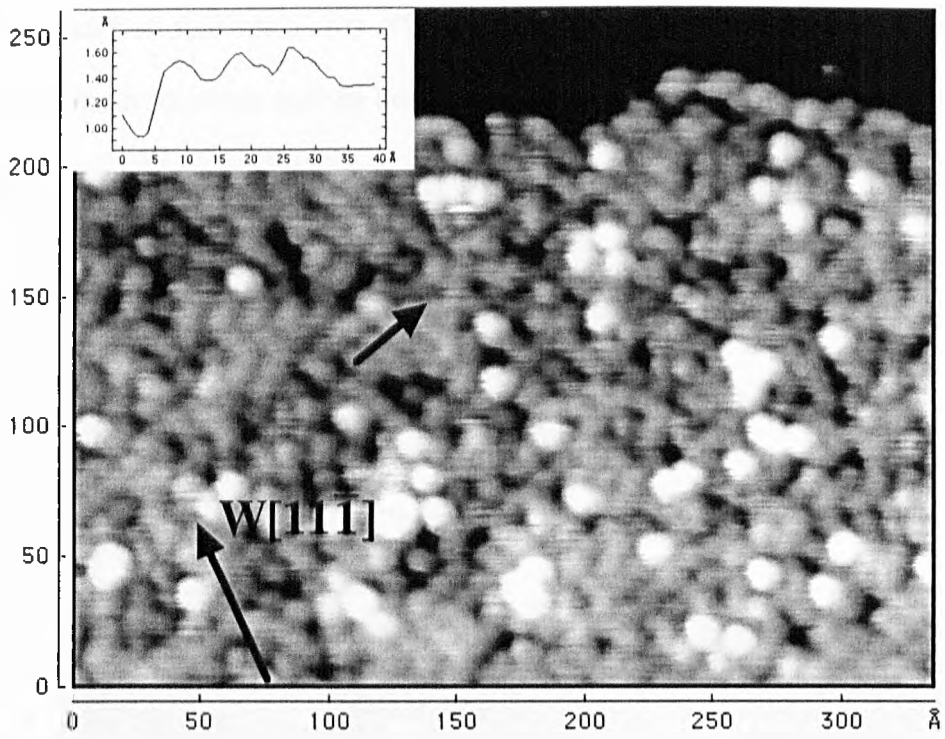

Fig.6.28. A close up view of one of the terraces of Fig.6.27. The inset is a profile of atomic rows along the arrow. U=-0.2 V, I=1.5 nA.

Chapter 7

Theory of the surface core–level shift

7. 1. Introduction

The core electrons were considered for many years uninteresting to chemists and physicists because they do not participate in the chemical bonding. With the advent of high resolution photoelectron spectrometers this belief was discarded especially after discovery by Hangstrom et al [162] that the binding energies of core levels are dependent on their chemical environment. This phenomena was first confirmed experimentally by Citrin et al in 1978 [52] for both noble metals and transition metals and was quickly followed by a series of other publications. Indeed, we presently know that the core levels are strongly modified by the valence electron distribution and their shifts in energy (called "chemical shifts") now form a most powerful tool applicable in many areas of research [163].

A fundamental kind of chemical shift is that occurring between the free atom and the atom in the solid. For an elemental solid it was recognised long ago [164] that the surface atoms must have a lower coordination number than their bulk counterparts. The result will be redistribution of the valence charge density at the surface which will be reflected in a chemical shift of the surface atoms core-level with reference to the bulk levels. It was for the 4f levels of tungsten that distinguishable bulk and surface contributions were first seen for a core level [165]. However, the charge transfer at the surface is much weaker than those occurring in compounds or overlayers.

It is now well understood that Surface Core–Level Shift (SCLS) spectroscopy can provide detailed information, not only concerning the adsorbate concentration profile, but also on the geometric and chemical nature of the interface and adsorbate layer. It is also well

established that the following criteria are essential for any observation and measurement of the SCLS.

a) The suitability of a particular core level for a SCLS monitoring: This is determined by its core hole binding energy and lifetime.

a–i) Core hole–binding energy: Shallow core levels that have significant overlap with neighbouring atom sites will exhibit band effects. This will become influential in photoemission if different regions of k–space are probed – i. e. when the emission angle or photon energy is varied. Therefore, these core levels are unsuitable because changes in binding energy or lineshape as a result of band effects might be misinterpreted as being due to a SCLS effect. It is, therefore preferable to study deep localised core levels.

a-ii) Core–hole lifetime: The core–level lifetime should be as long as possible so that the final state lifetime broadening is minimised. This criterion makes shallower core levels more suitable because the core hole decay process is predominantly via Auger transitions where Coster-Kronig transitions play an important role in the decay mechanism. The best core levels to study are those with largest orbital angular momentum number, *l*, for a given principal shell number. Therefore, core levels such as the 1s, 2p, 3d and 4f which do not de–excite via the fast Coster-Kronig processes are most suitable.

With these considerations, it can be seen that the localised W 4f level with an intrinsic lifetime broadening of about 60 (80) meV for bulk (surface) atoms [166] is an ideal candidate for an SCLS experiment.

b) Surface sensitivity: Surface sensitivity must be enhanced to ensure a surface signal large enough to be distinguished from the intense bulk signal. There have been many SCLS studies

using Mg and Al anode X-ray sources. However, the use of a tunable radiation source, such as a synchrotron, provides a means for selecting the kinetic energy of the photoemitted electrons from the desired core level to minimise their escape depth and, thereby, optimise the surface sensitivity of the experiment.

c) High energy resolution: This is essential in order to detect peak shifts of typically ~ 0.5 eV

d) Surface cleanliness: The surface must kept clean due to the large magnitude of impurity–induced chemical core–level shifts (> 1 eV). This is particularly important due to the enhancement of the surface sensitivity.

7. 2.The theoretical origin of Surface Core–Level Shift

7. 2.1. SCLS from Electronic Structure point of view (Band Approach)

This model was first described in reference [52] and developed more extensively later by many authors [61, 165, 167, 168]. To explain this model we will consider a typical band structure picture of a transition metal as having deep lying core levels and a hypothetical band structure which we will consider to be correspond only to the d-electrons, due to their predominance in bonding. The reduced number of bonds at the surface (due to reduced effective atomic coordination compared to the bulk) causes a narrowing of the surface density of states. The effect of this, in the case where there is a more than half filled d band is to bring unoccupied surface bands below the Fermi level which is pinned by the bulk (Fig. 7. 1). There is then charge transfer from the bulk states to these unoccupied surface bands. The amount of charge transfer involved is small enough to maintain layerwise charge neutrality [169, 170]. However, the resultant Coulomb potential raises the energy of the surface d-bands, i.e. causes

a shift in the centre of gravity of the surface density of states, and at the same time raises the energy of the surface core levels by a comparable amount. Thus the surface–atom core levels exhibit lower binding energies with respect to the Fermi levels than the core level of the bulk atoms.

In cases where there is a less than half-filled d-band the narrowing of the surface density of states results in occupied surface bands being raised above the Fermi level, in which case there is charge transfer in the opposite direction. An accompanying displacement of the centre of gravity of the surface d-band, and hence the core levels, is in the opposite sense to that described above.

It is now clear that according to this model there is a change of sign of SCLS in moving across the transition metal series from $n_d < 5$ to $n_d > 5$ and there should be zero shift for the case where the d-band is exactly half filled. In fact due to the often complex asymmetrical nature of the surface d-band, the change of sign occurs between Ta and W where the respective configurations are equivalent to $5d^{3.4}$ and $5d^{4.6}$. This has been confirmed experimentally (Fig. 7. 2) [171].

In this model the core levels rigidly follow the displacement of the valence d-band caused by the presence of the surface, such that

$$\Delta^{SB} \approx -1.1(E_d^S - E_d^B) \qquad (7.1)$$

where Δ^{SB} is the difference between surface and bulk core–level binding energy and $E_d^{B(S)}$ is the centre of gravity of the local d-band for the bulk (surface). The coefficient of -1.1 is predicted via a self-consistent renormalisation model due to Williams and Gelatt [172] that estimated that the core level shift is 10% more than the shift in the valence band.

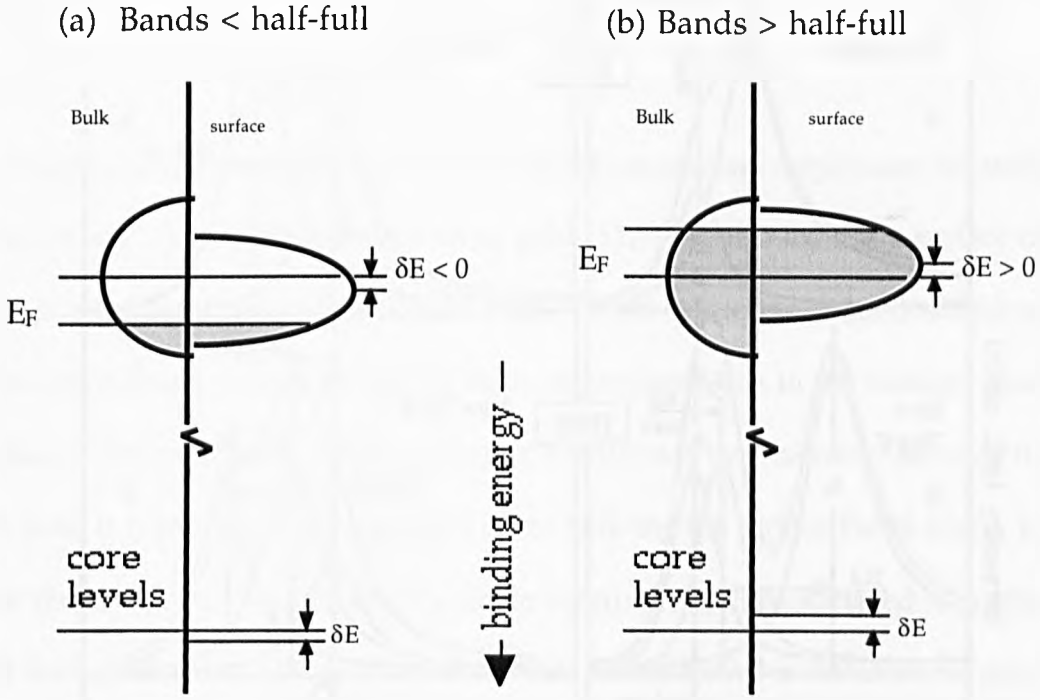

Fig. 7.1. Schematic of origin of SCLS in transition metals caused by the narrowing of the surface DOS result from reduced effective coordination . a) for n_d <5, the unoccupied surface band falling below the Fermi level therefore charge is transferred from the bulk states to unoccupied surface bands. b) for n_d >5, the occupied surface band rising above the Fermi level therefore charge is transferred from occupied surface bands to the bulk

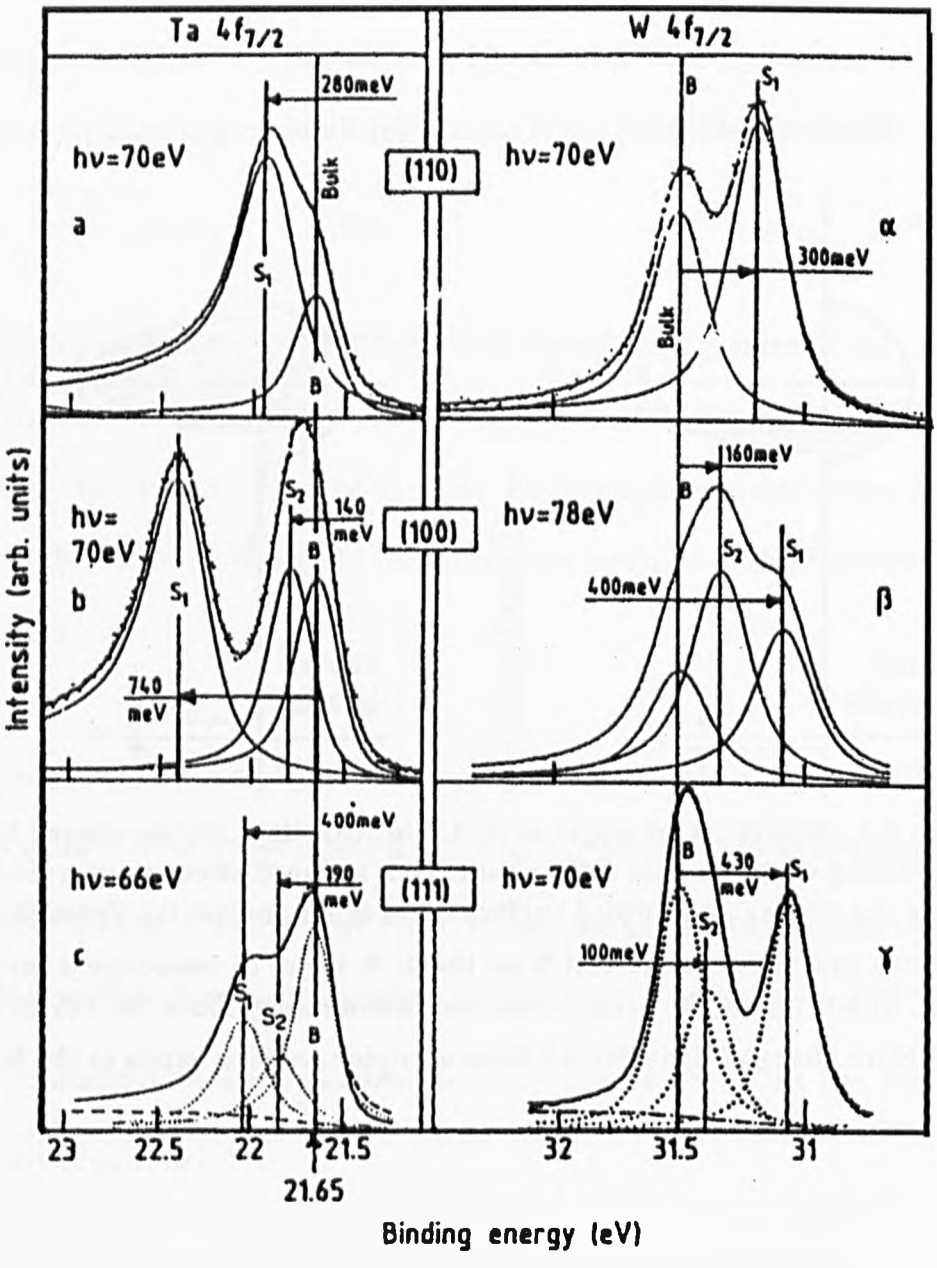

Fig. 7. 2. A compilation of SCLS results from different single crystal faces of Ta and W . Adapted from Ref [171].

This model is not only consistent with the change of sign observed experimentally between Ta and W (Fig. 7. 2) [171], but also produces a greater shift for more open surfaces where the effective coordination of the surface atom is reduced. This effect stems from the increased narrowing of the surface density of states caused by reduction in bonding, resulting in a greater overlap of the unfilled surface (bulk) bands with the filled bulk (surface) bands.

As it has been pointed out previously [171, 173], this viewpoint is weighted purely on

the side of initial-state causes of the surface core–level shift (see next section), relying on the change in the charge density prior to the formation of the core hole. The effect of final state in this model is to modify the magnitude of the shift observed.

For completeness it may be useful to describe the mechanism responsible for shifts in non-transition metals. The noble metals such as gold [52, 174] also exhibit a surface core–level shift despite having a completely filled d-band. To put it into the same descriptive terms as the above model, the surface density of states is narrowed due to the reduced coordination. The effect of this narrowing, where no charge transfer has been allowed between the surface and the bulk, is to produce a misalignment of the bulk and the surface Fermi levels. In the case of noble metals the only way in which a single Fermi level can be achieved is to allow charge transfer from the bulk into the surface bands. This causes a shift in the centre of gravity of the surface density of states and the associated core–level binding energies to lower values.

7. 2. 2. Initial state–Final state approach

According to the Williams and Long model [175], to evaluate the core level shift of an atom moved from a free state to the solid environment the shift can be divided into three main components:

1. Configurational change. This is due to the redistribution of electrons between s, p, d and f states in the free atom relative to the atoms in the solid environment.

2. Chemical shift. This is the degree of the core–level displacement due to change in the chemical environment before removal of an electron.

The above components are initial–state contributions. They will change the initial state

charge density on an atom that will directly change the potential in the core of the atom, thereby shifting the core–level binding energy.

3. Relaxation shift. This contains the final–state effects of the core hole on the observed core–level binding energy, i. e. the effects of screening the resultant core–hole positive charge.

Therefore the total shift can be written as

$$\Delta = \Delta_{config} + \Delta_{chem} + \Delta_{relax} \qquad (7.2)$$

7. 2. 2.1. Initial state contribution

Describing the core–level eigenvalue shift as being a direct quantitative measure of the initial–state charge density difference due to configurational and chemical environment change is natural, but somewhat arbitrary [176].

To emphasise this, consider core orbitals so deep that they lie (in space) entirely inside the valence electrons. The valence electrons are assumed to be responsible for any changes in the charge density of the atom from one chemical environment to another. In this context, a core energy eigenvalue for any atom will shift, from one environment to another, by an amount

$$\Delta E_i = \Delta \sum_j \left(\left\langle \frac{e^2}{r} \right\rangle_j + \left[\text{exchange terms} \right]_{ij} \right) \qquad (7.3)$$

which is just the sum of the changes occurring in the Coulomb and exchange terms of the normal one–electron Hamiltonian. Equation (7. 3) indicates that for a particular core-level, i, the shift in its core eigenvalue is governed by the sum, over all the valence electrons, *j*, of the changes in the Coulomb and exchange integrals between the core and valence electrons. For

cases in which the exchange terms are small (which is common) the eigenvalue shift is just a direct measure of the change in the value of the electrostatic Coulomb potential measured inside the valence electrons, i.e. a 1 eV potential shift will produce a 1 eV eigenvalue shift.

The core–level eigenvalue shift will follow directly that of the valence levels. This phenomenon can readily be understood by noting the classical electrostatic analogy of a potential inside a uniformly charged sphere [177]. If the valence d-orbitals are approximated by a spherical shell of radius R, then the distribution of charge will produce a constant Hartree potential energy inside the sphere given by

$$V_c = e^2 \frac{n_d}{R} \qquad (7.4)$$

where n_d is the number of valence d electrons. When n_d varies by Δn_d the variation of this Hartree potential is simply

$$\Delta V_c = e^2 \frac{\Delta n_d}{R} \qquad (7.5)$$

and therefore all the core levels are shifted by this quantity. If we make this simple model more sophisticated by straddling orbitals around the radius R, it is expected that the deeper core–levels will experience the larger shift. This has been supported by a self-consistent renormalised–atom model due to Williams and Gelatt [172] that estimated that the increase in the shifts of the core levels relative to the shifts of the valence d levels is 10%.

There is a qualification to this simplistic model. The classical picture does not hold very well for shallow core–levels, i.e. when the radial extents of the core–levels and valence levels are similar. These core levels will only experience part of the electrostatic effect caused by the

valence charge change, e.g. in Ni or Cu the 3s and 3p orbitals are only partly inside the valence 3d orbitals and thus experience less repulsion than the deeper core levels. Thus, in general, the magnitude of the initial-state contribution for shallow level is reduced [178].

7. 2. 2. 2. Final state contribution

The final state contribution to the SCLS is assumed to consist of everything that can not be accounted for by initial–state effects. In practice the final-state contribution consist only of the difference in core–hole screening between the surface and the bulk, i.e. the relaxation energy difference.

While the model of Williams and Long [175] refers to free atoms and solids, Spanjaard [171] and Desjonqueres et al [167] have extended this approach to surface and bulk atoms, i.e. the SCLS in transition metals. However, they do not include any final-state relaxation contributions, because they proposed that the screening is not modified when moving from the bulk to the surface. Although the relaxation energy is expected to be small compared to the initial–state energy shift, it is thought to play a significant role in explaining the magnitudes of the SCLS. Indeed it has become a convenient term used in the literature to account for discrepancies between theory and the experiment.

Screening may be either intra-atomic or extra-atomic. This breakdown is particularly useful, since for an elementary treatment the intra-atomic part is assumed to be independent of chemical environment and negligible in calculating the SCLS (see for example, Ref. [179]). This assumption is a good approximation as long as there is no change of the ground state valence configuration at the surface. However, if a valence band change at the surface occurs, neglecting this approximation can cause serious errors [172].

Differences in the extra-atomic screening between the surface and the bulk produce the final–state contribution to the SCLS. It is reasonable to think that the reduced coordination at the surface would always reduce the number of extra-atomic electrons available to flow onto the ionised atom and screen the final-state core hole. The screening term would always act so as to reduce the core–level binding energies , i. e. screening always make the SCLS more positive.

7. 2. 3. The Thermodynamic Approach

Johansson and Mårtensson [37] introduced a thermodynamical model based on a total–energy difference concept. This begins with a description of the free–atom to bulk–atom binding energy difference, expressing the SCLS as being the sum of various empirical quantities in the form of Born–Haber cycle. This approach does not attempt to separate initial–state and final–state contributions, but instead considers the change in total energy upon creation of a hole in the bulk or at the surface.

Here the shift in core level energy of an atom on moving from the free to the metallic state is defined as:

$$\Delta E_c = E_c^A - E_{c,F}^M \qquad (7.6)$$

Where E_c^A is the atomic binding energy of the core level in the free state and $E_{c,F}^M$ is the binding energy of the core level in the metallic state relative to Fermi level. The main axis of this approach lies in a Born-Haber cycle which break down the complex single–step determination of $E_{c,F}^M$ into a series of readily accessible parameters. Figure (7. 3) shows the Born-Haber cycle presented by Johansson and Mårtensson, in which:

E_{coh}^{Z} is the cohesive energy, i.e. the energy required to remove a single atom from the metal (atomic number Z) and arrive at the free atom state.

E_{c}^{A} is the energy required to core–ionise the free atom.

I^{Z^*} is the ionisation energy released when the core–ionised Z^* species is neutralised by acquisition of an electron into the valence shell of the Z^* atom.

$E_{coh}^{Z^*}$ is the cohesive energy released on bringing a Z^* atom to a Z^* solid.

$E_{Z^*}^{imp}(Z)$ is the energy involved in changing all Z^* atoms but one (in a Z^* solid) to Z type atom producing a Z metal with a Z^* atom as an impurity.

However, as thermodynamical data is not available directly for such a species as Z^*, the presence of these related terms in the cycle may appear initially to hinder the calculation process. However, there are two important assumptions to be made in this model. Firstly, the core–ionised Z atom shown as Z^*, can be approximated by a valence–ionised (Z+1) atom, as shown in Fig.7.3(b). In this manner a core with one electron removed from a deep–lying shell can be replaced quite accurately by the core of the (Z+1) atom. This has become widely known as the *(Z+1) approximation* (similar to the excited–atom model used by Williams and Long [175]). The neutralisation of this state yields the ionisation energy $I_{(Z)}^{Z+1}$. The second assumption is that the final state is considered as a fully screened Z+1 impurity site in an otherwise perfect metal. In this way the following expression for $E_{c,F}^{M}$ may be constructed;

$$E_{c,F}^{M} = E_{coh}^{Z} + E_{c}^{A} - I_{(Z)}^{Z+1} - E_{coh}^{Z+1} + E_{Z+1}^{imp}(Z) \qquad (7.7)$$

Therefore the shift in core–level binding energy on moving from the free state to the metal

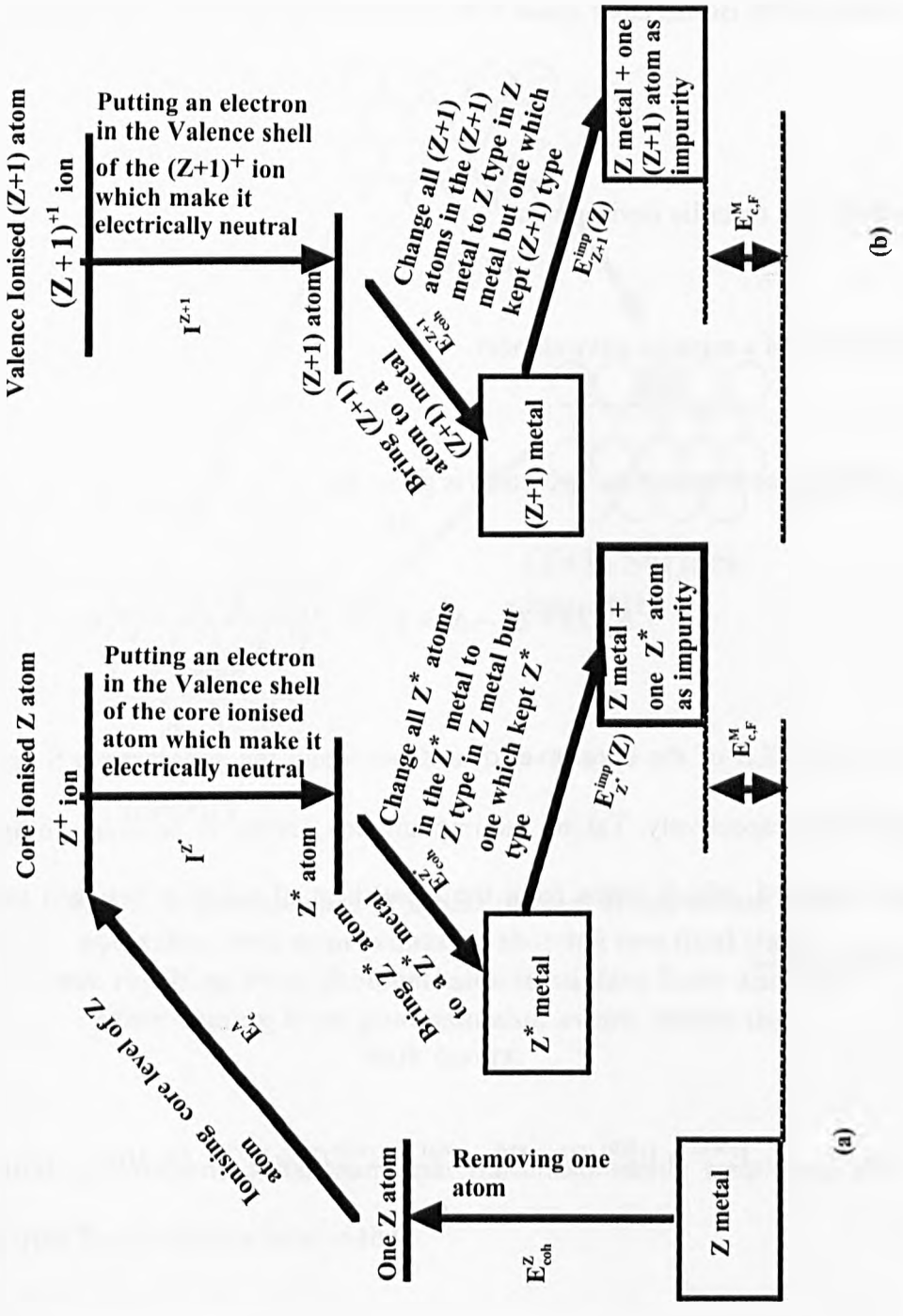

Fig 7. 3. (a) Born-Haber cycle produced by Johansson and Martenson used to determined free–atom to solid CLS from empirical quantities via calculation of $E^{M}_{c,F}$. (b) Z+1 approximation used to eliminate the Z^* from the calculations in Born-Haber cycle.

environment is given by;

$$\Delta E_c = I^{Z+1}_{(Z)} + E^{Z+1}_{coh} - E^{Z}_{coh} - E^{imp}_{Z+1}(Z) \qquad (7.8)$$

With modification, this cycle can be applied to the observation of surface CLS [180]. Fig (7. 4) shows a simplified Born-Haber cycle with two possible paths for the initial free atom to take

1. To the bulk of a metallic environment.

2. To the surface of a metallic environment.

The energy difference between the two paths is given by

$$\Delta_c(Z) = \Delta_c^S - \Delta_c^B = E_{c,F}^S - E_{c,F}^B \qquad (7.9)$$

Where $\Delta_c(Z)$ is SCLS of the core level of a Z atom and the superscripts S and B denote surface and bulk, respectively. Taking the implantation energy to be small compared to the other terms involved, which stems from the small heat of solution between neighbouring elements, this gives us

$$E_{c,F}^{S(B)} = E_{coh}^{S(B)}(Z) + E_c^A - I_{(Z)}^{Z+1} - E_{coh}^{S(B)}(Z+1) \qquad (7.10)$$

and so

$$\Delta_c(Z) = E_s(Z+1) - E_s(Z) \qquad (7.11)$$

where E_s is the surface energy defined as

$$E_S = E_{coh}^B - E_{coh}^S \qquad (7.12)$$

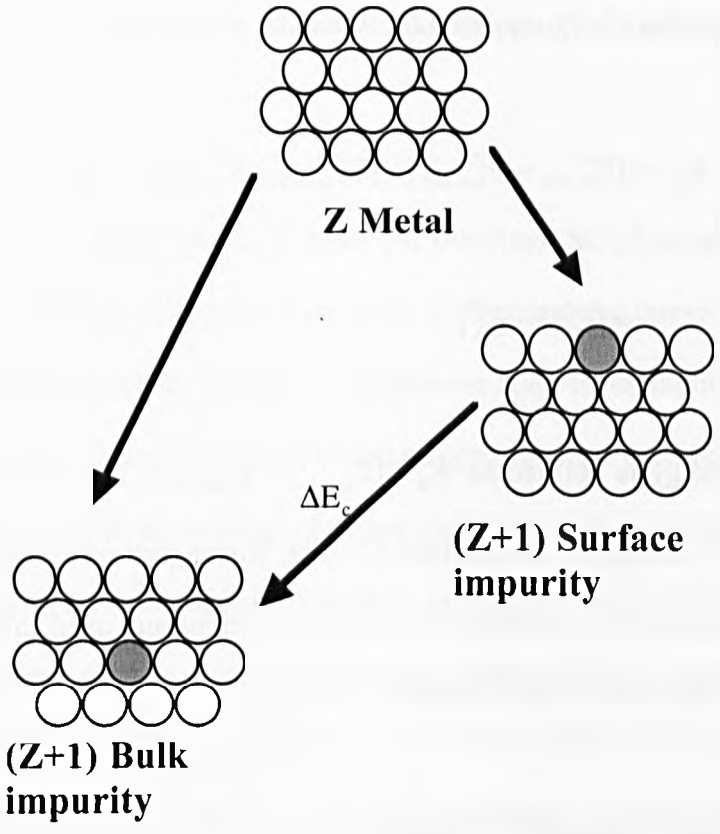

Fig. 7. 4. Relationship of initial to final states within the equivalent core approximation showing two final states one resulting from photoemission in surface layer and the other coming from photoemission events within the bulk layers.

In their initial calculations Johansson and Mårtensson have employed the empirical relationship from liquid–surface tension that

$$E_{coh}^{S} = 0.8E_{coh}^{B} \qquad (7.\ 13)$$

So the expression for the surface CLS of a Z metal further simplifies to become

$$\Delta_c = 0.2(E_{coh}^{Z+1} - E_{coh}^{Z}) \qquad (7.\ 14)$$

Since the cohesive energy model does not depend on surface structure, the model was extended [180] by dropping the assumption made in equation (7. 13). By neglecting the impurity terms in equation (7. 7), equation (7. 9) can be written as

$$\Delta_C = [E^{Z+1}_{coh,surf} - E^{Z}_{coh,surf}] - [E^{Z+1}_{coh,bulk} - E^{Z}_{coh,bulk}] \quad (7.\ 15)$$

$$= [E^{Z+1}_{S} - E^{Z}_{S}] \quad (7.\ 16)$$

where the surface energy is defined as $E_S = [E_{coh,surf} - E_{coh,bulk}]$. Instead of using the average surface tension of a liquid, as in equation (7. 13), Rosengren and Johansson [180] took calculated surface tensions for a variety of crystal orientations and used calculated bandwidths and band fillings to relate them to these surface energies.

The advent of super computers has enable theorists to now perform vastly complex bandstructure calculations routinely. Development of the basic electronic structure calculational schemes has enabled detailed surface calculations to find the SCLS self-consistently. However, the complexity of surface effects has limited the number of systems which can be studied by self-consistent calculations. Most of the surface theoretical work is concerned with the surface electronic structure (the bandstructure, DOS, surface states, etc) and not the SCLS itself, which is a side product of the calculations.

7. 2. 4. The effect of adsorption on substrate core level shift

It might be expected that the initial-state characteristics affect the magnitude and direction of the surface shift. Whereas previously for the clean surface the initial–state is altered as a result of charge transfer between the surface and the bulk, during adsorption charge transfer occurs between the adsorbate and the substrate. The direction of transfer is dependent on relative

electro-negativities of the two. For example when caesium is adsorbed onto tungsten there is electron donation to the substrate [181]. As a result, the surface–core–level binding energies are shifted in the opposite direction to that observed during oxygen adsorption where charge is donated to the adsorbate.

Within the band approach described earlier for the clean SCLS involving surface d-band narrowing, there is a change in the direction of the shift across the transition series. Given that the effect of adsorbing oxygen on tungsten is to increase core–level binding energies, we might expect within this model that the presence of the oxygen causes a broadening of the surface d-band. This would produce an overlap of filled surface bands with empty bulk bands (or alternatively, inducing a misalignment of surface and bulk Fermi levels). In a similar way to that argued for the clean surface shift, there must be a small amount of charge transfer from the surface to the bulk (or, realignment of bulk and surface Fermi levels). This behaviour is accompanied by a shift in the density of states of the surface layer with respect to the bulk in such a way as to produce the observed effect.

However, if we apply these arguments to those transition metals with less–than–half–filled d-bands they would predict a decrease in surface atom core–level binding energies. It has been shown that the shift induced by adsorption of oxygen and hydrogen is in the same direction for both tungsten and tantalum [171]. Clearly, this simple qualitative band–narrowing/broadening picture meets its limitations when it comes to predict adsorption–induced shifts.

However, within an initial–state interpretation it is possible to describe this behaviour of shifts in the same direction. Consider oxygen adsorbed on a tungsten surface (chemisorption). Since oxygen is more electronegative than tungsten there will be a small amount of charge transfer from tungsten to oxygen which will produce a dipole moment on the surface with

positive side on the tungsten. This will increase the potential energy of the tungsten core level in the same way as putting positive charge on a sphere will increase the potential energy of a negative charge inside the sphere and make it more difficult to remove the negative charge from the sphere. This story will be same for oxygen on tantalum. Even in physisorbed cases where there is no charge transfer between adsorbate and the substrate, any adsorption will produce an electrical dipole moment on the surface that will affect the valence electron distribution of the substrate (which are close enough) and therefore make a potential energy change inside the atom which will result in core–level shifts inside the adsorbate atom.

It is clear from this explanation that the greater the interaction, i. e. the larger the degree of charge transfer involved, then the greater will be the alteration of surface–atom core–level binding energy. In practice, this implies that a surface atom bound to two or more adsorbate atoms will experience a greater shift than one which is bound to a single adatom.

There is also an accompanying effect on the final-state screening potential. Reduction (increase) in screening charge density will lead to loss of (gain in) effective screening, the result of which is an apparently larger (smaller) core level binding–energy shift.

7.3. Lineshape

In the absence of any lifetime effects and with an ideal instrumental performance, the spectra may be described by a series of delta functions. However, in real systems the observed lines have a finite width and asymmetry. A range of line profiles are possible. In the case of metal samples it has been shown that an asymmetric profile should be expected [182]. However, recorded spectra exhibit deviations from idealised profiles due to a range of instrumental and physical effects:

1) response function of the electron analyser which may be asymmetric.

2) Profile of the X–ray lineshape, predicted to be asymmetric for unmonochromated metal anodes [182].

3) Intrinsic lifetime broadening of the core level–hole state, usually assumed to be Lorentzian in nature.

4) Phonon broadening

5) differential surface charging of the sample.

In addition to these instrumental and physical considerations the shape of a synthetic peak is also influenced by the choice of background algorithm used to remove 'extrinsic' electrons [183].

In the next sections the physical effects on lineshape will be discussed and finally a method for decomposing the lineshape will be explained.

7.3.1. Core–hole lifetime

For an experiment with fixed emission angle and photon energy the effect of core–hole lifetime would be to replace the delta function with a Lorentzian

$$I_S = \frac{I_o \omega}{(E_o - E_S)^2 + \omega^2} \qquad (7.17)$$

where E_o is the energy of the centre of Lorentzian peak, I_o is the height at energy E_o, I_S is the height at energy point E_S of the peak and ω is half of the FWHM. Then, τ, the lifetime is defined as

$$I_S = \frac{1}{\Delta E_S} = \frac{1}{2\omega} \qquad (7.18)$$

For tungsten 4f levels the accepted Lorentzian FWHM is 50 meV [184]. Riffe et al [166] claim that this degree of Lorentzian broadening differs for different environments, quoting 60 ± 3 meV for the bulk and 84 ± 3 meV for the surface of tungsten. They proposed the reason to be greater overlap between 4f and 5d orbital at the surface. This is because the d–band at the surface is more atomic–like and therefore is more (less) localised in energy (space). The result of this is to enhance the Auger decay rate relative to the bulk, thereby reducing core–hole lifetime and increasing the core–hole broadening.

It is also expected that a reduction in the valance band occupancy following charge transfer to an electronegative adsorbate would cause a reduction in the Auger decay rate, hence increasing the core hole lifetime and reducing the Lorentzian width. The opposite is therefore implied for an electropositive adsorbate.

7.3. 2. Phonon broadening

The sudden creation of a core hole during photoemission, Auger emission or X–ray absorption will cause a response by surrounding nuclei. The system will tend to reach a new equilibrium position yielding a relaxation energy E_R. The potential energy curves of atomic motion for the initial (V_i) and final (V_f) states as a function of nuclear position may be drawn (Fig.7. 5). Redistribution of charge during relaxation will displace the minimum of V_f from V_i. At 0 K temperature, only a transition from E_{io} to E_{fo} is possible, which will result in a delta function in photoemission. Small nuclear motion from the equilibrium position q_{io} caused by thermal vibration will result in a spread in energy of the final state (between E_{f1} and E_{f2} in Fig 7. 5) which is proportional to the gradient of V_f at q_{io}. This corresponds to excitation of a large number of phonons which will result in broadening of the photoemission line. Within this simple model, the phonon contribution to the line width in the limit of strong electron–phonon coupling is predicted to be Gaussian with temperature dependence [185, 186] given by

$$\Gamma = 2.35\left[\hbar\omega_{Lo} E_R \coth\left(\frac{\hbar\omega_{Lo}}{2kT}\right)\right] \qquad (7.\ 19)$$

$\Gamma$is proportional to the relaxation energy E_R and to the ratio of longitudinal optical phonon energy $\hbar\omega_{Lo}$ to the energy equivalent of temperature 2kT.

Phonons may also be induced by photoelectron–phonon scattering as the electron passes through the solid on its way to the surface. This process produces secondary electrons.

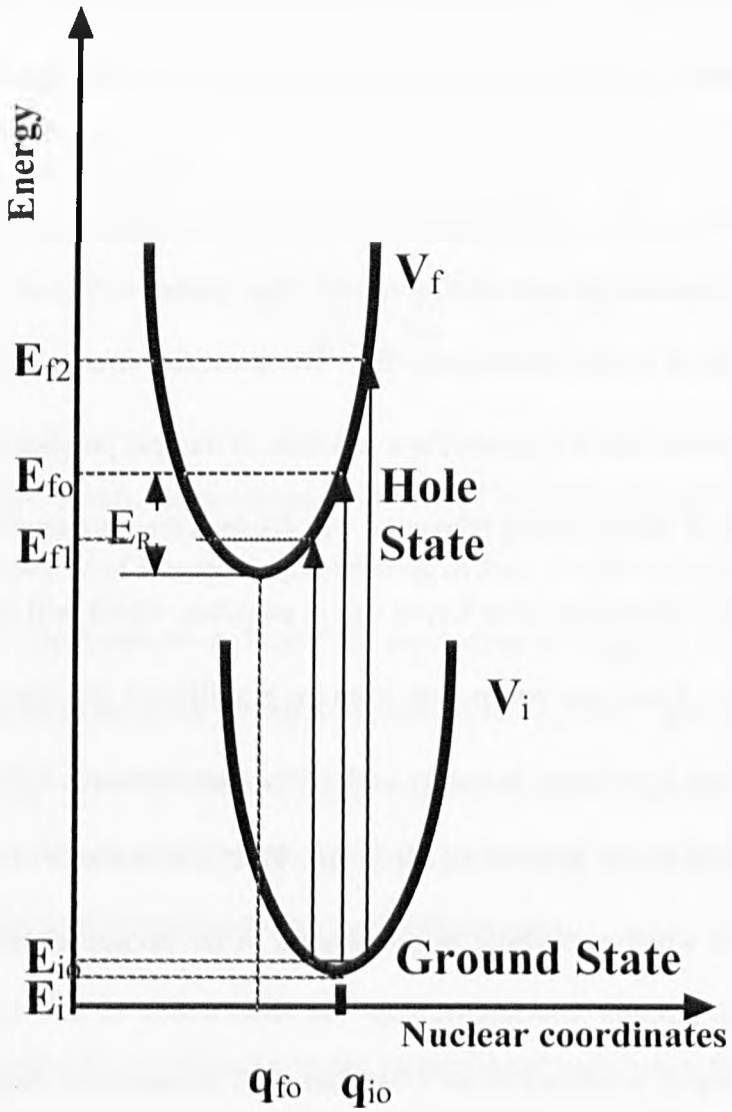

Fig. 7. 5. Potential energy curves of an atom for initial state V_i and final state (after photoemission) V_f.
At 0K, the atom is at q_{io} with energy E_i and the only possible final state is E_{fo}. At higher temperature atom has energy E_{io}, therefore is vibrating around q_{io}. This will cause the final state to be some amount between E_{f1} and E_{f2} which will result in broadening of the photoemission lineshape.

There is also an additional possible source of phonon excitation due to the recoil energy which the photoejected electron imparts to the ion. However, this effect is negligible for low–energy UV photoelectrons. The theoretical estimates for phonon broadening quoted by Sebilleau et al [187] show that at 77K on a W(100) surface there is no difference between surface and bulk phonon broadening, but at 300 K the surface levels show a phonon broadening which is 20

meV larger than that of the bulk. Riffe et al [166] found this difference for W(110) to be as little as 7 meV

7.3.3. Plasmon

Formation of a core hole within a metal causes the surrounding conduction electrons to undergo some rearrangement such that they screen the resultant charge. This charge rearrangement may induce excitations such as plasmons or electron–hole pairs. Plasmons created in this way are referred as intrinsic plasmons. (There may be excitation of extrinsic plasmons–these would be the result of disturbance of the conduction electrons by photoelectron as it makes its way through the solid to the surface). In the former situation where the Fermi sea reacts to the formation of the hole–photoelectron dipole there is no plasmon creation when the photoelectron binding energy within the atom is less or close to a threshold, since the hole and electron separate relatively slowly. It is possible to consider this as the intrinsic and extrinsic plasmons interacting destructively. In UV photoemission, where the kinetic energy of the escaping electron is less than 40 eV, we are most likely in this region [184]. However, if the kinetic energy is high and the two separate rapidly then the result is a large number of plasmon excitations, giving rise to satellites on the low–kinetic–energy side of the core lines. The separation of these satellites is $\hbar\omega_p$, where ω_p is the plasmon frequency. The effect of extrinsic plasmon losses is to add to the intensity of these satellites.

If a core hole is created at the surface of the metal then there is a possibility of forming surface plasmon modes, thereby creating two sets of plasmon frequencies and two sets of satellites. Bulk and surface losses occur at different energies in spectrum.

7.3.4. Electron hole pairs

Due to inelastic scattering of a photoelectron from the atom, it is possible that some energy transfers from the photoelectron to the atom. This can excite one of the electrons of the atom from the ground state to an excited state in which it is possible that a hole be produced. This is known as electron–hole creation. Under formation of a core hole the conduction electrons undergo some rearrangement. As a result the probability of filling a core hole by screening electrons, relaxed at E_f, is enhanced. In addition to this Anderson [184, 188] pointed out that when a screening cloud forms in a metal, in response to creation of a core hole, the final–state wavefunction of electrons in the conduction band is slightly modified relative to the initial state. The transition matrix element must not only contain the overlap of the initial and final state of the excited core electron, but also all other wavefunctions belong to the many–body system.

Many–body effects come in two types–those which provide width but maintain a symmetrical Lorentzian form and those that provide asymmetry and are directly associated with the edge effect, i. e. creation of a large number of low energy electron–hole pairs during the photoemission process.

7.3.5. Decomposing lineshape

In the absence of any lifetime broadening the delta function gains a tail on the high binding energy side due to inelastic scattering via the creation of electron–hole pairs. The result of combining this tail with the effect of a finite hole–state lifetime, i. e. Lorentzian broadening, is the well known Doniach–Sunjic (DS) lineshape which has been used frequently by experimenters over the last three decades to fit XPS data [182]

$$I(E) = I_o \left[\frac{\Gamma(1-\alpha)}{((E-E_o)^2+\gamma^2)^{\frac{(1-\alpha)}{2}}} \right] \cos\left\{ \frac{\pi\alpha}{2} + (1-\alpha)\arctan\left(\frac{E-E_o}{\gamma}\right) \right\} \qquad (7.20)$$

where

$$\Gamma(1-\alpha) = \int_0^\infty x^{-\alpha} e^{-x} dx \qquad (7.21)$$

and E_o is the position of the peak, I_o is the maximum intensity, α is the asymmetry term named singularity index and 2γ is the FWHM. This description of a photoemission lineshape gives a good fit over an energy range of a few eV.

Once the secondary electron background has been subtracted, which is usually significant due to the low kinetic energies involved in UPS, the spectra can be assumed to consist of a number of DS peaks, each convoluted with a Gaussian function representing the instrumental–resolution function and phonon–broadening contribution. Using a least–squares algorithm it is possible to change the parameters of the DS peaks until the best fit to the actual peaks is achieved.

Because of the influence of the background subtraction algorithm on lineshape, great care must be taken in choosing the type of background. For example, a Shirley background was introduced precisely to remove as much asymmetry as possible from the recorded data [183]. The Tugaard background algorithm [139-143] needs a wide energy range (~ 40 eV) on the higher kinetic energy side of the peak under investigation to account properly for the effect of higher kinetic electrons in the background. Since high energy resolution is essential in lineshape

analysis, this wide energy range requirement by the Tugaard background algorithm (comparing it with the 2 eV width of the W $4f_{7/2}$ level in this investigation) means a longer period of data acquisition which can be achieved only by increasing the the risk of surface contamination. Therefore, the best methods of lineshape analysis are (*i*) to use a linear background before decomposing the features or (*ii*) to decompose the features without a background subtraction and adding a Shirley background to the calculated lineshape.

Chapter 8

Electronic Structure of Dy/W(100) system

8.1. Introduction

The morphology of Dy/W(100) systems has been discussed in the previous chapters. There is a close relationship between the morphology of a system and the electronic structure of that system. Therefore, it is important to investigate the electronic structure of this system.

Core level shift (CLS) spectroscopy is a useful tool in elucidating changes in the environment of the topmost substrate atoms as an adsorbate is deposited. The 4f levels of W provided the first experimental evidence of the surface core level shift (SCLS) [165] – the large surface shift and narrow intrinsic line–width of these features make them suitable for observing the effect. Since then many SCLS studies have been performed on W surfaces, including clean [166] and stepped [189] W(100), Gd [190] and O [171, 191] adsorption on W(110), WC(0001) [192], adsorption of Gd, Y, and Yb [193], Li and K[194], C [195], O [196], H [197] and S [198] on W(100).

In this study CLS of the W 4f $_{7/2}$ is used to investigate surface reactions which will take place between Dy and W during growth and subsequent annealing to understand what will happen to this system under annealing processes, necessary for improving film structure.

To extract more precise qualitative and quantitative information from the spectra, a linear background was subtracted, to remove extrinsic electrons [199, 200] and then the spectra were decomposed into their components using least–squares fitting with Doniach–Sunjic line shapes [182]. Following the work of Mullins and Lyman [195], to minimise the number of free parameters in the fit, the Gaussian width, Lorentzian width and the Doniach–Sunjic asymmetry parameter were allowed to vary in the fit but were constrained to be the same for

all of the peaks in a given spectrum.

Furthermore as it is the valence levels that are involved in the formation of chemical bonds, Valence Band–Ultraviolet Photoemission Spectroscopy (VB–UPS) spectra provide much valuable information on the adsorption of Dy on W. The electronic band structure of Dy films, grown on W(100), was also monitored during growth and annealing processes by UPS using a synchrotron radiation source. The results will be discussed and compared with the other characteristics of the Dy/W(100) system obtained by complementary techniques such as W 4f core–level spectroscopy, LEED, STM and XPS.

8.2. Experimental details

XPS experiments were carried out at Surface Science Research Centre of the University of Liverpool. The X–ray source was a water cooled Henke type with twin anode source (Mg – Al) and the electron energy analyser was a hemispherical Vacuum Generator MDS50 type. The base pressure of the chamber was $8x10^{-11}$ mbar and during evaporation the pressure remained below 10^{-10} mbar.

The Ultraviolet Photoemission Spectroscopy (UPS) measurements were taken on beamline 4.1 [201] at the Synchrotron Radiation Source, Daresbury Laboratory, U. K. The data set was collected on a Scienta SES hemispherical analyser, which gave a total energy resolution (photon bandwidth and analyser resolution) of 90 meV at $h\nu$ = 70 eV. The chamber was equipped with Omicron 4 – grid Low Energy Electron Diffraction (LEED) optics. The chamber pressure remained below $3x10^{-10}$ mbar during evaporation and below $2x10^{-10}$ mbar during data acquisition.

The W(100) crystal was prepared by backfilling the chamber with ~10^{-6} mbar O_2 and heating the sample to 1800 K for 30 minutes to remove C, followed by cycles of flashing briefly to 2500 K when the pressure reached ~ 10^{-10} mbar. This process was repeated until the surface was judged to be clean and well–ordered by LEED, XPS and UPS – both valence band and W 4f core–level spectra are known to be sensitive to contamination [166]. Evaporation of Dy was carried out by a well–degassed WA Technology Knudsen cell (K–cell) evaporator which contained Dy of 99.99% purity.

The Dy coverage was calibrated using the known deposition rate of the source (which was regularly checked and remained stable over the experiments) and by the intensity of the W 4f levels in UPS and XPS. Due to the high reactivity of rare–earth metals [22], the sample was flashed every 30 minutes and new films were grown to ensure that the films were clean during the experiment. The substrate was at room temperature during growth.

8.3. Clean W(100)

Normalised spectra of the clean W 4f core levels are shown in Fig.8.1. At first it seems that the surface and bulk 4f components are much less well resolved than those for the W(110) surface, for example those obtained by Tucker *et al* on the same beamline [193]. However, the W(100) and W(110) surfaces have different unit cells and different interlayer spacings. The subsurface component of the W 4f lineshape lies at a binding energy between that of the bulk and the surface, and so its intensity can change the shape of the "valley" between the bulk and surface components. Compared to that of W(110), the subsurface component of the W(100) 4f lineshape has significant intensity and thus reduces

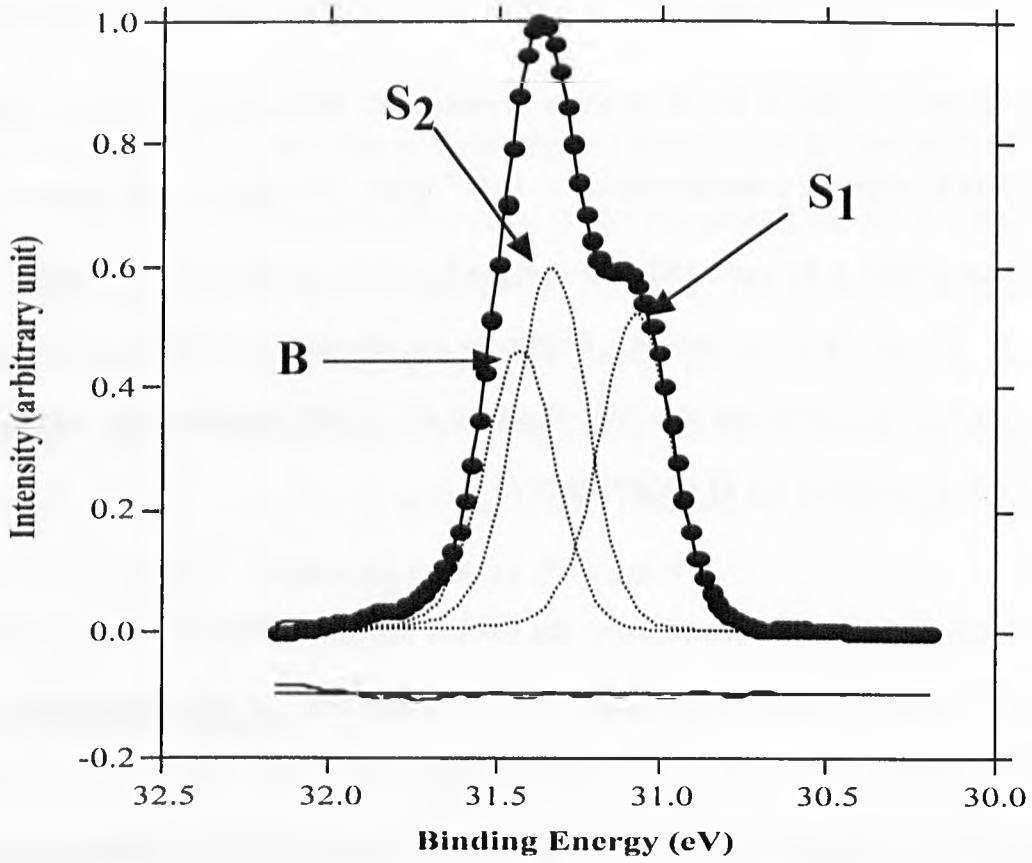

Fig.8.1. W 4f SCLS of clean W(100) SCLS at RT. The components shown by arrows correspond to the bulk (B), surface (S_1) and subsurface (S_2) atoms. Markers are experimental points and the solid line is resultant curve of the calculated components B, S_1 and S_2. At the bottom a residual curve between calculated and experimental curves is shown. Photoelectrons are collected normal to the surface.

the apparent resolution of the 4f spectrum. Practically, because of this reason the clean W(100) surface spectra has been decomposed into three features, with distinguishable binding energies, in literatures in which the bulk peak has been reported to have a binding energy of 31.44 ± 0.05 eV [171, 195, 198, 202]. Due to reduced coordination of the surface and the second atomic layer, their binding energies are shifted toward the Fermi level.

Fig.8.1 shows the W 4f spectrum of the W(100) sample used in this study. This spectrum was fitted using three components corresponding to the bulk (B), surface (S_1) and subsurface (S_2) atoms. The fit resulted in components at B=31.44 ± 0.02 eV, S_1=31.10 ± 0.02

eV, S_2 = 31.31 ± 0.02 eV, in agreement with previous data [171, 195, 197, 198, 202]. The errors in binding energies were obtained from the scatter of values determined by fitting to different spectra taken at different times.

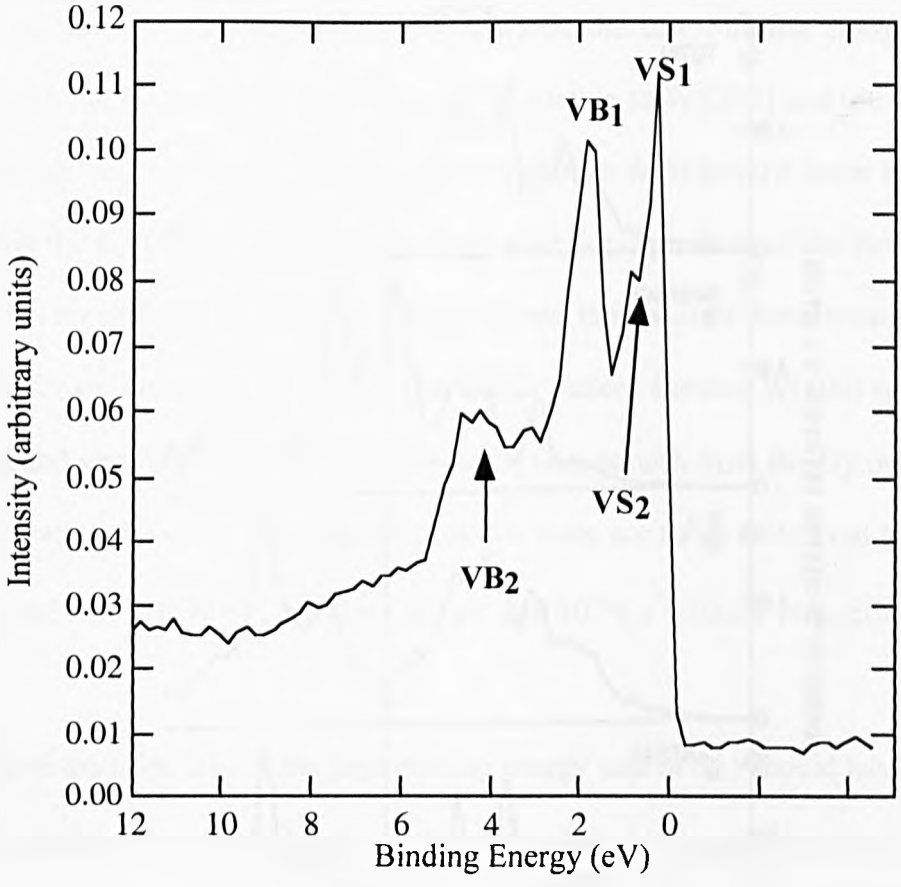

Fig.8.2. Normal–emission photoelectron spectra from clean W(100). hν = 70 eV.

Fig.8.2 shows an electron distribution curve (EDC) of a clean W(100) valence band. Comparison of this spectrum with density of state calculations of W(100), Fig.8.3 [203, 204], allows identification of many of the features: The sharp peak at 0.4 ± 0.2 eV binding energy (BE) close to the Fermi edge is the surface state (VS_1). The intensity of this feature indicates that the W(100) surface is clean and well–ordered, as has been confirmed by LEED, XPS and W 4f core level–spectroscopy. The feature at 1.0 ± 0.2 eV is another surface state (VS_2) while the other significant features are a bulk peak at 1.8 ± 0.2 eV (VB_1) and a broad feature at 4.5

± 0.2 eV (VB_2). The surface or bulk assignments have also been judged from normal–emission EDC's with various photon energies and further justified from impurity adsorption.

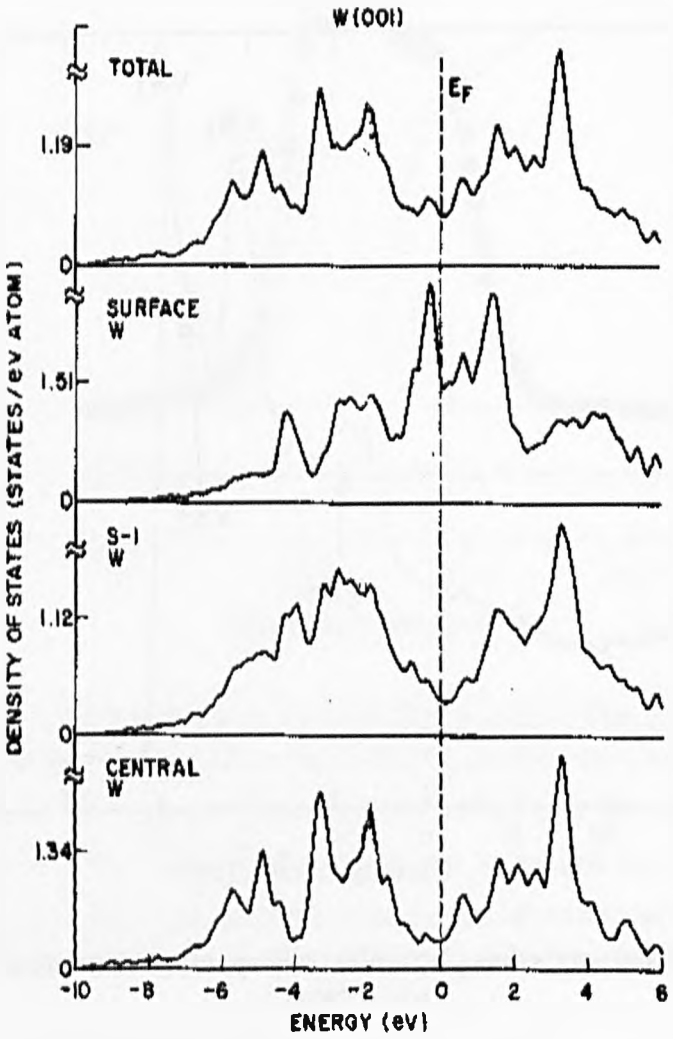

Fig.8.3. NTB total and projected DOS curves for a 19–layer W(100) film (omitting spin–orbit coupling). adopted from Ref. [204]

8.4. Growth at RT

In this part of the study Dy was grown on W(100) and W 4f and VB have been monitored during the growth. As Dy is deposited the features in the W4f spectra display significant changes by starting to broaden towards the low binding energy side. This is consistent with the lower electronegativity of Dy relative to W [205] and the theory of SCLS (see for example section 7.2.2.1). Fig.8.4 shows a shift in W 4f toward lower binding energies by increasing the coverage. This shift continued after the deposition of the first ML, but, after 1.2ML almost no shift can be resolved. Fig.8.5 shows the result of decomposition of the W 4f components for the coverage of 1.2ML. The LEED pattern showed W(100) spots with a high background and very faint spots in a pseudo–hexagonal pattern from the Dy overlayer. Fig.8.5 shows that despite the clean W(100) components, there are three additional components D_1, D_2 and D_3 at 31.24 ± 0.02 eV, 30.92 ± 0.02 eV and 30.74 ± 0.02 eV respectively. Since W is more

electronegative than Dy, D_1 (on the high binding energy side of S_1) should have its origin only in subsurface atoms. However, the large shifts of D_2 and D_3 suggest that they resulted from the surface atoms which can be interpreted as interfacial (D_2) and partially coordinated (D_3) components. An intensity investigation between components before and after deposition of Dy showed that on deposition of 1.2 ML of Dy atoms at room temperature, features B and S_1 decreased substantially but S_1 did not disappear. Also, D_2 and D_3 increased. This suggests that although most of the surface is covered by Dy, it does not cover the surface fully due to islanding. This assumption is in contradiction to XPS and STM results of this system that indicate a Stranski–Krastanov mode for the growth. Another possibility is that most of the surface was covered by isolated atoms in such a way that some W surface atom sites remain unaffected by Dy while some part of the overlayer have a close–packed structure. This interpretation is consistent with the reconstruction seen in the growth mode graph of this system just before completion of the first layer (Fig.4.11) and with the LEED pattern of this

system showing W spots with high background and very faint Dy spots. This is also supported by the annealing analysis, to be discussed in the next section.

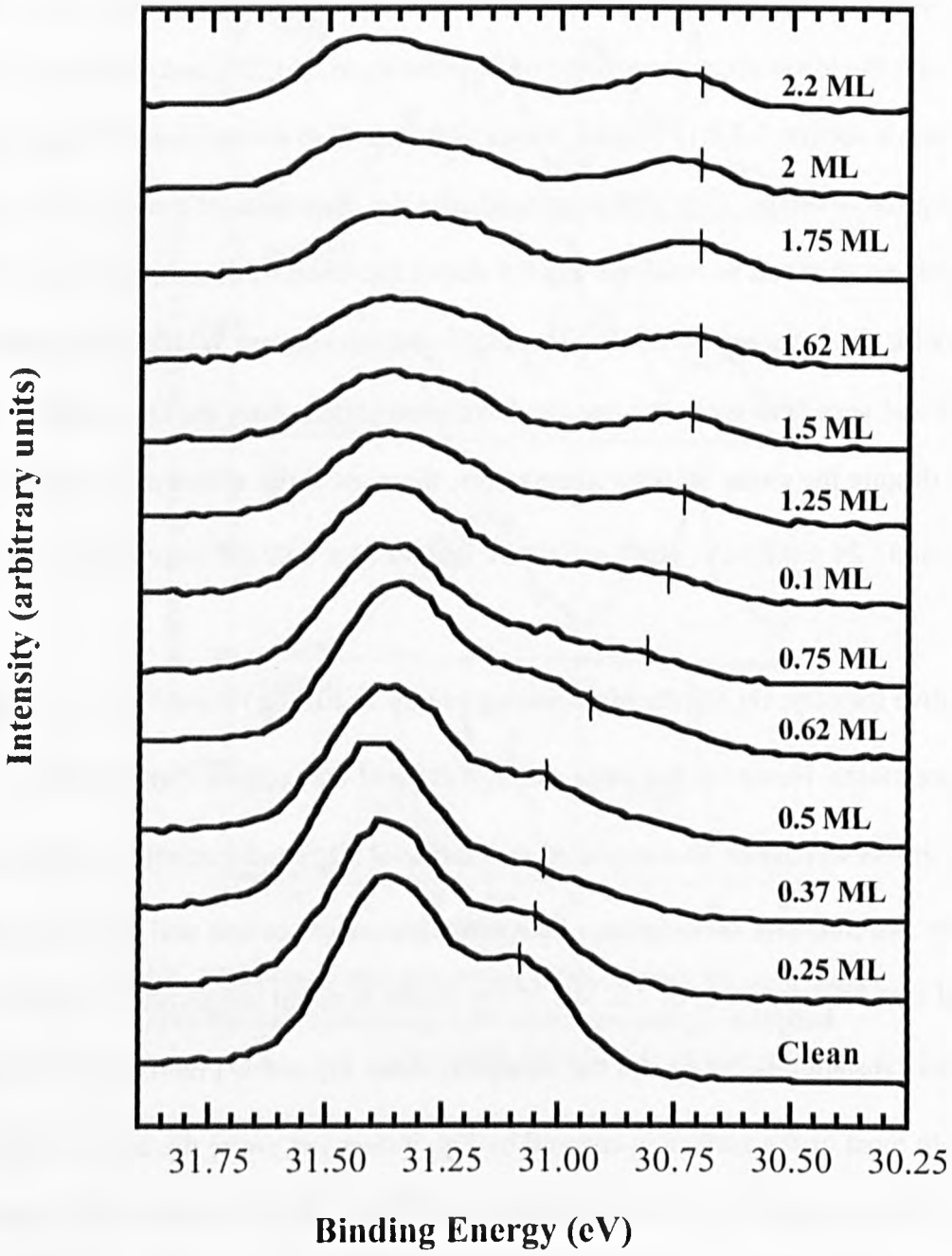

Fig.8.4. Flux–normalised W 4f UPS spectra of the clean and Dy/W(100) system during deposition of Dy at RT. h ν = 70 eV. All photoelectron are collected normal to the surface.

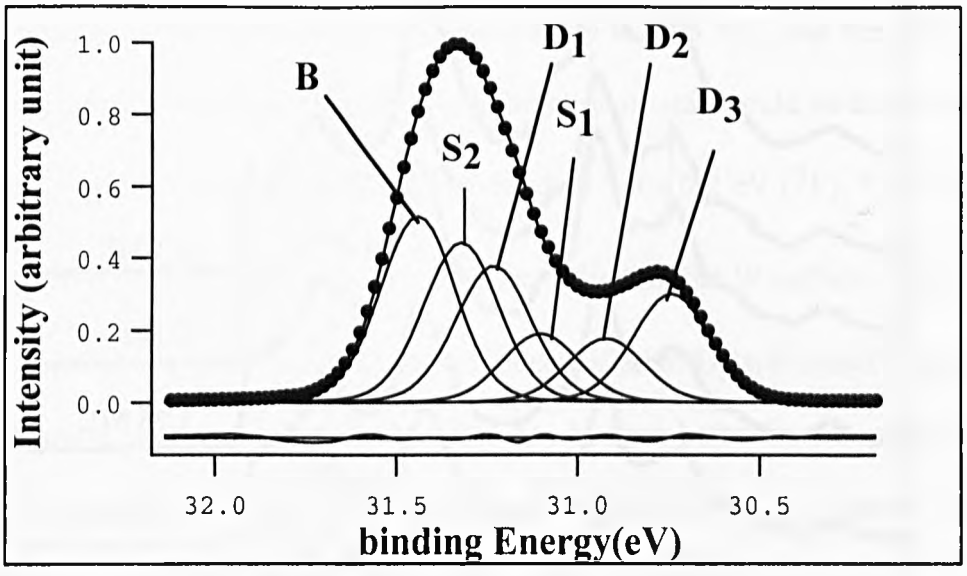

Fig.8.5. W 4f UPS spectra of the Dy/W(100) system after deposition of 1.2ML at room temperature. The spectrum has been normalised to the peak height.

Fig.8.6 shows VB spectra of Dy/W(100) during growth. It is clear from this figure that the intensities of VS_1, VS_2 and VB_1 of the clean W(100), defined in Fig.8.2, decreased by increasing the coverage. As is expected for the surface components, the decrease occurred more rapidly than that of the bulk components with increasing of the Dy. However, VB_2 shows an increase in intensity with increasing the coverage. This is due to hybridisation with the Dy 4f minority state (^7F). Absence of such a bulk state in the W(110) case [206] means that there will be no such hybridisation for Dy/W(110). This hybridisation can be one of the reasons responsible for the strong bonding between Dy and W, resulting in high thermal stability of Dy superstructures on W(100) (see Chapters 5 and 6). The Dy valence features resulting from the 4f multiplets can be identified by comparison with X–ray photoemission spectra (Fig.8.7) [207, 208]. The various multiplets for 1.2ML have binding energies at 4.0 ± 0.2 eV (^7F), known as 4f minority states, 8.0 ± 0.2 eV (^5L, ^5G) and 9.4 ± 0.2 eV (^5I, ^5H),

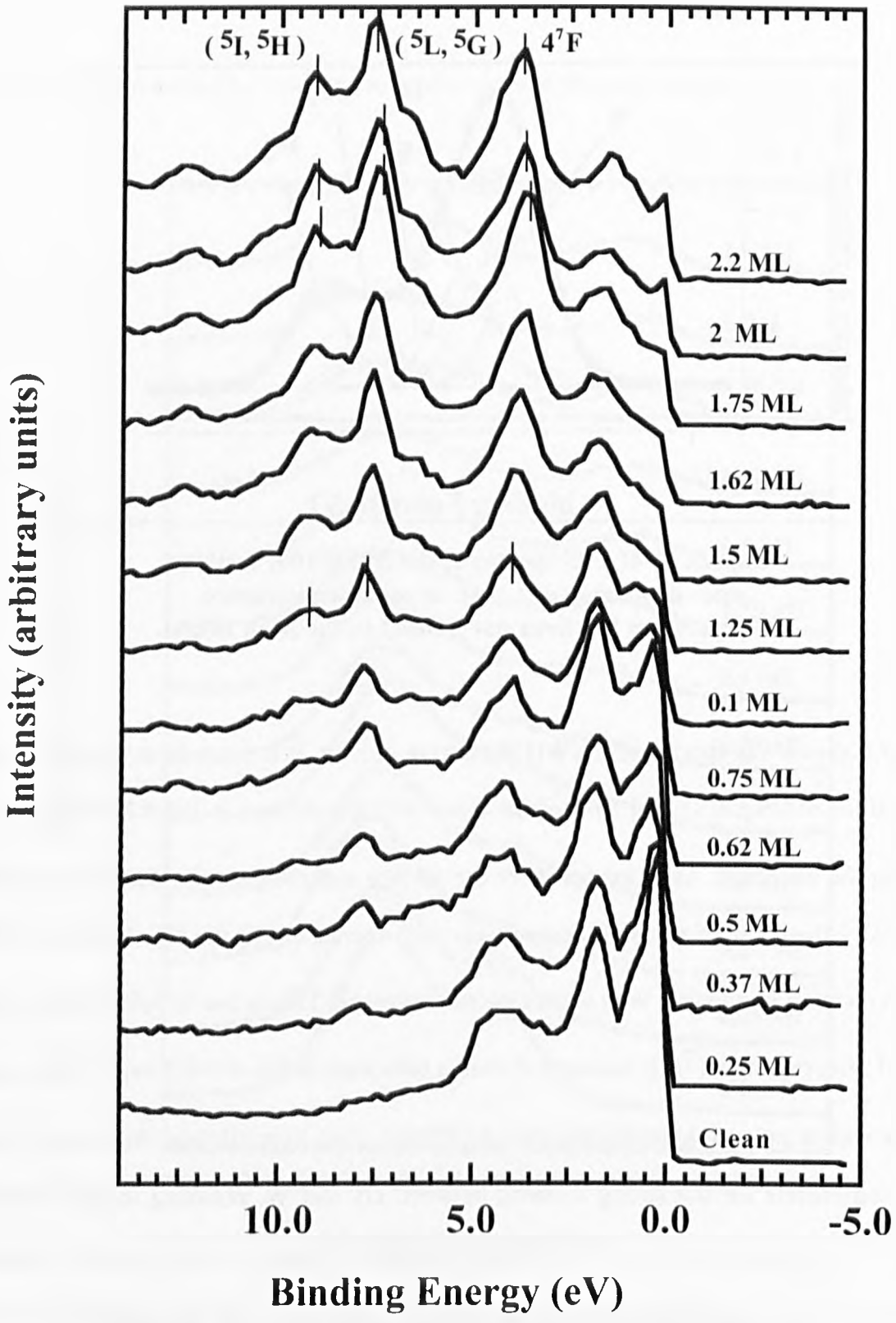

Fig.8.6. Flux–normalised UPS spectra from clean W(100) and Dy/W(100) during growth of Dy at room temperature. The identification of the Dy features between ~4–10 eV are described in the text and features of the clean W are shown in Fig.8.2. hν = 70 eV.

known as 4f majority states. The feature at 5.8 ± 0.2 eV is an intrinsic feature that has been attributed to a many–electron correlation satellite [106, 209]. By increasing the coverage the Dy 4f features are shifted to lower binding energies up to 1.75 ML, and then they showed a shift to higher binding energies. This change in direction of shift could be due to reduction of strain in the Dy film. At 2.2ML the Dy features are at 3.6 ± 0.2 eV (^{7}F), 7.6 ± 0.2 eV (^{5}L, ^{5}G) and 9.0 ± 0.2 eV (^{5}I, ^{5}H). It is also clear from Fig.8.6 that W surface states near to the Fermi edge decreased with coverage. Continuing deposition of Dy will result in appearance of new sharp features near to the Fermi edge, this can be seen better by comparing it with the VB_1 of the clean W. This can be interpreted to be a result of formation of dense islands of Dy which will produce Dy 5d–6s hybridisation and thus indicates that this feature has 5d character. The sharpness of this surface state reflects the degree of localisation of the Dy 5d band and is a sign of the extent of crystallographic ordering of the Dy film.

8.5. Annealing investigation

8.5.1. Annealing of 1.2 Dy on W(100)

Fig.8.5 shows W 4f core levels for Dy/W(100) system with 1.2 ML coverage. The LEED pattern corresponding to this spectrum showed W(100) spots with a high background and very faint spots in a pseudo–hexagonal pattern from the Dy overlayer. On annealing the quality of the LEED pattern improved and the optimum annealing temperature was found to be around 770 K, which produced patterns with sharp Dy spots and a low background. By annealing at different temperatures from 750 to 940 K and measuring total photoemission intensity of the W 4f peak (after Shirley background subtraction) at room temperature, the constant intensity indicates that no significant evaporation of Dy atoms from the surface occurs (Fig.8.8).

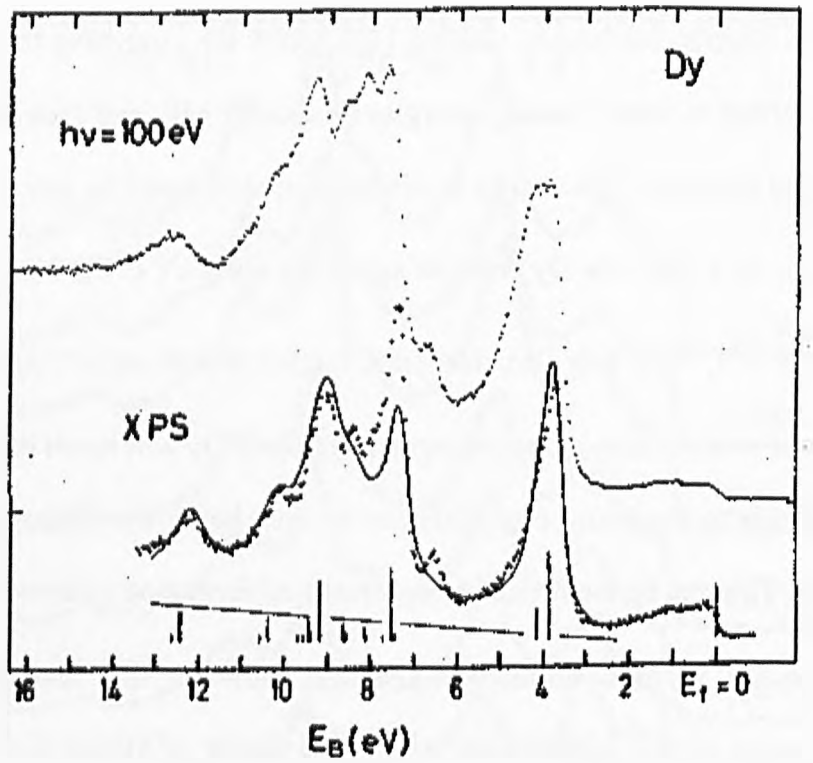

Fig.8.7. UPS and XPS spectra from Dy metal.
Adopted from Ref. [55].

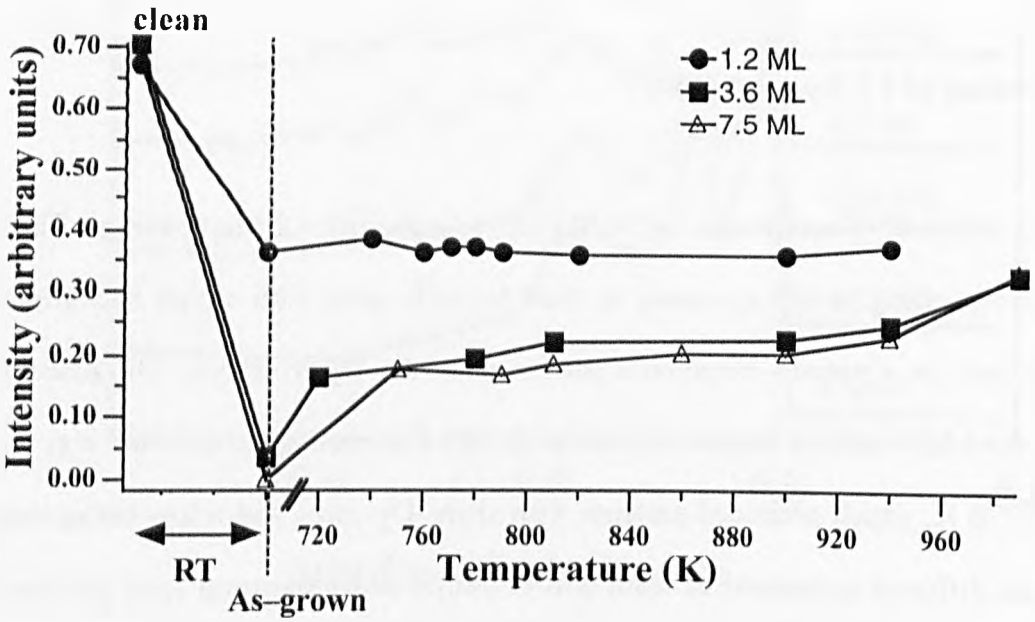

Fig.8.8. UPS intensity changes of the W 4f level on deposition of: 1.2 ML, 3.6 ML and 7.5 ML of Dy and successive annealing. The intensities were calculated by integrating the W $4f_{7/2}$ peak after subtraction of a Shirley background.

Fig.8.9 shows the results of decomposing W 4f levels at different annealing temperatures. The same components as that of the as grown case, Fig.8.5, have been resolved for all of them, though the intensities of the components have changed by annealing. Fig.8.10 shows the results of the intensity changes for this system. In the following section, the intensity changes of only surface–related components will be discussed, as the subsurface components are less sensitive to overlayer structure. In fact these components are more site–specific, i. e. intensity of these components are significantly dependent to type of sites that Dy atoms have on the surface. It is clear from this figure that on deposition of 1.2 ML of Dy atoms at room temperature, features B and S_1 decreased substantially but S_1 did not disappear. Also, D_2 and D_3 increased. This suggests that although most of the surface is covered by Dy, it does not cover the surface fully due to islanding. This assumption is in contradiction to XPS results of this system that indicate a Stranski–Krastanov mode for the growth. Another possibility is that most of the surface was covered by isolated atoms in such a way that some W surface atom sites remain unaffected by Dy while some parts of the overlayer have a close–packed structure. This interpretation is consistent with the LEED pattern of
this system showing W spots with a high background and very faint Dy spots. This is also supported by the following annealing analysis.

By annealing to 750 K, B and S_1 increased substantially. This suggest that the isolated atoms have joined the close–packed islands making the islands expand and reduce the total surface covered by Dy. At the same time the relative intensities of D_2 and D_3 are observed to change from ~ 1:2 to ~ 3:1. Component D_2 is interpreted as being derived from a W sites covered by close–packed pseudo–hexagonal c(8x2) overlayer, and component D_3 is interpreted as being derived from W atoms having isolated Dy atoms as neighbours. The binding energies of these components are consistent with those found for similar rare–earth metal coordinations on W(110) [193]. The changes in relative intensities of D_2

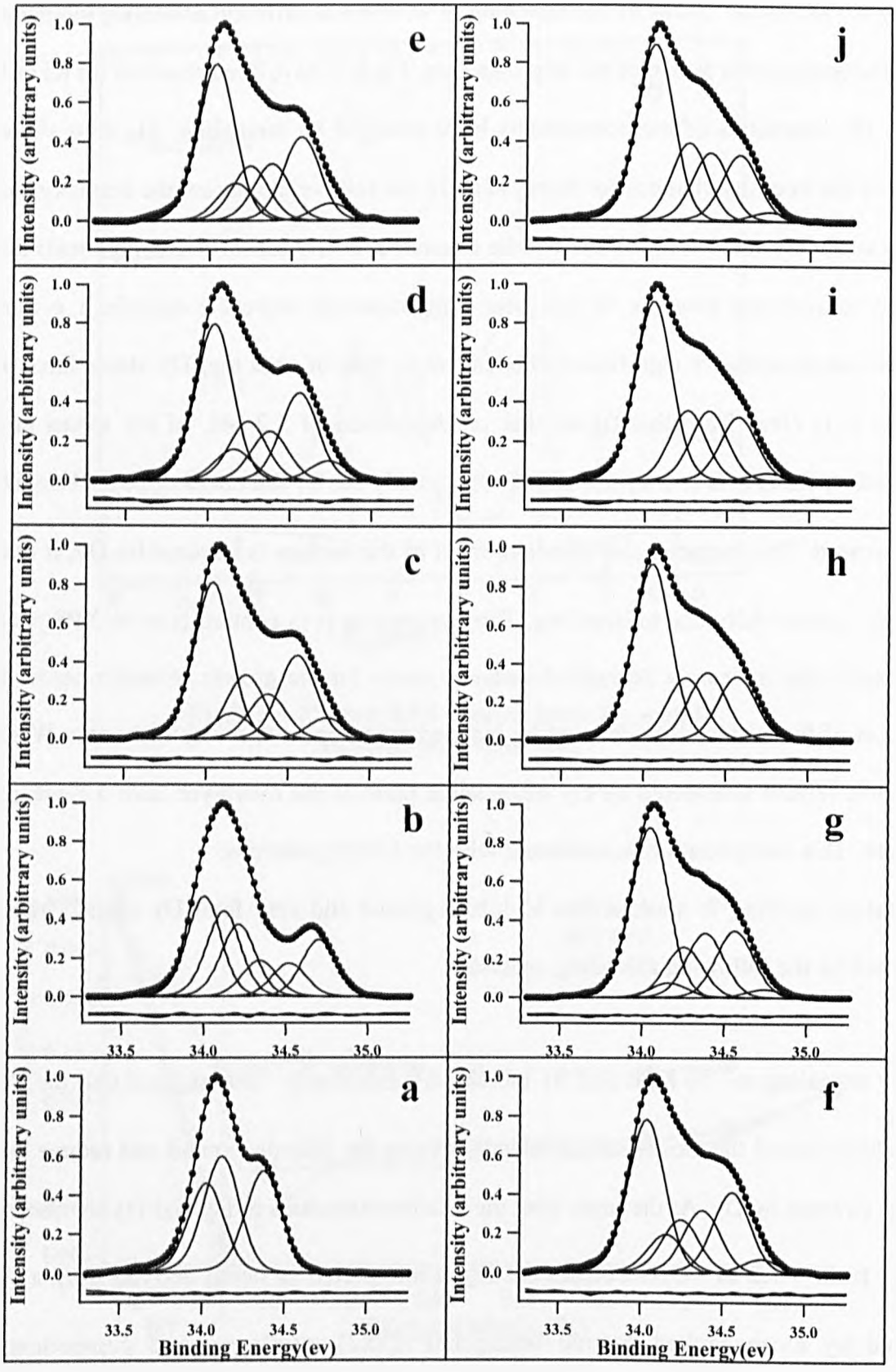

Fig.8.9. W 4f SCLS of Dy/W(100) system for: (a) clean W(100) SCLS, (b) 1.2 ML Dy at room temperature and annealed to: c) 750K, d) 760K, e) 770K, f) 780K, g) 820K, h) 870K, i)9 10K, j) 940K.

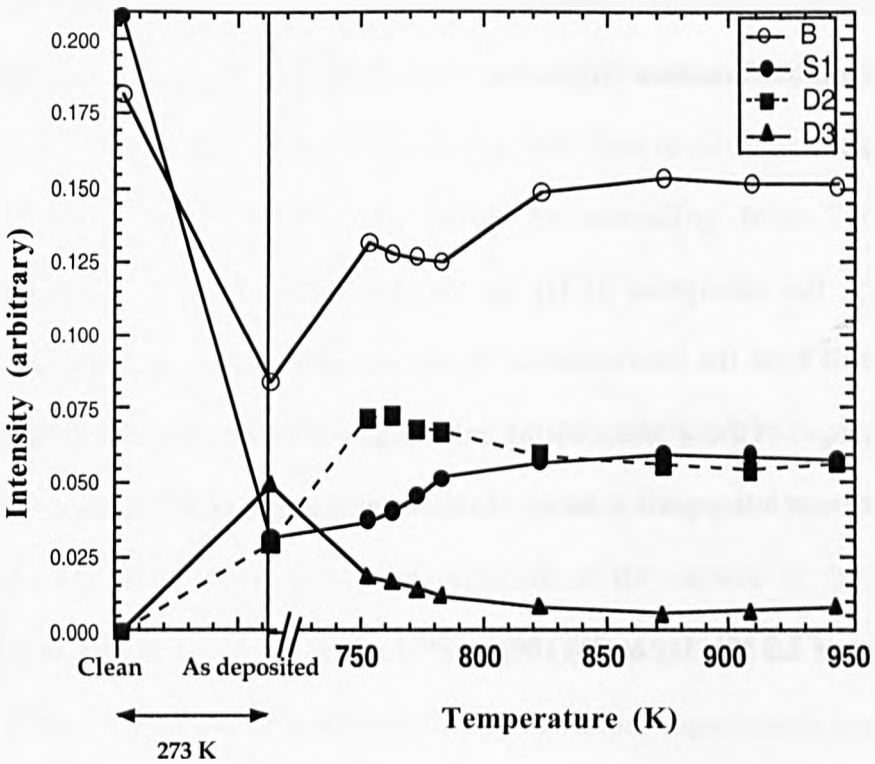

Fig.8.10. Intensity changes of surface W 4f components by deposition of 1.2 ML of Dy and successive annealing.

and D_3 then indicate that annealing the as–grown Dy layer comprises regions of c(8x2) symmetry and decreases region of isolated Dy atoms. On annealing the former grows at the expense of the latter, in agreement with the LEED observations of sharpened diffraction spots and reduced background intensity.

On annealing from 740 K to 780 K the bulk component (B) remains almost constant, which indicates no change in the total area covered by islands. The increase in S_1 and decrease in D_2 and D_3 suggest that some atomic rearrangement has occurred– one possibility is that isolated Dy atoms have moved from hollow sites to top (or bridge) sites.

The increase in B and S_1 on annealing from 780 K to 840 K suggest that thicker islands have formed on the surface. This will cause D_2 and D_3 to decrease as is seen in Fig.8.10.

It is clear from Fig.8.10 that after 840 K there are no significant changes in all components and they have almost constant intensities, revealing no changes in the surface in this temperature range.

In summary, the adsorption of Dy on W(100) results in three W 4f photoemission features that result from the interaction of Dy atoms with surface and subsurface W atoms. The intensity changes of these peaks during annealing are consistent with LEED results of this system and have been interpreted in terms of structural changes on the surface.

8.5.2. Annealing of 7.5 ML Dy on W(100)

Fig.8.11 shows valence band spectra of: (a) clean W(100), (b) W(100) after deposition of 7.5 ML Dy, and (c-h) successive annealing. Fig.8.11(b) illustrates photoemission electron energy distribution changes taken at normal emission for 7.5 monolayer (ML) of Dy grown on W(100) at room temperature. The spectrum exhibits substantial decreases of VS_1, VS_2 and VB1 while an increase in intensity of VB_2 is due to hybridisation with the Dy 4f minority state (^7F).

The Dy 4f level BE are observed to change with annealing (Fig.8.11 (b–h)). A shift of 0.4 ± 0.2 eV to lower BE is observed on annealing up to 940 K. Further annealing to 990 K increased the BE and in general reduced the sharpness of Dy photoemission features. This change can be attributed to evaporation of Dy and disordering of the surface (Fig.8.8).

Spectroscopy of the W 4f core levels after deposition of ~ 7.5 ML of Dy (Fig.8.12 b) shows two features which can be interpreted as interfacial (30.8 ± 0.02 eV) and partially coordinated (30.6 ± 0.02 eV) components. On annealing to 750 K (Fig.8.12 c) the intensity of the former increases and that of the latter decreases, indicating the formation of islands. The

Dy 4f levels show the same behaviour but in the opposite sense. It is clear from Fig.8.12 (c)-(i) that on annealing from 750 K to 940 K there is no significant shift in the W 4f core levels, while annealing to 990 K produces a shift to higher BE. This is consistent with the qualitative behaviour as observed for the Dy 4f levels on annealing from 750 K to 990 K (Fig.8.12 (c)–(h)).

As any adsorbate–induced shift on top of ~ 7.5 ML of Dy will not affect the substrate significantly, the shift in the Dy 4f and W 4f levels on annealing must be related to structural changes of the Dy film. In addition, contamination of the surface of the Dy film would manifest itself as a peak at ~ 6 eV in the UPS spectra [32, 55, 210], but no such feature was seen in any of the Dy spectra. This was confirmed by further experiments involving impurity adsorption (not discussed here).

In Fig.8.11 the simultaneous decrease of the feature close to the Fermi edge and the Dy 4f levels on annealing to 990 K suggests that the feature close to the Fermi edge in spectra (c)–(g) is derived purely from Dy. Photoemission intensity of this feature shows a slight increase on annealing up to 940 K, which is interpreted to be a result of formation of dense islands of Dy. This will produce Dy 5d–6s hybridisation and thus indicates that this feature has 5d character. The sharpness of this surface state reflects the degree of localisation of the Dy 5d band and is a sign of the extent of crystallographic ordering of the Dy film. The improvement of the crystallographic order on annealing is also manifest in the reduction of the binding energy of the Dy 4f levels.

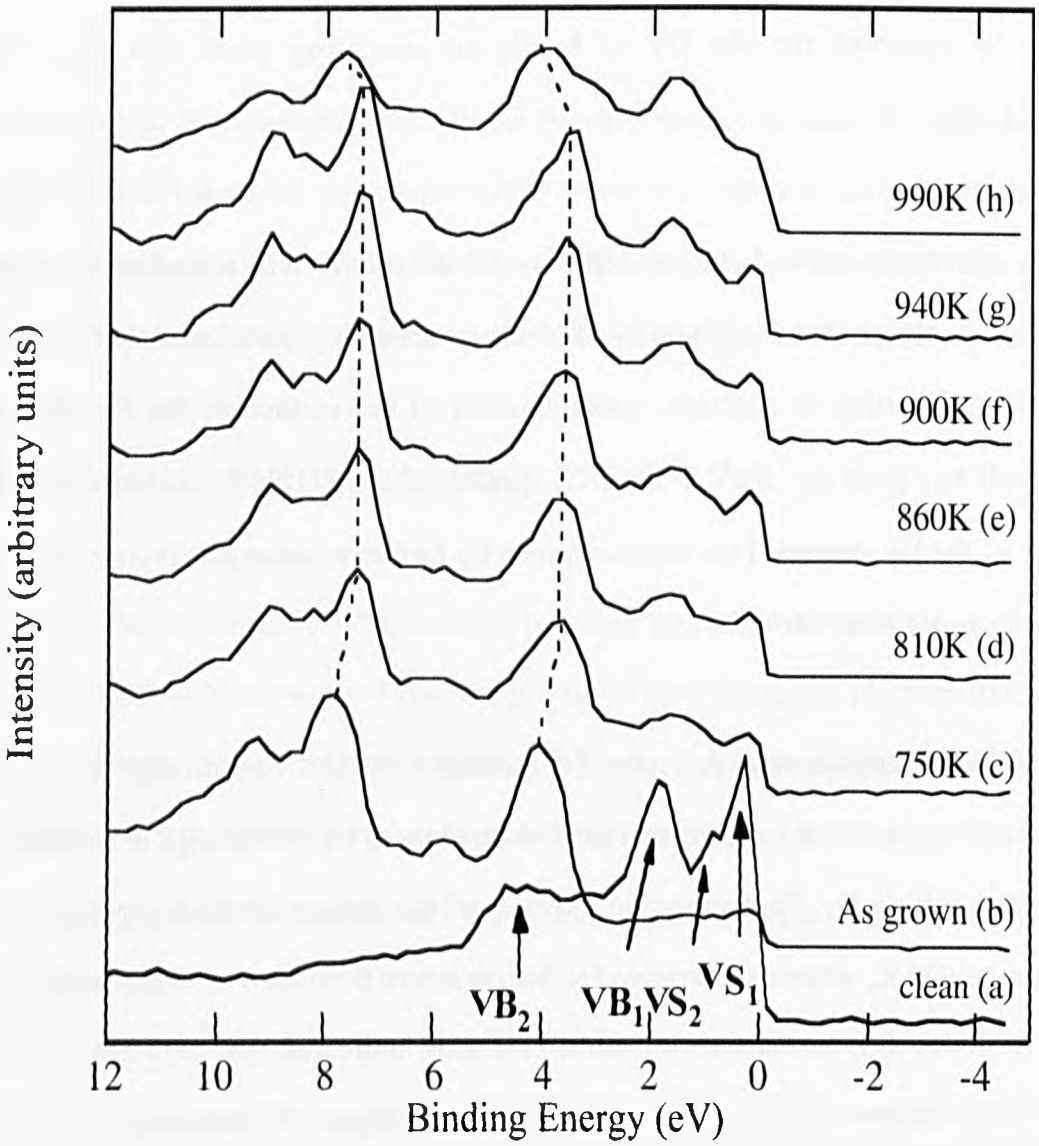

Fig.8.11. Flux–normalised UPS spectra from: (a) clean W(100), (b) ~7.5 ML Dy deposited at room temperature, (c)-(h) successive annealing from 750 K to 990 K. The identification of the Dy features between ~4–10 eV are described in the text. hν = 70 eV.

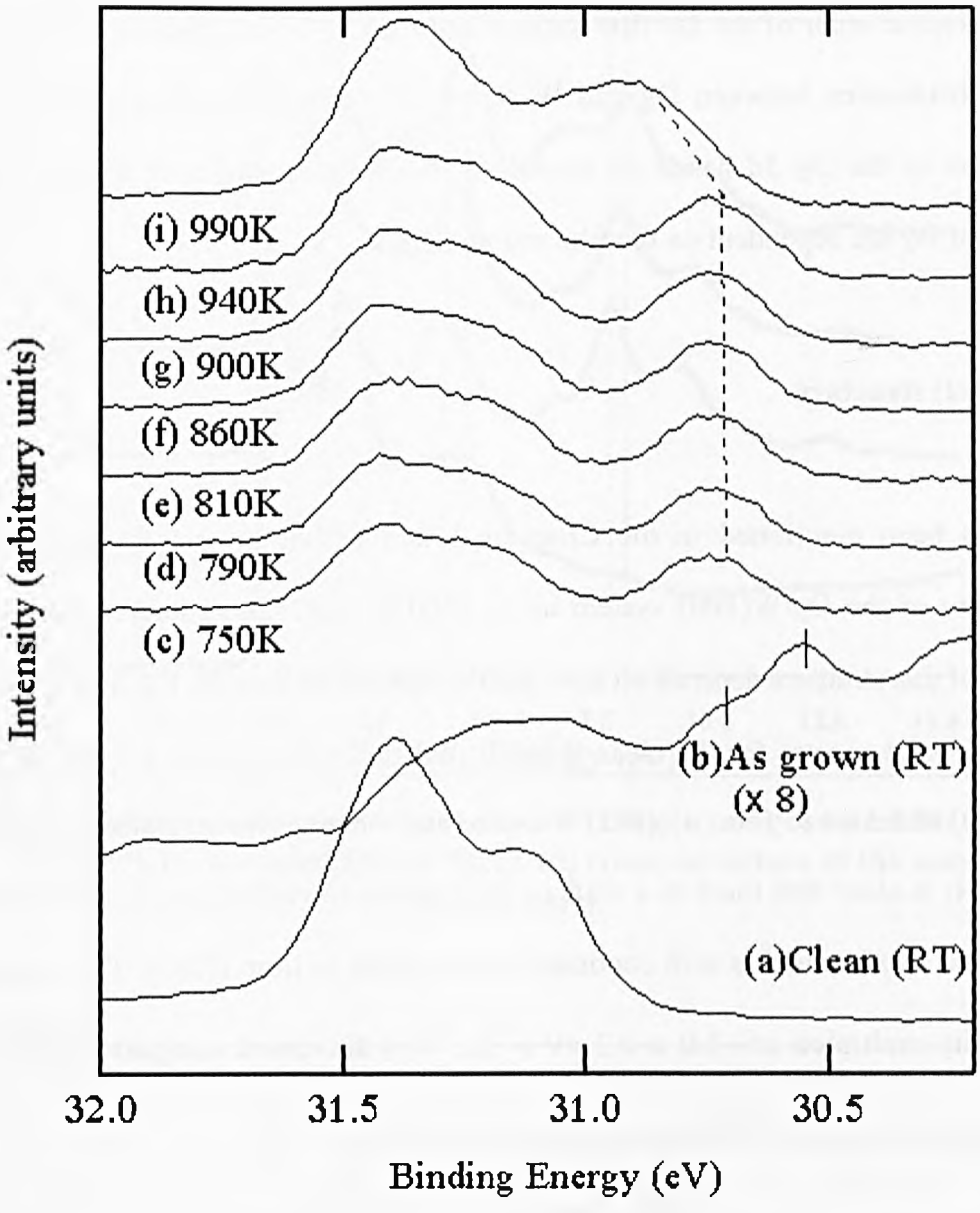

Fig.8.12. Flux–normalised W 4f UPS spectra of the Dy/W(100) system for (a) clean W(100), (b) ~7.5 ML Dy deposited at room temperature and (c)–(i) successive annealing from 750 K to 990 K. h ν = 70 eV. All photoelectron are collected normal to the surface.

In summary the Dy 4f levels in thin films grown on W(100) show an annealing–dependent shift in binding energies. In the early stages of annealing this shift is in the opposite direction to that of the W 4f levels, which is consistent with the fact that the substrate and adsorbate have opposite charge transfer and therefore opposite values of SCLS. On increasing the annealing temperature above 940 K the same direction of SCLS has been observed for Dy 4f levels and W 4f levels. This can be attributed to changes in the

crystallographic order of the Dy film surface and the Dy–W interface on annealing, and to strong hybridisation between Dy and W states. An increase in the Dy 5d intensity and localisation of the Dy 5d bands on annealing shows that changes in the electronic band structure of Dy are dependent on the film morphology.

8.5.3. c(2x2) structure

It has been mentioned in the Chapters 5 and 6 that by increasing the annealing temperature of the Dy/W(100) system up to 1400 K a c(2x2) structure is produced. The coverage of this structure depends on time and the number of anneals. Fig.8.13 shows changes of valence band spectra for the clean W(100), W(100) covered with 1.2 ML of Dy at RT, Dy/W(100) annealed to form a c(8x2) structure and when it was annealed to form a c(2x2) structure. It is clear that there is a shift in Dy features toward higher binding energy from as–grown to c(8x2) and this shift continued by annealing to form c(2x2). The intensity of the Dy majority multiplets at ~8.0 ± 0.2 eV (^{5}L, ^{5}G) decreased compared to Dy minority multiplets at ~4.5 ± 0.2 eV(^{7}F) during annealing to c(2x2).

Fig.8.14 shows W 4f core levels changes correspond to the spectra in Fig.8.13. It is clear from this figure that significant changes have occurred in c(2x2) compared to c(8x2) and the as–grown spectra. Fig.8.15 show the result of line shape analysis for the c(2x2) spectrum. Here all components were chosen to have same asymmetry and Gaussian broadening while all components corresponding to the bulk, surface (S) or sub surface layers (SS) had the same Lorentzian coefficient as components in the same layer.

Table 8.1 shows the result of this analysis. For comparison the results of the line shape analysis for the clean W, as–grown and the c(8x2) (both for 1.2ML Dy), drawn in previous sections, are also presented in this table.

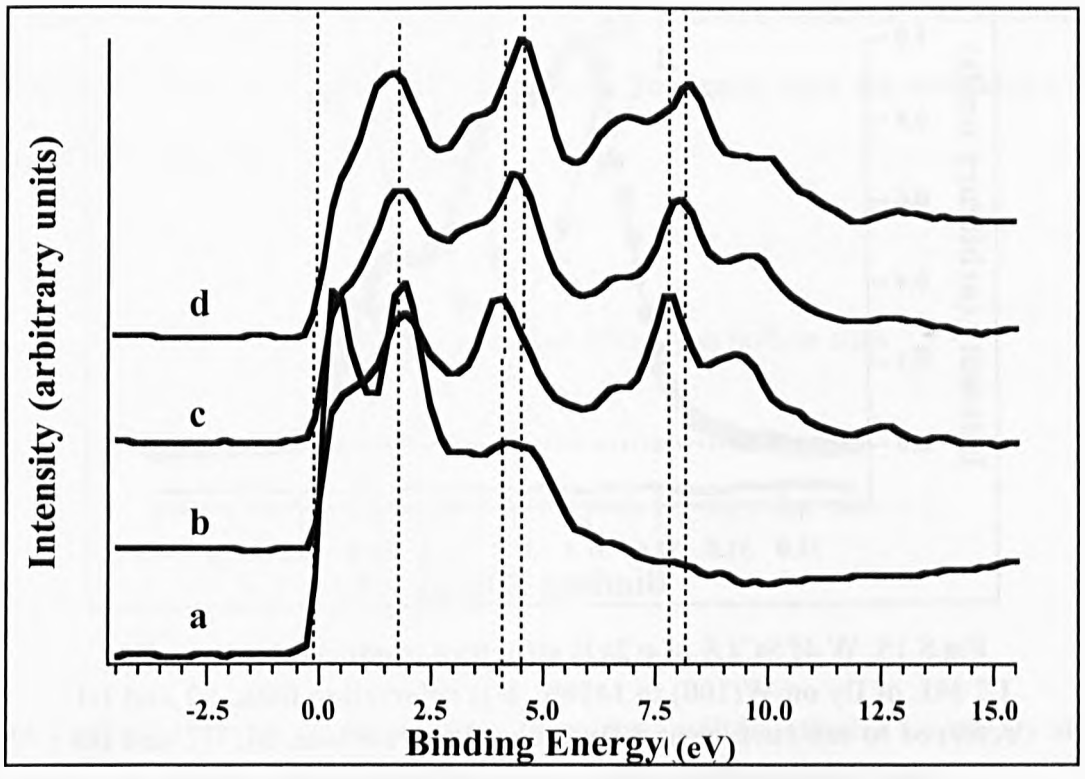

Fig.8.13. Valence band spectra of (a) clean W(100), (b) as–grown 1.2 ML Dy on W(100), (c) annealed film of fig(b), (d) c(2x2) structure of the same film as in fig(c)

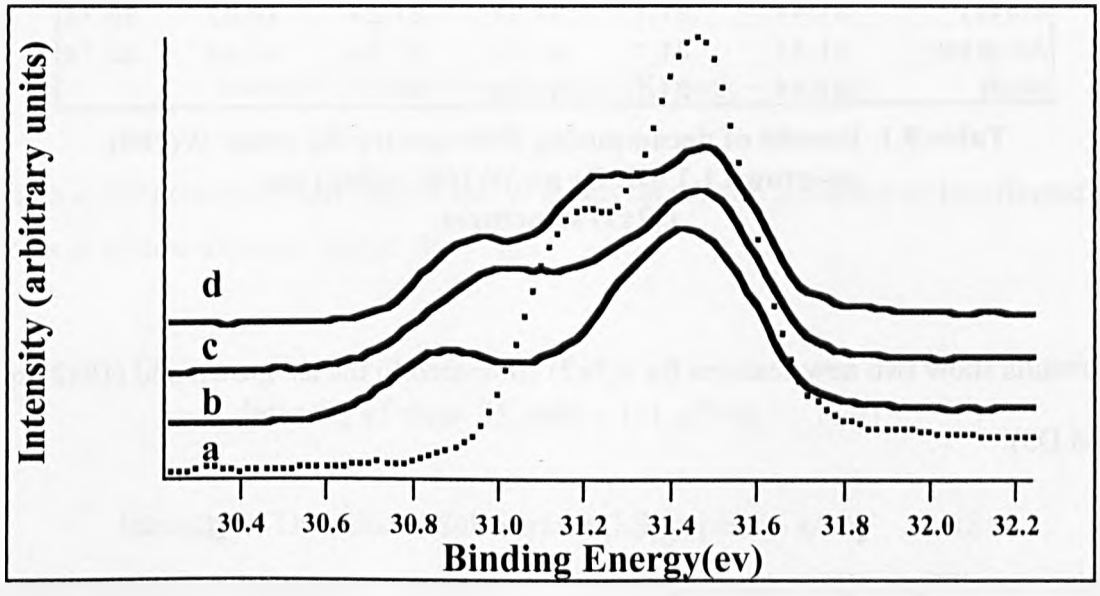

Fig.8.14. Flux–normalised W 4f UPS spectra of the (a) clean W(100), (b) as–grown spectra 1.2 ML Dy on W(100), (c) annealed film (c(8x2) structure) of fig(b), (d) c(2x2) structure of the same film as in fig(c)

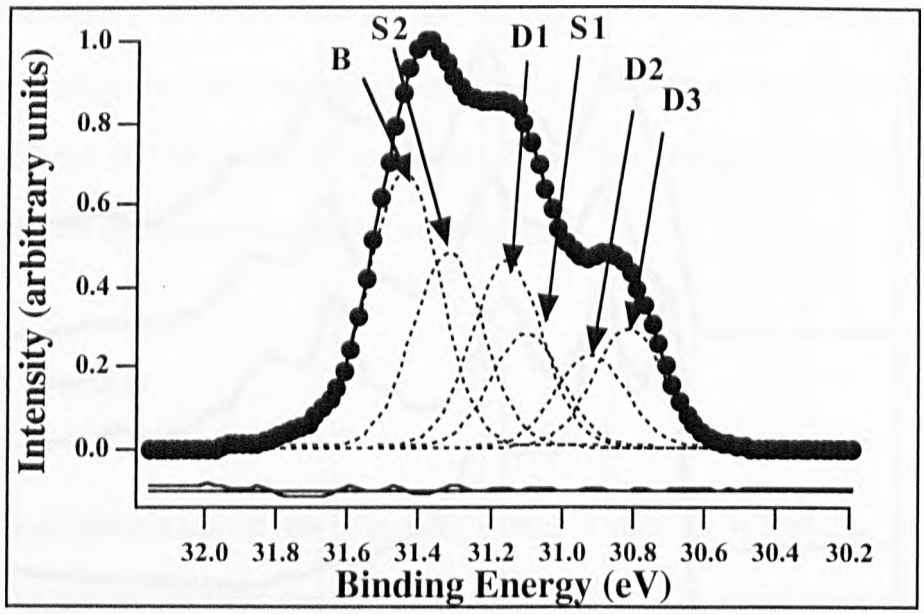

Fig.8.15. W 4f SCLS of c(2x2) structure produced by annealing 1.2 ML of Dy on W(100) to 1400K. B is referred to bulk, S2 and D1 referred to sub surface and Dy induced sub surface, S1, D2 and D3 referred to surface and Dy induced surface components.

	B (eV) (± 0.02)	S1 (eV) (± 0.02)	S2 (eV) (± 0.02)	D1 (eV) (± 0.02)	D2 (eV) (± 0.02)	D3 (eV) (± 0.02)
c(2x2)	31.44	31.1	31.31	31.25	30.92	30.82
c(8x2)	31.44	31.1	31.31	31.24	30.92	30.74
As-grown	31.44	31.1	31.31	31.24	30.92	30.74
clean	31.44	31.1	31.31			

Table.8.1. Results of decomposing W4f spectra for clean W(100), as-grown 1.2 ML Dy on W(100), c(8x2) and c(2x2) structures.

These results show two new features for c(2x2) compared to the as-grown and c(8x2) spectra (D1 and D3).

Assuming that different Dy induced surface (S_{Dy}) peaks are correspond to different registry of Dy atoms on the surface, it is possible to check the consistency of these results by the following considerations. Since at high annealing temperature used to form c(2x2) structure, Dy atoms have enough energy to move around, it is less likely that Dy atoms will choose top sites which are the most unstable registry from an energy point of view. Therefore in the

following analysis only hollow and bridge sites are going to be considered. Furthermore, in the following discussion, the intensity of components from each layer are normalised to total intensity of that layer. Now imagine that:

ratio of the surface area covered with Dy at hollow sites = x

ratio of the surface area covered with Dy at bridge sites = y

Since in a c(2x2) structure all W atoms on the surface will be affected by the Dy atoms in hollow sites (or bridge site) then :

Intensity of S_{Dy} peaks correspond to hollow sites ~ x (8.1)

Intensity of S_{Dy} peaks correspond to bridge sites ~ y (8.2)

Intensity of total clean Surface (S) peak ~ 1-(x+y) (8.3)

Since in a c(2x2) structure half (all) of the W atoms on the sub surface will be affected by the Dy atoms in hollow sites (or bridge site) then

Intensity of clean SS peak ~ 1- (x/2+y) (8.4)

Intensity of Dy induced Sub Surface (SS_{Dy}) peak ~ x/2+y (8.5)

The intensities of S, S_{Dy}, SS and SS_{Dy} peaks were measured (Table 8.2). Then by choosing different values for x and y, the intensities for the other peaks were calculated using equations 8.1 to 8.5 and the most consistent set of results are shown in Table 8.2. It is clear from these

results that the calculated results are consistent with the experimental results. Therefore, 34% of the surface is uncovered and 66 % of it was covered with Dy in a way such that 38% had Dy at hollow sites (x = D_3) and 28% had Dy at bridge sites (y = D_2). However, the total intensity of W 4f was dropped from 0.6 in the clean surface case to 0.36 in the c(2x2) case. This change can be interpreted by assuming that the surface area covered with bridge sites (y) was made of partially covered areas with double layer thickness.

	Measured intensity	Calculated intensity
Surf(S1)	0.34	0.34
SDy-1(D2)	0.28	
SDy-2(D3)	0.38	
total Surface	1	1
SS (S2)	0.51	0.53
SSDy(D1)	0.49	0.47
total Sub Surface	1	1
x		0.38
y		0.28

Table.8.2. Measured and calculated intensities for different component in Fig.8.15. Intensities of components of each layer are expressed relative to total intensity of that layer.

Diameter of Dy atom (~ 3.5 Å) is slightly higher than size of the hollow between Dy atoms in c(2x2) structure (~2.8 Å), as a result separation of c(2x2) layers is very small. Therefore it is likely that by slight movement of Dy atoms a flat layer with strained c(2x2) structure was produced. Since this did not show in the LEED pattern this is certainly not the case. Another possibility is that the bridge site area is covered with a double layer of more dense and disordered structure. For example, it is possible that by annealing to such a high temperature (1400K) the c(8x2) structure, formed at 800 K prior to c(2x2), became slightly disordered while Dy atoms at bridge sites are still in position. This disordered structure then will only participate as background in the LEED pattern. This model is supported by the observation that the position of the peak of $S_{Dy\text{-}1}$ at (30.92 ± 0.02 eV) is almost same as the position of the ordered close packed c(8x2), discussed in section 8.5.1.

Chapter 9

Summary and conclusions

9.1. Growth mode studies

The growth mode of Dy on different W substrates (W(100), W(112) and W(110)) at RT and at elevated temperatures was determined by XPS of Dy $3d_{3/2}$ and W 4f intensities. A relatively complicated growth mode was found for Dy on W(100) which can be described by a SK growth mode. The growth mode showed that restructuring of the Dy film occurs from a thickness of approximately one monolayer, in a manner which has been found to be very reproducible. For Dy on W(112) a laminar growth was found at RT up to 3 ML. At elevated temperature (570K) this laminar growth continued up to 4ML. At RT Dy grew laminar up to two ML on W(110) and then changed to island growth. At elevated temperature (570K) Dy grew laminar up to three ML and then changed to island growth.

9.2. Structural analysis using LEED

9.2.1. LEED studies of Dy/W(100)

LEED has been used to study the structure and growth mechanism of Dy thin films on W(100), W(112) and W(110).

The LEED results showed that Dy films grown on W(100) at RT were highly disordered. By growing Dy on W(100) at 470K, an epitaxial relation was found for Dy/W(100) in which Dy(0001) || W(100) and Dy[$11\bar{2}0$] || W[010]. Annealing to 770 K would significantly improve the quality of the LEED pattern.The Dy hexagonal lattice is slightly distorted along the [010] and [001] axes of the W(100) substrate, resulting in a c(8x2)

commensurate unit cell with respect to the W substrate. In this case the lattice constants of the Dy overlayer have been found to be extended by 0.69% (along W[010]) and by 1.47% relative to the Dy bulk lattice constant. Therefore, the unit mesh of the Dy overlayer is expanded by 1.88% relative to the basal plane of the Dy.

Another interesting structure was observed in the case of the Dy/W(100) system. This was a c(2x2) structure at submonolayer coverage produced by annealing the Dy film to high temperature which showed high–temperature stability up to 1500 K

9.2.2. LEED I–V

LEED I–V curves have been collected for clean W(100) and Dy/W(100) systems (c(8x2) and c(2x2)). Computer calculations based on these LEED I–V curves are now in progress by the Rare Earth Group of the University of Liverpool.

9.2.3. LEED studies of Dy/W(112)

For more than 1ML of Dy grown on W(112) at RT, an epitaxial growth mode was found in which **Dy**(0001)||**W**(112) with **Dy**$[11\bar{2}0]$||**W**$[11\bar{1}]$. However a high background intensity and a limited energy range over which the Dy spots were visible suggests that the film was not well ordered. Annealing the as–grown film up to 500 K improved the intensity of the spots and reduced the background slightly. By annealing Dy/W(112) to 800 K the LEED pattern changed to streaks along the W [110] direction.; annealing above 1200K, the streaks disappeared and extra spots appeared in the pattern; annealing to 1370 K produced a complicated pattern which could be seen up to 1670K.

Unlike growth at RT, growth of Dy when the substrate was kept at 470 K and 570 K produced a LEED pattern with streaks. Despite this difference, the effect of annealing

temperature on LEED pattern was the same as for the case of RT growth.

9.3. STM analysis

Clean surfaces of W(100) and W(112) and the growth of Dy on W(100) and W(112) were studied by STM. The effects of the substrate and also the effects of annealing temperature on the morphology of the Dy film were investigated.

9.3.1. STM studies of Dy/W(100)

This study confirmed SK growth for Dy on W(100) at RT and that 770 K is the optimum annealing temperature for Dy/W(100) which will produce flat and well–ordered films of c(8x2) structure. It was also found that annealing to 820 K produced well–ordered islands of Dy with c(8x2) structure. Further investigation showed that unlike Gd on W(100), the direction of increase in terrace heights for Dy islands is same as the step height of bulk.

STM studies of the c(2x2) structure at submonolayer coverage showed that domains of c(2x2) were formed near to the step edges.

9.3.2. STM studies of Dy/W(112)

In the submonolayer regime, STM showed that Dy grew with domains of atomic rows which were along W[1 $\bar{1}$ 0]. For coverages between 1ML and 2ML the surface is covered with string–like atomic rows, with irregular lengths and distances, on top of the first ML of Dy. The rows were aligned almost along W[11 $\bar{1}$]. For 5ML of Dy grown at RT on W(112) flat terraces of Dy were observed.

By annealing to 500K, Dy films changed to elongated islands which were strained along W[1 1 $\bar{1}$]. This is in agreement with the appearance of streaks in the **W**[1 $\bar{1}$ 0] direction in the LEED pattern. The domains were mono–atomic Dy layers with a thickness of 2.8 Å and a average width of ~30 Å.

Annealing to 1100 K produced flat domains of Dy elongated along W[1 1 $\bar{1}$]. The distance between stripes along **W**[1 $\bar{1}$ 0] was found to be irregular. This irregularity is the reason of appearance of streaks in the LEED pattern along **W**[1 $\bar{1}$ 0]

Annealing to 1500 K produced flat and well–ordered films. Atomic resolution of the STM images showed that the surface was made from furrow–shaped domains along W[1 1 $\bar{1}$] which contained atomic rows parallel to the steps.

Annealing to 1600 K produced another structure of Dy on W(112) in which steps were almost along **W**[1 $\bar{1}$ 0] and had teeth–like edges. The edges of these teeth were sharp with an average angle of 66° and pointed towards W[1 1 $\bar{1}$]. It was also possible to resolve atomic rows on the surface.

9.4. Electronic properties of Dy/W(100)

9.4.1. SCLS analysis

CLS measurements of the W 4f 7/2 peaks have been performed for clean W(100), during the growth of Dy on W(100) and for Dy/W(100) after annealing at different temperatures (including c(8x2) and c(2x2) structures). The spectra obtained were fitted with convoluted Doniach-Sunjic/Gaussian lineshapes. CLS of 0.11 ± 0.02 eV and 0.34 ± 0.02 eV

toward lower binding energies were found for the clean W(100) which correspond to surface and subsurface layers. For 1.2 ML of Dy grown on W(100) at RT, three additional features were found that had CLS of 0.20 ± 0.02 eV, 0.52 ± 0.02 eV and 0.70 ± 0.02 eV toward lower binding energies. The first one is an Dy induced subsurface feature and rest of them are Dy induced surface features. By annealing from 750 K to 940 K the morphology of the Dy film on the surface has changed which resulted in changes of intensities of these features. However, no additional features were observed. By investigating intensity changes for these components, structural changes of Dy film during annealing were interpreted. These considerations suggest that the Dy induced surface feature with SCLS of 0.52 ± 0.02 eV is an interfacial feature related to the well ordered c(8x2) structure and the other Dy induced surface feature with SCLS of 0.7 ± 0.02 eV is from disordered Dy structure on the surface. CLS analysis of W $4f_{7/2}$ after formation a c(2x2) structure showed that Dy induced subsurface feature has a CLS of 0.26 ± 0.02 eV and the Dy induced surface features are at 0.52 ± 0.02 eV and 0.62 ± 0.02 eV. Analysis of intensities of components suggest that the surface induced component with a CLS of 0.62 ± 0.02 eV is from the area with a c(2x2) structure positioned at hollow sites. The other Dy induced surface component is from an area in which Dy atoms are at bridge sites. This can be either a double layer c(2x2) structure or most likely from a denser but disordered double layer structure.

9.4.2. Valence band studies

A valence band study of Dy/W(100) showed that there is an interfacial hybridisation between Dy 4f (^7F) and a broad feature of W(100) at binding energy ~4.5 ± 0.2 eV. This hybridisation can be one of the reasons responsible for the strong bonding between Dy and W resulting in high thermal stability of Dy superstructures on W(100). By increasing the Dy coverage up to 1.75ML the Dy 4f features are shifted to lower binding energies; for higher coverages they showed a shift to higher binding energies. This change in direction of the shift

could be due to reduction of strain in the Dy film. Annealing the as–grown film shifted the Dy 4f features to higher binding energies. These shifts to higher binding energies were also observed for the c(2x2) structure. Increasing the Dy overlayer thickness, during growth at RT, to more than 2 ML contributes to bulk–like Dy which will produce Dy 5d–6s hybridisation. This can be interpreted to be a result of formation of dense islands of Dy. Annealing the as–grown film and producing a well–ordered film of c(8x2) structure will intensify the Dy 5d–6s hybridisation. While during the growth, direction of shift for the W $4f_{7/2}$ and the Dy VB is the same (toward lower binding energy), they showed an opposite direction of shift on annealing (Dy toward higher binding energies and W toward lower binding energies). Since W is more electronegative than Dy the opposite direction of shift on annealing can be attributed to the charge transfer between Dy and W. However, the same direction of shift during the growth can not be a result of charge transfer between Dy and W and it is most likely due to strain in the overlayer film.

9.5. Summary

In summary, the growth modes of Dy on different W substrates (W(100), W(112) and W(110)) at RT and at elevated temperatures have been determined. Film morphology of Dy on W(100) and W(112) has been investigated by LEED and STM, and the results were found to be completely consistent with each other. For Dy on W(100) the best annealing temperatures at which flat and well–ordered films can be produced have been determined and different structures resulting from different annealing conditions have been found, including c(8x2), c(2x2) and (6x2) . In the case of Dy on W(112), a complicated LEED pattern was found after high temperature annealing and the atomic structure of the film was resolved by STM. Finally electronic changes of Dy and W(100) during deposition and in different film morphologies, resulting from different annealing conditions, have been investigated with UPS of core levels and the valence levels. As an example of application of the results of these

studies, they can be used as a complementary technique to LEED, to monitor film morphology in preparation of different structures by annealing. This can be of significant importance when a Dy film is investigated with synchrotron radiation and the chamber is not equipped with STM.

9.6. Future work

It is now understood how a flat and well–ordered film of Dy can be produced on W(100) (with a c(8x2) structure) and electronic changes of Dy and W have been investigated. It is important to complete our knowledge about the electronic structure of this film by investigating the band structure of Dy in this film and comparing to it that of the bulk Dy. This can be done, for example, by Angle Resolved Photoemission Spectroscopy and Inverse Photoemission experiments. It is also useful to take advantage of the easy preparation of Dy films and use them as substrates for growth of other metals, especially rare earth metals. For example, remembering that the annealing temperature of Dy for c(8x2) is higher than that of Gd [147], it should be possible to anneal Gd on top of a c(8x2) film of Dy to produce well–ordered Gd films on Dy. It would also be interesting to study the magnetic properties of Dy in the c(8x2) structure and to compare them to those of bulk Dy. This can be done by different experiments such as Magnetic Circular (and Linear) Dichroism and Spin Polarised Photoemission Spectroscopy. To find out what is the actual registry of Dy atoms in the c(8x2) and c(2x2) structures, the results of LEED I-V (or similar experiments such as Photoelectron Diffraction) seems crucial.

In the case of Dy/W(112) first it is important to find out what is the real structure of the lattice determined by LEED and STM (chapters 5 and 6). Following that studies can be made of the electronic structures of the interface by performing SCLS and VB–UPS experiments. Finally, all future work mentioned for Dy/W(100) can be applied for Dy/W(112) to study the

effect of different surface structures of the substrate. In the case of Dy/W(110), first STM studies of the films are necessary and then all future work mentioned for Dy/W(112) can be applied.

List of acronyms and abbreviations

AES	Auger electron spectroscopy
ARUPS	angle-resolved UPS
As-t	Auger signal–time
BE	binding energy
BG	background
dhcp	double hexagonal close-packed
DOS	density of states
DS	Doniach-Sunjic
EDC	energy distribution curve
fcc	face centred cubic
FFT	Fast Fourier Transform
FM	Frank-van der Merwe
FWHM	full width at half maximum
hcp	hexagonal close-packed
HFM	horizontal focusing mirror
IMFP	inelastic mean free path
IPE	inverse photoemission
I-V	intensity-voltage
LEED	low energy electron diffraction
LSDA	local–spin–density approximation
MBE	Molecular Beam Epitaxy
MCP	microchannel plate
mfp	mean free path
ML	monolayer
MOKE	magneto-optic Kerr effect
MSM	Monolayer Plus Simultaneous Multilayer
MSR	magnetic surface reconstructions

PBN	Pyrolytical Boron Nitride
PE	photoemission
PEs-t	Photoemission signal–time
RE	rare earth
REG	rare earth group
RHEED	reflectance high energy electron diffraction
RKKY	Ruderman-Kittel-Kasuya-Yoshida
RM	refractory metal
SCF-LMTO-ASA	Linear Muffin–Tin Orbital method coupled with the Atomic–Sphere–Approximation
SCLS	surface core level shift
SEMO	surface-enhanced magnetic order
SK	Stransky-Krastanov
SM	Simultaneous Multilayer
SODS	surface-order-dependent state
SPARUPS	spin-polarised ARUPS
SPPD	spin–polarised photoelectron diffraction
SPSEES	spin–polarised secondary electron emission spectroscopy
SRS	Synchrotron Radiation Source
STM	scanning tunnelling microscope
TM	transition metal
TSP	Titanium Sublimation Pump
VB	valence band
VW	Volmer–Weber
UHV	ultra-high vacuum
UPS	ultraviolet photoelectron spectroscopy
VFM	Vertical Focusing Mirror
XPS	x-ray photoelectron spectroscopy

References

[1] C. F. Majkrzak, J. Kwo, M. Hong, Y. Yafet, D. Gibbs, C. L. Chien and J. Bohr, *Adv. Phys.* **40** (1991) 99-189.

[2] B. Demri, C. Burggraf and N. Mesboua, *Appl. Surf. Sci.* **65/66** (1993) 59-62.

[3] F. P. Netzer, *J. Phys.: Condens. Matter* **7** (1995) 991.

[4] R. Rossi, *Surf.Sci. Rep.* **7** (1987) 1.

[5] W. A. Henle, P. P. Netzer, R. Cimino and W. Brauns, *Surf. Sci.* **221** (1998) 131.

[6] S. D. Barrett and S. S. Dhesi, *The structure of rare-earth metal surfaces*, (World Scientific,Singapore,2001).

[7] B. Jorgensen, M. Christiansen and J. Onsgaard, *Surf.Sci.* **251/252** (1991) 519.

[8] H. Li, D. Tian, J. Quinn, Y. S. Li, S. C. Wu and F. Jona, *Phys. Rev. B* **45** (1992) 3853-3856.

[9] A. T. Loburets, A. G. Naumovets and Y. S. Vedula, *Surf. Sci.* **399** (1998) 279-304.

[10] Y. B. Losovyj, N. T. Dubyk and F. M. Gonchar, *Vacuum* **50** (1998) 85-87.

[11] Y. Ufuktepe, *Physica status solidi(b)* **167** (1991) K17-L20.

[12] Y. Ufuktepe, *J. Phys: Condens. Matter* **5** (1993) L213-L216.

[13] E. Bauer, *Appl. Surf. Sci.* **11-2** (1982) 479-494.

[14] F. M. Gonchar, V. K. Medvedev, T. P. Smereka, Y. B. Lozovyi and G. V. Babkin, *Fiz. Tverd. Tela* **29** (1987) 2833-2836.

[15] S. A. Shakirova, V. A. Pleshkov and G. A. Rump, *Surf. Sci.* **279** (1992) 113-118.

[16] R. Du and C. P. Flynn, *J. Phys.: Condens. Matter* **2** (1990) 1336.

[17] T. P. Smereka, I. M. Ubogyi and Y. Losovyi, *Vacuum* **46** (1995) 429-432.

[18] F. M. Gonchar, V. K. Medvedev, T. P. Smereka and G. V. Babkin, *Fiz. Tverd. Tela* **32** (1990) 1872.

[19] V. K. Medvedev, T. P. Smereka, L. P. Zadorozhnyi and F. M. Gonchar, *Fiz. Tverd.*

Tela **35** (1993) 1251.

[20] A. Ciszewski and A. J. Melmed, *J. Cryst. Growth* **69** (1984) 253-259.

[21] S. D. Barrett, S. S. Dhesi, M. P. Evans and R. G. White, *Meas.Sci.Technol* **4** (1993) 114-119.

[22] B. J. Beaudry and K. A. Gschneidner, in *Handbook on the Physics and Chemistry of Rare Earths*, Eds: K. A. Gschneidner and L. Eyring, (North-Holland,,1978) ,vol. 1,pp. 173.

[23] Becker, *j. Appl. Phys* **41** (1970) 1055.

[24] R. J. Radwanski, J. J. M. Franse and S. J. Sinnema, *j. Magn. Magn. Mater.* **70** (1987) 313.

[25] J. S. Kang et al., *Phys. Rev. B* **48** (1993) 10327.

[26] M. H. Lee, *Electronic and structure studies of Gd/W and Y/W thin films*, PhD thesis, University of Liverpool, Liverpool, 1997.

[27] W. E. Wallace, *Chem. Tech.* (1982) 752.

[28] W. A. Henle, M. G. Ramsey, F. P. Netzer and K. Horn, *Surf. Sci.* **254** (1991) 182.

[29] K. N. Tu, R. D. Thompson and B. Y. Tsaur, *Appl. Phys. Lett.* **38** (1981) 326.

[30] H. L. Skriver, in *Systematics and Properties of the Lanthanides*, Eds: S. P. Sinha, (Reidel,Dordrecht,1982) .

[31] Z. B. Goldschmidt, in *Handbook on the Physics and Chemistry of Rare Earths*, Eds: K. A. Gschneidner and L. Eyring, (North-Holland,Amsterdam,1978) ,vol. 1,pp. 173.

[32] S. D. Barrett, *Surf. Sci. Rep.* **14** (1992) 271.

[33] N. P. Tucker, *Magnetic structure of Gd thin-film surfaces*, PhD thesis, University of Liverpool, Liverpool, 1997.

[34] M. Winter, *WebElements TM* (1993-2001), http://www.webelements.com/, last update: 30.7.2001, date of access: 10.8.2001.

[35] W. M. Temmerman, Z. Szotek and H. Winter, *Physical Review B* **47** (1993) 1184-1189.

[36] W. A. Henle, M. G. Ramsey, F. P. Netzer, S. Witzel and W. Braun, *Surf. Sci.* **243**

(1991) 141-150.

[37] B. Johansson and N. Martensson, *Phys. Rev. B* **21** (1980) 4427.

[38] B. Johansson, *Phys. Rev. B* **20** (1979) 1315.

[39] B. Johansson, *Phys. Rev. B* **19** (1979) 6615.

[40] G. K. Wertheim and G. Crecelius, *Phys. Rev. Lett.* **40** (1978) 813.

[41] F. Gerken, A. S. Flodstrom, J. Barth, L. I. Johansson and C. Kunz, *Physica Scripta* **32** (1985) 43-57.

[42] M. Domke, C. Laubschat, M. Prietsch, T. Mandel, G. Kaindl and W. D. Schneider, *Phys. Rev. Lett.* **56** (1986) 1287.

[43] F. Patthey, E. L. Bullock, W. D. Schneider and F. Hulliger, *Zeitschrift fur Physik B: Condensed Matter* **93** (1993) 71-76.

[44] M. Lubcke, B. Sonntag, W. Neimann and P. Rabe, *Phys. Rev. B* **34** (1986) 5184.

[45] B. Johansson and N. Martensson, in *Handbook on the Physics and Chemistry of Rare Earths*, Eds: K. A. Gschneidner, L. Eyring, and S. Hufner, (North-Holland,Amsterdam,1987) ,vol. 10,pp. 173.

[46] M. Campagna, G. K. Wertheim and E. Bucher, *Struct. Bonding* **30** (1976) 99.

[47] G. Kaindl, C. Laubschat, B. Reihl, R. A. Pollak, N. Martensson, F. Holtzberg and D. E. Eastman, *Phys. Rev. B* **26** (1982) 1713.

[48] Y. Baer and W. Schneider, in *Handbook on the Physics and Chemistry of Rare Earths*, Eds: K. A. Gschneidner, L. Eyring, and S. Hufner, (North-Holland,Amsterdam,1987) ,vol. 10,pp. 1.

[49] W. T. Carnall, P. R. Fields and K. Rajnek, *J. Chem. Phys.* **49** (1968) 4424.

[50] F. Gerken, *J.Phys.F:Met.Phys.* **13** (1983) 703-713.

[51] S. D. Barrett and R. G. Jordan, *Z. Phys. B (Condens. Matter)* **66** (1987) 375.

[52] P. H. Citrin, G. K. Wertheim and Y. Baer, *Phys. Rev. Lett* **41** (1978) 1425.

[53] S. F. Alvarado, M. Campagna and W. Gudat, *J. Electron Spectrosc. Rel. Phen.* **18** (1980) 43.

[54] A. M. Begley, R. G. Jordan, W. M. Temmerman and P. J. Durham, *Phys. Rev. B* **41** (1990) 11780.

[55] F. Gerken, J. Barth and R. Kammerer, *Surf. Sci.* **117** (1982) 468-474.

[56] R. Kammerer, J. Barth, F. Gerken, A. Flodstrom and L. I. Johansson, *Solid State Commun.* **41** (1982) 435.

[57] D. R. Penn, *Phys. Rev. B* **13** (1976) 5248.

[58] S. D. Barrett, A. M. Begley, P. J. Dorham, R. G. Jordan and W. T. Temmerman, *J. Phys; Condes. Matter* **1** (1989) SB 243.

[59] S. D. Barrett, A. M. Begley, P. J. Dorham and R. G. Jordan, *Solid State Communication* **71** (1989) 111.

[60] M. Erbudak, P. Kalt, L. Schlapbach and K. Bennemann, *Sur. Sci.* **126** (1983) 101.

[61] P. J. Feibelman and D. R. Hamann, *Solid State Commun.* **31** (1979) 413.

[62] D. N. McIlroy, C. Waldfried, Dongqi Li, J. Pearson, S. D. Bader, D. J. Huang, P. D. Johnson, R. F. Sabiryanov, S. S. Jaswal and P. A. Dowben, *Phys. Rev. Lett.* **76** (1996) 2802.

[63] J. Kondo, *Theory of dilute magnetic alloys*, vol. 23, (Academic Press,New York,1969).

[64] A. J. Freeman, in *Magnetic Properties of Rare Earth Metals*, Eds: R. J. Elliott, (Plenum, London) .

[65] C. Schussler-Langeheine, E. Weschke, C. Mazumdar, R. Meier, A. Y. Grigoriev, G. Kaindl, C. Sutter, D. Abernathy, G. Grubel and M. Richter, *Phys. Rev. Lett.* **84** (2000) 5624-5627.

[66] C. Schussler-Laneheine, E. Weschke, H. Ott, A. Y. Grigoriev, A. Moller, R. Meier, C. Mazumdar and G. Kaindl, *J. Electron Spectrosc. Relat. Phenom.* **114** (2001) 795-799.

[67] S. K. Sinha, in *Handbook on the Physics and Chemistry of Rare Earths*, Eds: K. A. Gschneidner and L. Eyring, (North-Holland,Amsterdam,1978) ,vol. 1,pp. 173.

[68] C. Rau, *J. Magn. Magn. Mat.* **31** (1983) 874.

[69] C. Rau, *J. Magn. Magn. Mat.* **30** (1982) 141.

[70] D. Weller, S. F. Alvarado and M. Campagna, *Physica B* **130** (1985) 72.

[71] D. Weller, S. F. Alvarado, M. Campagna, W. Gudat and D. D. Sarma, *J. Less-Common Metals* **111** (1985) 277.

[72] D. Weller, S. F. Alvarado, W. Gudat, K. Schroder and M. Campagna, *Phs. Rev. Lett.* **54** (1985) 1555-1558.

[73] J. Tang, J. M. Lawrence and J. C. Hemminger, *Phys. Rev. B* **48** (1993) 15342.

[74] J. Tang, J. M. Lawrence and J. C. Hemminger, *Phys. Rev. B* **47** (1993) 16477.

[75] E. Vescovo, C. Carbone and O. Rader, *Phys. Rev. B* **48** (1993) 7731.

[76] E. D. Tober, F. J. Palomares, R. X. Ynzunza, R. Denecke, J. Morais, Z. Wang, G. Bino, J. Liesegang, Z. Hussain and C. S. Fadley, *Phys. Rev. Lett.* **81** (1998) 2360.

[77] D. M. Bylander and L. Kleinman, *Phys. Rev. B* **50** (1994) 4996.

[78] O. Eriksson, R. Ahuja, A. Ormeci, J. Trygg, O. Hjortstam, P. Söderlind, B. Johansson and J. M. Wills, *Phys. Rev. B* **52** (1995) 4420.

[79] J. J. Yeh and I. Lindau, *Atomic Data and Nuclear Data Tables* **32** (1985) 1-155.

[80] J. A. Scarfe, A. R. Law, H. P. Hughes, J. A. C. Bland, G. M. Roe and A. P. Walker, *Phs.Stat.sol.(b)* **171** (1992) 377-391.

[81] T. Kachel, R. Rochow, W. Gudat, R. Jungblut, O. Rader and C. Carbone, *Phys. Rev. B* **45** (1992) 7267-7271.

[82] M. Kai, A. Tanaka and T. Jo, *J. Phys. Soc. Japan* **64** (1995) 2356-2359.

[83] A. Moewes, M. M. Grush, T. A. Callcott and D. L. Ederer, *Phys. Rev. B* **60** (1999) 15728-15731.

[84] O. P. Sairanen, *Physica Scripta* **T41** (1992) 163-167.

[85] N. P. Tucker, R. I. R. Blyth, R. G. White, M. H. Lee, A. W. Robinson and S. D. Barrett, *J. Synch. Rad.* **2** (1995) 252-255.

[86] T. P. Smereka, I. M. Ubogyi and Y. Losovyi, *Vacuum* **46** (1995) 429-432.

[87] M. P. Seah and W. A. Dench, *Surf. and Interface Anal* **1 (1979) 2.** (1979) 2.

[88] V. R. Dhanak, *Station 4.1* (2001), http://srs.dl.ac.uk/station/4.1/, last update: 31 October 2000, date of access: 15 th October.

[89] V. R. Dhanak, A. G. Shard, C. A. Muryn, P. L. Wincott and G. Thornton, *J. Synch. Rad* (1997) .

[90] S. D. Barrett, *Image SXM* (1994), http://reg.ssci.liv.ac.uk, last update: 2001, date of access: .

[91] F. C. Frank and J. H. van der Merwe, *Proc. R. Soc. A* **198** (1949) 205.

[92] E. Bauer, *Z. Kristallogr.* **110** (1958) 372.

[93] A. Y. Cho, *J. Cryst. Growth* **95** (1989) 1.

[94] H. Luth, *Surfaces and Interfaces of Solids*, (Springer - Verlag Press,1993).

[95] R. G. White, *Photoemission studies from epitaxialGd and Y thin films*, PhD thesis, University of Liverpool, Liverpool, 1996.

[96] Volmer.M and A. Weber, *Z. Phys. Chem.* **119** (1926) 277.

[97] H. J. Gossmann and G. J. Fisanick, *Surs. Sci. Letters* **244** (1991) L117.

[98] M. H. Grabow and G. H. Gilmer, *Surf. Sci.* **194** (1988) 333.

[99] M. Zinke–Allmang, L. C. Feldman and M. H. Grabow, *Surf. Sci.* **200** (1988) L427.

[100] A. Faldt and H. P. Myers, *Phys. Rev. B* **30** (1984) 5481-5486.

[101] A. Faldt and H. P. Myers, *Phys. Rev. B* **34** (1986) 6675-6680.

[102] R. Fasel, M. Gierer, H. Bludau, P. Aebi, J. Osterwalder and L. Schlapbach, *Surf. Sci.* **374** (1997) 104-116.

[103] I. Chorkendorff, J. Kofoed and J. Onsgaard, *Surf. Sci.* **152/153** (1985) 749.

[104] T. Gourieux, B. Kierren, F. Bertran, D. Malterre and G. Krill, *Surf. Sci.* **352** (1996) 557-561.

[105] V. Schorsch, E. Beaurepaire, A. Barbier, J. P. Deville, B. Carriere, T. Gourieux and K. Hricovini, *Surf. Sci.* **309** (1994) 603-607.

[106] D. LaGraffe, P. A. Dowben, L. Dottl, Y. Ufuktepe and M. Onellion, *Zeitschrift fur Physik B: Condensed Matter* **82** (1991) 47-52.

[107] J. N. Andersen, I. Chorkendorff, J. Onsgaard, J. Ghijsen, R. L. Johnson and F. Grey, *Phys. Rev. B* **37** (1988) 4809-4812.

[108] A. Faldt and H. P. Myers, *J. Magn. Magn. Mater.* **47-8** (1985) 225-227.

[109] W. Schneider, S. L. Molodtsov, M. Richter, T. Gantz, P. Engelmann and C. Laubschat, *Phys. Rev. B* **57** (1998) 14930-14936.

[110] A. Faldt, K. Kristensson and H. P. Myers, *Phys. Rev.* ***B*** **37** (1988) 2682.

[111] C. Carbone, R. Rochow, L. Braicovich, R. Jungblut, T. Kachel, D. Tillmann and E. Kisker, *Phys. Rev. B* **41** (1990) 3866-3869.

[112] M. Taborelli, R. Allenspach and M. Landolt, *Phys. Rev. B* **34** (1986) 6112-6116.

[113] M. Taborelli, R. Allenspach, G. Boffa and M. Landolt, *Phs. Rev. Lett.* **56** (1986) 2869-2872.

[114] J. N. Andersen, J. Onsgaard, A. Nilsson, B. Eriksson and N. Martensson, *Surf. Sci.* **202** (1988) 183-203.

[115] A. Stenborg and E. Bauer, *Surf. Sci.* **189** (1987) 570-577.

[116] A. Stenborg and E. Bauer, *Surf. Sci.* **185** (1987) 394-412.

[117] A. Stenborg, J. N. Andersen, O. Bjorneholm, A. Nilsson and N. Martensson, *Phs. Rev. Lett.* **63** (1989) 187-190.

[118] D. Weller and S. F. Alvarado, *Phys. Rev. B* **37** (1988) 9911-9914.

[119] A. Stenborg and E. Bauer, *Phys. Rev. B* **36** (1987) 5840-5847.

[120] N. Martensson, A. Stenborg, O. Bjorneholm, A. Nilsson and J. N. Andersen, *Phs. Rev. Lett.* **60** (1988) 1731-1734.

[121] C. Rau, C. Jin and M. Robert, *Physics Letters a* **138** (1989) 334-338.

[122] M. P. Evans, *Surface Structural and Electronic Properties of Sc and Dy*, PhD thesis, University of Liverpool, Liverpool, 1996.

[123] C. Carbone, J. Nogami and I. Lindau, *Journal of Vacuum Science & Technology a-Vacuum Surfaces and Films* **3** (1985) 972-973.

[124] A. Franciosi, P. Perfetti, A. D. Katnani, J. H. Weaver and G. Margaritondo, *Phys. Rev. B* **29** (1984) 5611-5616.

[125] J. Nogami, C. Carbone, D. J. Friedman and I. Lindau, *Phys. Rev. B* **33** (1986) 864-872.

[126] R. Du, F. Tsui and C. P. Flynn, *Phys. Rev. B* **38** (1988) 2941-2943.

[127] S. D. Barrett, R. I. R. Blyth, A. M. Begley, S. S. Dhesi and R. G. Jordan, *Phys. Rev. B* **43** (1991) 4573-4578.

[128] C. Argile and G. E. Rhead, *Surf. Sci. Rep.* **10** (1989) 277-356.

[129] D. P. Woodruff and T. A. Delchar, *Modern Techniques of Surface Science*, (Cambridge University Press,1994).

[130] M. G. Bartheslabrousse and G. E. Rhead, *Surf. Sci.* **116** (1982) 217-224.

[131] J. W. Cooper, *Phys. Rev.* **128** (1962) 681.

[132] L. E. Davis, N. C. MacDonald, P. W. Palmberg, G. E. Riach and R. E. Weber, *Handbook of Auger Electron Spectroscopy*, (Physical Electronics Industries,Minnesota,1972).

[133] W. Lenth, F. Lutz, J. Barth, G. Kalkoffen and C. Kunz, *Phys. Rev. Lett.* **41** (1978) 1185.

[134] W. F. Egelhoff, *Phys. Rev. B* **30** (1984) 1052-1055.

[135] W. F. Egelhoff, *Critical Reviews in Solid State and Materials Sciences* **16** (1990) 213-235.

[136] D. Briggs and M. P. Seah, *Practical Surface Analysis*, vol. 1, (John Wiley & Sons,Chichester,1990).

[137] P. M. A. Sherwood, in *Practical Surface Analysis by Auger and X–ray Photoelectron Spectroscopy*, Eds: D. Briggs and M. P. Seah, (John Wiley and Sons,Chichester,1983) ,pp. 447–475.

[138] D. A. Shirley, *Phys. Rev. B* **5** (1972) 4709.

[139] S. Tougaard, *Surf. Sci.* **139** (1984) 208-218.

[140] S. Tougaard, *Phys. Rev. B* **34** (1986) 6779.

[141] S. Tougaard, *Applied Surf. Sci.* **32** (1988) 332.

[142] S. Tougaard, *Surface and Interface Analysis* **11** (1988) 453.

[143] S. Tougaard, *Surf. Sci.* **216** (1989) 343.

[144] M. A. Van Hove and S. Y. Tong, *Surface Crystallography by LEED*,

(Speringer,Berlin,1979).

[145] J. B. Pendry, *Low Energy Electron Diffraction*, (Academic,London,1974).

[146] M. Domke, C. Laubschat, E. V. Sampathkumaran, M. Prietsch, T. Mandel, G. Kaindl and H. U. Middelmann, *Phys. Rev. B* **32** (1985) 8002-8006.

[147] R. G. White, M. H. Lee, N. P. Tucker, S. D. Barrett and P. W. Murray, *Phys.Rev.B* **56** (1997) R10071.

[148] V. K. Medvedev, T. P. Smereka, S. I. Stepanovski and F. M. Gonchar, *Ukr Fiz Zhurn* **37** (1992) 1053.

[149] C. Waldfried, P. A. Dowben, O. Zeybek, T. Bertrams and S. D. Barrett, *Thin Solid Films* **338** (1999) 1-4.

[150] Y. Losovyj, B, *Vacuum* **48** (1997) 195-198.

[151] J. Kolaczkiewicz and E. Bauer, *Surf. Sci.* **175** (1986) 487-507.

[152] A. Zangwill, *Physics at surfaces*, (Cambridge University Press,Cambridge,1996).

[153] T. Flores, M. Hansen and M. Wuttig, *Surf. Sci.* **279** (1992) 251.

[154] Y. Gauthier, M. Poensgen and M. Wuttig, *Surf. Sci.* **303** (1994) 36.

[155] M. Henzler, *Electron Diffraction and Surface Defect Structure*, (Speringer-Verlag, Berlin, Heidelberg, NewYork,1977).

[156] M. A. Stevens and G. J. Russell, *Surf. Sci.* **104** (1981) 354-364.

[157] J. Kolaczkiewicz and E. Bauer, *Surf. Sci.* **154** (1985) 357-370.

[158] M. W. Holmes and J. E. Inglesfield, *Surf. Sci.* **89** (1979) 133.

[159] Y. Kuk, in *Scanning Tunnelling Microscopy I*, Eds: H. J. Guntherodt and R. Wiesendanger, (Speringer–Verlag,Berlin Heidelberg) .

[160] N. J. DiNardo, *Nanoscale Characterization of Surface and Interfaces*, (VCH verlagsgesellschaft mbH,1994).

[161] H. Wengelink, D. Badt and H. Neddermeyer, *Surf. Sci.* **307-309** (1994) .

[162] S. B. M. Hågstrom, C. Nordling and K. Seigbahn, *Z,phys.* **178** (1964) 433.

[163] K. Wandelt, *Surf. Sci. Rep.* **2** (1982) 1.

[164] U. Gelius, *Phys. Scripta* **9** (1974) 133.

[165] T. M. Duc, C. Guillot, Y. Lassailly, J. Lecante, Y. Jugnet and J. C. Verdine, *Phys. Rev. Lett* **43** (1979) 789.

[166] D. M. Riffe, G. K. Wertheim and P. H. Citrin, *Phys. Rev. Lett.* **63** (1989) 1976-1979.

[167] M. C. Desjonqueres, D. Spanjaard, Y. Lassailly and C. Guillot, *Solid State Communications* **34** (1980) 807.

[168] P. J. Feibelman, *Phys. Rev. B* **27** (1983) 2531.

[169] D. G. Dempsey and L. Keleinman, *Phys. Rev. B* **16** (1977) 5356.

[170] S. G. Louie, *Phys. Rev. Lett.* **40** (1978) 1525.

[171] D. Spanjaard, C. Guillot, M. C. Desjonquères, G. Tréglia and J. Lecante, *Surf. Sci. Rep* **5** (1985) 1-86.

[172] A. M. Begley, *Surface and bulk electronic structure in rare–earth metals*, PhD thesis, University of Birmingham, Birmingham, 1990.

[173] P. H. Citrin and G. K. Wertheim, *Phys. Rev. B* **27** (1983) 3176.

[174] P. H. Citrin, G. K. Wertheim and Y. Baer, *Phys. Rev. B* **27** (1983) 3160.

[175] A. R. Williams and N. D. Lang, *Phys. Rev. Lett.* **40** (1978) 954.

[176] N. D. Lang and A. R. Williams, *Phys. Rev. B* **16** (1977) 2408.

[177] C. S. Fadley, S. B. M. Hagstrom, M. P. Klein and D. A. Shirley, *J. Chem. Phys.* **48** (1968) 3779.

[178] D. A. Shirley, *Advan. Chem. Phys.* **23** (1973) 85.

[179] D. A. Shirley, R. L. Martin, S. P. Kowalczyk, F. R. McFeely and L. Ley, *Phys. Rev. B* **15** (1977) 544.

[180] A. Rosengren and B. Johansson, *Phys. Rev. B* **22** (1980) 3706.

[181] P. Soukiassian, R. Riwan, J. Cousty, J. Lecante and C. Guillot, *Sur. Sci.* **152/153** (1985) 290.

[182] S. Doniach and M. Sunjic, *J. Phys. C: Solid St. Phys.* **3** (1970) 285-291.

[183] J. E. Castle, H. Chapman–Kpodo, A. Proctor and A. M. Salvi, *J. Electr. Spectr.*

Related Phenom. **106** (2000) 65.

[184] G. P. Derby, *Surface core level shift studies of adsorbate covered Tungsten single crystal surfacec*, PhD thesis, University of Liverpool, Liverpool, 1989.

[185] P. Unsworth, J. E. Evans, P. Weightman, A. Takahashi, J. A. D. Matthew and Q. C. Herd, *Phys. Rev. B* **54** (1996) 286.

[186] G. D. Mahan, *Phys. Rev. B* **21** (1980) 4791.

[187] D. Sebilleau, G. Treglia, M. C. Desjonqueres, C. Guillot, D. Chauveau and D. Spanjaard, *J. Phys. C: Solid State Phys.* **20** (1987) 2647.

[188] P. W. Anderson, *Phys. Rev. Lett.* **18** (1967) 1049.

[189] D. M. Riffe, B. Kim, J. L. Erskine and N. D. Shinn, *Phys. Rev. B* **50** (1994) 14481.

[190] R. G. White, R. I. R. Blyth, N. P. Tucker, M. H. Lee and S. D. Barrett, *J. Synch. Rad.* **2** (1995) .

[191] D. M. Riffe and G. K. Wertheim, *Surf. Sci.* **399** (1998) 248-263.

[192] K. L. Håkansson, H. I. P. Johansson and L. I. Johansson, *Phys. Rev. B* **49** (1994) 2035.

[193] N. P. Tucker, R. I. R. Blyth, R. G. White, M. H. Lee, C. Seale and S. D. Barrett, *J.Phys.:Condens.Matter* **10** (1998) 6677-6686.

[194] H. W. Kim, J. R. Ahn, J. W. Chung, B. D. Yu and M. Scheffler, *Surf.Sci.* **430** (1999) L515–L520.

[195] P. F. Lyman and D. S. Mullins, *Phys. Rev. B* **51** (1995) 13623-13630.

[196] P. Alnot, D. J. Auerbach, J. Behm, C. R. Brundle and A. Viescas, *Surf. Sci* **213** (1989) 1.

[197] J. Jupille, K. G. Purcell and D. A. King, *Surf. Sci.* **367** (1996) 149-161.

[198] D. R. Mullins and P. F. Lyman, *Surf. Sci.* **285** (1993) L473.

[199] J. F. van der veen, F. J. Himpsel and D. E. Eastman, *Solid State Commun.* **40** (1981) 57.

[200] J. F. van der veen, F. J. Himpsel and D. E. Eastman, *Phys.Rev.B* **25** (1982) 7388.

[201] V. R. Dhanak, A. W. Robinson, G. Van der Laan and G. Thornton, *Rev. Sci.Instrum.*

63 (1992) 1342.

[202] J. Jupille, K. G. Purcell and D. A. King, *Solid State Commun.* **58** (1986) 529.

[203] M. Posternak, H. Krakauer, A. J. Freeman and D. D. Koelling, *Phys.Rev.B* **21** (1980) 5610.

[204] L. F. Mattheiss and D. R. Hamann, *Phys. Rev. B* **29** (1984) 5372-5381.

[205] A. M. James and M. P. Lord, *Macmillan's Chemical and Physical Data*, (Macmillan, London, UK,1992).

[206] T. W. Pi, L. H. Hong, R. T. Wu and C. P. CHENG, *Surface Review and Letters* **4** (1997) 1197-1201.

[207] Y. Baer and G. Busch, *J. Electron Spectrosc.* **5** (1974) 611.

[208] J. K. Lang, Y. Baer and P. A. Cox, *J. Phys. F:Metal Phys.* **11** (1981) 121-138.

[209] Y. Ufuktepe, *J. Phys: Condens. Matter* **5** (1993) L213-L216.

[210] L. Dottl, M. Onellion, L. Dongqi and P. A. Dowben, *Zeitschrift fur Physik B: Condensed Matter* **90** (1993) 93-102.